A Maximum-Likelihood Approach for Localizing and Characterizing Special Nuclear Material with a Dual-Particle Imager

by

John Kyle Polack

A dissertation submitted in partial fulfillment
of the requirements for the degree of
Doctor of Philosophy
(Nuclear Engineering and Radiological Sciences)
in the University of Michigan
2016

Doctoral Committee:

Professor Sara A. Pozzi, Chair
Professor Jeffrey A. Fessler
Assistant Professor Marek Flaska, Penn State University
Professor Zhong He
Peter Marleau, Sandia National Laboratory

Those who stay will be champions

-Bo Schembechler, 1969

Dedication

For my wife, Rachel.

You believed in me even when I did not and were right far more often than I liked to admit.

I could not have asked for a better companion on this journey

Acknowledgements

There are several people without whom this thesis would not have been a success. First, Professor Pozzi, who has provided significant support to me over during my graduate studies in the form of advice, funding, and unique research opportunities. Her willingness to take me on as a researcher opened the door to my continuation into the Ph.D. program. The remaining members of my committee have all had significant influences on my development beyond their contributions as committee members. Professor He first sparked my interest in radiation measurements during NERS 315 back in 2009. Professor Fessler has provided me with a wealth of knowledge related to image reconstruction; his incredible patience during our discussions truly underscores his passion for teaching. Marek and Pete are both wonderful mentors and have individually inspired some of my best work.

In my six years as a member of the DNNG team, I have had the opportunity to work with some very bright people. A great deal of my progress was a direct result of the strong foundations laid by the DNNG team, both past and present. Shaun Clarke has been a great resource for all things simulation related and has taught me a great deal about the how to best "tell the story". The two other long-standing members of the DPI project, Michael Hamel and Alexis Poitrasson-Rivière, were not only great colleagues, but are also great friends. We grew a lot during our time together, and always made sure to set aside time for the important things.

My family and friends have been incredibly supportive. Their patience and understanding throughout this process means a great deal to me, and their uncanny ability to provide me with necessary diversions from work have certainly helped keep me sane.

My work was made possible through various funding opportunities. This work was supported in-part by the National Nuclear Security Administration through NA-22 funding opportunity DE-FOA-0000568. It was also funded in-part by the Consortium for Verification Technology under Department of Energy National Nuclear Security Administration award number DE-NA0002534. The prototype system was funded in-part by the Department of Energy, Nuclear Energy University Program, Award number DE-NE0000324. My final three years of graduate school were sponsored by Sandia National Laboratories and the University of Michigan College of Engineering through the Excellence in Engineering Fellowship.

Thank you to everyone who has helped make this work a success!

.

Table of Contents

List of Figures

List of Tables

List of Appendices

Chapter 1. Introduction

1.1. Motivation

The threat of nuclear warfare is an ongoing global concern. The reduction of this threat is an international effort that is approached from two fronts. The first is the general agreement between (most) nations to prevent the proliferation of nuclear weapons, as well as any knowledge, technology, or materials that could allow the development of nuclear weapons [1]. This effort is governed by the 1968 Treaty on the Non-Proliferation of Nuclear Weapons (NPT), which acknowledges the existence of five nuclear-weapons states and outlines policies to prevent non-nuclear-weapons states from obtaining nuclear weapons.

The second front is the effort to reduce the magnitude of previously developed nuclear arsenals. While also addressed in the NPT, this effort is governed by additional treaties, such as the 2010 "New Start" treaty between the United States and Russia, which calls for a reduction to a specified number of deployed warheads and delivery vehicles by February 2018 [2].

Both fronts are heavily aided by numerous technologies aimed at the detection, localization, and characterization of special nuclear material (SNM) [3], [4]. SNM includes plutonium, ^{233}U, and uranium enriched above 20% in ^{235}U, and is further classified into categories based on the materials' mass as it relates to the development of a nuclear weapon [5]. Detection efforts related to non-proliferation include the search for diverted SNM and the safeguarding of nuclear materials to prevent the development of clandestine weapons

programs [6]. Additionally, emergency responders may need to investigate unknown objects to determine the presence of a potential radiological threat. If a threat is found, then it is particularly important to determine if the threat is a nuclear weapon. Such determinations are possible by characterizing the nature of the radioactive material, including its isotopic composition, size and mass, and determining if high explosives are present. Similar information is important to treaty verification applications because it is necessary to verify that an inspected object is consistent with what is expected. For example, an inspector can confirm through measurements that an object is indeed a dismantled warhead and not a hoax [7].

1.2. Measuring Special Nuclear Material

An effective method for obtaining information about SNM is by measuring the associated photon and neutron signatures. Both signatures provide unique information about the SNM sample and can also be used to infer information about any present shielding material. While there are many photon-emitting sources in the environment, neutron emitting sources are less likely to be present, and are therefore more likely to signify the presence of SNM.

Photon signatures from SNM will appear as both fixed-energy decay lines and broad distributions associated with nuclear fission [3]. Photons are also frequently created through the interaction of neutrons with other material in the surrounding environment. Neutron signatures will appear in a variety of energy distributions, the most notable of which is the Watt distribution, which is representative of neutrons originating from fission [3]. Also notable are the energy distributions associated with (α, n) reactions, which contribute to the neutrons emitted by SNM in oxide form. (α, n) distributions are also associated with ^{9}Be(α, n) sources, which often contain plutonium and can therefore be classified as SNM [3],

[8]. The specifics of the key photon and neutron signatures will be explained in greater detail as they become relevant to the measurements presented in this work.

It is possible to reduce the detectability of both photon and neutron signatures through the use of shielding. However, each particle interacts in a different, distinct manner depending on the material. Photons will preferentially interact with high-Z materials, and can therefore be effectively shielded by materials such as lead and tungsten [8]. Neutrons are more effectively moderated by low-Z materials, and can therefore be shielded by hydrogenous materials such as polyethylene. As a result, it is more difficult to shield a source from detection if a measurement system is sensitive to both photon and neutron signatures.

The amount of information contained in the photon and neutron signatures of SNM have led to the development of many measurement systems relevant to the non-proliferation and treaty verification fields [3], [4]. Some devices focus solely on count rates, while other devices aim to take advantage of the information contained in energy spectra and particle multiplicity distributions [3].

1.3. Radiation Imaging for Nuclear Non-Proliferation and Treaty Verification

Radiation imaging systems have a distinct advantage over more traditional systems in that they are able to provide localized information. While a particle counter can tell you if something is present and a spectrometer can tell you what is present, an imaging system can tell you what is present and where. Of course, it is also possible to obtain localized information with non-imaging systems. However, this requires actively measuring each location of interest with a well collimated detector, which can quickly become impractical if source locations are unknown. Imaging systems, on the other hand, can collect information

from many locations simultaneously, producing a single snapshot of the entire radiation field.

Many of the detection applications mentioned in Section 1.1 will benefit from the ability to obtain localized information of a radiation field. Search applications derive an obvious benefit from radiation imaging as the source location is inherently unknown. The International Atomic Energy Agency (IAEA) has publicly stated its interest in imaging systems for a variety of safeguards applications [6]. Emergency responders may wish to investigate and characterize a suspicious object without having to physically enter or open the object. Finally, arms-control inspectors can use imaging techniques to individually characterize several objects in close proximity to one another such as multiple reentry vehicles contained within a single warhead [9] or numerous plutonium pits stored in a dismantlement container [7].

Numerous imaging systems have been (and are currently being) developed to aid in the endeavors listed above. These systems leverage various imaging modalities including coded aperture [10]–[12], particle scattering [9], [13]–[15], and time-encoding imaging [16], [17]. Many of these imaging systems were developed to detect a single particle type of interest, either photons or neutrons. However, the benefits afforded by sensitivity to both neutrons and photons have led to the development of new systems [18]–[20] and new capabilities [21]. Realizing the full potential of these imaging systems requires the development of robust reconstruction and analysis algorithms capable of detecting, localizing, and characterizing any radioactive materials that might be present.

1.4. Contributions of This Work

This thesis presents a versatile detection system and powerful data-processing algorithm that, when combined, are well-suited to meeting many present challenges in the nuclear non-proliferation and treaty verification fields. The detection system, known as the Dual-Particle Imager (DPI), is a device capable of performing both imaging and spectroscopy with photons and fast neutrons [20]. These four data pathways make the DPI particularly well suited for the measurement of SNM.

The DPI was first presented in 2011 as a three-plane system designed with standoff detection in mind [22], [23]. In the 5 years since, the project has been fully developed from concept to functional prototype with significant contributions made by myself, as well as many other students and mentors. The system has gone through a complete design overhaul [24] and re-optimization [25], and has been used to successfully measure Category-III [25]–[27] and Category-I [28], [29] SNM samples. However, the development of the DPI is not the direct focus of this thesis and therefore much of the detailed information of the development process has been relegated to citations. Nonetheless, the existence of the DPI in its current form is an important contribution of this work.

The versatility of the DPI has facilitated the development of various image and spectrum reconstruction techniques [26], [30], [31]. One algorithm in particular, which I refer to as the "spectrum-isolation technique" [32], is the focus of this thesis. This technique leverages the maximum-likelihood expectation-maximization (MLEM) [33] and a robust system matrix, simulated in MCNPX-PoliMi [34], [35], to perform image reconstruction and simultaneously unfold localized energy spectra for each pixel in the image. The localized energy spectra make it possible to analyze multiple detected sources simultaneously and the spectrum

unfolding capabilities significantly improve the information available for characterizing the sources. Combining this algorithm with the DPI allows for localized spectra to be computed for photons *and* neutrons, which is particularly useful for the localization and characterization of SNM.

Accurate characterization of detected sources requires a robust algorithm with well characterized uncertainties that is capable of delivering consistently reliable information. This work presents a rigorous analysis of the spectrum-isolation technique and will demonstrate that it is indeed capable of accurately characterizing all detected radioactive material, even in complex multi-source environments. Additionally, the results will show that by leveraging the four major data pathways afforded by the DPI, it is not only possible to characterize shielded sources, it is also possible to make determinations on the type of shielding present. While the spectrum-isolation technique and the DPI are not inherently tied to one another, the union between the two results in an incredibly powerful and versatile tool.

1.5. Thesis Overview

Chapter 2 will discuss the theory and design of the DPI, as well as the standard image and energy reconstruction techniques that are based on the physical principals upon which the DPI is built. An overview will be given of the simulation techniques used throughout this work and an in-depth analysis of the factors impacting the energy and angular resolution of the DPI will be presented. Chapter 3 will outline the MLEM algorithm and the specifics of the binned system matrix, which together form the foundation of spectrum-isolation technique. Chapter 4 will present several experimental results of increasing complexity to demonstrate the utility of the spectrum-isolation technique for detecting, localizing, and characterizing

radioactive materials. Chapter 5 will investigate how statistical uncertainties in the measured data propagate through the reconstruction process and will also explore the impact of systematic uncertainties within the system matrix. This investigation will demonstrate the robustness of the system matrix and reliability of the spectrum-isolation technique for estimating the shape of localized energy spectra. Chapter 6 will test the claims made in the previous chapters by analyzing two complex experiments involving SNM. These experiments emphasize the extent of information that can be obtained about radioactive and shielding materials when using the spectrum-isolation technique. Finally, Chapter 7 will provide some final remarks and will also provide suggestions for future work towards further improving the capability of the DPI to detect, localize, and characterize SNM and other nuclear and non-nuclear materials.

Chapter 2. The Dual-Particle Imager

2.1. Concept and System Overview

This chapter, which is based in-part on work previously published in [15], [24], [25], and [36], will be used to give a detailed overview of the measurement system used in this work: the Dual-Particle Imager. The DPI is a radiation detection system capable of imaging photons and fast neutrons. The DPI was designed for localization and energy spectroscopy for both particle types. These capabilities make the DPI a powerful measurement tool for applications that necessitate the detection, localization, and characterization of SNM.

The DPI combines the concepts of a Compton camera and a neutron-scatter camera into a single device. The Compton camera is a mature concept for photon imaging that has been used for many years in fields such as medical imaging and astronomy [37]–[42]. Neutron-scatter cameras are the fast-neutron analog to Compton cameras. Recently, Compton cameras and neutron-scatter cameras have been developed for non-proliferation and safeguards applications [13], [14], [18], [19], [43].

Compton cameras and neutron-scatter cameras fall into a subset of imaging devices known as scatter cameras. Scatter cameras leverage the mechanics of particle elastic scattering to determine the incident energy and direction of a detected particle. To make these determinations, scatter cameras require that an incident particle undergo a minimum of two interactions within the system, including at least one elastic scatter. The detection

mechanisms for photons and neutrons within the framework of the DPI are described in detail in Sections 2.2.1 and 2.2.2 .

The DPI uses a two-plane geometry, similar to the one depicted in Figure 2.1, in which each plane is comprised of a 4×4 array of scintillators [20]. The front plane uses EJ-309 organic liquid scintillators as a scattering medium for both neutrons and photons. The back plane uses EJ-309 organic liquid scintillators as a neutron scattering medium, and NaI(Tl) scintillators, as a photon absorption medium. The reasons for choosing these detectors will be discussed in Section 2.3.

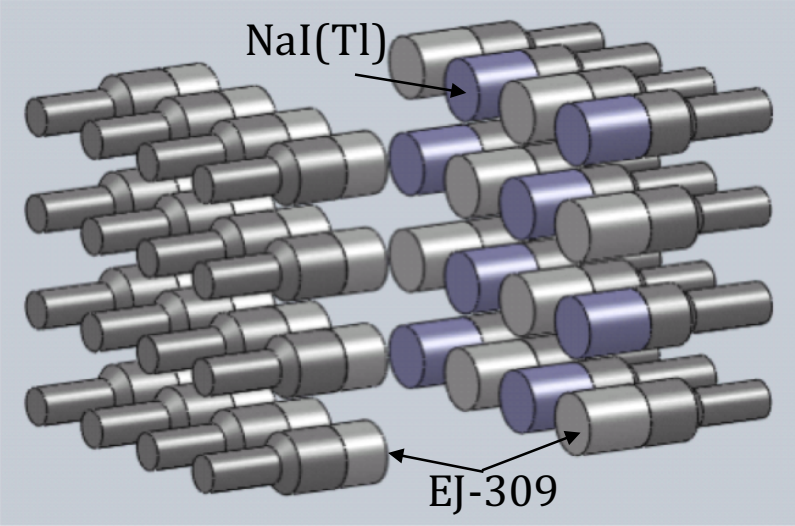

Figure 2.1. Schematic of the DPI geometry. Silver detectors represent EJ-309 organic liquid scintillators while blue detectors represent NaI(Tl) scintillators.

The two detector types in the second plane are arranged in a checkerboard pattern as seen in in Figure 2.1. All detectors are oriented such that the photomultiplier tubes face outward from the center of the system, which reduces the probability of scatters occurring between an interaction in the front plane and an interaction in the back plane. While the DPI is 4-π sensitive, the best results are achieved when the system is oriented such that the front plane is between the radioactive material (source) and the back plane [44]. In practice, if a

source is detected behind the system, the system should be rotated such that the front plane points towards the source.

2.2. Detection Mechanisms in the DPI

2.2.1. Photon Detection

Detection of a photon by the DPI relies on two types of photon interactions: Compton scattering and photoelectric absorption. In Compton scattering, a photon with incident energy, $E_{0,p,}$ elastically scatters off of an electron, depositing some of its energy in the process [8]. The scattered photon travels with an energy $E_{1,p}$ at an angle, θ_p, relative to its initial path. The relationship between θ_p, $E_{0,p}$, and $E_{1,p}$ is

$$\theta_p = \cos^{-1}\left(1 - \frac{m_e c^2\left(E_{0,p} - E_{1,p}\right)}{E_{0,p}E_{1,p}}\right) \quad (2.1),$$

where m_e=0.511 MeV/c^2 and is the rest mass of an electron. In photoelectric absorption, the incident photon deposits its full energy on the target atom, disappearing and producing a photoelectron and characteristic X-rays (or potentially an Auger electron) in the process [8]. These products have a short range and it is therefore safe to assume that photoelectric absorption results in a full transfer of the incident photon energy to the interaction medium.

Figure 2.2 diagrams a typical photon interaction within the DPI. In this diagram, $E_{d1,p}$ represents the energy deposited by the photon through a Compton scatter in a front plane detector, while $E_{d2,p}$ represents the energy deposited through photoelectric absorption in a back plane detector. Assuming that only a single scatter occurs in the scattering detector and the interaction in the absorption detector is a photoelectric absorption, then the scattered

energy of the photon, $E_{1,p}$, is equal to $E_{d2,p}$ and the incident energy of the photon is calculated as

$$E_{0,p} = E_{d1,p} + E_{d2,p} \tag{2.2}.$$

Substituting these equalities into Equation (2.1) yields the scattering angle in terms of the detected energies:

$$\theta_p = \cos^{-1}\left(1 - \frac{m_e c^2 (E_{d1,p})}{(E_{d1,p} + E_{d2,p})E_{d2,p}}\right) \tag{2.3}.$$

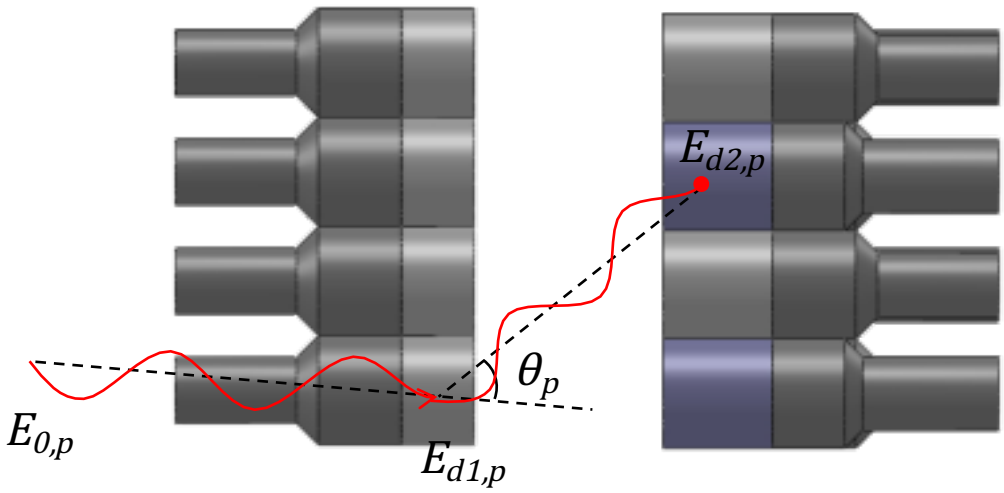

Figure 2.2. Schematic diagramming the interaction sequence of a photon in the DPI. $E_{0,p}$ and θ_p are the incident energy and the scattering angle of the photon, respectively. $E_{d1,p}$ and $E_{d2,p}$ are the energies deposited in the scatter detector and absorption detector, respectively.

While Figure 2.2 shows the photon interaction sequence in two dimensions, the process is three-dimensional and therefore θ_p defines the opening angle of a cone with an axis that is the vector between the Compton scatter and the photoelectric absorption. The surface of the resulting cone encompasses the possible locations of the photon's source, i.e. the radioactive material.

It is also possible to determine the incident energy and scattering angle of a photon through different interaction sequences than the one shown in Figure 2.2. For example, a photon could Compton scatter in a back plane EJ-309 detector prior to being absorbed in a NaI(Tl) detector. This event type is excluded from the remainder of this work due to the poor reconstruction properties associated with having a cone axis defined between two detectors of the same plane. The succession of three or more distinct interactions (i.e. 3 Compton scatters) also facilitates the calculation of a photon's incident energy and angle. This event type has a low probability of occurrence and is therefore excluded from the remainder of this work.

2.2.2. Neutron Detection

Neutron detection in the DPI relies on the neutron elastic scattering interaction. In this interaction, a neutron with incident energy $E_{0,n}$ interacts with the nucleus of an atom in a scatter detector, depositing some of its energy in the process [8]. The scattered neutron travels with an energy $E_{1,n}$ at an angle, θ_n, relative to its initial path, while the recoil nucleus travels with an energy E_R at an angle θ_R relative to the incident neutron's initial path. If it is assumed that the target nucleus is at rest, then E_R is equal to the energy deposited by the neutron. Equation (2.4) defines E_R in terms of the mass of the target nucleus, A [8]:

$$E_R = \frac{4A}{(1+A)^2}(cos^2\theta_R)E_{0,n} \tag{2.4}.$$

In organic scintillators, such as the EJ-309 liquid scintillators used in the DPI, neutrons will interact with either hydrogen or carbon nuclei. While a single neutron scatter on hydrogen (A=1) can result in a full energy transfer to the recoil nucleus (a single proton), a single neutron scatter on carbon (A=12) can transfer, at most, 28.4% of the neutron's energy

to the recoil nucleus. Additionally, due to their mass and charge, recoil carbon nuclei have a larger stopping power, dE/dx, than recoil protons. The increased stopping power results in more quenching, reducing the scintillation efficiency of recoil carbon nuclei relative to recoil protons. As such, interactions with carbon produce a small amount of scintillation light relative to interactions on hydrogen and it can be safely assumed that the vast majority of detected light is produced by a neutron scattering off hydrogen [45]. However, it should be noted that when "invisible" scatters off of carbon occur in coincidence with a hydrogen scatter, the kinematic assumptions made in the following discussion are incorrect and result in a miscalculated scattering angle.

When neutrons scatter off hydrogen nuclei, $\theta_R+\theta_n=90°$ as a result of the hydrogen nucleus (a single proton) having approximately the same mass as a neutron. This relation allows for the substitution

$$cos^2\theta_R = 1 - cos^2\theta_n \tag{2.5}.$$

For A=1, the fractional term in Equation (2.4) drops out. Then, using Equation(2.5) and noting that $E_R=E_{0,n}-E_{1,n}$, Equation (2.4) can be reduced to

$$\theta_n = \cos^{-1}\left(\sqrt{\frac{E_{1,n}}{E_{0,n}}}\right) \tag{2.6},$$

which defines the scattering angle of the neutron in terms of its initial and scattered energies.

At neutron energies relevant to this work (less than 10 MeV), it is reasonable to use the classical approximation of kinetic energy because it deviates less than ~1.5% from the relativistic calculation. Therefore, the relationship between the energy of a neutron, E_n, the neutron rest mass, m_n, and the velocity of the neutron v_n is defined as:

$$E_n = \frac{1}{2} m_n v_n^2 \tag{2.7}$$

If the time and distance between two consecutive neutron interactions are known, then it is possible to use Equation (2.7) to calculate the energy of the neutron between interactions.

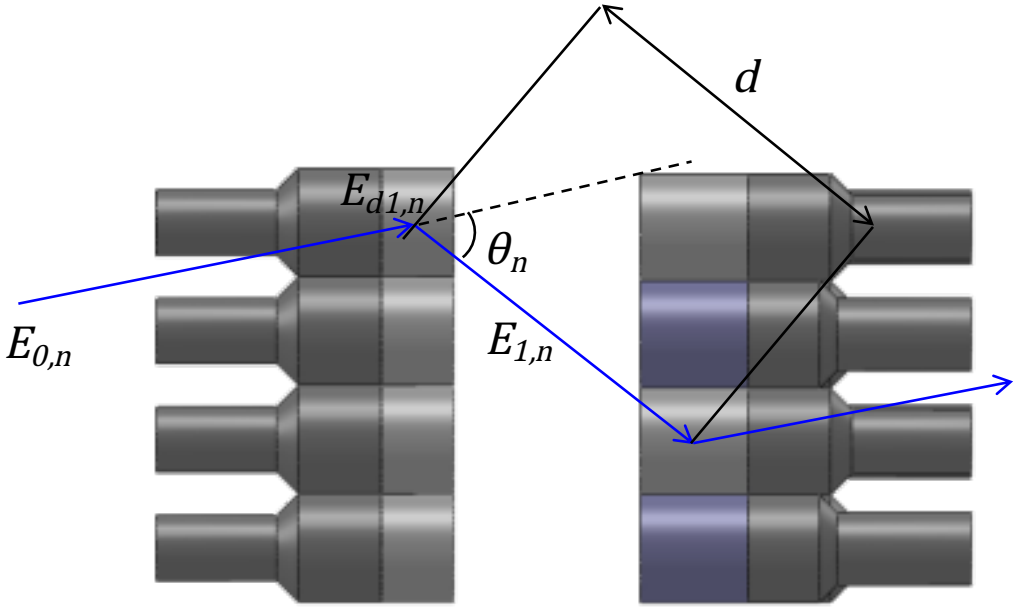

Figure 2.3. Schematic diagramming the interaction sequence of a neutron in the DPI. $E_{0,n}$ and θ_n are the incident energy and the scattering angle of the neutron, respectively. $E_{d1,n}$ is the energy deposited by the first neutron interaction. $E_{1,n}$ is the energy of the neutron as it travels a distance, d, prior to its second interaction.

Figure 2.3 diagrams a typical neutron interaction within the DPI that produces a cone of possible origin directions. In this diagram, $E_{d1,n}$ is the energy deposited by the neutron through an elastic scatter in a front plane liquid scintillator and $E_{1,n}$ is the energy of the neutron as it travels distance d before interacting in a back plane liquid scintillator. The time between these interactions is commonly referred to as the time-of-flight (TOF). Using the known detector separations for d and the measured TOF, $E_{1,n}$, is found by using Equation (2.7):

$$E_{1,n} = \frac{1}{2} m_n \left(\frac{d}{TOF}\right)^2 \tag{2.8}$$

Then, assuming only a single scatter occurs in the front plane detector, the incident energy of the neutron, $E_{0,n}$, is computed as

$$E_{0,n} = E_{d1,n} + E_{1,n} \quad (2.9).$$

The scattering angle, θ_n, can then be calculated using Equation (2.6). Similar to Compton scatters, θ_n defines the opening angle of a cone whose axis is defined by the vector between the elastic scatters in the front and back plane. The resulting cone encompasses the possible neutron source locations.

Equations (2.6) and (2.9) assume that the first neutron interaction is in the front plane. Given that the maximum scatter angle of a neutron on hydrogen is 90°, almost all non-accidental coincidence events will begin with an interaction in the front plane. However, if a source is located behind the system, then it becomes more likely that the first interaction is in a back plane detector. It is possible to accurately reconstruct these events by modifying Equations (2.6) and (2.9) such that $E_{d1,n}$ is the energy deposited in the back plane and θ_n is measured relative to the back plane detector rather than the front plane detector. The experiments performed in this thesis only include sources located in front of the DPI, and therefore neutron coincidence events that begin with an interaction in the back plane will be ignored.

2.3. System Geometry and Components

All measurements discussed in this work use the geometry depicted in Figure 2.4. This geometry features a 15-cm spacing between detectors centers in the front plane, a 25-cm spacing between detector centers in the back plane, and a 30-cm spacing between detector faces for each plane. Optimization of the system geometry is difficult because system

efficiency is improved by having a close packed detector arrangement while resolution is improved by well separated detectors. The chosen separations provide a good balance between these two parameters; a full discussion of the methodology used to determine these separations is discussed by Poitrasson-Rivière, et al. in [25].

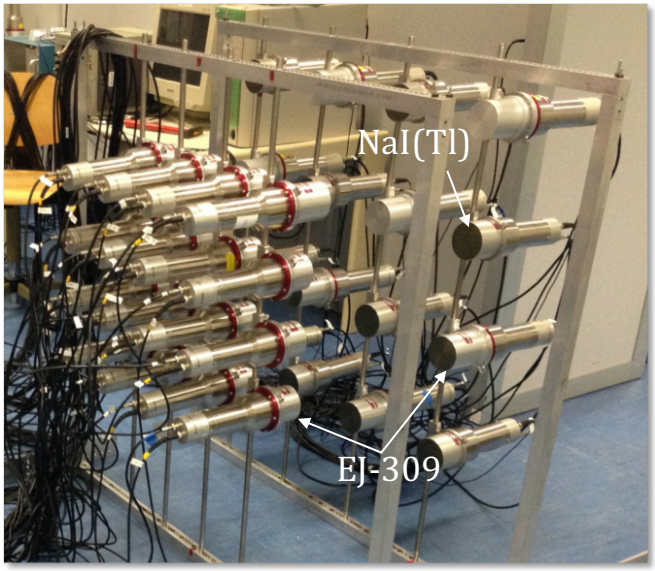

Figure 2.4. Prototype geometry of the DPI. Front plane detectors have a 15-cm separation (measured between centers of adjacent detectors). Back-plane detectors have a 25-cm separation (measured between centers of adjacent detectors). Detector planes are separated by 30 cm.

2.3.1. EJ-309 Organic Liquid Scintillators

EJ-309 organic liquid scintillators were chosen for the scattering detectors because of their relatively low cost, commercial availability, and, most importantly, sensitivity to both photons and fast neutrons [46]–[48]. The detectors in the front plane are cylindrical with a diameter of 7.62 cm and a thickness of 5.08 cm. The detectors in the back plane are cylindrical with a diameter of 7.62 cm and a thickness of 7.62 cm. The choice of detector material and size are discussed in detail in [15]. The energy resolution of the Ø7.62×762 cm^3 EJ-309 scintillators was studied by Enqvist, et al. and found to be approximately 15% at energy ranges of interest to this work [49]. The signals for these detectors are read out

through fast photomultiplier tubes (PMT) manufactured by Electron Tubes [50]. These PMTs have a 2.2 ns single electron jitter full-width at half-maximum (FWHM), and are capable of capturing the quick rise and decay of EJ-309 pulses, which facilitates the use of the charge-integration pulse-shape discrimination as described in Section 2.3.1.1.

2.3.1.1. Pulse-Shape Discrimination

Discriminating between photons and neutrons in organic scintillators, such as EJ-309, is commonly performed using the charge-integration pulse-shape discrimination (CIPSD) method. In CIPSD, pulses are identified based on the fraction of the pulse that falls within the "tail" region of the pulses. This fraction is dictated by the amount of phosphorescent and delayed fluorescent light produced, which is dependent on the density of triplet states induced along the charged-particle interaction path [8]. Heavier charged particles will produce a higher density of triplet states because they exhibit a higher density of energy loss, dE/dx [8]. For equivalent energy depositions, protons recoiling from neutron elastic interactions result in a larger tail (slow) component than electrons recoiling from photon Compton interactions [8]. In CIPSD, the integral of a pulse is taken over two regions to determine the fraction of the pulse that occurs in the tail. The first region includes the entire pulse and, for fast organic scintillators such as EJ-309, typically ranges from several nanoseconds prior to the peak of the pulse to several hundred nanoseconds after the peak of the pulse [51]. The integral of this region is referred to as the "total integral". The second region includes only the tail portion of the pulse and, for fast organic scintillators, typically begins several nanoseconds after the pulse maximum and extends to the same time as the total integral region [51] The integral of this region is referred to as the "tail integral". The

definition of the integration regions is important to the overall performance of the CIPSD method and must be optimized for the type of detectors used [51].

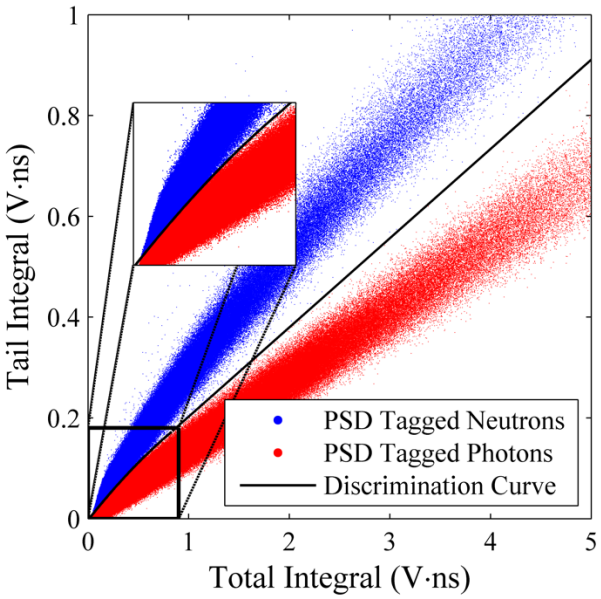

Figure 2.5. Typical tail-integral-vs.-total-integral scatter plot resulting from the use of CIPSD. The discrimination curve used to classify particles is shown in black with pulses classified as neutrons plotted as blue points and pulses classified as photons plotted as red points. The inset emphasizes cluster overlap at low-energy depositions and is representative of the 40-keVee thresholds typically used in this work.

With the computed tail and total integrals, it is possible to generate a scatter plot of pulses with axes for the tail integral and total integral. This scatter plot will show two clusters of points, as seen in Figure 2.5. The points in the upper cluster signify pulses with a higher relative fraction of light in the tail region and correspond to pulses from heavier particles. Conversely, the points in the lower cluster correspond to pulses with a lower relative fraction of light in the tail region. A "discrimination curve" (or line) can be defined that separates the neutron and photon clusters. This curve is used to classify pulses as coming from photons (if they are located below the discrimination curve) or neutrons (if they are located above the discrimination curve). The distribution shown in Figure 2.5 is representative of a typical CIPSD plot for the EJ-309 detectors used in this work. When using

low energy thresholds, such as the 40 keVee thresholds used in this work, the two clusters overlap at low total-integral values. This overlap introduces misclassification (i.e. a neutron may be classified as a photon, or vice-versa) because the discrimination curve cannot accurately separate the clusters in the overlapping region. The misclassification problem can be mitigated by increasing the energy threshold of the detector; however, increasing the threshold reduces the measureable neutron energy range.

For optimum classification of pulses, the discrimination curve for each detector should be calibrated individually and on a regular basis. The calibration process can become very time consuming for a large, multi-detector system such as the DPI. To facilitate this process, an algorithm, called Auto Slice PSD, was developed, which automates the CIPSD method. Auto Slice PSD determines a discrimination curve by first binning the data into smaller subsets, then by fitting the distribution of tail-to-total-integral ratios in each slice, and finally by using the fits to find the optimal discrimination points that minimize pulse misclassification in each bin. Once identified, these points are used to fit a discrimination curve through the data set. Through additional analysis of the slice-by-slice fits, it is possible to estimate the fraction of misclassified neutrons and photons. A more detailed description of the methodology used in this algorithm can be found in Appendix B. A full description of the algorithm and an assessment of its performance is described in [36].

2.3.2. NaI(Tl) Scintillators

NaI(Tl) scintillators were chosen for use as the photon absorption detectors due to their relatively high photoelectric absorption efficiency at relevant energy ranges [21], relatively low cost [8], [52], and energy resolution as good as 6.5% [53]. This resolution is adequate for being paired with EJ-309 detectors because the total energy resolution of a coincidence

event will be dominated by the lower resolution in the EJ-309. The NaI(Tl) scintillators are cylindrical with a diameter of 7.62 cm and a thickness of 7.62 cm. The choice of detector material and size are discussed in detail in [15].

2.3.3. Waveform Digitization

The waveforms produced by both detector types are collected using digitization. In parts of this work, four eight-channel CAEN V1720 digitizers were used. These digitizers have a 250-MHz sampling rate and 12-bit resolution [54]. In other parts of this work two 16-channel CAEN V1730 digitizers, which have a 500-MHz sampling rate and 14-bit resolution were used [55]. Despite having twice the sampling frequency of the V1720s, the V1730s facilitate increased data throughput for the DPI by leveraging advancements in on-board pulse processing, including on-board charge integration, which eliminates the need to transfer the entire waveforms.

2.4. Basic Reconstruction Techniques

The detection principles described in Section 2.2 lead directly to the most basic image and energy spectrum reconstruction techniques used by the DPI. Although these basic reconstruction principles facilitate straightforward imaging and spectroscopy, they are limited due to their convolution with intrinsic detector effects. These effects include energy, timing, and spatial resolution; their impact on location and energy reconstruction will be discussed in further detail in Section 2.6. In order to improve on these basic reconstruction principles, it is important to understand how they can be used to locate and characterize radioactive sources detected by the DPI.

2.4.1. Backprojection Imaging

In backprojection imaging, the cones defined by the scattering angles computed using Equations (2.3) and (2.6) are projected onto a distant surface. In the case of the DPI, this surface is typically a sphere. As detected events are accumulated, the projected cones from each event overlap. When many cones from the same source overlap, a "hotspot" will form. The location of the hotspot signifies the azimuthal and inclination angle of the detected source relative to the DPI. When only direction is relevant, coordinates will be reported as (azimuthal angle, inclination angle). When standoff distance is relevant, coordinates will be reported as (standoff, azimuthal angle, inclination angle). The coordinate system of the DPI is set such that (90°, 90°) corresponds to a point directly in front of the system at the center of the field of view (FOV). Figure 2.6 shows an example of how a typical backprojection image develops as the number of detected events increases; in this example the source was located at (90°, 90°).

If multiple sources are present, then multiple hotspots will appear. However, if the sources are located in close proximity to one another, the intrinsic angular resolution of the DPI can cause multiple, separated sources to appear as a single extended source. This effect demonstrates the importance of deconvolving intrinsic system response during image reconstruction.

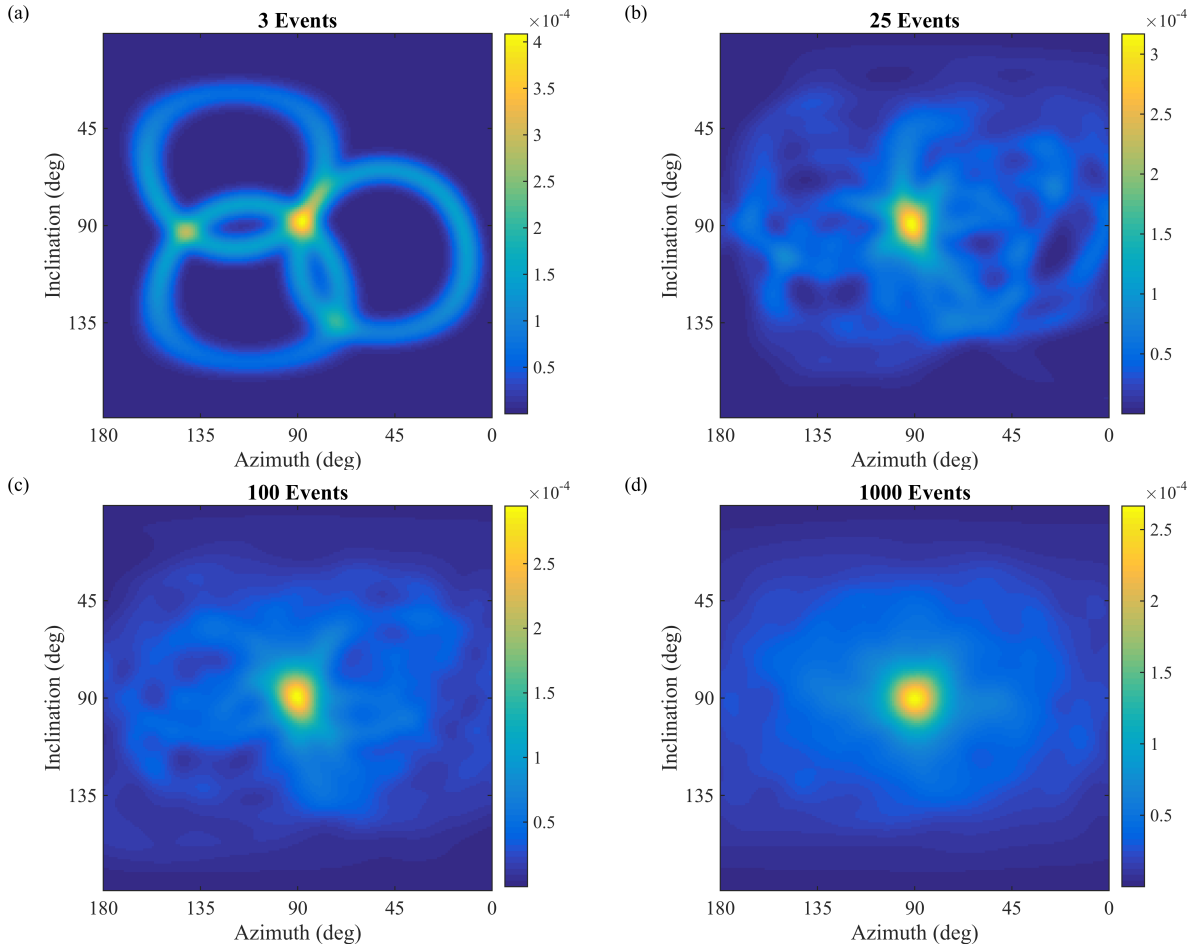

Figure 2.6. Backprojection image using 3 events (a), 25 events (b), 100 events (c), and 1000 events (d). As more events accumulate, the overlapping backprojection cones show the location of the source to be (90°, 90°).

2.4.2. Energy Spectroscopy

Energy spectra can be created by generating a histogram of the reconstructed energies for each detected event. The reconstructed energies are computed using Equations (2.2) and (2.9) for photons and neutrons, respectively. As with any basic energy spectroscopy technique, these spectra are convolved with the intrinsic detector response of the DPI. Spectra created using this technique will be referred to as "coincidence spectra" throughout the remainder of this work.

This basic technique is suitable for energy spectrum reconstruction across the entire FOV. Coincidence spectra, however, are less informative if multiple sources or a significant

contribution from environmental background is present. It is possible to use the basic reconstruction technique to estimate localized energy spectra by creating a histogram of the energies for each cone that overlaps any location of interest. However, because a single cone overlaps many locations in addition to the correct source location, the localized spectra will suffer from cross-contamination with the spectra of non-local regions. The spectrum-isolation technique, which will be discussed in Chapter 3, mitigates the issues of cross-contamination.

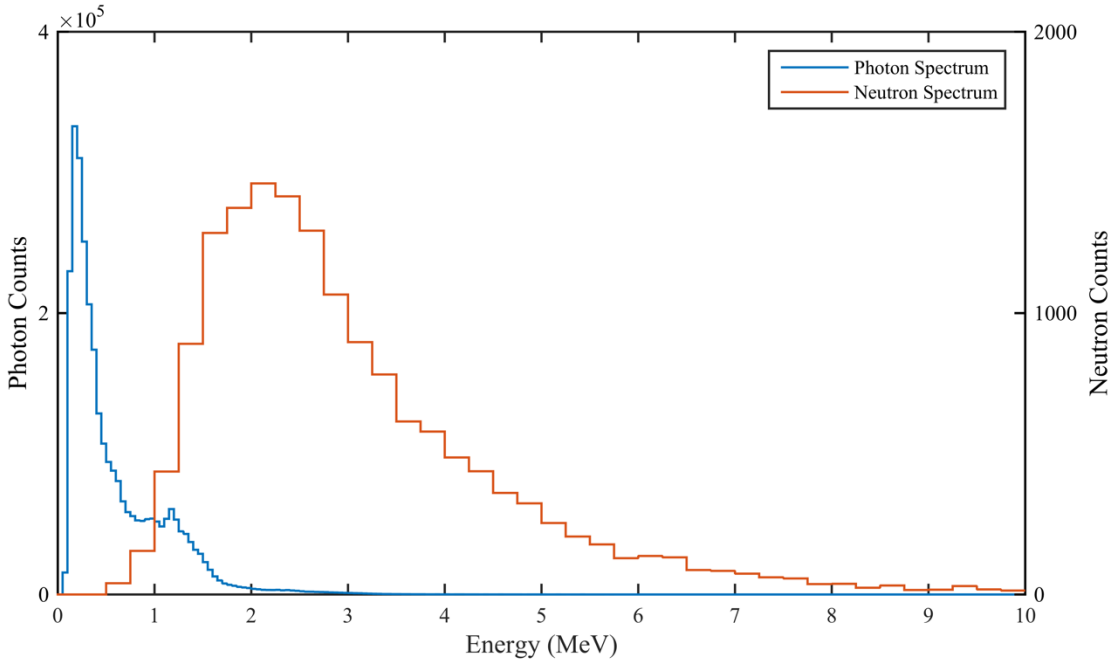

Figure 2.7. Coincidence photon and neutron energy spectra for a measurement of ^{252}Cf and ^{60}Co. Photon spectrum uses 0.05 MeV bins while neutron spectrum uses 0.250 MeV energy bins.

Figure 2.7 shows the photon and neutron coincidence spectra for a measurement of ^{252}Cf and ^{60}Co point sources, which were located at (114°, 93°) and (58°, 84°), respectively. The photon spectrum contains contributions from the decay lines of ^{60}Co (1.17 and 1.33 MeV), the exponentially decaying spontaneous fission spectrum of ^{252}Cf [3], and the natural photon background. The neutron spectrum contains neutrons from the spontaneous fission

spectrum of ^{252}Cf and a negligible contribution from the natural neutron background in the laboratory. Previous studies have shown that neutron background count rates in the EJ-309 detectors used in the DPI are less than 10 counts-per-second [56]. However, the requirement of coincident interactions reduces the neutron background count rate in the DPI to below 1 count-per minute. While the spectra are somewhat indicative of the emitted spectra, they are degraded due to intrinsic detector effects and, for photons, the cross-contamination between sources. In Chapter 4, this measurement will be presented in greater detail to help demonstrate the improvements in reconstruction afforded by the spectrum-isolation technique.

2.5. Simulation Techniques

Much of the work in this thesis relies on the ability to accurately simulate the response of the DPI. During development of the system, simulation tools facilitated the choice of detector materials and sizes as well as system geometry [25]. Reliable simulation techniques also facilitate the characterization of the system performance by enabling a variety of metrics to be assessed over a wide range of source-energy and -location distributions that may be impractical (or in some cases impossible) to measure. This idea will be further explored in Chapter 3, which will discuss the role of simulations in modeling the system response of the DPI for use with the spectrum-isolation technique. Sections 2.5.1 and 2.5.2 describe the simulation and detector-response post-processing tools used to make accurate simulation of measured data possible.

2.5.1. Radiation Transport Code

MCNPX-PoliMi is a modified version of the MCNPX Monte Carlo transport code [57]. MCNPX-PoliMi allows the user to track detailed interaction information in user-specified

cells [34], [35]. The information recorded includes, but is not limited to, the physical interaction process, the energy deposited by an interaction, and the location of interaction. Tracking this information in detector cells provides the requisite information to generate realistic detector responses.

MCNPX-PoliMi includes a variety of source models of interest to the DPI project including spontaneous fission sources such as ^{252}Cf, ^{238}Pu, ^{240}Pu, ^{242}Pu, and ^{238}U, as well as (α, n) sources such as Am-Be, Am-Li, and PuO_2 variants. The included source models account for particle birth parameters including energy, multiplicity, and directional anisotropy. The full list of available sources is found in [58].

2.5.2. Detector-Response Calculations

MPPost is a dedicated post-processing software package for use with the MCNPX-PoliMi simulation tool [59], [60]. MPPost uses a multi-step process to convert the detailed interaction output file from MCNPX-PoliMi to a realistic detector response. Each pulse is defined solely by its pulse height and the time of interaction. When modeling scintillators, such as EJ-309 or NaI(Tl), MPPost first converts energy depositions into light. If multiple interactions in a single detector fall within the pulse generation time of that detector, they are combined into a single pulse. If multiple interactions are combined, the light produced by each interaction is summed and the time is taken as the time of the first interaction in the series. Because the full pulse is not modeled, misclassification due to pulse-shape discrimination is not currently accounted for in MPPost. Time and energy resolutions are applied to each pulse prior to applying measurement specific filtering, such as the energy thresholds and limits that define the dynamic range of the waveform digitization process.

The accuracy of the parameters used in the post-processing step is crucial for accurate modeling. Much of the previous work on the DPI converted energy to light for neutron interactions using the functional form described by Enqvist et al. [49]. However, recent work by Norsworthy et al. [61] suggests that a more accurate conversion can be made using physical models of proton stopping power proposed by Birks [62] and Voltz [63]. The results presented in this work utilize an updated model from [61]. Published energy resolution functions were used for both EJ-309 [49] and NaI(Tl) [64] detector responses. The time resolution for NaI(Tl) detectors was sampled from a Gaussian with a full-width half-maximum (FWHM) of 10 ns [8], [44]. The time resolution for EJ-309 detectors was measured to be Gaussian with a FWHM of approximately 1 ns [20], [44].

After MPPost generates an individual response for each detector, an additional subroutine specific to the DPI is used to identify coincident events, which are pulses that occur in separate detectors within a specific coincidence time window. In this work, successive neutron pulses are in coincidence if they occur between 5 and 100 ns of each other. The size of this window encompasses the expected TOFs for the system geometry and energies of interest. Photon pulses are in coincidence if they occur within 25 ns of each other, which is approximately ± 3 standard deviations for a 10 ns FWHM. This window was found empirically to be sufficiently large enough window to capture all true photon coincidences. If more than two photon pulses fall within the coincidence window, the pulses are discarded because the time resolution makes it difficult to accurately determine the interaction order. It is worth noting that further analysis of the energy depositions and detector locations might make it possible to determine the interaction order with reasonable accuracy; such an investigation is encouraged as future work.

For each coincident event, the incident energy and scatter angles are computed as discussed in Section 2.2. This information is stored in an output file along with other relevant information, including detector location for each interaction, order of interactions, light produced in each detector, and time between interactions. The same coincidence subroutine is also used to process measured data and produces a similar output file, which makes it straightforward to compare measured and simulated data sets. A comparison between measured and simulated data experiments is discussed in [25].

2.6. System Resolution

The detection theory described in Section 2.2 will provide accurate estimates of the incident energy and scattering angle of a particle in the absence of any resolution related uncertainties. Section 2.5.2 discussed how energy and time resolution must be accounted for to produce realistic simulation results. The uncertainty due to energy and time resolution are two of the three major contributors to the overall angular and energy resolution of the DPI. The third contributor is the spatial resolution within individual detector cells. The detectors used in the DPI are not position sensitive and it is therefore assumed that any detected interaction occurs at the center of the detector. This assumption results in uncertainty of the interaction location within a voxel.

It is important to understand how each of these components impacts the overall resolution of the DPI. Equations (2.6), (2.8), and (2.9) suggest that the uncertainty in incident energy and scattering angle of a neutron will depend on all three resolution components. Time resolution will impact the *TOF* term. Energy resolution will impact the accuracy of the $E_{d1,n}$ term. Spatial resolution will impact the d term, because d is calculated using the center of each detector rather than the true (unknown) interaction locations. Spatial resolution will

also impact the accuracy of the backprojection cone axis. Equations (2.2) and (2.3) suggest that uncertainty in incident energy and scattering angle of a photon will only depend on the energy resolution component. However, as with neutrons, the spatial resolution component will impact the accuracy of the backprojection cone axis.

It is possible to analytically determine the uncertainty introduced by each of these resolution components by propagating the resolution terms through the computation of incident energy and angle. However, such a computation ignores the uncertainties introduced by simplifications such as assuming single interactions in the front plane, assuming full energy deposition of photons in the back plane, ignoring neutron scatters off carbon, and assuming that incident particles only interact in the detector materials. While these effects may not typically be deemed "resolution effects" they will introduce additional uncertainties and biases in the reconstructed solutions. An understanding of these additional effects is important to implementing an accurate unfolding algorithm, such as the spectrum-isolation technique described in Chapter 3.

A simulated data set was used to explore how resolution and additional effects impact accuracy in the reconstructed energy and angle. The data set included photons with energies between 0 and 5 MeV and neutrons with energies between 0 and 10 MeV, which allowed for the resolution to be studied as a function of incident particle energy. These energy ranges are sufficient for the study of non-proliferation and treaty-verification applications and correspond to the energy ranges used for the spectrum-isolation technique. All particles were emitted isotropically from (90°, 90°) at a 5-m standoff. Energy thresholds were set at 0.04 MeVee for all detectors, which equates to a 0.04 MeV deposition for photons and a 0.366 MeV deposition for neutrons. Because two interactions are needed to obtain a coincidence

event, these thresholds correspond to minimum detectable energies of 0.08 MeV for photons and 0.732 MeV for neutrons.

The data set was processed using five different MPPost resolution settings. The first assumed the exact energy, time of interaction, and location of interaction are known, i.e. perfect energy, time, and spatial resolution. The next assumed operational resolution, which applied the appropriate uncertainty to each of these three parameters. The final three scenarios applied uncertainty to each of the three parameters individually while leaving the other two parameters assuming perfect resolution. For example, if energy resolution was applied, timing and spatial information were assumed to be perfect.

2.6.1. Angular Resolution

The angular resolution was studied by computing the difference, Δ_θ, between the reconstructed scattering angle, θ, and the angle required for the cone to intersect the known source location, θ_{true}, which is defined as

$$\theta_{true} = \cos^{-1}(\vec{\boldsymbol{v}}_s \cdot \vec{\boldsymbol{v}}_d) \tag{2.10}.$$

In Equation (2.10), $\vec{\boldsymbol{v}}_s$ is the unit vector that points from the interaction in first detector to the true source location and $\vec{\boldsymbol{v}}_d$ is the unit vector that defines axis of the cone. If spatial resolution was applied, then θ_{true} was computed based on the center of each detector.

2.6.1.1. Neutrons

The neutron data set was divided into 0.5 MeV bins with a range of 1 to 10 MeV. In each energy bin, a histogram of the angular resolution parameter, Δ_θ, was computed for each of the five resolution settings. Figure 2.8 (a) shows the five resolution functions for events with energies between 2.0 and 2.5 MeV. As expected, the "operational resolution" curve is the broadest; this is followed in order by the spatial, energy, timing, and perfect curves.

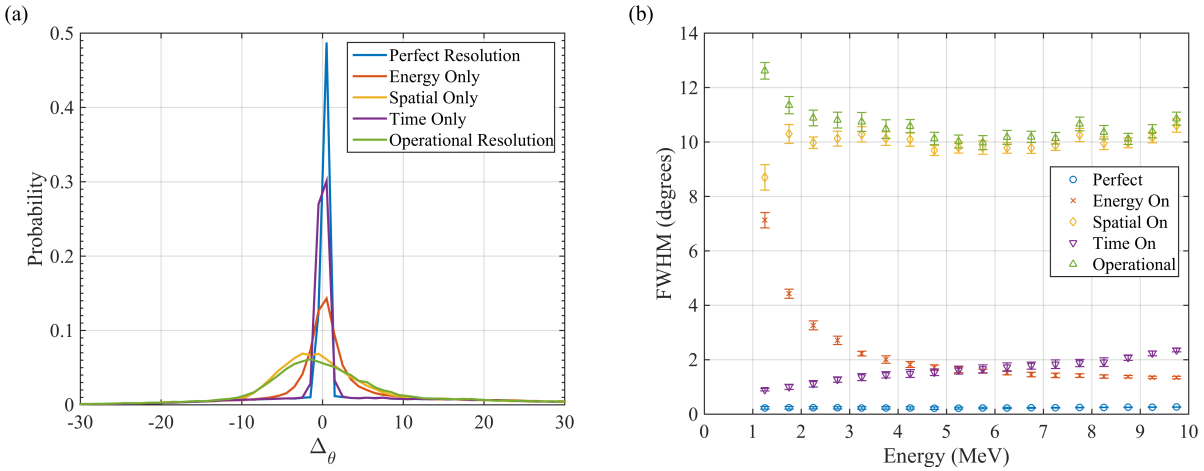

Figure 2.8. Angular resolution components for neutrons between 2.0 and 2.5 MeV (a). FWHM of neutron angular resolution components as a function of incident energy (b).

A small negative bias occurs in the means of the operational resolution and spatial resolution curves, which suggests that setting the interaction location to be the center of a voxel introduces a systematic bias. An artificial inflation of the distance travelled by a scattered neutron would produce a systematic bias towards a higher interplanar energy, E_1, which would in turn result in the calculation of a smaller scattering angle, θ_n. It is worth noting that this bias is not easily accounted for as the interaction location will vary as a function of the incident energy (which will determine the mean free path of the neutron in the detector) and also as a function of the incident direction.

Figure 2.8 (b) shows the FWHM for each of the five resolution curves as a function of incident energy. The FWHM was computed using the width parameter from a Gaussian fit of the central region each resolution curve. While some components are expected to follow a Gaussian behavior, others are not; however, a Gaussian was found to be a reasonable approximation for all curves at amplitudes above their half-maximum. Error bars are included with the estimated FWHM values to account for the uncertainty introduced by the fitting approximation. The error bars represent the appropriately scaled the 95% confidence interval on the estimated Gaussian width parameter.

The trends presented in Figure 2.8 show that the neutron angular resolution, which is equivalent to the FWHM, is approximately 11° over the full energy range investigated. Spatial resolution is the dominant component of the overall angular resolution, with energy resolution becoming the larger contributor below approximately 3 MeV. The magnitude of perfect resolution curve is small relative to the other curves, which suggests that secondary effects are negligible relative to the major resolution components.

2.6.1.2. Photons

The same technique was used to determine the photon angular resolution. 0.25 MeV incident energy bins were used over the 0-5 MeV range. Figure 2.9 (a) shows the resolution curves for events with incident energies between 1.0-1.25 MeV. Again, spatial resolution is the broadest of the three individual components, followed by the energy resolution. The timing resolution curve is identical to the perfect resolution curve, which was predicted by Equation (2.3). Figure 2.9 (b) shows the FWHM of each of the resolution curves as a function of incident energy. Similar to neutrons, the overall angular resolution is approximately 11° and is dominated by the spatial resolution component over most of the investigated range. Below 1 MeV, energy resolution becomes a larger contributor and becomes the dominating factor for photons between 0.25 and 0.5 MeV. Similar to neutrons, the perfect curve is low in magnitude relative to the resolution components, suggesting that secondary effects have a negligible impact on the accuracy of the reconstructed scatter angle.

It is worth noting that the spatial resolution component was only expected to impact photon angular resolution through its involvement in the determination of the cone axis. Due to the similarity in magnitudes between the spatial resolution component for photons and

neutrons, it can be argued that error in cone axis (rather than error in neutron travel distance) is the driving component in neutron angular resolution as well.

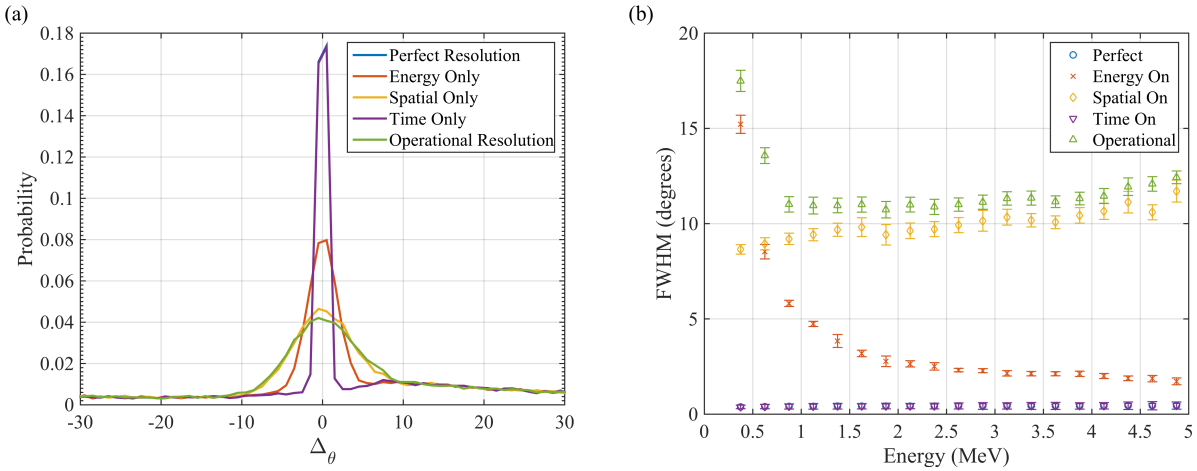

Figure 2.9. Angular resolution components for photons between 1.0 and 1.25 MeV (a). FWHM of photon angular resolution components as a function of incident energy (b). In both figures the time resolution curve overlaps the perfect resolution curve.

2.6.2. Energy Resolution

The energy resolution was studied with a similar technique to the angular resolution; the difference in energy, Δ_E, was calculated between the reconstructed energy and the emitted energy. Individual resolution curves were then fit as a Gaussian to determine the FWHM and associated 95% confidence interval.

2.6.2.1. Neutrons

Figure 2.10 (b) shows the reconstructed energy resolution curves for neutrons with an incident energy between 2.0 and 2.5 MeV. Similar to neutron angular resolution, a small bias is seen in the means of the operational and spatial resolution curves. The energy bias is positive, which corresponds to the theory of an artificially inflated travel distance between detectors.

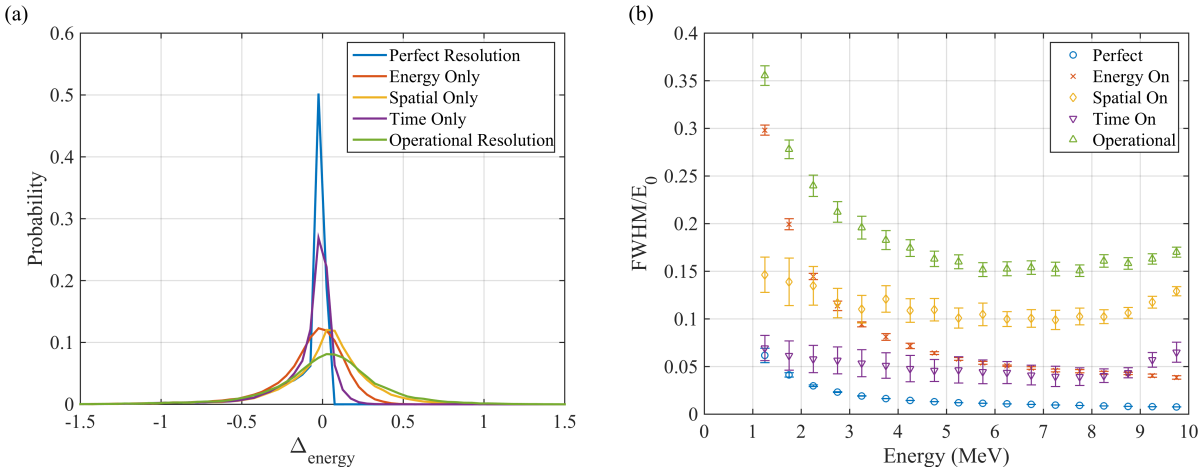

Figure 2.10. Energy resolution components for neutrons between 2.0 and 2.5 MeV (a). FWHM of neutron energy resolution components as a function of incident energy (b).

Figure 2.10 (b) shows the reconstructed neutron energy resolution components as a function of incident energy. To represent the standard definition of energy resolution, the FWHM has been scaled by the mean incident energy for each bin. Similar to neutron angular resolution, the spatial component is the driving factor over most of the investigated range. Energy resolution, however, has the largest impact below 3 MeV. The relative magnitude of the three individual components are more similar for neutron energy than what was observed for neutron scattering angle. This observation supports the theory that the error in cone axis due to spatial resolution (which does not impact energy reconstruction) is the driving factor in angular resolution. The perfect resolution component grows at lower energies, which suggests that effects outside of spatial, energy, and time resolution are contributing. These effects include scattering in materials outside of the detector active volumes and multiple scatters in the front plane detectors with “invisible” scatters on carbon.

2.6.2.2. Photons

Figure 2.11 (a) shows the reconstructed energy resolution components for photons with an incident energy between 1.0 and 1.25 MeV. Both Figure 2.11 (a) and (b) show that, as expected, energy resolution is the only component impacting the overall reconstructed photon energy resolution. In both figures the time and spatial resolution components overlap the perfect resolution curve while the operational curve overlaps the energy resolution component. Similar to neutrons, there is an increase in the contribution of the perfect component at low energies, which suggests that there are additional effects outside of spatial, energy, and time resolution. These effects include interacting in material outside the active detector volume and Compton scattering in the NaI(Tl) detectors rather than undergoing photoelectric absorption.

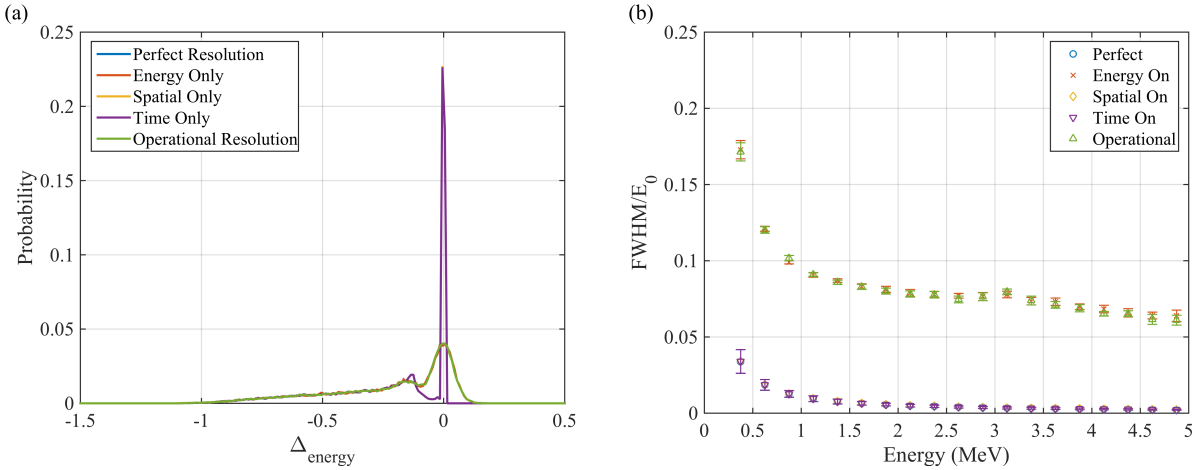

Figure 2.11. Energy resolution components for photons between 1.0 and 1.25 MeV (a). FWHM of photon energy resolution components as a function of incident energy (b). In both figures the time and spatial resolution components overlap the perfect resolution curve while the operational curve overlaps the energy resolution component.

The curves shown in Figure 2.11 (a) are reminiscent of a typical photon energy spectrum in that they include a full energy photopeak as well as a Compton continuum. The Compton continuum is caused by photons that Compton scatter in the NaI(Tl) detectors rather than undergoing photoelectric absorption. It should be noted that while the incident photon

energy for the curves shown fall between 1.0 and 1.25 MeV, the photons incident on the NaI(Tl) detectors have already scattered and will therefore span a range of energies lower than the initial energy. Thus, for a given incident energy, the Compton edge is closer to the photopeak than in a single-detector spectrum for the same incident energy. While incomplete energy deposition is not accounted for in the FWHM calculation, the presence of such events significantly impacts the quality of the coincidence spectrum. The spectrum-isolation reduces the presence of Compton continua by correcting for this effect during the unfolding process.

2.6.3. Remarks

Figure 2.8 through Figure 2.11 suggest the spatial resolution is the largest source of uncertainty. Improvements in spatial resolution could be accomplished by using smaller detector cells relative to the flight path distance between scatter planes, or by increasing the detector spacing. Both options will cause a reduction in system efficiency, unless more detectors are added. It would also be possible to improve the spatial resolution by using position sensitive detectors. Silicon photomultipliers (SiPMs) have been shown to be capable of performing PSD [65]–[67]. Replacing the PMTs in the DPI with SiPMs would allow for pixelated readout detector cell, enabling some position sensitivity and would reduce the size of the DPI. Recent work by Ruch et al. has demonstrated the possibility of creating a handheld neutron-scatter camera using SiPMs coupled to 5×5×50 mm^3 stilbene pillars [68].

As incident energy decreases, the energy resolution becomes a more important contributor to the overall system resolution than spatial resolution. It would possible to improve photon energy resolution by using higher resolution material including, but not limited to CsI, $LaBr_3$, or CdZnTe. However, due to the summation of front and back plane

energy depositions, the resolution improvements would be tempered by the lower resolution of the EJ-309 detectors. Neutron energy resolution may be more difficult to improve as it is also important to maintain adequate particle discrimination capabilities.

In addition to the resolution components, there are other secondary effects that reduce the overall imaging and spectroscopy accuracy of the DPI. These effects include particles that interact outside of the active detector volumes, particles that undergo multiple scatters in the front plane detector (which can produce a large error in cone axis), and photons that do not undergo photoelectric absorption in the back plane. One of the goals of the spectrum-isolation technique described in Chapter 3 is to reduce the impact of both primary and secondary resolution effects by accounting for them in the system response matrix.

Chapter 3. Spectrum-Isolation Methodology

3.1. Motivation

Chapter 2 discussed the basic image and spectrum reconstruction techniques used by the DPI. These techniques produce images and spectra that are convolved with the intrinsic response of the system. This chapter, which is based in-part on work published in [30] and [32], will outline a more advanced reconstruction methodology, which approaches image and energy spectrum reconstruction as an inverse problem. This methodology will reduce the impact of the system response effects discussed in Chapter 2 and will allow for the estimation of localized energy spectra. The ability to estimate localized spectra is important for identifying multiple radioactive sources in the FOV. This technique is also beneficial when imaging only a single source because it will reduce the contribution of background radiation to that originating from the region of interest. As discussed in Chapter 2, it is possible to isolate the energy spectra for particular regions of interest using the energy associated with each backprojection cone. However, the spectrum-isolation technique outlined in this chapter enhances this capability by also unfolding the isolated spectra.

3.2. Inverse Methods

3.2.1. Formalisms

In general, both image and energy spectrum unfolding can be formulated as

$$b(d) = \int A(d,s)x(s)ds \qquad (3.1),$$

where $b(d)$ describes the data observed when measuring the emissions from a source distribution, $x(s)$, with an instrument having a detector response function, $A(d,s)$. The response function defines how a particle of source-space parameter s will be observed by the system and is responsible for the aforementioned convolution. If $A(d, s)$ is known, or can at least be well-approximated, then it is possible to estimate $x(s)$ from $b(d)$ using inverse methods. The accuracy of this estimation will depend on the accuracy of $A(d,s)$, and the algorithm chosen to perform the estimation. A well-defined response function will include any effects that prevent the quantity of interest from being measured exactly by the system, such as system resolution and sensitivity to particles of source-space parameter s. As written, Equation (3.1) is a noiseless model, but in reality the observed data will always be subject to noise. Therefore, the amount of noise in the observed data will also impact the accuracy of the inverse estimation. There may also be noise present in the system matrix, depending on the method used for system matrix computation. While system matrix noise is not explicitly addressed in this work, the impact of statistical noise in the observed data will be further explored in Chapter 5.

In practice, it is common to discretize Equation (3.1) to the linear system defined by

$$\boldsymbol{b} = \boldsymbol{A}\boldsymbol{x} \tag{3.2},$$

where $\boldsymbol{b}$ is an $D\times1$ vector that holds the observed data, $\boldsymbol{x}$ is an $S\times1$ vector that defines the true source distribution, and $\boldsymbol{A}$ is a $D\times S$ matrix that maps between source space ($\boldsymbol{x}$) and observation space ($\boldsymbol{b}$). In this formalization, each of the S columns of $\boldsymbol{A}$ represents a source-space quantity to be unfolded, and each of the D rows of $\boldsymbol{A}$ represents an observation-space quantity measured by the system. The specific source-space and observation-space

quantities used in this work will be discussed in Section 3.4.2.1 and Section 3.4.2.2, respectively.

In this work, $\boldsymbol{A}$ will be referred to the system matrix, $\boldsymbol{b}$ will be referred to as the observation vector, and $\boldsymbol{x}$ will be referred to as the source vector. Going forward, bold uppercase variables will be used to represent matrices, while bold lowercase variables will be used to represent vectors. Matrix and vector elements will be denoted using subscripts on non-bold variables (as they now represent a scalar). Parenthetical superscripts will be used to represent an iteration number.

3.2.2. Applications of Inverse Methods

Inverse methods have been used with great success in image reconstruction problems across many fields. Two especially relevant fields include medical imaging and energy spectrum unfolding. The development of image reconstruction methods for the medical imaging field has led to an extensive body of work spanning topics including algorithm development, modeling techniques, regularization techniques, and performance metrics. An excellent overview of these topics can be found in Professor Fessler's 2004 short course [69] and can be digested in greater detail in his (currently under progress) book [70].

Inverse methods are also commonly used for energy spectrum unfolding [71]–[76]. While much of the spectrum unfolding literature is focused on unfolding the response of a single detector, Brennan et al. [14] and Hamel et al. [26] have shown that spectrum unfolding improves the spectroscopy capabilities of neutron-scatter cameras.

Xu and He [77], [78] combined image reconstruction and spectrum deconvolution into a single inverse problem with their "energy-imaging integrated deconvolution" (EIID) technique. This technique estimates unfolded energy spectra for each pixel in the

reconstructed image. EIID has been successfully implemented using a list-mode MLEM algorithm [79] for a CdZnTe Compton camera [77], [78], [80].

The work presented in this thesis significantly expands on that technique to estimate the photon *and* neutron spectra for each pixel in the FOV of the DPI. This new technique relies on a simulated system matrix and makes use of standard bin-mode MLEM [33]. The MLEM algorithm is described in Section 3.3. Sections 3.4 gives a general overview of the system matrix and how it is calculated while Section 3.5 investigates some variable properties of a system matrix. Finally, Section 3.6 gives an example of the images and energy spectra produced using this methodology.

3.3. Maximum-Likelihood Expectation-Maximization

3.3.1. Theory

Maximum-likelihood expectation-maximization is an iterative, statistical inverse method that is used for image reconstruction in problems involving Poisson-distributed data [33], [73], [81]–[83]. As the name suggests, the goal is to maximize the likelihood function, $L(\boldsymbol{x})$, which is done using the expectation maximization technique.

The likelihood function can be interpreted as the probability of measuring $\boldsymbol{b}$ if the source distribution is $\boldsymbol{x}$. The observed value in each element of $\boldsymbol{b}$, denoted as b_d, is an independent Poisson measurement of $\boldsymbol{x}$ and is therefore distributed as

$$\mathrm{P}(b_d \; observed \; events) = \frac{\bar{b}_d{}^{b_d} e^{-\bar{b}_d}}{b_d!} \tag{3.3},$$

where $\bar{b}_d$ is the expected value of b_d, which has can be represented in terms of the system matrix and source distribution as

$$\bar{b}_d = \sum_{s=1}^{S} a_{d,s} x_s \tag{3.4}$$

This summation will be represented as $[\boldsymbol{Ax}]_d$ in the following equations.

$L(\boldsymbol{x})$ is then defined using the joint probability of obtaining measurement vector $\boldsymbol{b}$ as

$$L(\boldsymbol{x}) = \prod_{d=1}^{D} \frac{[\boldsymbol{Ax}]_d^{\,b_d} e^{-[\boldsymbol{Ax}]_d}}{b_d!} \tag{3.5}$$

This becomes more tractable as the log-likelihood, $l(\boldsymbol{x})$, which is found by taking the natural logarithm of Equation (3.5).:

$$l(\boldsymbol{x}) = \sum_{d=1}^{D} b_d \ln[\boldsymbol{Ax}]_d - [\boldsymbol{Ax}]_d - \ln b_d! \tag{3.6}$$

The maximum-likelihood estimator of $\boldsymbol{x}$ is then defined as

$$\hat{\boldsymbol{x}} = \arg\max_x \sum_{d=1}^{D} b_d \ln[\boldsymbol{Ax}]_d - [\boldsymbol{Ax}]_d \tag{3.7}$$

where the factorial term was dropped because it is not a function of $\boldsymbol{x}$. It is not straightforward to solve Equation (3.7) directly, but it is possible through iterative techniques. The expectation-maximization algorithm is a commonly utilized technique [33], [81] that leads to the iterative update-algorithm shown in Equation (3.8).

3.3.2. Algorithm

The computation performed at each iteration of the MLEM algorithm is shown in Equation (3.8):

$$\hat{x}_s^{(k+1)} = \hat{x}_s^{(k)} \left\{ \frac{1}{\sum_{d=1}^{D} a_{d,s}} \sum_{d=1}^{D} \left\{ \frac{b_d}{\sum_{s'=1}^{S} a_{d,s'} \hat{x}_{s'}^{(k)}} a_{d,s} \right\} \right\}, s = 1, \dots, S, \tag{3.8}$$

where $\hat{\boldsymbol{x}}$ is the estimate of the true distribution after k iterations. To further understand the MLEM algorithm, it is helpful to break it down into the following four steps:

1. Forward-project the current source-vector estimate, $\widehat{\boldsymbol{x}}^{(k)}$, through the system matrix to generate, $\widehat{\boldsymbol{b}}^{(k)}$, which is the expected data vector given the current source-vector estimate:
$$\widehat{\boldsymbol{b}}^{(k)} = \boldsymbol{A}\widehat{\boldsymbol{x}}^{(k)} \quad (3.9).$$

2. Compute data scaling factors, $\boldsymbol{c}^{(k)}$, by taking the ratio between the measured data vector and the expected data vector:
$$\boldsymbol{c}^{(k)} = \boldsymbol{b}/\widehat{\boldsymbol{b}}^{(k)} \quad (3.10).$$

3. Back-project the data scaling factors through the system matrix to obtain source scaling factors, $\boldsymbol{q}^{(k)}$:
$$\boldsymbol{q}^{(k)} = \boldsymbol{A}^T\boldsymbol{c}^{(k)} \quad (3.11).$$

4. Update the source vector estimate using the source scaling factors and account for sensitivity, which is defined as the column-wise sum of the system matrix ($\mathbf{1}^T\boldsymbol{A}$):
$$\widehat{\boldsymbol{x}}^{(k+1)} = (\widehat{\boldsymbol{x}}^{(k)} \cdot \boldsymbol{q}^{(k)})/(\mathbf{1}^T\boldsymbol{A}) \quad (3.12).$$

Note that the · and / operators in steps 2 and 4 are used to explicitly denote element-by-element multiplication and division as opposed to matrix multiplication and division.

The MLEM algorithm has several desirable reconstruction properties [33], [70], [81], [84]:

1. The estimator will converge to the maximum-likelihood estimator and each iteration will increase the likelihood.
2. If the initial guess, $\hat{x}_s^{(0)}$, is greater than 0 for all s, then $\hat{x}_s^{(k)}$ will also be greater than 0 for all s (assuming there are detected events and all sensitivity bins are greater than 0).
3. The number of measured counts will be conserved at every iteration, subject to sensitivity scaling:
$$\mathbf{1}^T\boldsymbol{A}\widehat{\boldsymbol{x}}^{(k)} = \mathbf{1}^T\boldsymbol{b} \quad (3.13).$$

3.3.3. Termination Criteria

Although MLEM will increase the likelihood of the solution with each iteration, too many iterations can introduce high-frequency noise in the reconstructed solution, which is a result

of the over-fitting of a generally ill-posed problem. Various methods have been proposed [85]–[89], but there are no generalized conditions for terminating the iteration procedure.

One method to determinate the termination iteration is to analyze the normalized data residual, which is defined as

$$\boldsymbol{r}^{(\boldsymbol{k})} = \frac{\boldsymbol{b} - \widehat{\boldsymbol{b}}^{(k)}}{\sqrt{\widehat{\boldsymbol{b}}^{(k)}}} \tag{3.14},$$

where $\widehat{\boldsymbol{b}}^{(k)}$ was defined in Equation (3.9) and the division and square root are taken on an element-by-element basis. This residual, $\boldsymbol{r}^{(\boldsymbol{k})}$, is representative of the relative error between the measured data and the "estimated data". This method was chosen for use in this work because it gives insight to how well the solution estimate "matches" the measured data but requires no *a priori* knowledge of the measurement scenario. Bissantz et al. [87] suggest that if $\widehat{\boldsymbol{x}}^{(k)}$ is a good approximation to $\boldsymbol{x}$, then $\boldsymbol{r}^{(\boldsymbol{k})}$ will have a mean of approximately 0 and a variance of approximately 1. For the reconstructions performed in this work, the variance of $\boldsymbol{r}^{(\boldsymbol{k})}$ will typically decay as a function of k to a plateau. The best reconstructions are found by choosing a k such that it is close to the start of the plateau. The effect of k on the accuracy of the reconstruction is further explored in Chapter 4.

3.4. The System Matrix

This work uses a bin-mode system matrix that is computed via Monte Carlo simulation. The general structure of the system matrix is such that each element, $a_{d,s}$, is the probability that an event from source bin s is observed by the DPI in observation bin d. These probabilities are computed simply by dividing the number of events detected in each observation bin by the total number of particles simulated from s, which is denoted as M_s. The sum of column s gives the probability of the DPI detecting an event from s in any

observation bin, which is known as the sensitivity (or efficiency). Not all emitted events will be detected and therefore each column in $\boldsymbol{A}$ will sum to a sensitivity value that is less than 1.

Over the course of this work, the system matrix has evolved in complexity. Early work was focused solely on image reconstruction of SNM. These system matrices were simulated using the energy distributions emitted by the common SNM surrogate ^{252}Cf, and did not include any energy information in source space. As expected, these response matrices worked well for laboratory measurements of ^{252}Cf and simulated measurements of other fission sources. However, because the system matrix assumed the observed data would be distributed similar to a ^{252}Cf source, image reconstruction degraded for measurements of sources whose energy distributions differed significantly from a fission distribution. This degradation was particularly problematic for photon sources with energy distributions dominated by decay lines.

The system matrix was first generalized by creating multiple system matrices, each for a specific neutron or photon energy range. The energy binned system matrices were then combined as a weighted sum with the weight of each energy bin being the intensity of the corresponding energy bin in the reconstructed spectrum. This method worked well and improved reconstruction for photon sources with discrete energies [30].

As the project evolved, it became desirable to improve upon the reconstructed energy spectra, which led to the spectrum unfolding techniques investigated by Hamel, et al. in [26]. The success of these techniques motivated the investigation of the simultaneous unfolding of source location and energy spectra. In addition to improving the quality of the energy spectra, simultaneous unfolding has the added benefit of providing an unfolded spectrum for each location in the image, which makes it straightforward to generate localized energy

spectra for any region of interest (ROI). This "spectrum-isolation technique" is the method used throughout the remainder of this work.

3.4.1. System Matrix Simulation

3.4.1.1. Spatial Sampling

The system response matrix is computed using the simulation techniques described in detail in Section 2.5. Neutrons and photons are simulated separately due to the different number of simulated particles required to achieve a reasonable level of statistics (see Section 3.5.2). Spatially, the source was uniformly distributed as a 2π hemisphere located in front of the system. The radius of this hemisphere was chosen to be 2 m, which is a typical source-to-detector distance used in experiments. However, very little uncertainty is introduced when reconstructing a source located at a different radius. The details of this claim are discussed further in Chapter 5.

The continuous hemispherical distribution allows for the image-pixel bin sizes to be determined at will during the binning process. If the image pixels are binned uniformly in degrees along the azimuthal and inclination direction, then pixels near the image poles (ϕ={0,180}) will have smaller area (and therefore fewer emitted counts) than those towards the equator (ϕ=90). This trend is shown in Figure 3.1 (a), which displays the number of particles emitted from each bin for 5°×5° image pixels.

The distribution shown in Figure 3.1 (a) is somewhat advantageous because most experiments are performed with the source close to ϕ=90°, which makes it desirable to have lower relative uncertainty in this region. While sources will not always be well aligned with the DPI in field use, Chapter 5 will demonstrate that the DPI will still be able to detect and accurately characterize sources at off-center inclinations (and azimuths). If higher statistical

fidelity is required, then a field-deployable DPI could be rotated to better position the source within the FOV. Alternatively, a new simulation technique could be developed to account for this statistical bias at the expense of increased simulation time.

The area of a pixel centered at an arbitrary inclination ϕ relative to a pixel centered at an inclination of 90° is distributed as cos(ϕ-90°), as shown in Figure 3.1 (b). If during the binning process pixels near the poles are found to have undesirably low statistics, then those pixels can be ignored by reducing the FOV. The relative area of each pixel is accounted for when determining M_s for each s.

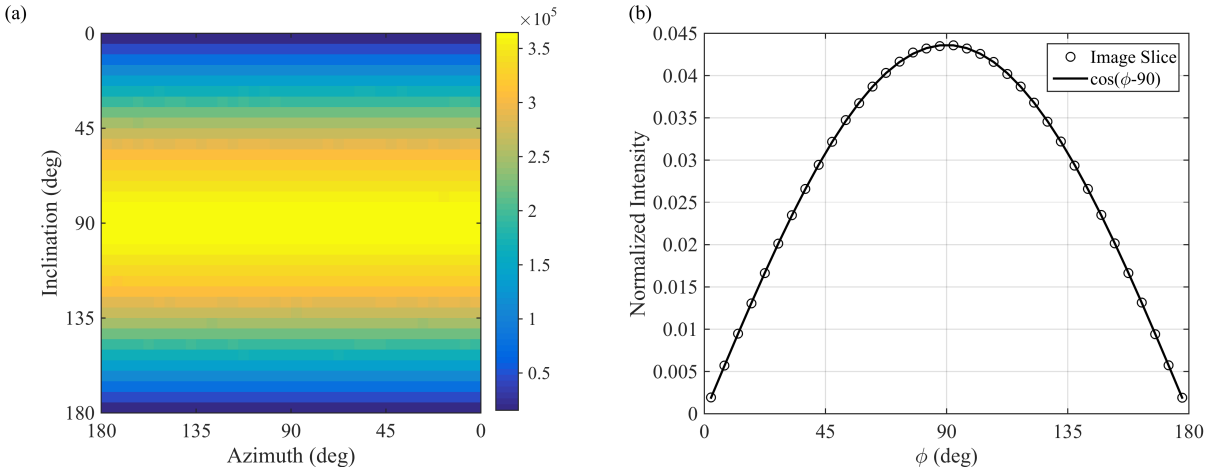

Figure 3.1. Image of the number of particles emitted from each 5°×5° pixel for a hemispherically distributed source with 3×10^8 total emissions (a). Number of emissions from each pixel in a vertical slice of (a) plotted with the shifted cosine function that determines this distribution (b). Both curves in (b) are normalized by their integral.

To improve simulation efficiency, the direction of the emitted particle was sampled from a cone with an axis drawn between the randomly sampled emission position and the geometric center of the DPI. The opening angle of the cone was defined such that the cone would be tangent to a sphere fully encompassing the DPI, as shown in Figure 3.2. The system sphere radius is 76.5 cm and so for a fixed source hemisphere radius of 200 cm, the opening angle is 22.5°. This angle corresponds to a solid angle of 0.48 steradians, which is ~3.8% of a fully isotropic source. The result of this conical sampling is that each $a_{d,s}$ is the probability

of measuring a particle emitted towards the DPI from source bin *s* in observation bin *d*. Therefore, the solution yields an estimate of the number of particles emitted by source distribution ***x*** toward the system.

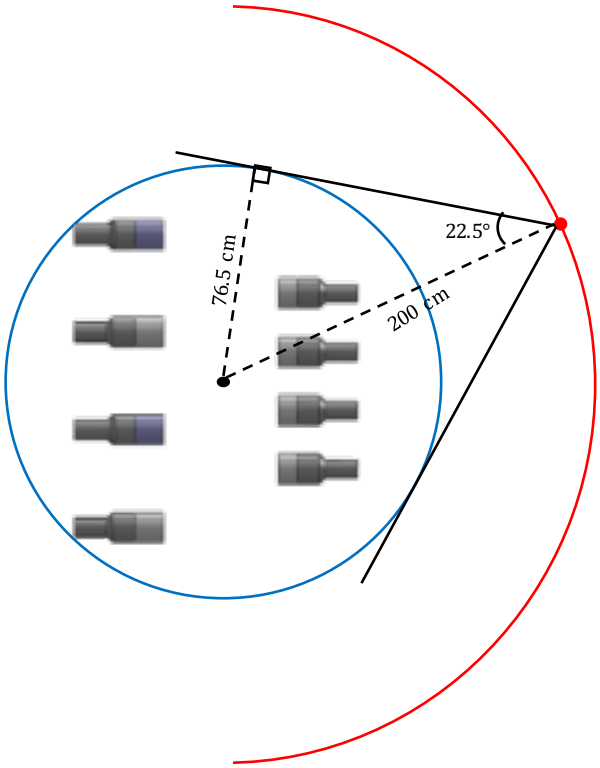

Figure 3.2. Schematic of system matrix simulation technique. The red curve represents the hemisphere of possible source locations and the blue circle represents the sphere encompassing the DPI. Particles are emitted from a conical distribution tangent to the system sphere. Schematic is not to scale.

MCNPX does not provide the capability to define the emission direction as function of a continuously sampled source space. This functionality was added through a patch to the MCNPX-PoliMi source code[1]. The simulation was set up such that, regardless of the starting position, particle direction was sampled from a cone aligned with the positive the *z*-axis. The patch computes the rotation matrix required to rotate between the positive *z*-axis and the

[1] A special thank you is owed to Matthew Marcath for his assistance in the development of this patch.

desired cone axis, which points between the starting position of the particle and center of the DPI. This matrix rotates the original sampled direction such that the particle is emitted towards the DPI.

3.4.1.2. Energy Sampling

For neutrons, the source energy was distributed between 0 and 10 MeV. This range accounts for 96% of the neutrons emitted by ^{252}Cf as found by integrating the Watt distribution with parameters defined in the MCNPX-PoliMi 2.0 manual: 1.18 and 1.03419 [58]. For photons, the source energy was distributed between 0 and 5 MeV. This range was chosen to include gamma rays resulting from neutron capture that may be useful in characterizing a material. One example is the 2.2 MeV gamma produced by neutron capture on ^{1}H that could signify the presence of a neutron source surrounded by a hydrogenous shielding material. Another example is the 4.4 MeV gamma resulting from the de-excitation of ^{12}C, which is a product of (α, n) reactions involving ^{9}Be.

For both particles, the energy distributions were continuous but not uniform. The continuous distribution allows for the energy bin sizes in source space to be tailored to particular applications. The non-uniform weighting increases the number of particles simulated in energy ranges of lower efficiency. This weighting encourages *source space* energy bins to be populated with similar statistical uncertainties (i.e. the number of detected events will be similar regardless of the emission bin they originated in). This weighting scheme must be appropriately accounted for when determining M_s for each s.

3.4.1.3. Computation Time

The overall simulation of the system matrix was spread across many seeds, each responsible for emitting of 3×10^{8} particles. Each seed was identical except for the initial

condition of the pseudo-random number generator used by MCNPX. All seeds were simulated on the University of Michigan's Flux Cluster [90], which housed 2.67 GHz Intel Xeon X5650, 2.60 GHz Intel Xeon E5-2670, 2.8 GHz Intel Xeon E5-2680v2, and 2.5 GHz Intel Xeon E5-2680v3 processors at the time of the system matrix simulation. While simulation and post processing were performed on all four processor types, run times were found to be comparable regardless of the processor allocated to the job. Each neutron seed took approximately 11.5 hours to simulate and 3 hours to post process. Each photon seed took approximately 10.5 hours to simulate and 1 hour to post process. With 40 keVee thresholds set for all detectors, a single neutron seed generated approximately 2.7×10^4 coincidence events and a single photon seed generated approximately 3.2×10^4 correlated events. The number of seeds required to achieve reasonable statistics depends on the number of pixels and energy bins used to discretize source space, as shown in Section 3.5.2. The bin sizes utilized required thousands of seeds, and therefore tens-of-thousands of computational hours. This immense computational cost is certainly a disadvantage of a fully simulated system matrix. However, the availability of large-scale computing environments, such as the Flux Cluster, make such computations possible in time-scales on the order of weeks.

3.4.2. System Matrix Structure

3.4.2.1. Source Space

Recall that each column in $\boldsymbol{A}$ is a source bin that corresponds to a source specific parameter to be estimated, such as source energy and/or location. When the reconstruction problem was focused solely on image reconstruction, each s represented a source location within the FOV and therefore $S=N_\theta N_\phi$ where N_θ and N_ϕ are respectively the number of azimuthal-angle and inclination-angle bins in the image. For the spectrum-isolation

technique, each s represents an emitted energy bin for a specific spatial bin and now $S=N_\theta N_\phi N_{UE}$ where N_{UE} is the number of unfolded energy bins. The term "unfolded energy" should not be confused with the term "reconstructed energy", which is the energy computed using the scattering kinematics discussed in Chapter 2.

The solution vector, $\hat{\boldsymbol{x}}$, naturally follows the same binning structure and therefore, each element in $\hat{\boldsymbol{x}}$ contains the number of unfolded counts in a particular energy bin of a particular image pixel. Binning the source space in this manner makes it is possible to view the unfolded spectrum at a specific pixel (or region of pixels). An image is formed over the entire energy range by summing over all energy bins in each pixel and reshaping the vector into an $N_\phi \times N_\theta$ image matrix. Similarly, an image can be created for a specific energy range by summing only the appropriate energy bins at each pixel.

3.4.2.2. Observation Space

In general, an observation bin may correspond to any quantity (or combination of quantities) measured by the DPI. For this system matrix the measured quantities include detector pair, reconstructed energy, and reconstructed angle. Reconstructed energies and angles are computed using the equations defined in Sections 2.2.1 and 2.2.2 for photons and neutrons, respectively. Detector pairs are indexed over all possible pairs between front-plane and back-plane detectors resulting in 128 detector pairs for both particle types (sixteen liquid scintillators in the front plane and either eight liquid scintillators or eight NaI(Tl) scintillators in the back plane).

The observation bins are ordered such that detector pair changes most frequently, and reconstructed energy changes least frequently. Thus, for an event occurring in detector pair

p with reconstructed energy falling in energy bin E and reconstructed angle falling in angle bin ω, the observation bin index is computed as

$$d = (E-1)N_{RE} + (\omega - 1)N_{\omega} + p \quad (3.15),$$

where N_{RE} and N_{ω} denote the total number of reconstructed energy bins and reconstructed angle bins, respectively. This binning structure is easy to conceptualize and makes sense physically, but it is not guaranteed to be optimal. Some investigations have been made into using principal-component analysis (PCA) to re-bin observation space. However, this technique alters the Poisson nature of the system matrix (and observation vector) and also significantly reduces the sparsity of the system matrix, which is a valuable property (as described in Section 3.5.3). Due to these caveats, further work is encouraged to investigate the utility of a PCA-based re-binning as well as other binning strategies.

3.5. System Matrix Properties

While the bin structure is set, the size of each bin can be decided by the user and may be altered depending on the nature of the experiment being performed. Choosing bin sizes in both source space and observation space is an important, but difficult decision that impacts several properties of the system matrix. Finer source-space binning enables finer resolution, which is inherently good. However, finer source-space bins will also require a higher number of seeds to achieve similar statistics for each s. Finer observation-space bins will lead to the measured counts being spread over more bins. For the same measured data, a more finely binned observation vector will have a higher bin-wise relative Poisson error. Chapter 5 will describe a methodology for estimating how statistical errors in measured data are propagated through the reconstruction process. Bin sizing will also impact the memory required to hold the system matrix and the time required to compute the MLEM solution.

3.5.1. Bin Sizes

In the observation space, bin sizes are determined using the resolution metrics presented in Section 2.6, which are directly related to the achievable precision in the observation vector. Reconstructed angle and energy bins were chosen to be approximately 1-σ based off the minimum FWHM found for each parameter in Section 2.6. Table 3.1 outlines the values chosen.

Table 3.1. Observation space bin sizes chosen based off the 1-σ value corresponding to the minimum FWHM found for each reconstructed attribute.

Attribute	$FWHM_{min}$	1-σ	Selected Bin Size
θ_n	10.6°	4.5°	5°
θ_p	10.8°	4.6°	5°
$E_{0,n}$	420 keV	180 keV	200 keV
$E_{0,p}$	57 keV	24 keV	25 keV

The similarity of the parameters used in observation space and source space suggest that source space bins should be of similar size as the observation space bin sizes. Many different bin sizes were investigated throughout the course of this work and the most reliable binning structure was found to be 5°×5° image pixels with 400 keV and 50 keV unfolded energy bins for neutrons and photons, respectively. In most experiments, the noise introduced by finer binning did not justify the theoretical increase in precision. However, Chapter 6 will present an experiment in which finer photon energy bins were justified due to the large number of measured events. While the proposed binning structure may not be optimal, it provided reliable solutions with a sufficient energy and spatial resolution for this work. The further optimization of the bin sizes is an interesting, but open, problem that remains outside the scope of this work.

The image domain does not include the full 2π hemisphere that was simulated. In the azimuthal direction, 35 pixels were used spanning 2.5°<θ<177.5°. In the inclination direction, 33 pixels were used spanning 7.5°<ϕ<172.5°. The 2.5° offset allowed for (90°, 90°) to fall at the center of a pixel rather than at the corner of four pixels. The bins nearest the poles were discarded due to their high relative error, as discussed in Section 3.4.1.1.

For the neutron system matrix, reconstructed energy ranges between 0 and 15 MeV resulting in N_{RE}=75. Reconstructed angle ranges between 0° and 90° resulting in N_{ω}=18. With 128 detector pairs, the number of observation-space bins is 172,800. Unfolded energy ranges between 0 and 10 MeV resulting in N_{UE}=25. With N_{θ}=35 and N_{ϕ}=33, the number of source-space bins is 28,875. The reconstructed energy spans a higher energy range than the unfolded energy to accommodate neutrons that reconstruct above their emitted energy due to system response effects.

For the photon system matrix, reconstructed energy ranges between 0 and 6 MeV resulting in N_{RE}=240. Reconstructed angle ranges between 0° and 180° resulting in N_{ω}=36. With 128 detector pairs, the number of observation-space bins is 1,105,920. Unfolded energy ranges between 0 and 5 MeV resulting in N_{UE}=100. With N_{θ}=35 and N_{ϕ}=33, the number of source-space bins is 115,500. Again, the reconstructed energy spans a higher energy range than the unfolded energy to accommodate photons that reconstruct to too high of an energy due to system response effects.

3.5.2. System Matrix Uncertainty

Uncertainty in the system matrix is a function of both the number of particles simulated during computation and the size of the bins chosen. The level of statistical uncertainty present in the system matrix is assessed based on the relative error of the sensitivity map.

The sensitivity map is defined as the column-wise sum of the system matrix and, in this work, defines the total probability of the DPI detecting a particle emitted toward the system from each source-space bin, *s*. Uncertainty in each sensitivity bin is defined as the square root of the number of counts detected in each sensitivity bin. While the sensitivity term for each *s* accounts for the number of particles emitted from *s*, the sensitivity uncertainty term is only dependent on the number of counts detected.

During the simulation process, uncertainty in the sensitivity bins was tracked for the bin sizes proposed in Section 3.5.1 by successively populating new system matrices with increasing numbers of total counts. Figure 3.3 plots, as a function of seeds simulated, the fraction of sensitivity bins that have obtained 10%, 5%, and 2.5% relative uncertainty. This plot shows that almost 100% of sensitivity bins have achieved better than 10% relative uncertainty for both particle types. For neutrons, greater than 99% of sensitivity bins have better than 5% uncertainty and over 80% have better than 2.5% uncertainty. For photons, greater than 90% of sensitivity bins have better than 5% uncertainty and over 35% of sensitivity bins have better than 2.5% uncertainty. For a given number of seeds, the photon system matrix has a lower number of statistically significant sensitivity bins than the neutron system matrix because the photon system matrix has four times more source-space bins. As a result, more photon seeds were simulated in an attempt to achieve similar levels of overall uncertainty.

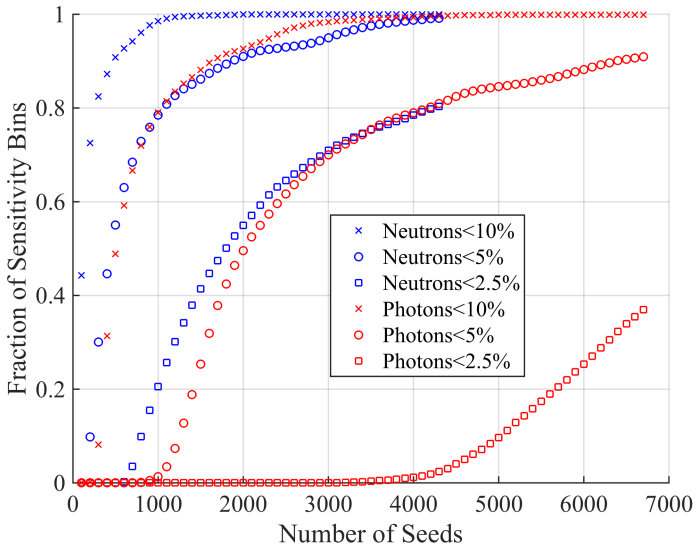

Figure 3.3. Fraction of sensitivity bins that have achieved a 10%, 5%, and 2.5% relative uncertainty. Neutrons are shown in blue and photons are shown in red. Each step along the x-axis represents a system matrix populated using the events for that number of seeds.

While Figure 3.3 gives a reasonable understanding of the system matrix as a whole, it is also useful to know how the uncertainty varies in source space. This information is available through the sensitivity images and their associated error maps. The sensitivity image for a particular energy bin shows the efficiency as a function of emission location (i.e. the number of particles detected divided by the number of particles emitted). Higher intensity in the sensitivity map indicates source locations that will be more efficiently measured by the DPI. The error map for a particular energy bin shows the relative error associated with each location, which is found by dividing the Poisson uncertainty by the number of particles detected. The shape of a sensitivity image and its associated error map will be similar (but inverted); however, the error maps will be impacted by the $\cos(\phi\text{-}90°)$ trend (discussed in Section 3.4.1.1) because they are dependent only on the number of particles detected and not the number of particles emitted. When viewing these images, note that the color bars are allowed to vary with energy so that the shapes of each image is apparent.

Figure 3.4 shows the neutron sensitivity images and the associated uncertainty maps for the source-space energy bins ranging between 2.0 and 2.4 MeV (a, b), between 4.8 and 5.2 MeV (c, d), and between 8.0 and 8.4 MeV (e, f). The shape of the sensitivity images is similar at all three energies, which is expected because the scattering angle probability distribution for a neutron elastic scattering on ^{1}H is not dependent on energy. The maximum efficiency decreases as a function of energy: dropping from ~0.022% to ~0.013% between 2 and 8 MeV.

The highest sensitivity is found ~20° from the center of the FOV with a slight drop toward the center. This drop in sensitivity is a result of the system geometry, which dictates a lower scatter angle between detector pairs for neutrons incident from the center of the FOV. Low-angle scatters deposit a lower fraction of incident energy, and are therefore are more likely to fall below threshold in the front plane. A drop in sensitivity is also seen towards the edges of the FOV, which corresponds to locations that predominantly require large scatter angles for a neutron to travel toward a back plane detector. As a result, these neutrons are less likely to have enough energy to interact above threshold in the back plane.

The uncertainty maps show that the lowest uncertainty is towards the center of the FOV and that a relative error below 2.5% has been achieved at all energies for a large portion of the FOV, with higher uncertainties appearing towards the edges (especially the poles). The uncertainty maps also show that there are similar levels of uncertainty at all energy ranges, which is a result of the weighting applied to the simulated energy spectrum.

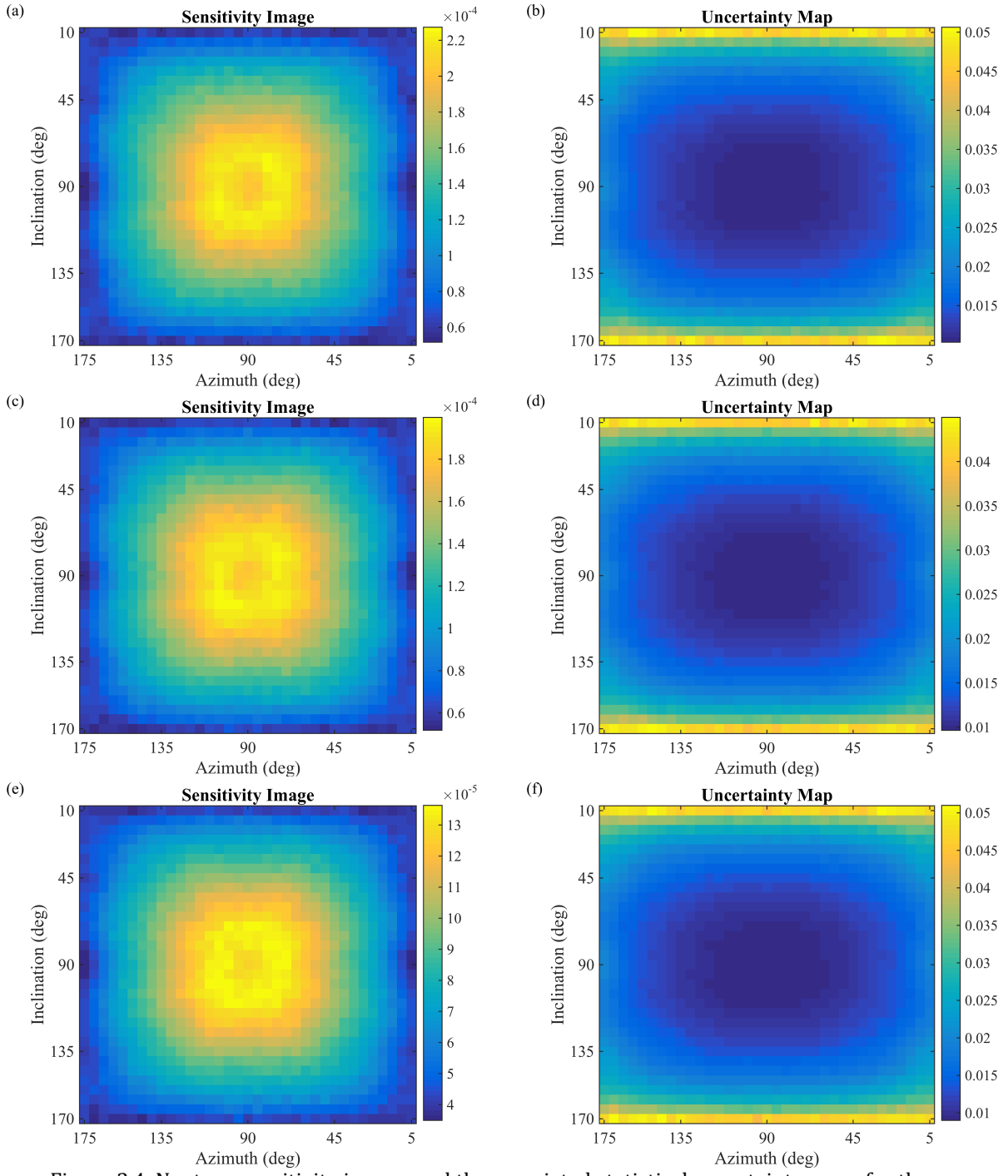

Figure 3.4. Neutron sensitivity images and the associated statistical uncertainty maps for the source-space energy bins ranging between 2.0 and 2.4 MeV (a, b), between 4.8 and 5.2 MeV (c, d), and between 8.0 and 8.4 MeV (e, f). The color scale for the sensitivity images represent detection efficiency while the color scale for the uncertainty maps represent the relative Poisson error.

Figure 3.5 shows the photon sensitivity images and the associated uncertainty maps for the source-space energy bins ranging between 300 and 350 keV (a, b), between 650 and 700 keV (c, d), and between 1300 and 1350 keV (e, f). Similar to the neutron sensitivity maps, the photon sensitivity maps show a drop in sensitivity towards the center and edges of the FOV, which is due to the system geometry. Unlike neutrons, the shape of the sensitivity images changes as a function of energy. This variation is because the scattering angle probability distribution for Compton scattering changes as a function of energy as determined by the Klein-Nishina formula [8]. Higher energy photons have a more forward-directed scatter probability, and therefore, the sensitivity image for higher energy photons is also more forward directed. Similar to the neutron uncertainty maps, the photon uncertainty maps show that the highest areas of uncertainty are towards the edge of the FOV. Again, the range of uncertainty is relatively constant at all energy ranges as a result of the energy spectrum weighting.

It is important to remember that the uncertainty in each sensitivity bin is a function of the bin sizes chosen. That is, for the same set of system matrix data, the uncertainty in each sensitivity bin can be reduced by simply moving to coarser binning. For example, doubling the size of the energy bins used will result in half as many source-space bins and will improve uncertainty in each sensitivity bin by a factor of approximately $\sqrt{2}$. The reduction in uncertainty would of course be accompanied by a loss of precision.

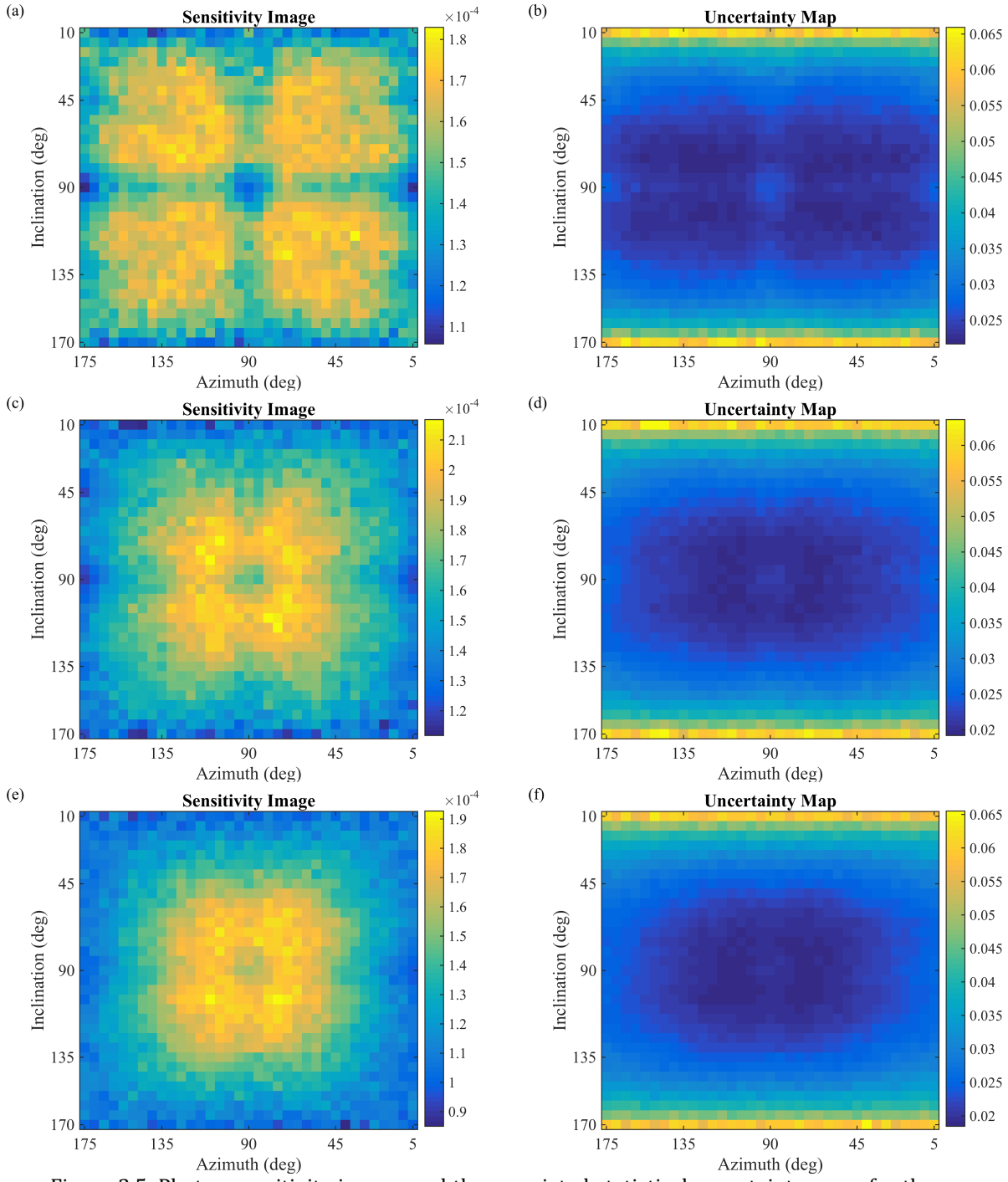

Figure 3.5. Photon sensitivity images and the associated statistical uncertainty maps for the source-space energy bins ranging between 300 and 350 keV (a, b), between 650 and 700 keV (c, d), and between 1300 and 1350 keV (e, f). The color scale for the sensitivity images represent detection efficiency while the color scale for the uncertainty maps represent the relative Poisson error.

3.5.3. Sparsity

It is important to note that not all observation bins in a specific source bin have non-zero probability due to physical constraints. However, the specific location of the zero-probability observation bins will change from source bin to source bin. For example, it may *not* be possible for a particle from location s_1 to be detected in bin $a_{d,1}$ while it *is* possible for a particle from location s_2 to be detected in in bin $a_{d,2}$. With extensive enough binning, only a small fraction of the system matrix elements will be non-zero, resulting in a sparse matrix.

MATLAB has a built-in sparse matrix framework based on the compressed-sparse-column format [91]. This technique reduces the data being stored to only the non-zero elements and their respective indices. Computation time is also reduced by ignoring unnecessary operations involving zero-valued elements.

The use of sparse matrices makes the binning sizes suggested in Section 3.5.1 possible. Storing full response matrices of these sizes in double precision would require ~40 GB and ~1 TB for neutrons and photons, respectively. However, taking advantage of sparsity reduces the memory requirements to less ~1.6 GB for neutrons and ~6.0 GB for photons.

3.5.4. Solution Computation Time

The computation time required to perform an MLEM reconstruction is determined by the size and sparsity of the system matrix, the sparsity of the data vector, the number of iterations performed, and the speed of the processor. For the system matrix parameters defined in Section 3.5.1, neutron reconstructions take approximately 0.2 seconds per iteration and photon reconstructions take approximately 0.7 seconds per iteration on a 3.0 GHz Intel Xeon E5 processor. Accurate solutions typically require between 50 and 100 iterations, so reconstruction times on the order of tens-of-seconds can be expected. These

computation times account for only the MLEM iterations. However, for reasonable count rates the data binning procedure (including the computation of the reconstructed energy and reconstructed angle) can be performed in pseudo-real time. This approach makes it possible to perform MLEM reconstruction (as well as other reconstruction techniques) on the fly.

3.6. Reconstructed Solutions

3.6.1. Formalisms

In this work, the color bars on MLEM reconstructed images and the y-axis on unfolded spectra will represent the number of unfolded counts. If any normalization of the unfolded spectra (or any reference spectra) occurs, it will be specifically stated. Spectra will typically be presented as a sum over several pixels. This summation helps to reduce noise in the spectra by capturing more of the source signal, which is typically not localized in a single pixel. Any source-space energy bins falling below the detection threshold are omitted during reconstruction. 0.04-MeVee detector thresholds (which are frequently used) approximately equate to a 0.04 MeV deposition for photons and a 0.366 MeV deposition for neutrons. Because two interactions are needed to obtain a correlation, these thresholds correspond to minimum detectable energies of 0.08 MeV for photons and 0.732 MeV for neutrons. In the case of 0.4 MeV neutron bins and 0.05 MeV photon bins, the unfolded neutron spectrum will begin at 0.8 MeV and the unfolded photon spectrum will begin at 0.1 MeV. These energies correspond to the first energy bins fully above the coincidence energy threshold.

3.6.2. Example Reconstruction

The reconstruction capabilities provided by this system matrix are shown in Figure 3.6 and Figure 3.7 for neutrons and photons, respectively. Figure 3.8 presents, for comparison, the backprojection images for each particle type. The data comes from a simulated 10-minute measurement of a 4.4 mCi (~5×10^6 fissions-per-second) ^{252}Cf located at (2m, 60°, 60°). A similar source will be used in a variety of laboratory experiments discussed in Chapters 4-6. The source was simulated using the same conical distribution used when simulating the system matrix. As a result, a perfectly unfolded spectrum should match the emitted spectrum exactly.

In both the neutron and photon images, the source is correctly located at (60°, 60°). The neutron image has a more tightly converged hotspot than the photon image. This trend is also seen in the backprojection images shown in Figure 3.8 for comparison. The isolated spectra match the shape of the emitted spectra very well. The unfolded neutron spectrum is a better match to the emitted magnitude than the photon spectrum. The lower number of counts in the isolated photon spectrum (relative to the emitted number) is anticipated by the reconstructed photon image, which shows more signal outside of the 5×5-pixel ROI centered at (60°, 60°) than the neutron image. The effect of ROI size on isolated spectra will be further explored using a measured data set in Chapter 4.

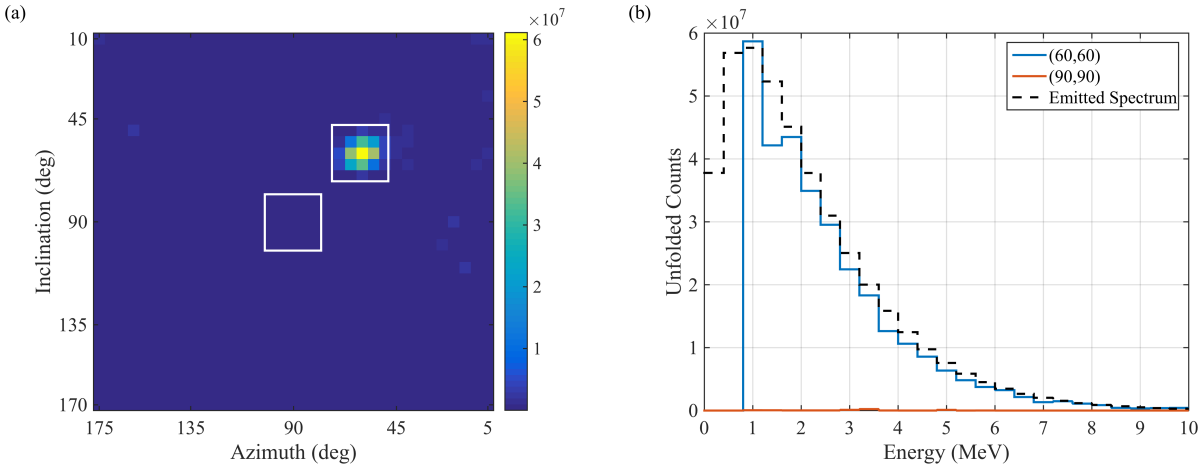

Figure 3.6. MLEM reconstructed neutron image of a simulated ^{252}Cf source located at (60°, 60°) (a). Isolated spectra for the 5×5 pixel regions centered at (60°, 60°) (blue) and (90°, 90°) (red) compared to the emitted spectrum (black) (b). The (90°, 90°) region is shown to demonstrate the reduced signal for areas with no source present.

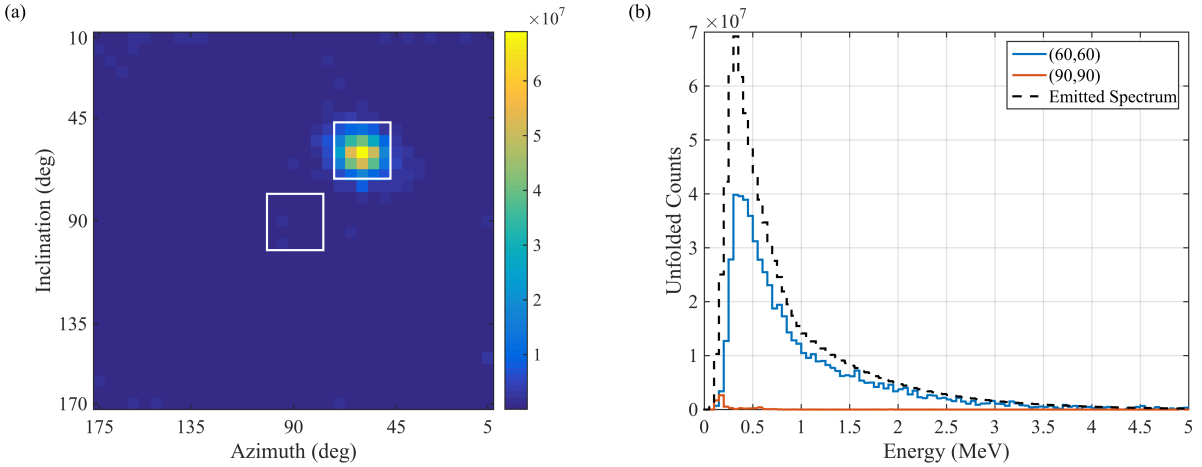

Figure 3.7. MLEM reconstructed photon image of a simulated ^{252}Cf source located at (60°, 60°) (a). Isolated spectra for the 5×5 pixel regions centered at (60°, 60°) (blue) and (90°, 90°) (red) compared to the emitted spectrum (black) (b). The (90°, 90°) region is shown to demonstrate the reduced signal for areas with no source present.

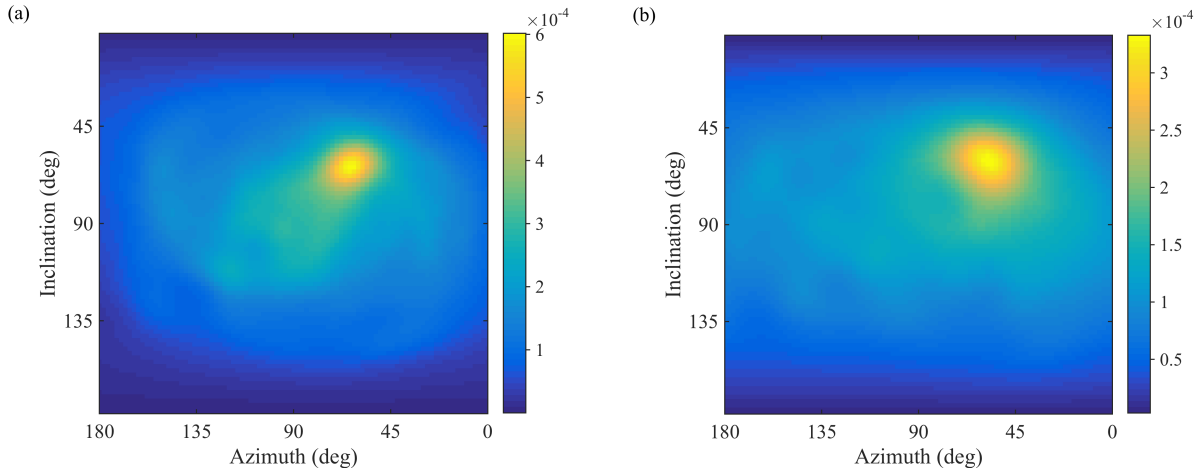

Figure 3.8. Backprojection images for neutrons (a) and photons (b) emitted by a simulated ^{252}Cf source located at (60°, 60°). Images are normalized by their integral.

3.7. Remarks

This chapter outlined the MLEM-based spectrum-isolation technique used to produce images and generate localized spectra for individual regions of interest. Some consideration was given to the bin sizes used in the system matrix and a sample reconstruction of a simulated data set was presented for analysis. The simulated results show a great improvement over the simple-backprojection imaging and coincidence spectrum reconstruction techniques discussed in Chapter 2. However, measured data will present additional challenges due to discrepancies between the simulated system matrix and reality. The following chapters will demonstrate the utility of the spectrum-isolation technique for experimental and field use through the exploration of a variety of measured data sets.

Chapter 4. Demonstration of Spectrum Isolation

4.1. Introduction

Chapter 3 outlined a technique for performing simultaneous reconstruction of both image and energy spectrum. This method makes it possible to determine the energy spectrum for each pixel in the reconstructed image. A system matrix was described and was used to produce images and localized spectra for a simulated measurement of a ^{252}Cf source. This chapter, which includes work previously published in [32], will demonstrate the performance and capabilities of the spectrum-isolation technique on measured data. A measurement of a single ^{252}Cf source will be used to understand the impact of certain reconstruction parameters. This discussion will be followed up with two multi-source measurements that further demonstrate the capabilities of the spectrum-isolation method.

4.2. ^{252}Cf Measurement

To investigate the impact of various reconstruction parameters, a measurement of a 4.4-mCi ^{252}Cf source, located at (2m, 90°, 90°), was performed. At the time of the measurement, the source underwent approximately 5×10^{6} fissions-per-second, resulting in approximately 1.9×10^{7} neutrons-per-second and 4.0×10^{7} photons-per-second emitted from fission. The measurement lasted for 10 minutes, resulting in approximately 4.4×10^{4} measured neutron events and approximately 4.0×10^{5} measured photon events, which are more than enough events to produce reasonably converged isolated spectra, as shown in Chapter 5. The source is relatively new and should be free of any significant buildup of decay

products (although decay gammas from short-lived fission products will still be present). Therefore, the emitted photon and neutron energy spectra are well approximated by the theoretical spectra used by MCNPX-PoliMi, which are shown for reference in Figure 4.1 and will be compared to various reconstructed spectra over the coming sections.

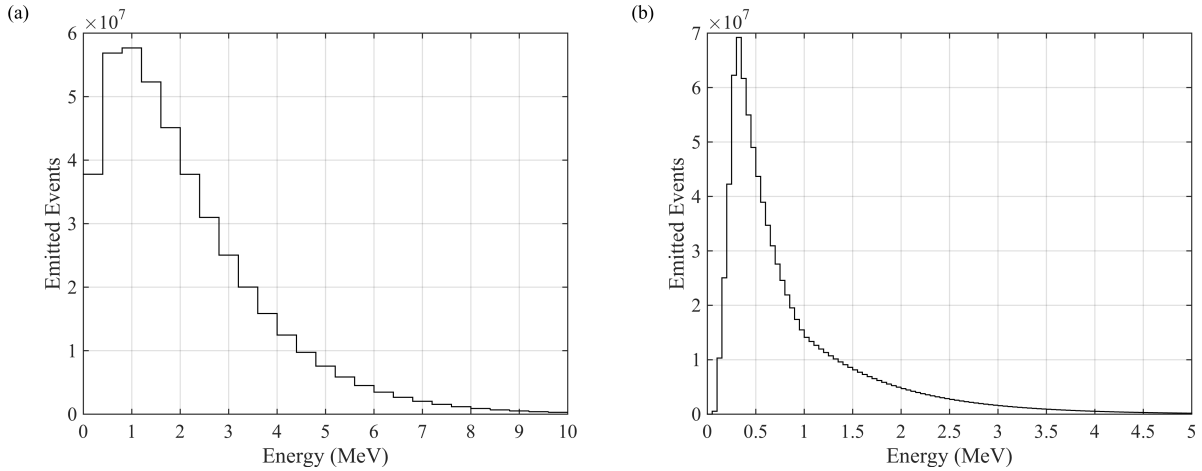

Figure 4.1. Theoretical neutron (a) and photon (b) spectra from spontaneous fission in ^{252}Cf. The magnitudes of the spectra correspond to the expected number of counts in a perfectly unfolded spectrum for a 10-minute measurement of a 4.4-mCi ^{252}Cf source.

Figure 4.2 and Figure 4.3 show the reconstructed image and isolated spectra for neutrons and photons, respectively. Both images show a hot-spot centered at the correct location with the photon image suffering from more noise than the neutron image. The noise in the photon image is due primarily to photons below 0.3 MeV (resulting from background radiation and room return from the source) and can be significantly reduced by windowing the image to display only the energies above 0.3 MeV, as shown in Figure 4.4.

The isolated spectra are shown for the summation of the 5×5-pixel region centered at (90°, 90°). For both photons and neutrons, the isolated spectra reconstructed to the less than the expected magnitudes shown in Figure 4.1. The reason for the disagreement in magnitude will be discussed further in Section 4.2.1. Before reaching that discussion, the shapes of the

isolated spectra will be compared against normalized versions of the theoretical spectra presented in Figure 4.1

Figure 4.2 (b) compares the isolated neutron spectrum to the theoretical spectrum, which is scaled to match the magnitude of the measured spectrum in the 2.0-2.4 MeV bin. The energy bins between 0.8 and 2.0 MeV, are lower than expected (note that the 0-0.4 MeV and 0.4-0.8 MeV bins are excluded by the 0.04-MeVee energy threshold, as discussed in Chapter 3).

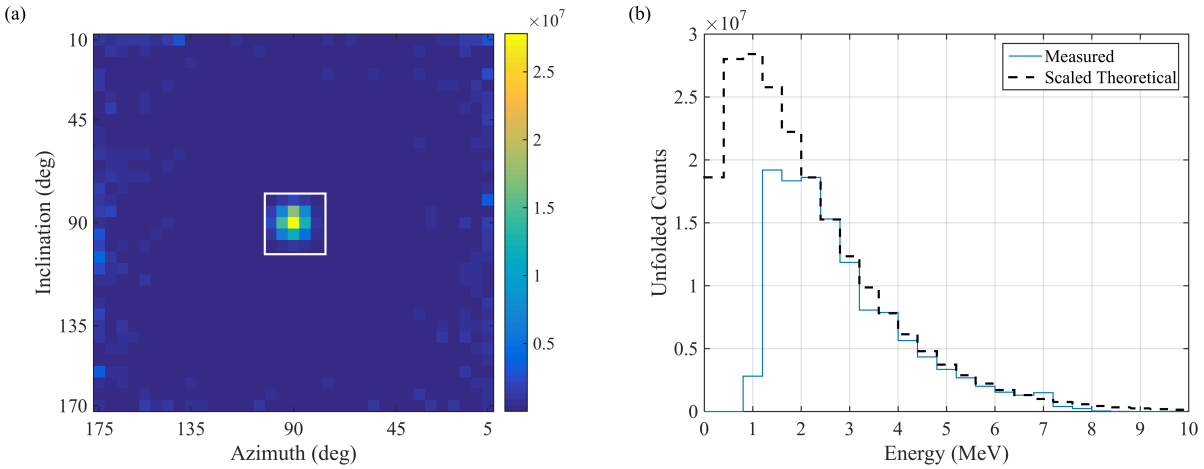

Figure 4.2. Neutron reconstructed image (a) and spectrum (b) for a 10-minute measurement of a 4.4 mCi ^{252}Cf located at (2 m, 90°, 90°). The white box on the image outlines the pixels used to define the spectrum ROI. The theoretical spectrum has been scaled to match the measured in the 2.0-2.4 MeV bin.

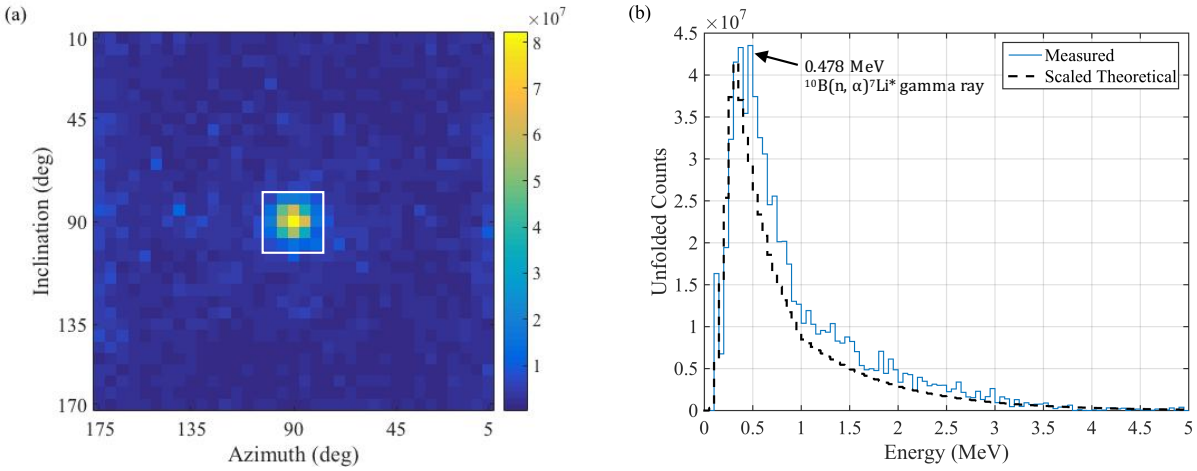

Figure 4.3. Photon reconstructed image (a) and spectrum (b) for a 10-minute measurement of a 4.4 mCi ^{252}Cf located at (2 m, 90°, 90°). The white box on the image outlines the pixels used to define the spectrum ROI. The theoretical spectrum has been scaled to match the measured in the 2.0-2.4 MeV bin. The prominent peak at 0.478 MeV is a result of photons produced through the ^{10}B(n, α)^{7}Li reaction.

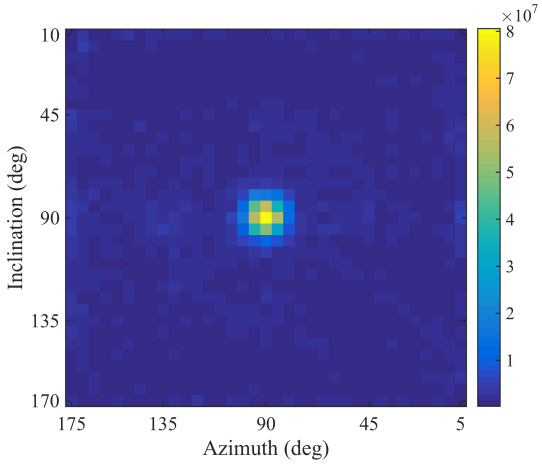

Figure 4.4. Photon image for energies between 0.3 and 5 MeV. Windowing the image has reduced the noise present by reducing the number of events not coming directly from the source.

The low-energy discrepency seen in Figure 4.2 (b) is a result of differences between the simulated system matrix and reality (which will be referred to as model mismatch). One source of model mismatch, that would be especially amplified at low energies, is particle misclassification in the pulse-shape discrimination process. PSD misclassification increases significantly for low energy depostions (below approximately 0.1 MeVee in light output).

Complete misclassification of a neutron coincidence event as a photon coincidence event is unlikely as both front-plane and back-plane interactions would need to be misclassified. However, if only one of these interactions is misclassified, the event will not score as a coincidence event and will be lost. Because PSD misclassification is not included in the system matrix model, this loss of efficiency is not accounted for during the unfolding process.

The light-to-energy conversion model used in this work is also expected to be a source of model mismatch. A comparison between simulated data and measured data shows that the model used tends to overpredicts the number of simulated interactions for a given energy [61]. This comparison also shows that the overprediction increases at lower energies. An overprediction in simulated events would result in an overprediction of the sensitivity terms in the system matrix, which would in-turn lead to lower than expected number of unfolded events. While this overprediction is not enough to account for the disagreement in magnitude across the entire spectrum, it is expected to play a role in the additional disagreement seen at low energies.

Figure 4.3 (b) compares the isolated photon spectrum to the scaled theoretical spectrum, which is scaled to match the magnitude of the measured spectrum in the 0.3-0.35 MeV bin. This bin corresponds to the peak of the theoretical spectrum. Similar to the isolated neutron spectrum, the isolated photon spectrum is representative of the expected shape of the photon spontaneous fission spectrum. The first bin above threshold shows some unexpected behavior due to low-energy noise in the coincidence spectrum. At energies above the 0.3-0.35 MeV bin used for scaling, the measured spectrum has a higher magnitude than the theoretical spectrum. This excess signal is a result of measuring decay gammas from fission products that are not included in the theoretical spectrum. Additionally, the measured

spectrum includes photons that do not come directly from the source, such as room return (from the same direction of the source) and photons produced in the laboratory environment and the DPI, as discussed below.

There is a prominent peak present in the 0.45-0.50 MeV bin that is not predicted by the theoretical spectrum. This source of this peak was investigated via simulation and the most likely cause is the $^{10}B(n, \alpha)^{7}Li$ reaction. Approximately 94% of these reactions populate the excited state of ^{7}Li, which de-excites through the emission of a 0.478 MeV gamma ray [8]. This reaction occurs in the PMTs and the BK7 optical window of the EJ-309 detectors which both contain boron. ^{10}B is ~20% abundant in natural boron (with the rest being ^{11}B). Although boron is only present in small quantities in these materials, the thermal neutron cross section for this reactions is approximately 3800 barns[2] [92]. The detection of these gamma rays are facilitated by the geometry of the DPI, which places the PMTs and optical windows for the front plane in front of the active detector volumes.

This peak will show up frequently throughout this work and therefore several important points should be kept in mind. The cross section for this interaction is dominated by neutrons with energies well below the detectable range of the DPI. As such, this reaction is not expected to reduce the number of neutrons measured by the DPI. Additionally, the majority of these low energy neutrons will not come directly from the source, but will reach the DPI after being moderated in the surrounding environment. As such, the strength of this signal will not scale directly with the strength of the source signal. Rather, it will scale with the amount of room-return neutrons, which is not easily quantifiable but is affected by the geometry and composition of the experimental environment and the location of the source

[2] A plot of this cross section, along with other cross sections relevant to this work, can be found in Appendix D.

within it. Finally, the gamma rays are being emitted by the residual ^{7}Li atom and are therefore not expected to be limited to the direction of the source or to the direction of the interacting neutron. The non-directionality of this signal has been verified via simulation.

4.2.1. Impact of ROI Size

The isolated spectra shown in Section 4.2 were generated using the 5×5-pixel region centered at (90°, 90°). The shapes of the spectra were representative of the normalized theoretical spectra, but the magnitudes were lower than the theoretical values, which were presented in Figure 4.1,. Because these sources are essentially points, only a single pixel would be required to determine the shape and magnitude of an isolated spectrum in an ideal reconstruction. However, in this case, even a 5×5 region under predicted the magnitude. This under prediction is due to imperfect reconstruction, i.e. the measured data has been assigned a non-zero probability of being generated by a source distribution outside of the ROI. As such, the number of counts in an isolated spectrum will be directly related to the size of the ROI chosen to isolate the source.

4.2.1.1. Neutrons

Figure 4.5 shows the number of counts in an ROI as a function of ROI size. ROI sizes ranged from a single pixel to the full image. Each ROI was centered at (90°, 90°) and had equal height and width, with the exception of the final data point, which was 33×35 pixels and encompassed the entire image. The dashed line shows the theoretical number of neutron counts expected in the unfolded spectrum. This value is determined by scaling the total number of neutrons emitted by source (between 0.8 and 10 MeV) by the solid angle of the system matrix. The trend shows a plateau between 5×5 and 13×13 with a rise toward the expected number of counts as the ROI size is further increased. Integrating the full image

should give a reasonable approximation of the number of neutrons emitted toward the system from all sources (including background and room return). The theoretical value is likely surpassed due to contribution from room return and accidental coincidences, which appear as unexpected peaks in the first and last energy bins in the 33×33-pixel isolated spectrum shown in Figure 4.6 (b).

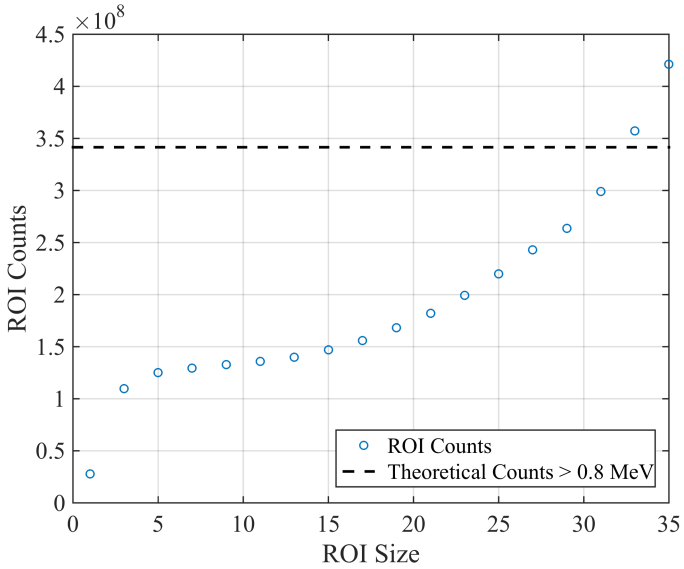

Figure 4.5. Number of unfolded neutron counts as a function of ROI size. All ROIs were boxes of equal height and width centered at (90°, 90°) with the exception of the final data point, which was 33×35 pixels and encompassed the full image. The dashed line shows the theoretical number of neutron counts expected in the unfolded spectrum between 0.8 and 10 MeV.

The spectra for several ROI are plotted in Figure 4.6. Figure 4.6 (a) shows how the shape of the spectrum converges at a size of 5×5 pixels, while Figure 4.6 (b) shows how the spectrum converges in magnitude with the theoretical spectrum as the ROI size is increased. As the size of the ROI is increased, the relative magnitude of the 0.8-1.2 MeV bin increases disproportionally to the rest of the spectrum and appears as a peak for the 33×33 ROI. This peak is due to a combination of room return and reconstruction noise towards the edges of the image. Additionally, the 13×13 and 33×33 ROIs introduce some erroneous high-energy counts that are likely due to accidental coincidences.

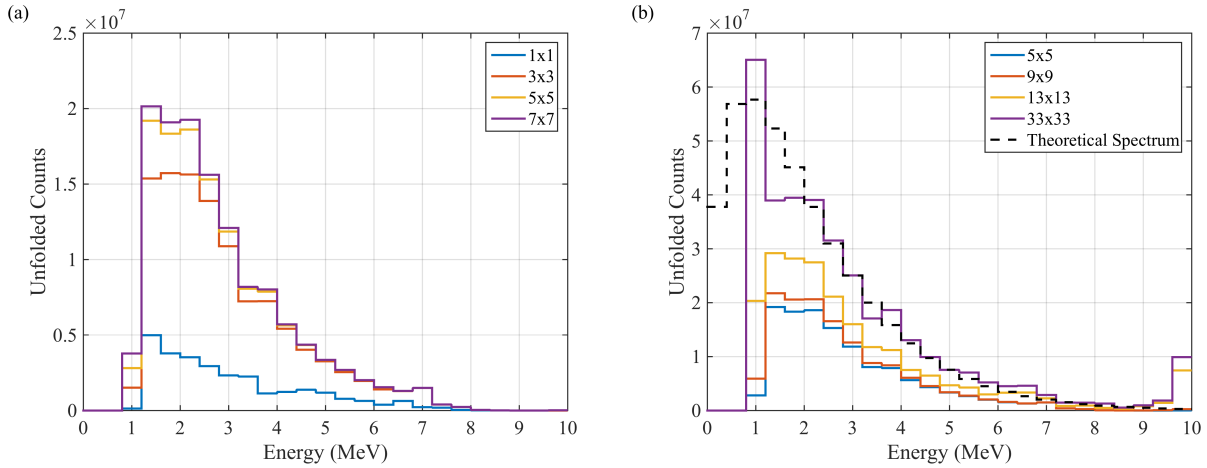

Figure 4.6. Neutron spectra as a function of ROI size. Spectra converge in shape at 5×5 pixels (a) and converge in magnitude to the theoretical values as more of the image is integrated (b).

4.2.1.2. Photons

Figure 4.7 shows the number of counts in an ROI as a function of ROI size for photons. The ROIs are the same as those used for neutrons. Again, the dashed line shows the theoretical number of counts emitted toward the DPI by the ^{252}Cf source. Similar to the neutron trend in Figure 4.5, the photon trend shows a "knee" at the 5×5 ROI. However, the photons do not experience the extended plateau displayed by the neutrons. The continuous increase is a due mostly to room return, which is demonstrated in Figure 4.8 (b).

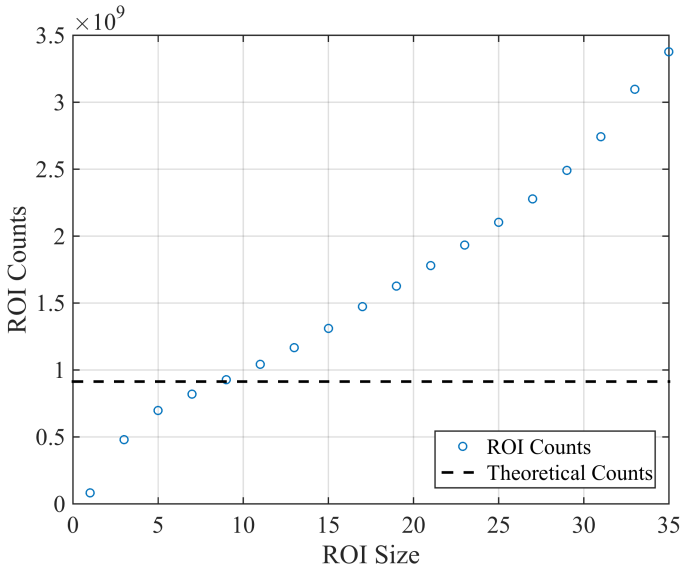

Figure 4.7. Number of unfolded photon counts as a function of ROI size. All ROIs were boxes of equal height and width centered at (90°, 90°) with the exception of the final data point, which was 33×35 pixels and encompassed the full image. The dashed line shows the theoretical number of photon counts expected in the unfolded.

Figure 4.8 shows the unfolded spectra for various ROI sizes. Similar to the neutron spectra, the photon spectra in small ROIs display a similar shape to the expected ^{252}Cf distribution. This trend holds through a ROI size of 9×9 pixels, which produces a spectrum that is representative of the theoretical spectrum in both shape and magnitude. However, unlike for neutrons, the shape of the spectrum changes as the size of the ROI is increased. Figure 4.8 (b) shows that as the size of the ROI increases past 9×9 pixels, energies below 0.3 MeV have a larger relative contribution to the unfolded spectrum. These lower energy photons are due to room return, which is more likely to be detected at larger angles (larger ROIs). The larger ROIs will include more of the laboratory walls and floor and will also include the broader incident angles required for lower-energy photons to undergo two interactions above threshold. While some of the increase in low-energy photon events can be attributed to background radiation, a 10-minute background measurement yields a spectrum (shown in Figure 4.9) two orders of magnitude below the 33×33-pixel spectra

shown in Figure 4.8 (b), which suggests that most of the additional counts are due to room-return of photons emitted by ^{252}Cf.

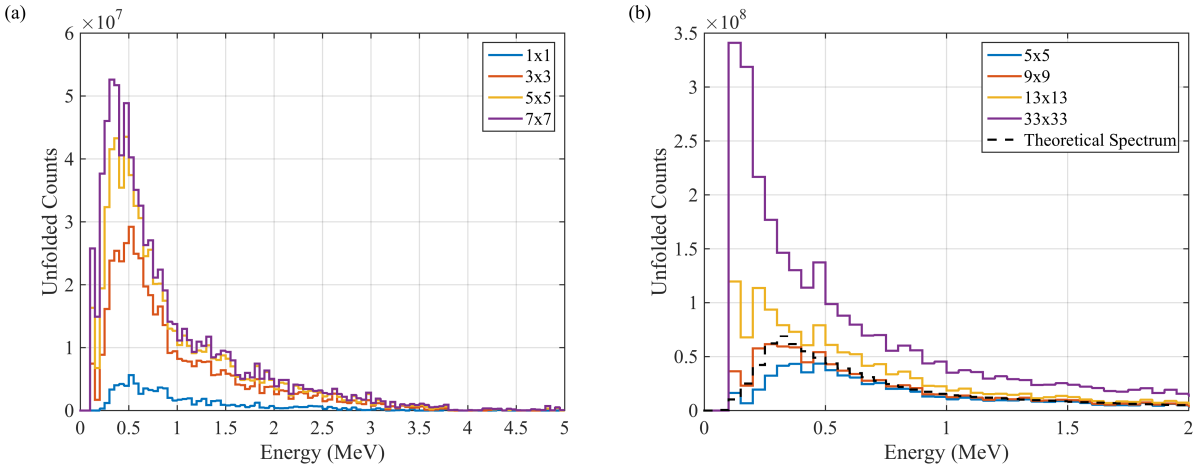

Figure 4.8. Photon spectra as a function of ROI size. The shape of the spectra remains representative of the ^{252}Cf distribution through a 9×9-pixel ROI. Larger ROIs include more low-energy photons resulting from room-return. The maximum energy has been reduced to 2 MeV in (b) to emphasize the difference in shape below ~0.5 MeV caused by the integration of room return.

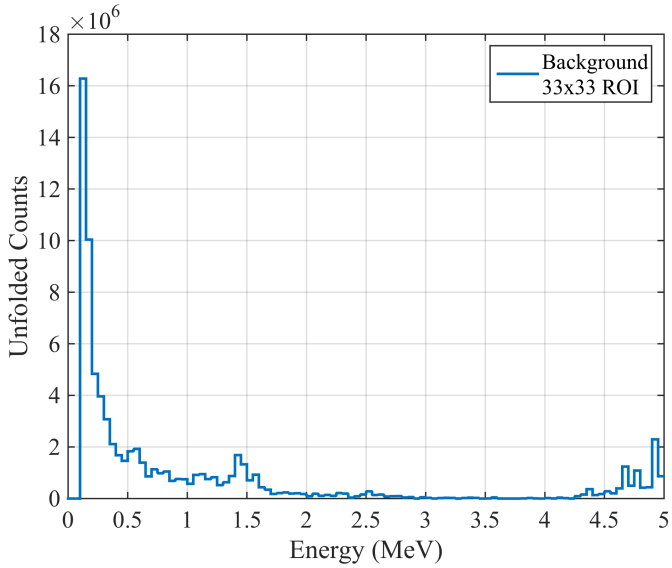

Figure 4.9. Unfolded photon spectrum for a 10-minute measurement of background. ROI was the 33×33-pixel region centered at (90°, 90°).

4.2.1.3. Choice of ROI

It is clear that the ROI used to evaluate a source can impact both the shape and magnitude of the unfolded spectrum. The measurement of a single point source made it possible to explore the impact over the full extent of the image. However, if multiple sources are present, the size of the ROIs should be limited to prevent contributions from different sources.

Figure 4.5 Figure 4.7 suggest that a 5×5-pixel ROI will result in a converged spectrum with regards to shape. While neutrons required almost the full image to reach the expected magnitude, photons reached the expected magnitude much sooner. However, even a 9×9-pixel ROI would require that sources be separated by 45° to prevent ROI overlap. Therefore, a 5×5-pixel ROI will be used for the remainder of this work. This ROI size facilitates qualitative comparisons of spectral shapes. Relative magnitudes of spectral features can also be compared with reasonable accuracy (as will be demonstrated in Section 4.3.2). It may be possible to derive correction factors to scale between a specific ROI size and the true source strength; however, the development of reliable correction factors, which will rely on a variety of parameters, is beyond the scope of this work.

4.2.2. Choosing a Termination Criterion

The number of MLEM iterations performed will impact the quality of the solution. Over the course of this work, it has been found that once enough iterations have been performed the dominant features of the isolated spectra will stabilize in shape and magnitude but noise will begin to appear, and amplify, in low-intensity regions of the image and spectra. Fortunately, the noise is typically not extensive enough to interfere in accurate localization or characterization of detected sources and therefore it is more important to avoid under-iterating than over-iterating.

Figure 4.10 and Figure 4.11 show how the spectra and images evolve as a function of iteration for neutrons and photons, respectively. Figure 4.10 and Figure 4.11 (a) plot the variance of the normalized data residual (defined below in Equation (4.1), and previously in Chapter 3), and the 'x' denotes the iteration determined by the stopping criterion defined below. For both neutrons and photons, the isolated spectra show significant changes in shape and magnitude over the first 40 iterations. The spectra eventually converge, showing only marginal increases in magnitude at select energy ranges as iterations are increased. The reconstructed images show a larger intensity near the (90°, 90°) pixel as iterations are increased; however, this is accompanied by an increase in noise.

Both Figure 4.10 and Figure 4.11 suggest that very similar results can be achieved over a large range of iterations (assuming the solution has converged). This flexibility is desirable because it puts less importance on the exact iteration chosen and more importance on determining when the solution is stable. Nonetheless, it is desirable to automate a stopping criterion to reduce human bias in producing solutions.

Chapter 3, proposed an MLEM stopping condition based on the variance of the normalized data residual. The data residual was defined as:

$$\boldsymbol{r}^{(k)} = \frac{\boldsymbol{b} - \widehat{\boldsymbol{b}}^{(k)}}{\sqrt{\widehat{\boldsymbol{b}}^{(k)}}} \qquad (4.1),$$

where $\boldsymbol{b}$ is the data vector and $\widehat{\boldsymbol{b}}^{(k)}$ is the forward projection of the current solution estimate, $\widehat{\boldsymbol{x}}^{(k)}$, through the system matrix $\boldsymbol{A}$. The data residual is useful because it gives insight to how well the solution estimate "matches" the measured data but requires no *a priori* knowledge of the measurement scenario.

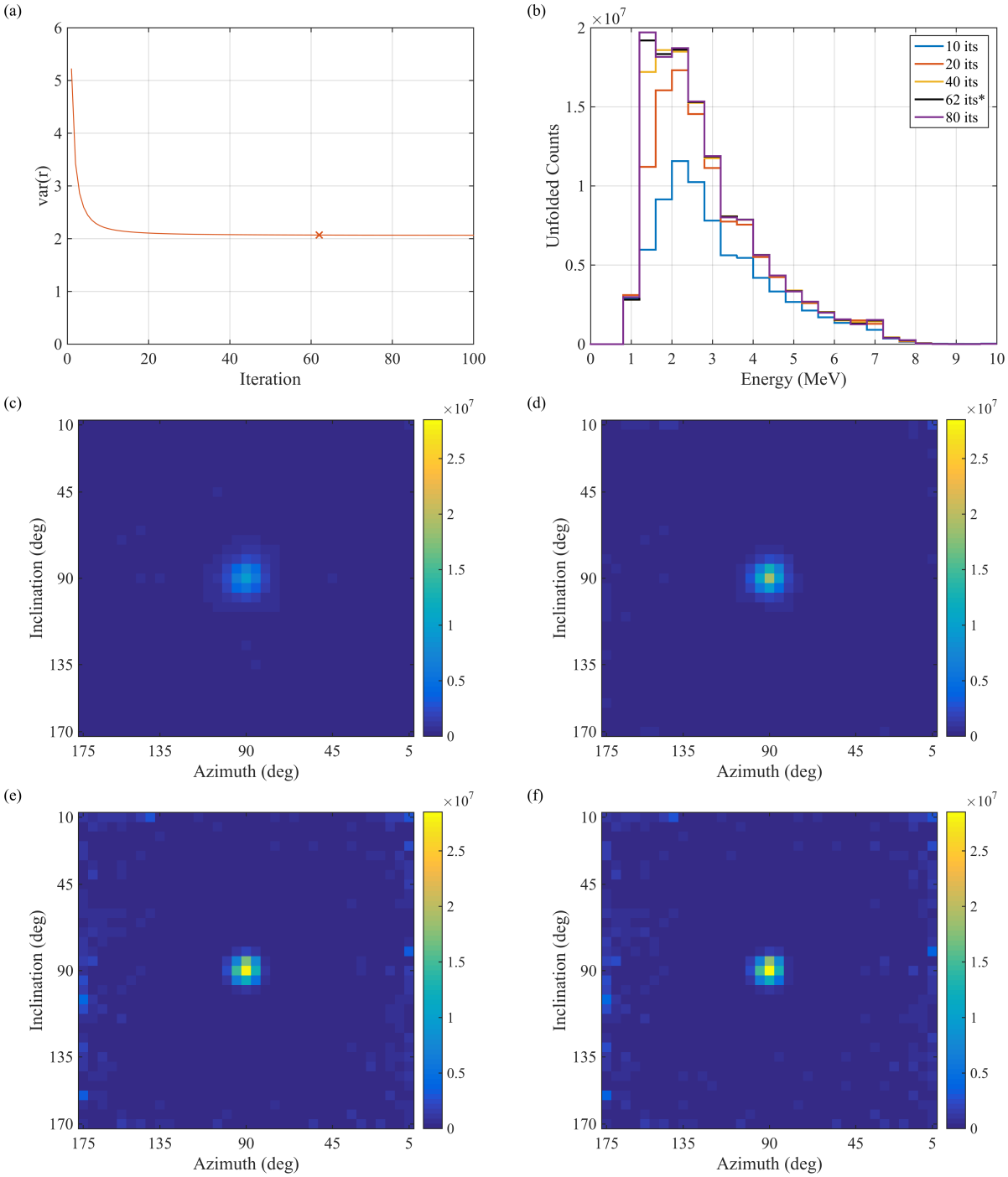

Figure 4.10. Evolution of isolated neutron spectrum and reconstructed image as a function of iterations. The stopping iteration was determined to be 62, as denoted by the 'x' on the variance curve shown in (a). Isolated neutron spectra for a 5×5 ROI are shown for 10, 20, 40, 62, and 80 iterations (b). Images are shown on a fixed color scale for 10 (c), 20 (d), 62 (e), and 80 (f) iterations.

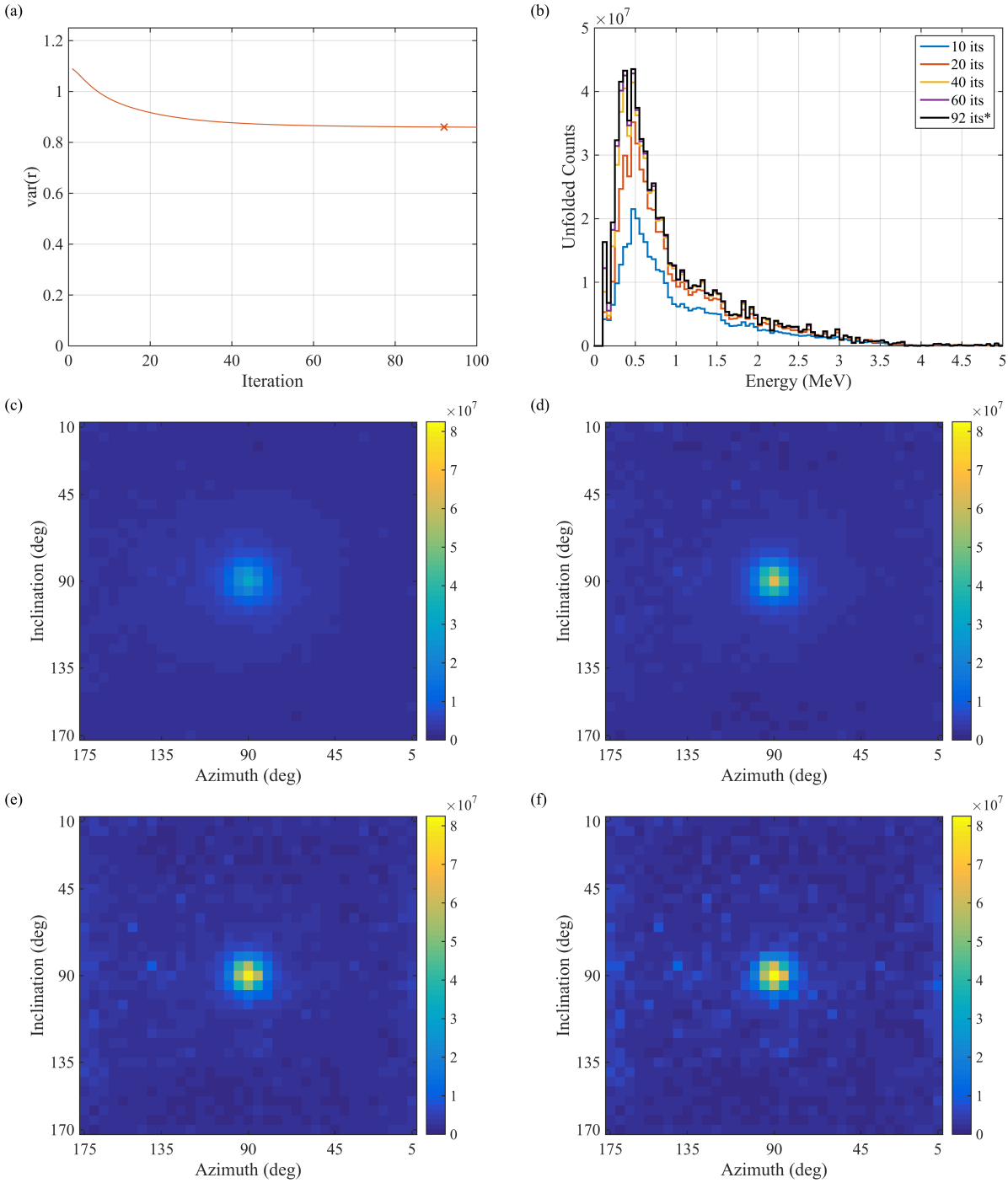

Figure 4.11. Evolution of isolated photon spectrum and reconstructed image as a function of iterations. The stopping iteration was determined to be 92, as denoted by the 'x' on the variance curve shown in (a). Isolated photon spectra for a 5×5 ROI are shown for 10, 20, 40, 60, and 92 iterations (b). Images are shown on a fixed color scale for 10 (c), 20 (d), 40 (e), and 92 (f) iterations.

Throughout this work, it was found that the variance of the data residual decays to a plateau as a function of iteration and the best solutions are found once the plateau has reached a "reasonably flat" slope. In this work, "reasonably flat" is determined to be when the relative difference of the residual variance between iterations, δ, is less than 10^{-4}, as defined in Equation (4.2):

$$\delta \equiv \frac{\mathrm{var}(\boldsymbol{r}^{(k-1)}) - \mathrm{var}(\boldsymbol{r}^{(k)})}{\mathrm{var}(\boldsymbol{r}^{(k-1)})} < 10^{-4} \tag{4.2}$$

The threshold of 10^{-4} was found by assessing normalized mean square error (NMSE) and the signal-to-noise ratio (SNR) for the image and the NMSE for the isolated spectrum as a function of δ. While both NMSE and SNR are useful for evaluating known data sets, they cannot be used for field measurements because they require *a priori* knowledge of the source location and energy spectrum.

NMSE is defined as:

$$\mathrm{NMSE}^{(k)} = \frac{\sum\left(\boldsymbol{x}^{(k)} - \boldsymbol{x}_{true}\right)^2}{\sum(\boldsymbol{x}_{true})^2} \tag{4.3}$$

where in this specific case we take $\boldsymbol{x}$ to represent either the image vector or the isolated spectrum rather than the full solution vector. These solution subsets are compared against $\boldsymbol{x}_{true}$, which is the expected solution. When analyzing the image, $\boldsymbol{x}_{true}$ is an image with 0 intensity at all locations except for (90°, 90°), which is where the source was known to be located. For spectrum analysis, truncated versions of the theoretical spectra shown in Figure 4.1 are used to define $\boldsymbol{x}_{true}$. The first three energy bins were removed during this analysis because the first two bins are not used during reconstruction due to the energy threshold and the third bin suffered from consistently poor reconstruction for both photons and neutrons (as previously discussed in Section 4.2). The isolated spectra were generated

using a 5×5 ROI centered at (90°, 90°). For both image and spectrum analysis $\boldsymbol{x}^{(k)}$ and $\boldsymbol{x}_{true}$ were normalized to their integrals such that the NMSE metric was assessing the "shapes" of the images and spectra.

SNR is defined as:

$$\text{SNR} = \frac{\mu_{signal}}{\sigma_{noise}} \tag{4.4}$$

where, μ_{signal} is the intensity of the image in the (90°, 90°) pixel and σ_{noise} is the standard deviation of pixel values in the rest of the image.

Figure 4.12 plots image and spectrum NMSE as well as image SNR as a function of δ. The quality metrics were generated for the full 10-minute measurement as well as for 2.5-minute, 5-minute, and 7.5-minute subsets. The δ-axis is reversed such that it decreases in value from left to right, which corresponds to an increase in iteration number. For reference, Figure 4.13 plots var(**r**) and δ as a function of iteration number.

Each metric follows a similar trend for the three data sets greater than 2.5 minutes. The 2.5-minute data set did not contain enough counts to produce fully converged spectra, which resulted in slightly different trends. The NMSE metric for both images and spectra plateau between $\delta=10^{-3}$ and $\delta=10^{-4}$. The SNR curves behave differently for neutrons and photons with the neutron SNR showing more gradual decline after reaching a peak than the found for the photons. In general, the SNR curves peak prior to the NMSE curves reaching a plateau, which suggests that some noise must be tolerated to achieve well converged spectra. In this work, more importance was placed on the accuracy of the spectra and so the tradeoff between spectrum NMSE and image SNR was deemed acceptable. Therefore, $\delta=10^{-4}$ was

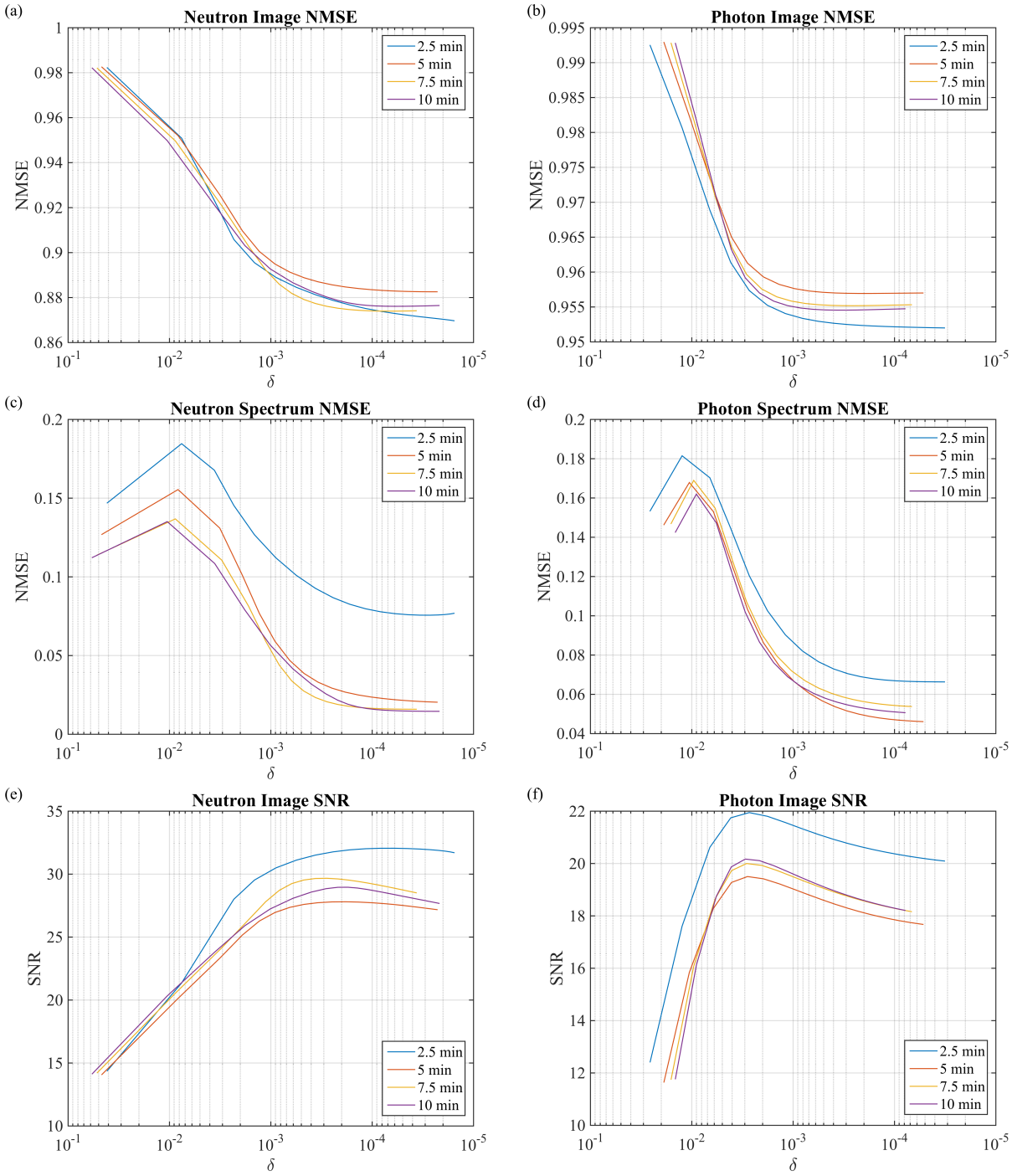

Figure 4.12. Image NMSE for neutrons (a) and photons (b). Isolated spectrum NMSE for neutrons (c) and photons (d). Image SNR for neutrons (e) and photons (f). Quality metrics are plotted against δ on an axis that decreases from left to right (iteration number increases from left to right). Quality metrics were assessed for the full 10-minute measurement as well as for 2.5-minute, 5-minute, and 7.5-minute subsets.

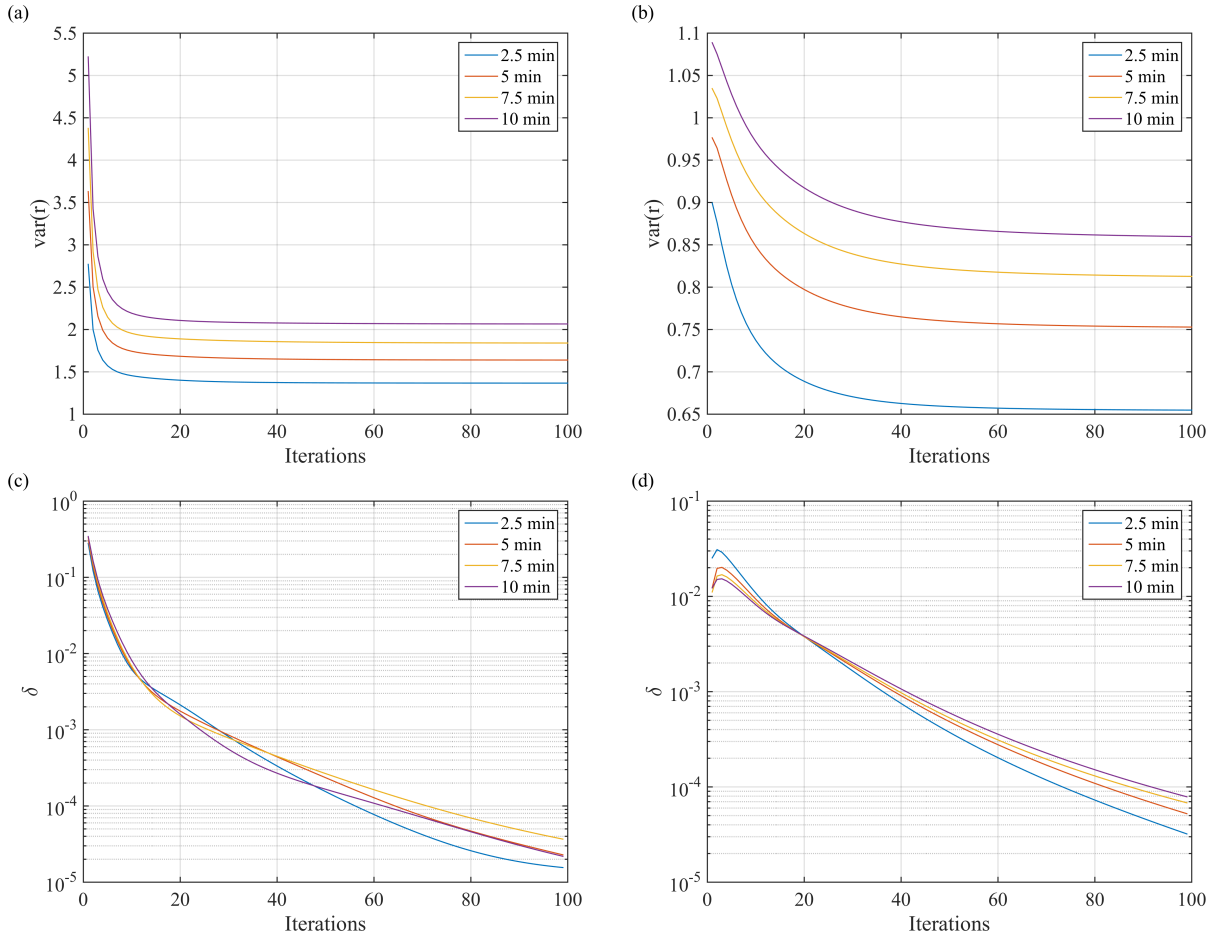

Figure 4.13. var(**r**) as a function of iteration number for neutrons (a) and photons (b). δ as a function of iteration number for neutrons (c) and photons (d). Trends are plotted for the full 10-minute measurement as well as for 2.5-minute, 5-minute, and 7.5-minute subsets.

chosen as the stopping criterion for the remainder of this work. While it is not guaranteed to be optimal for all measurements, this value of δ consistently results in well converged solutions across all data sets analyzed. It is worth noting that in practice, it is not necessary to use images and spectra from the same iteration. For example, an earlier iteration could be used to determine the location of sources and then further iterations could be performed to improve the quality of the spectra.

4.3. Gamma-Ray Experiment

To demonstrate the performance of the spectral isolation technique at localizing gamma-ray peaks, a 15-minute measurement was made of an 87.4-μCi ^{137}Cs source and an 88.6-μCi

^{22}Na source. Both sources were at a 2-m standoff with the ^{137}Cs located at (60°, 90°) and the ^{22}Na located at (120°, 90°). A total of 8.97×10^{4} photon events were recorded. A photograph of the experimental setup is shown in Figure 4.14.

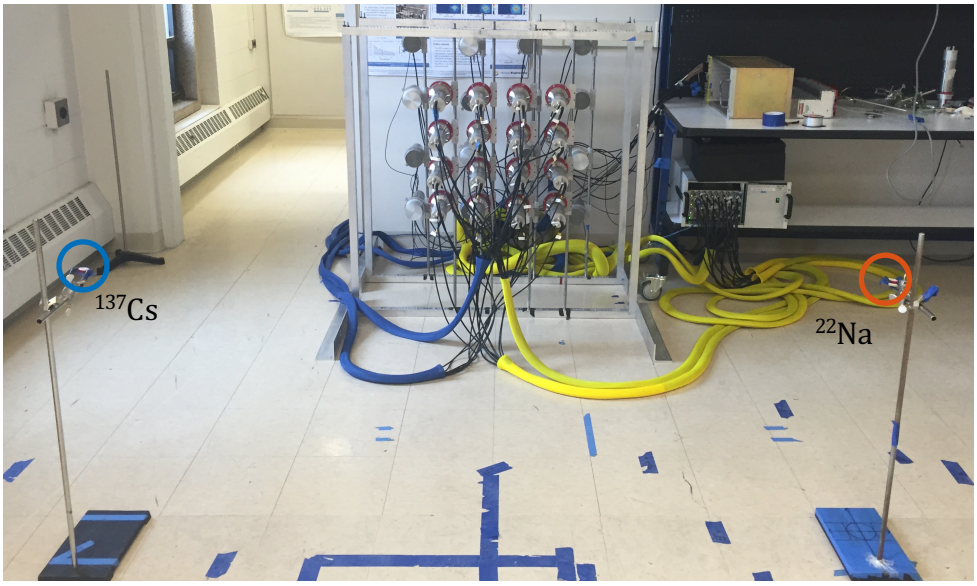

Figure 4.14. Photograph of the experimental setup. The 87.4 μCi ^{137}Cs source is located at (2 m, 60°, 90°) and the 88.6-μCi ^{22}Na source is located at (2 m, 120°, 90°).

Table 4.1 lists the intensities of the gamma rays emitted by these sources as well as the expected number of gamma rays emitted toward the DPI during a 15-minute measurement (i.e. the amount that would be expected in a perfectly unfolded spectrum). The 0.511 MeV gammas are not emitted directly by ^{22}Na, but are instead caused by positron annihilation resulting from a β^{+} decay of ^{22}Na.

Table 4.1. Intensity of gamma-ray emissions from ^{137}Cs and ^{22}Na and the expected number of unfolded counts from a 15-minute measurement using a 2-m standoff.

Source	Energy (MeV)	Intensity	Expected Counts
^{137}Cs	0.662	0.851	9.41×10^{7}
^{22}Na	0.511	1.808	2.02×10^{8}
^{22}Na	1.274	0.999	1.12×10^{8}

Figure 4.15 shows the reconstructed image as well as the isolated photon spectra for the two 5×5 ROIs outlined on the image. The two hotspots are both centered at the correct locations. The isolated spectra are also well aligned with the expected energies. The ROI centered at (60°, 90°) shows a peak in the energy bins ranging between 0.6 and 0.7 MeV, encompassing the 0.662 MeV emission from ^{137}Cs. The ROI centered at (120°, 90°) shows one peak in the energy bins ranging between 0.45 and 0.55 MeV and one peak in the energy bins ranging between 1.2 and 1.3 MeV, which encompass the 0.511 MeV and 1.274 MeV peaks from ^{22}Na, respectively.

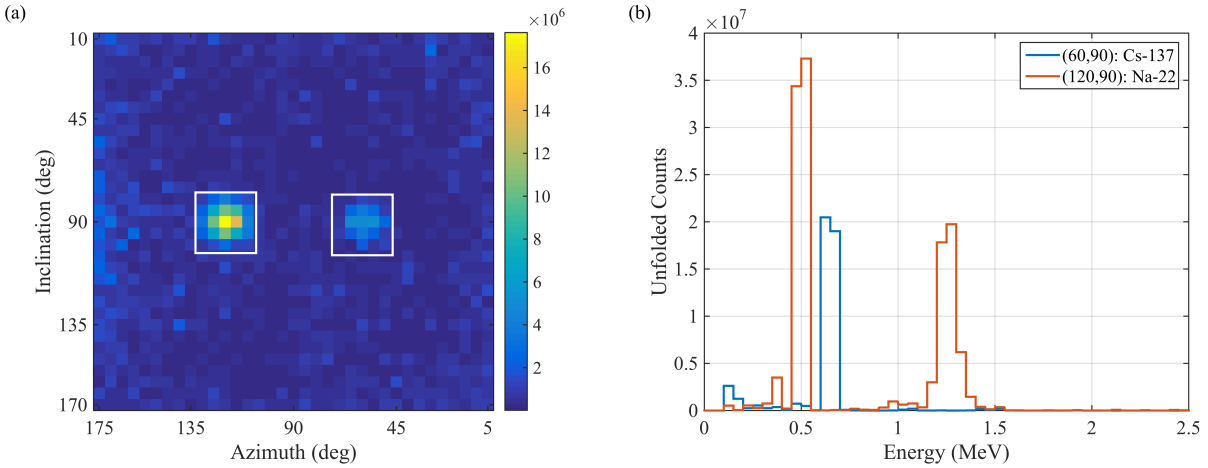

Figure 4.15. Reconstructed image (a) and isolated spectra (b) for a 15-minute measurement of .an 87.4 µCi ^{137}Cs source located at (2m, 60°, 90°) and an 88.6-µCi ^{22}Na source located at (2m, 120°, 90°). White boxes in the image denote the 5×5 pixel ROIs used to generate the isolated spectra.

4.3.1. Improvement Over Basic Reconstruction Techniques

For comparison, Figure 4.16 shows the simple-backprojection image and coincidence spectrum for the same data. It is clear that the MLEM-based reconstruction technique has improved the visibility of the ^{137}Cs hotspot in the image. Additionally, the unfolded spectra provide a more accurate representation of the emitted distributions than the coincidence spectrum, which includes background events and significant contributions from the Compton continuum of each photopeak.

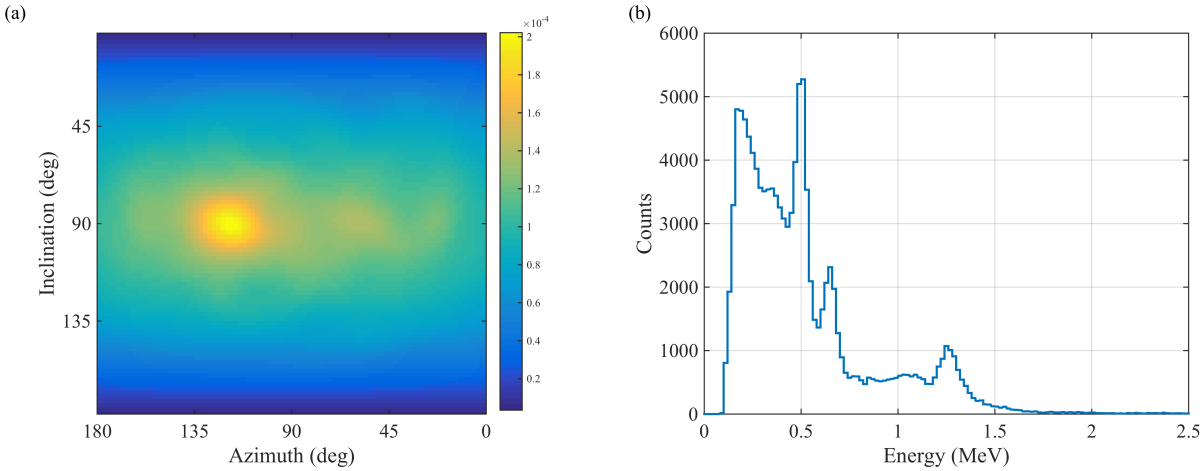

Figure 4.16. Simple backprojection image (a) and coincidence spectrum (b) for a 15-minute measurement of .an 87.4 μCi ^{137}Cs source located at (2 m, 60°, 90°) and an 88.6-μCi ^{22}Na source located at (2 m, 120°, 90°).

4.3.2. Relative Peak Counts

Table 4.2 shows how the number of unfolded counts in each of the three photopeaks shown in Figure 4.15 compared to the expected number of counts. Table 4.3 shows the number of counts in each photopeak relative to the number of counts in the ^{137}Cs 0.662 MeV photopeak. The ranges used to integrate each photopeak are also shown in Table 4.2. A larger range was used for the 1.274 MeV peak to account for its larger spread. Both tables show that the 0.662 MeV and 1.274 MeV peaks reconstruct to a similar fraction of the expected number of events with the 0.511 MeV peak reconstructing to a slightly lower fraction. The sources of statistical and systematic uncertainty that might impact these values will be explored further in Chapter 5.

Table 4.2. Unfolded photopeak counts relative to the expected number of unfolded counts.

Energy (MeV)	Integration Range (MeV)	Photopeak Counts	Fraction of Expected
0.662	0.6-0.7	3.95×10^{7}	0.419
0.511	0.45-0.55	7.17×10^{7}	0.355
1.274	1.15-1.35	4.68×10^{7}	0.417

Table 4.3. Ratio of photopeak counts relative to the 0.662 MeV peak.

Energy (MeV)	Ratio to 0.662 Peak	Expected Ratio	Fraction of Expected
0.662	1.00	1.00	1.00
0.511	1.82	2.15	0.85
1.274	1.18	1.19	0.99

4.3.3. Image Energy Windowing

In Figure 4.15 (a), the ^{137}Cs hotspot has a lower intensity than the ^{22}Na hotspot, which is expected due to the relative number of gamma emissions between the two sources. It is possible to improve the contrast of the ^{137}Cs hotspot by restricting the energy range of the image. Figure 4.17 (b), which shows the image for the 0.6-0.7 MeV energy range, demonstrates this effect. In addition to improving the contrast of the ^{137}Cs hotspot, the use of an energy window has removed the ^{22}Na hotspot from the image, and has also reduced the image noise. A similar technique can also be used on the ^{22}Na hotspot, which is demonstrated in Figure 4.17 (c) and (d) for the 0.45-0.55 MeV range and the 1.15-1.35 MeV range, respectively. In all three images, only the expected hotspot is shown, which is encouraging considering the proximity of the 0.511 MeV and 0.662 MeV lines (relative to the energy resolution of the system). Additionally, the improved contrast of the ^{137}Cs hotspot provided by the windowed image demonstrates the utility of the spectrum-isolation technique for analyzing environments containing multiple sources of different intensities.

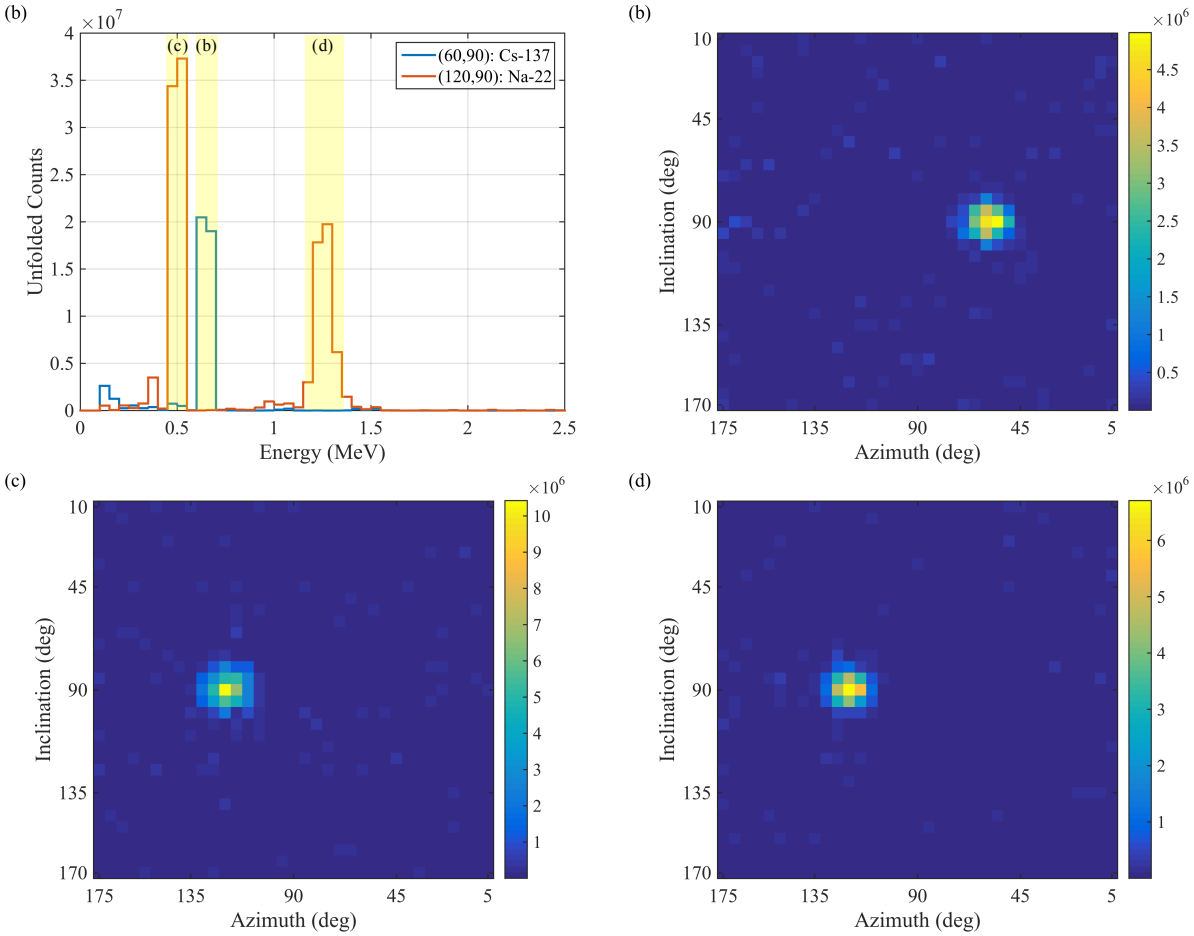

Figure 4.17. Images reconstructed over various energy ranges of the isolated spectra shown in (a). ^{137}Cs hotspot is shown using the 0.60-0.70 MeV energy range (b). ^{22}Na hotspot is shown using two different energy ranges: 0.45-0.55 MeV (c) and 1.15-1.35 MeV (d).

4.4. Measurement of Two Sources at Arbitrary Distances

The results presented in Sections 4.2 and 4.3 were for strategically positioned sources located at the center of a pixel at the 2-m source-to-detector distance used in the simulation of the system matrix. In the field, it may not always be possible to achieve such desirable source locations (or the source location may be unknown). This experiment will be used to demonstrate the utility of the spectrum-isolation technique for source localization and characterization when the sources are not well aligned with the system matrix radius. Similar results can be found in [32], which analyzed the same data set using a system matrix computed with a 5-m standoff and discrete source locations as opposed to the continuously

distributed source used in this work. As a reminder, the coincidence spectra for this experiment are shown in Chapter 2.

The DPI was used to simultaneously measure a 25.7μCi ^{252}Cf source and a 62.9 μCi ^{60}Co source. The ^{252}Cf source underwent approximately 3×10^4 fissions-per-second, resulting in approximately 1.1×10^4 neutrons-per-second and 2.3×10^5 photons-per-second emitted from fission. The ^{60}Co source emits 2 gammas of nearly equal intensity (1.173 MeV with 99.85% intensity and 1.332 MeV with 99.98% intensity) resulting in approximately 4.7×10^6 photons-per-second. The ^{252}Cf source was located at (1.75 m, 114°, 93°) and the ^{60}Co source was located at (3.9 m, 58°, 84°). The measurement was carried out for 350 minutes and a total of 1.27×10^4 neutron events and 9.09×10^5 photon events were collected by the system. 40-keVee thresholds were used in all detectors, which exclude the first two source space energy bins from reconstruction. The measurement set up is shown in Figure 4.18.

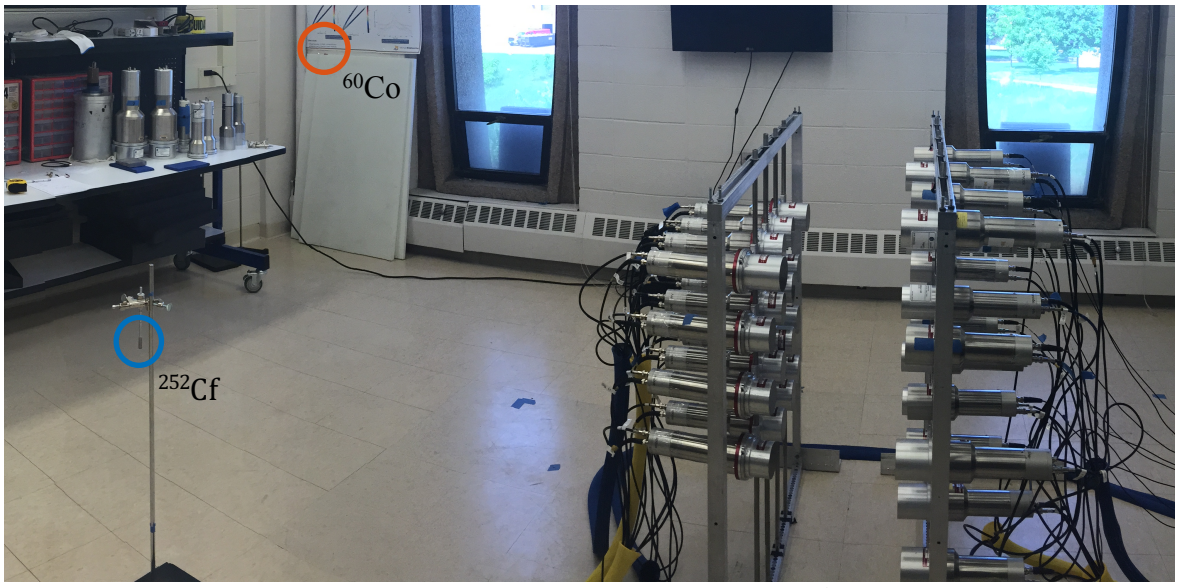

Figure 4.18. Photograph of the experimental set up. The 25.7-μCi ^{252}Cf source is located at (1.75 m, 114°, 93°) and the 62.9-μCi ^{60}Co source is located at (3.9 m, 58°, 84°).

The ^{252}Cf source used in this measurement is much older and weaker than the source used in Section 4.2. The neutron spectrum is expected to have the same shape as shown in

Figure 4.1 (a); however, some differences are anticipated in the photon spectrum. The source is expected to have contributions due to impurities in the source. When a ^{252}Cf source is produced, it contains a small fraction of chemical impurities such as ^{249}Cf and ^{250}Cf [93]. These isotopes have longer half-lives ($T_{1/2}$=351 years and $T_{1/2}$=13.1 years, respectively) than ^{252}Cf ($T_{1/2}$=2.6 years). The source used in this measurement is over 20 years old therefore much of the ^{252}Cf has decayed resulting in a higher relative contribution of the impurities. The largest effect of this grow-in of impurities is the 0.388 MeV gamma ray, which is emitted by ^{249}Cf [93].

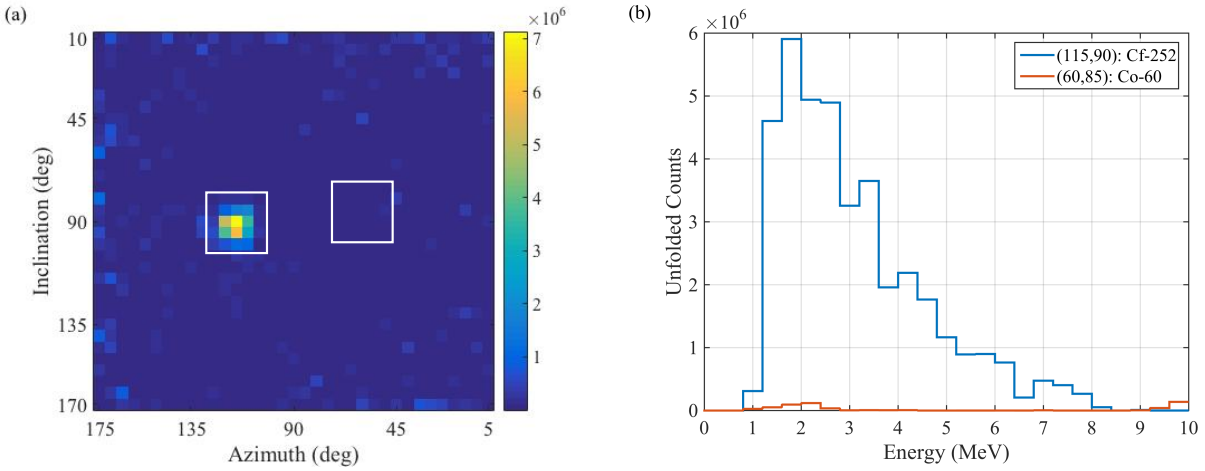

Figure 4.19. Neutron reconstructed image (a) and spectrum (b) for a 350-minute measurement of a 25.7-µCi ^{252}Cf source located at (1.75 m, 114°, 93°) and a 62.9-µCi ^{60}Co source located at (3.9 m, 58°, 84°). The white boxes on the image define the ROI used to generate the spectra shown in (b).

Figure 4.19 shows the reconstructed neutron image as well as the isolated neutron spectra for the two 5×5 ROIs outlined on the image. The image shows one hotspot, centered at (115°, 95°), which corresponds with the location of the ^{252}Cf source. As expected, no hotspot is visible at the location of the ^{60}Co source. The isolated spectrum for the ^{252}Cf source is representative of the expected Watt distribution, but is noisier than the isolated spectrum shown in Figure 4.2 (b). The noise is primarily due to the lower number of measured neutron events (1.27×10^4 compared to 4.4×10^4) and, to a lesser extent, the additional model

mismatch introduced by the source being located closer to the system than the 2-m standoff used in the system matrix. The isolated spectrum for the ^{60}Co ROI shows very little intensity, encompassing only 5.4×10^{5} unfolded counts compared to the 3.9×10^{7} unfolded counts contained in the ^{252}Cf ROI. The non-zero neutron intensity of the ^{60}Co region is a result of imperfect reconstruction, as discussed in Section 4.2.1.

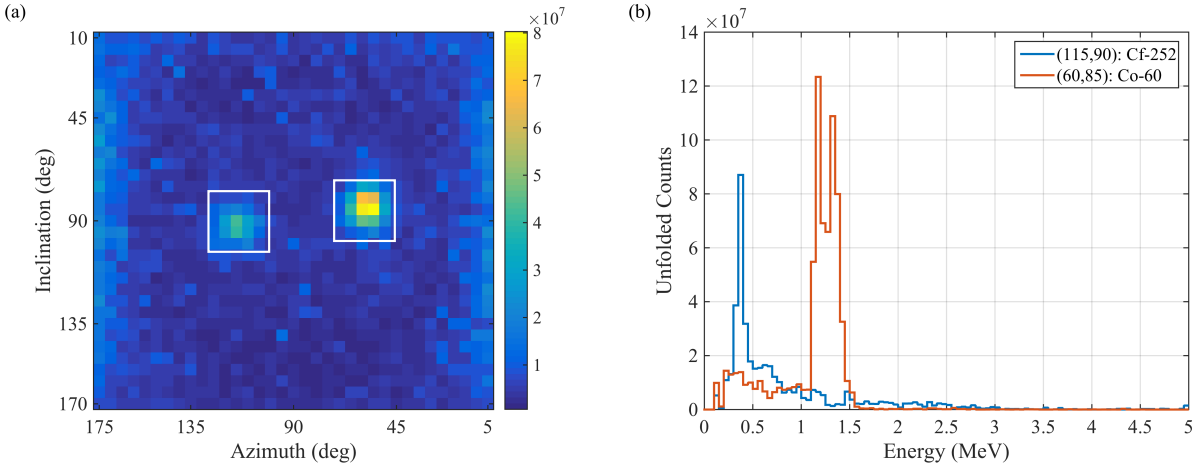

Figure 4.20. Photon reconstructed image (a) and spectrum (b) for a 350-minute measurement of a 25.7-µCi ^{252}Cf source located at (1.75 m, 114°, 93°) and a 62.9-µCi ^{60}Co source located at (3.9 m, 58°, 84°). The white boxes on the image define the ROI used to generate the spectra shown in (b).

Figure 4.20 shows the reconstructed photon image as well as the isolated photon spectra for the two 5×5 ROIs outlined on the image. A hotspot is visible at (55°, 85°), which corresponds with the location of the ^{60}Co source. A second hotspot is also visible in the photon image at the location of the ^{252}Cf source. The ^{252}Cf photon hotspot is at a lower intensity than the ^{60}Co hotspot, which is expected due to the relative photon emissions (despite the ^{252}Cf being closer). Some reconstruction artifacts are present along the azimuthal edges of the photon image. These artifacts are a result of reconstructing over 2π rather than 4π, and are due to background photons incident from behind the system. Figure 4.21 shows the isolated photon spectra for two regions along the edge of the image. Both regions show a similar response with a large low energy contribution similar to the

unfolded background spectrum shown in Figure 4.9. The edge artifacts are more noticeable than in previously presented measurements because of the relatively lower signal-to-background ratio in this measurement.

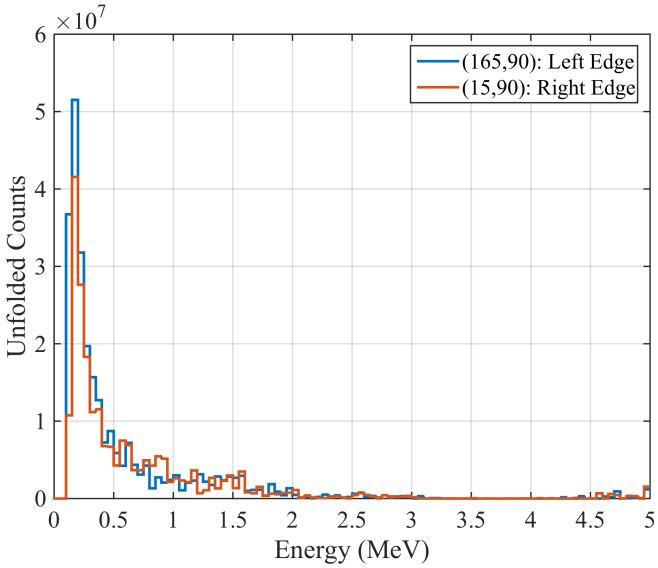

Figure 4.21. Isolated photon spectra for the 5×5-pixel regions centered at (15°, 90°) and (165°, 90°). Spectra suggest that the artifacts present along the edges of the reconstructed image shown in Figure 4.8 (a) are due to background photons.

The photon spectrum for the ^{60}Co region shows a high intensity region between 1.1 and 1.45 MeV with two peaks are present: one in 1.15-1.20 MeV bin and one in the 1.3-1.35 MeV bin. These peaks correspond well with the expected gamma-ray energies of 1.17 and 1.33 MeV. While the peak bins are not of equal intensity, a summation of the 1.10-1.25 MeV range and the 1.25-1.4 MeV range yields 2.47×10^8 and 2.55×10^8 unfolded counts, respectively. The peaks are not completely separable but these summations suggest that the individual peaks are of approximately equal intensity. A more pronounced continuum is present in the ^{60}Co spectrum than was seen in either the ^{137}Cs or ^{22}Na spectrum shown in Figure 4.20 (b). This continuum is likely caused by close proximity of the ^{60}Co source to the laboratory wall, which increases the amount of localized room return. While it may be tempting to attribute this to

model mismatch arising from the larger standoff of the source, Chapter 5 will show that this is not the case.

The photon spectrum for the ^{252}Cf region is similar to the theoretical distribution presented in Figure 4.1 (b). However, this distribution is superimposed with two notable features. The first is the 0.388 MeV ^{249}Cf peak which appears in the 0.35-0.45 MeV bin and has become a dominant feature of the significantly aged ^{252}Cf source. The second is a small protrusion between 0.60 and 0.70 MeV, which is likely due to the buildup of ^{137}Cs (a common fission product with $T_{1/2}$=30.1 years). While the^{10}B(n, α) gamma is expected due to the presence of neutrons, the signal is indistinguishable from the edge of the dominant ^{249}Cf peak.

Similar to Section 4.3.3, it is possible to isolate the hotspots using energy windowing. Figure 4.22 shows the reconstructed photon image over three different energy ranges, which are highlighted in Figure 4.22 (a). The ^{60}Co hotspot is enhanced using the 1.10-1.45 MeV range in in Figure 4.22 (b). While this range increases the contrast of the ^{60}Co hotspot, some signal is present in the ^{252}Cf location, which is expected due to the continuous fission photon spectrum of ^{252}Cf. The ^{252}Cf hotspot is windowed in two different ways. Figure 4.22 (c) shows the result of a window between 0.30 and 0.45. This window results in increased contrast of the ^{252}Cf hotspot but is noisier than the isolated ^{60}Co hotspot. It is also possible to isolate the ^{252}Cf hotspot using a window above the ^{60}Co energies, which is demonstrated in Figure 4.22 (d) for a window between 1.50 and 5.00 MeV.

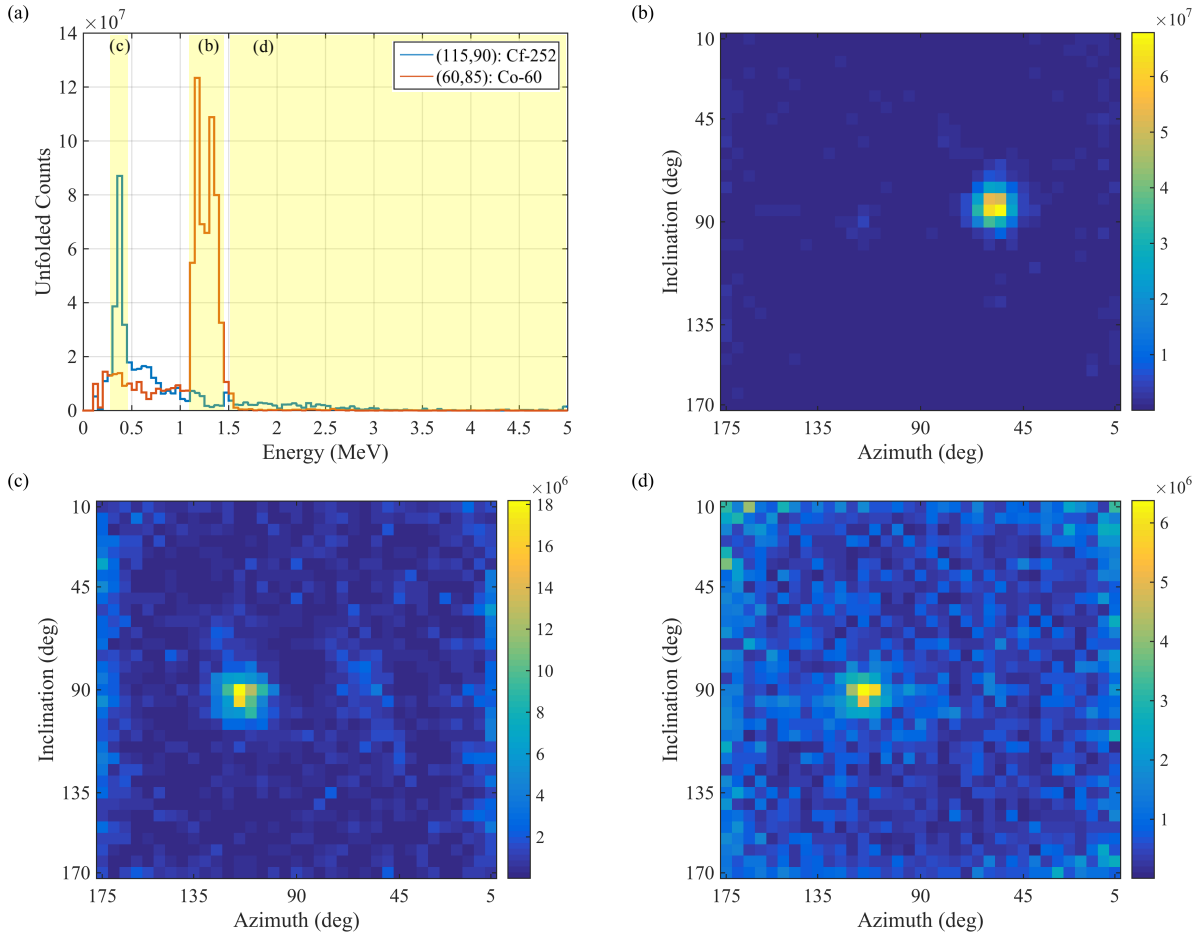

Figure 4.22. Images reconstructed over various energy ranges of the isolated spectra shown in (a). ^{60}Co hotspot is shown using the 1.10-1.45 MeV energy range (b). ^{252}Cf hotspot is shown using two different energy ranges: 0.30-0.45 MeV (c) and 1.50-5.00 MeV (d).

4.5. Remarks

This chapter utilized three different measurement scenarios to demonstrate the utility of the spectrum-isolation reconstruction technique. The results show that the technique produces accurate images and, at the very least, qualitatively accurate localized spectra for both photons and neutrons. The use of small ROIs allowed for the analysis of individual sources and reduced the contribution of background and scattered radiation, which was identified elsewhere in the images. While the 5×5 ROIs used to evaluate the sources did not yield spectra that matched the emitted magnitude, spectral features were found to be accurately represented. It was also demonstrated that reconstruction is not

limited to the 2-m standoff used to compute the system matrix. The apparent accuracy of this technique leaves one to question how much uncertainty is present in the solutions, which will be further explored in Chapter 5.

Chapter 5. Uncertainties in Spectrum-Isolation Solutions

5.1. Motivation

Chapter 3 demonstrated that the spectrum-isolation technique is able to accurately estimate localized energy spectra within the reconstructed image. It is important to understand the uncertainties associated with these solutions, both with the reconstructed images and the isolated spectra. Additionally, it is important to understand how various factors, such as source location or number of measured events, might impact the uncertainties associated with a specific measurement. Furthermore, uncertainty quantification is a necessary step in moving toward quantitative analysis of solutions.

This chapter will demonstrate how a technique known as bootstrapping can be used to reliably estimate how the uncertainties resulting from measurement statistics propagate through the MLEM algorithm. After the validity of the bootstrapping method has been established, it will be used to explore how statistical uncertainty varies as a function of measured events.

In addition to statistical uncertainty, it is important to understand how systematic uncertainties within the system matrix impact the accuracy and uncertainty of the solution. If multiple sources from a single FOV are to be compared reliably, it is especially important to understand how these uncertainties might change the isolated spectra for the same source measured at different locations. The impact of systematic uncertainties within the system matrix will be explored by measuring a ^{252}Cf source at various locations in the FOV. The effect

of measuring at distances other than the 2-m standoff used in the system matrix will also be explored. The observed data collected from these different locations and standoffs will preferentially probe different regions of the system matrix during the reconstructions process. By comparing the isolated spectra generated from each of these measurements, it is possible to determine if systematic uncertainties will significantly impact the ability to characterize sources at different locations within the FOV.

5.2. Statistical Uncertainty

As with any radiation measurement, the data collected by the DPI is subject to the statistical deviations associated with a Poisson process. That is, two measurements of the same source distribution will yield different measured data. If the measurement time is long enough, then the underlying distributions will prevail and multiple realizations will converge to the same result within the limits of their associated statistical uncertainty. In the typical Poisson counting process, the standard deviation of a measured quantity can be calculated as the square root of the number of measured events. This straightforward technique can be directly applied, for example, to the coincidence spectra reconstructed by the DPI. However, the unfolded counts calculated by the spectrum-isolation technique are a result of propagating a measured distribution through a non-linear process (namely MLEM) [94]. While it is certainly important to quantify the uncertainty in ML solutions, the propagation of statistical uncertainty through the MLEM algorithm is not straightforward.

As with any measurement, the variance in the solution can be estimated by performing multiple, repetitive measurements of the same distribution. However, in many non-proliferation and safeguards applications it is unfeasible, or sometimes impossible, to perform multiple measurements. The need to perform multiple measurements could be

alleviated by dividing the measured data set into several smaller subsets; however, this comes at the cost of higher statistical fluctuations due to the reduced number of events in each data subset. The bootstrap technique, described below in Section 5.2.1, facilitates estimation of statistical uncertainty without the need to perform multiple measurements or subdivide the measured data.

5.2.1. Bootstrapping

The bootstrap is a statistical technique used for estimating the variance in a measurement when it is impractical to perform multiple repetitive measurements [95]. The technique has been used with success in several medical imaging studies related to positron-emission tomography [96]–[101]. The bootstrap works by resampling (with replacement) the measured data set to produce K-1 bootstrap data realizations. Each of the bootstrap realizations, as well as the measured realization, can then be processed with MLEM resulting in K bootstrap solutions from which the variance can be estimated. It is worth noting that generating K bootstrap solutions will increase the computation time by approximately a factor of K. However, this additional cost could be easily reduced by processing each realization in parallel across several cores.

In this work, the bootstrap data realizations are generated from the list-mode data used to fill the binned data vector $\boldsymbol{b}$. As a reminder, the list mode data contains the information required to sort each event into bins, namely the reconstructed energy, reconstructed angle, and detector pair. If a data set contains N measured events, then each bootstrap data set will also contain N total events. While the measured list mode data will include one entry for each individual measured event, the bootstrap realizations may include zero, one, or many entries for each event. This approach is similar to the non-parametric list-mode technique proposed

by Dahlbom [98] and tested by Lartizien et al. [100] and (with some modifications) Ibaraki et al. [101].

The variation in the bootstrap data-sets will result in variation across the bootstrap solutions, which can be used to estimate the statistical properties of the measured data set. For example, the variance, σ^2, of a region of interest, R, can be calculated as:

$$\sigma^2 \equiv \mathrm{var}(R) = \frac{1}{K-1}\sum_{k=1}^{K}(R_k - \mu)^2 \quad (5.1),$$

where R_k is the number of counts in R for the k^{th} bootstrap solution and μ is the mean counts in R across all realizations:

$$\mu = \frac{1}{K}\sum_{k=1}^{K} R_k \quad (5.2).$$

Haynor and Woods established that for an image, R can include any number of contiguous or disjoint pixels [96]. This idea can be extended to the spectrum-isolation technique by defining R to be an individual energy bin of the isolated spectra. In this way, the uncertainty of each energy bin in the isolated spectrum can be estimated regardless of the size or shape of the ROI used to generate the spectrum.

5.2.2. Validation of Bootstrapping

Prior to relying on the bootstrap technique to estimate solution variance, it is important to validate that the error predicted through bootstrapping is representative of the error across repetitive measurements. A series of 50 5-minute measurements were performed with a 4.4-mCi ^{252}Cf source located at (2 m, 90°, 90°). These measurements resulted in an average of 22,221 neutron counts and 206,939 photon events per 5-minute segment. Aside from the measurement time, which is reduced by a factor of 2, this measurement is identical

to the ^{252}Cf measurement presented in Chapter 4. As such, the isolated spectra and images presented in this study are expected to be similar to those presented in Chapter 4 (within the limits of increased statistical uncertainty).

Equations (5.1) and (5.2) are also used to assess the mean and variance across measured data sets. However, for measured data sets, k now represents a solution from a unique measurement rather than a bootstrapped realization. The termination criterion defined in Section 4.2.2 is used to determine the final iteration for each realization (both measured and bootstrapped).

The following two sections will assess how well the statistical properties estimated using 50 bootstrapped realizations of a single 5-minute measurement compare to the statistical properties computed directly from the full set of 50 repeated measurements. Comparisons will be made for isolated spectra, full images, and gross counts within an image ROI. These sections will show that bootstrapping provides a reasonable estimate of the relative uncertainty, defined as σ/μ, in a solution. However, while the measured estimate of μ will increase in accuracy with the number of independent measurements, the bootstrapped estimate of μ does not vary significantly from the μ of the original data. An improved estimate in μ is not obtained via bootstrapping because the bootstrapped realizations are still subject to the statistical fluctuations of the single data set from which they were generated. These fluctuations are averaged out when multiple independent measurements are performed. These findings are consistent with conclusions drawn by Dahlbom [98], Lartizien et al. [100], and Ibaraki et al. [101].

5.2.2.1. Statistical Uncertainties in the Isolated Spectra

As described in Section 5.2.1, the mean and standard deviation can be computed for each energy bin in the isolated energy spectrum. In the spectra shown below, the magnitude of each energy bin represents the mean of that energy bin across all measured (μ_M) or bootstrapped (μ_B) realizations. The error bars shown represent ±1σ where σ_M and σ_B are the standard deviation across the measured and bootstrapped realizations, respectively. In all cases, the isolated spectra were generated using the 5×5-pixel ROI centered at (90°, 90°). Figure 5.1 (a) compares the measured and bootstrapped mean neutron energy spectrum while Figure 5.1 (b) compares the relative uncertainty as a function of energy. Figure 5.2 makes the same comparison for photons. A constrained energy range is also shown in Figure 5.2 (c) and (d) to emphasize the agreement below 2 MeV. These figures are presented first as a qualitative comparison between the statistical quantities computed using bootstrapped and measured realizations and are followed by a more quantitative assessment.

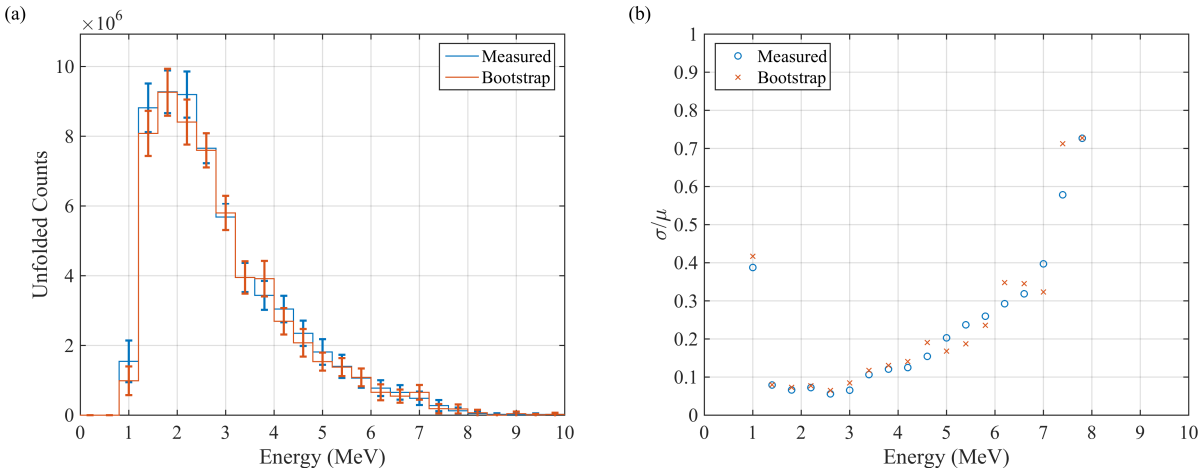

Figure 5.1. Comparison between the measured and bootstrapped mean neutron spectrum (a), and relative uncertainty as a function of energy (b). Relative uncertainties above 1 are not shown.

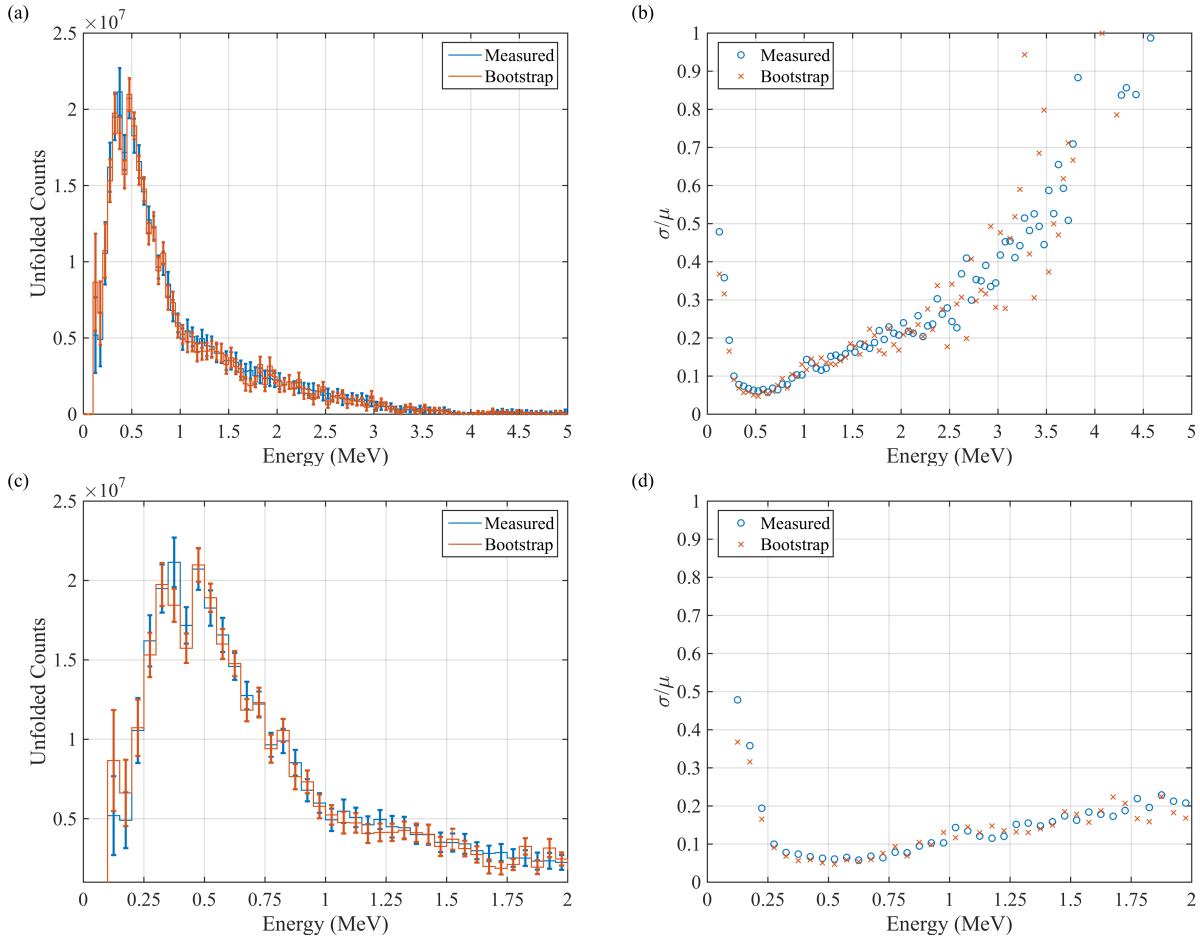

Figure 5.2. Comparison between the measured and bootstrapped mean photon spectrum (a) and (c), and relative uncertainty as a function of energy (b) and (d). Relative uncertainties above 1 are not shown.

For both photons and neutrons, the mean spectra and relative uncertainty plots compare well between methods. As expected, the relative uncertainty increases as the number of unfolded counts decreases. The bootstrapped relative uncertainty tracks the measured relative uncertainty very well for the most frequently observed energies. However, the agreement becomes worse at higher energies, as the trends in the curves become more erratic. The measured relative uncertainty curves suffer less from this erratic behavior, which is a result of the mean being averaged over 50 independent data sets. The bootstrapped estimate of the mean benefits significantly less from the averaging process because each of the 50 bootstrapped realizations come from the same data set. At some of

the higher energies the relative uncertainty (either measured or bootstrapped) is greater than 1. These data points have been omitted from the relative uncertainty plots for clarity but are included in the analysis made later in this section.

Equation (5.3) defines the fractional deviation metric, Δ, that is used to assess the agreement between bootstrapped and measured estimates of a statistical quantity:

$$\Delta_S = \frac{S_B - S_M}{S_M} \tag{5.3}$$

In Equation (5.3), S_B is the bootstrapped estimate, S_M is the measured estimate, and S represents the statistical quantity of interest (such as μ or σ/μ). Figure 5.3 shows the fractional deviation in σ/μ and μ for neutrons. Figure 5.4 shows the same for photons. All four figures have a y-axis ranging from -1 to +1. However, only 1 neutron data point and 2 photon data points fall outside this range.

As predicted by Figure 5.1 and Figure 5.2, the fractional deviation in σ/μ is closer to 0 in the energy ranges that have more of counts. As energy increases, a larger deviation is seen between the measured and bootstrapped estimates. This deviation is in-part due to the bootstrapped μ failing to converge to the measured μ (i.e. a large deviation in μ will typically result in a large deviation in σ/μ). Unfortunately, these large deviations in μ make it difficult to assess the performance of the bootstrapping in regions of high relative uncertainty. However, it is reasonable to expect that if a similar relative uncertainty were achieved across all energies, the bootstrapping technique would perform well across the entire spectrum.

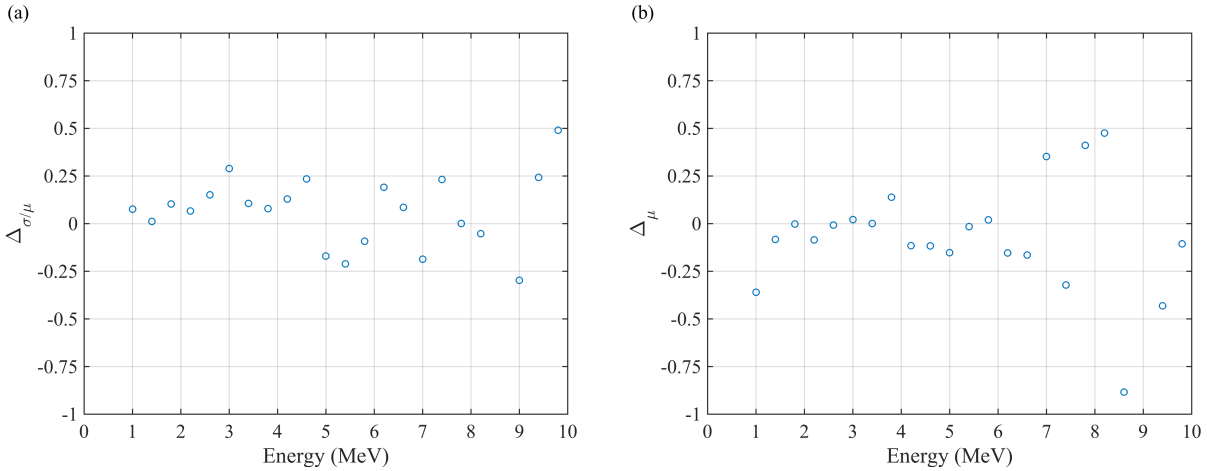

Figure 5.3. Fractional deviation in σ/μ (a) and μ (b) for neutrons. Fractional deviations greater than ±1 are omitted.

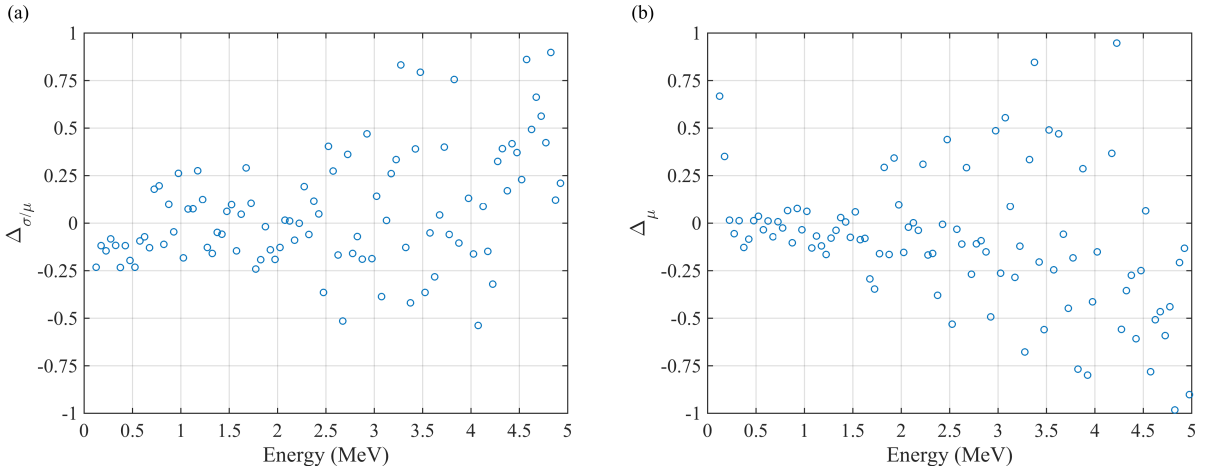

Figure 5.4. Fractional deviation in σ/μ (a) and μ (b) for photons. Fractional deviations greater than ±1 are omitted.

While a higher deviation in μ is expected in regions of lower counts, it is important to understand if that deviation is statistical or systematic. Figure 5.5 plots the magnitude of Δ_μ alongside the relative uncertainties estimated via repeated measurements and bootstrapping. In these plots, Δ_μ values that fall below the σ/μ curves are within ±1σ of the expected mean, while Δ_μ values that fall above the σ/μ curves are greater than ±1σ of the expected mean. It is clear from these plots that most Δ_μ values fall below the σ/μ curves, which suggests that the deviations in μ are indeed statistical. Table 5.1 quantifies the number of energy bins that fall within ±1 and ±2 standard deviations.

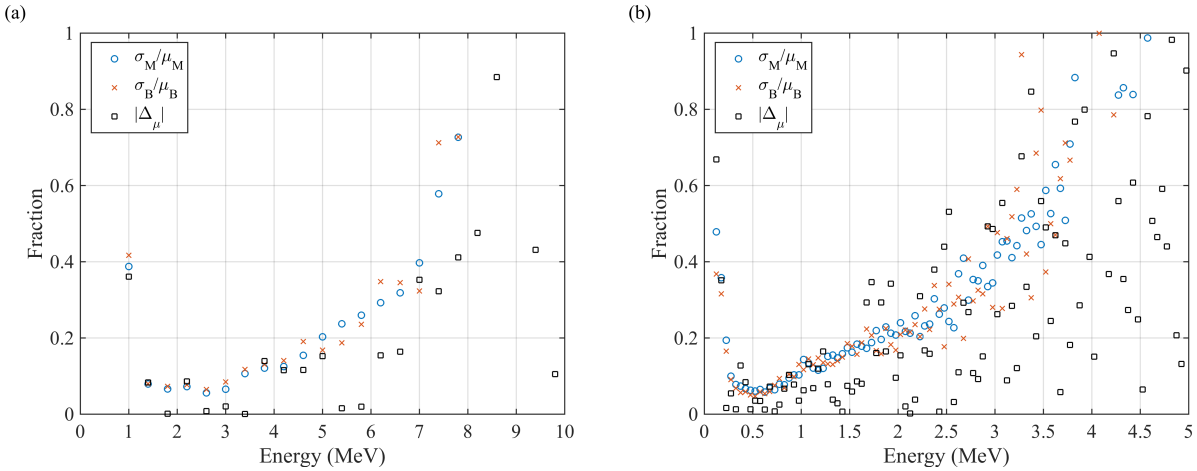

Figure 5.5. Magnitude of fractional deviation in μ (black) for neutrons (a) and photons (b). The deviation is compared to the relative uncertainty in μ as estimated via repeated measurement (blue) and bootstrapping (red). Energy bins where the deviation has a lower magnitude than the relative uncertainty represent bins at which the deviation in μ is within $\pm 1\sigma$ of the expected mean.

Table 5.1 Number of energy bins that have $\Delta_{\sigma/\mu}$ whose magnitude falls within ±1 and ±2 standard deviations. Percentage of total shown in parentheses.

	±1σ	**±2σ**
Neutrons	21/23 (91%)	23/23 (100%)
Photons	89/98 (91%)	97/98 (99%)

Figure 5.6 shows the fraction of energy bins that have $\Delta_{\sigma/\mu}$ whose magnitude falls below a given deviation value. Curves are plotted for both photons and neutrons over the full energy range as well as for neutrons between 0 and 4 MeV and photons between 0 and 2 MeV. These ranges were chosen based on Figure 5.3(b) and Figure 5.4(b) to be representative of energy ranges where the μ_B compared well with μ_M. These curves confirm the better agreement in σ/μ at lower energies where nearly all energy bins agree to within 30% for both photons and neutrons. For the full energy range, approximately 90% of neutron energy bins and approximately 70% of photon energy bins agree to within 30%.

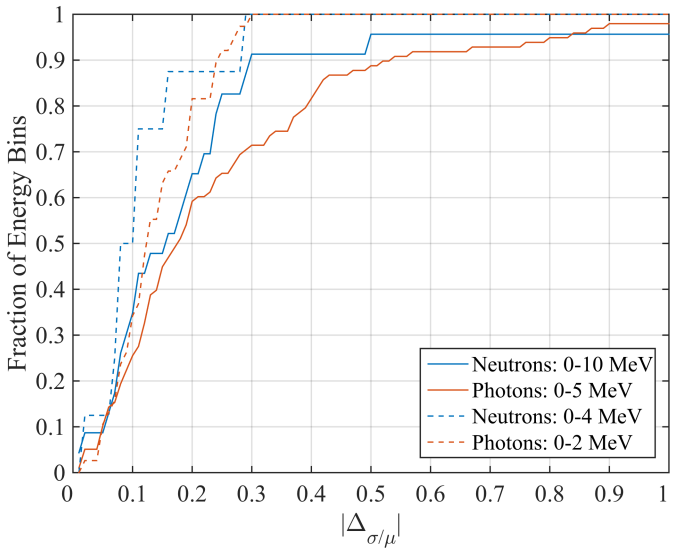

Figure 5.6 Fraction of energy bins that have $\Delta_{\sigma/\mu}$ whose magnitude falls below a given deviation value. Curves are plotted for the full unfolded energy range as well as for a constrained energy range that shows better agreement between the spectrum.

The curves shown in Figure 5.6 and the qualitative agreement demonstrated in Figure 5.1 and Figure 5.2 suggest that the bootstrapping technique provides a reasonable estimation of how the statistical uncertainty in a measurement propagates through to the isolated spectra, especially considering that the bootstrap estimation used $1/50^{\text{th}}$ of the measured data. A better agreement was found in regions where Δ_{μ} was small. Additionally, Δ_{μ} was found to fall within the statistical limits of the measurement at all energies, which suggests that agreement between σ_M/μ_M and σ_B/μ_B should increase with the number of measured events. It is worth noting that it may be possible to improve agreement in σ/μ by increasing the number of bootstrap realizations used [98], [100], [102]. An increase in realizations would be accompanied by an increase in computation time; in practice a balance should be struck between the required agreement and the time and computational resources available.

5.2.2.2. Statistical Uncertainties in the Reconstructed Images

Figure 5.7 presents a comparison between μ, σ, and σ/μ images for neutrons. Figure 5.8 makes the same comparisons for photons. For both neutrons and photons, the bootstrapped images are qualitatively representative of the repeated measurement images. The μ_B images suffer from more noise than the μ_M images. Again, this is expected because the bootstrap data does not receive the benefit of averaging over multiple independent data sets. A similar effect is seen in the σ_B and σ_B/μ_B images. The σ images show that the σ is high where μ is high, which is consistent with previous findings by Barrett et al. [94] and Wilson et al. [103], [104].

The σ/μ images show that the relative error is lower in the region where the source is located, which suggests that the relative uncertainty could be used to aid in the algorithmic detection of source locations, even when relying on bootstrapping to estimate the uncertainty. While not apparent in the σ/μ spectra shown in Section 5.2.2.1, a similar trend was found for prominent gamma peaks, suggesting that such a technique would also be applicable to spectral features. The further development of detection algorithms for use with the spectrum-isolation method is encouraged as future work.

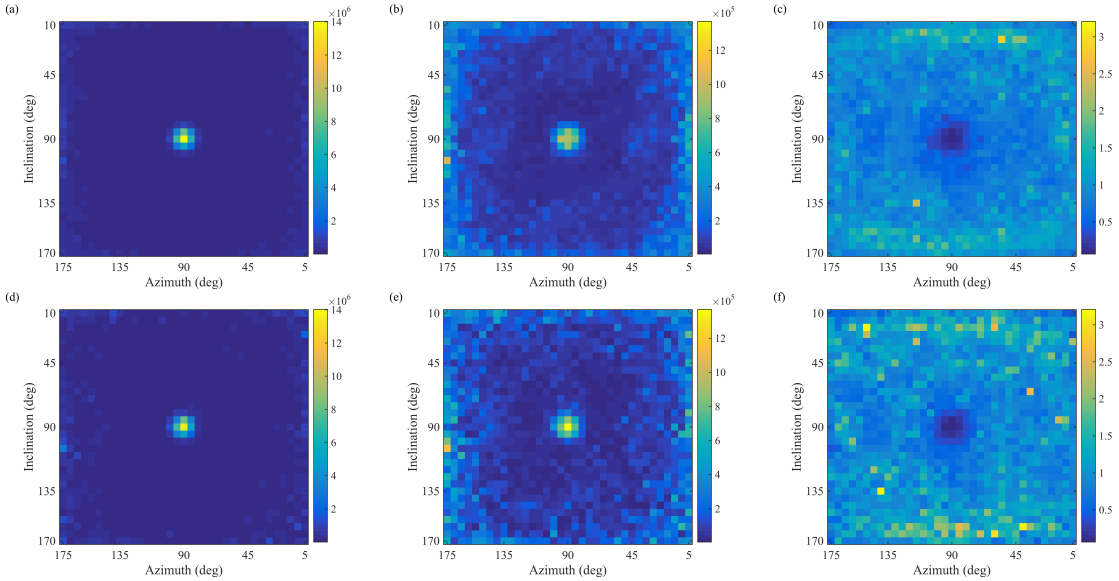

Figure 5.7. Neutron mean (left column), standard deviation (center column), relative uncertainty (right column) images for the measured (top row) and bootstrapped (bottom row) realizations.

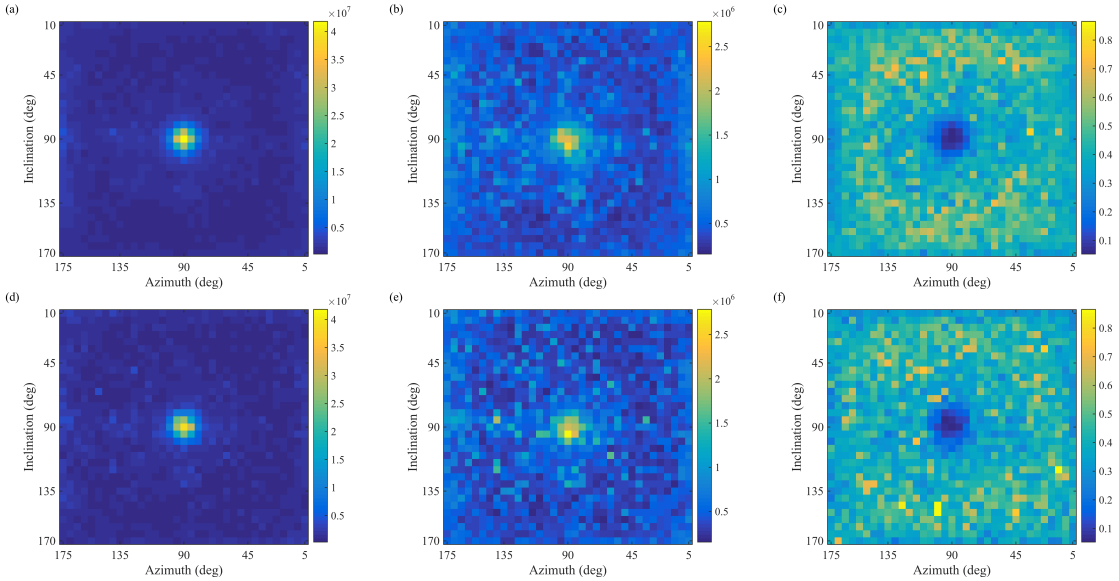

Figure 5.8. Photon mean (left column), standard deviation (center column), relative uncertainty (right column) images for the measured (top row) and bootstrapped (bottom row) realizations.

A more quantitative analysis of the gross number of counts located in the 5×5 ROI centered at (90°, 90°) is provided in Table 5.2 and Table 5.3 for neutrons and photons, respectively. These tables further suggest that the bootstrapped statistics show a reasonable level of agreement with the measured statistics. The largest fractional deviation, which

occurs in the photon relative error, is 0.16. However, it is worth noting that the magnitude of this deviation is quite small: 0.0023 in terms of σ/μ. For neutrons, the deviation between μ values is slightly larger than 2σ. This deviation is larger than was typically seen in the isolated spectra, but is still reasonably within the bounds of statistical uncertainty. For photons, the deviation between μ values is approximately 1.35σ (relative to σ_M), which again suggests that the deviation is statistical in nature. Overall, the σ/μ values are lower in magnitude than those seen in the isolated spectra, which is because the gross counts in the ROI directly represents the integral of the isolated spectra. As such, a smaller relative uncertainty is expected due to the larger number of measured events associated with the ROI.

Table 5.2. Comparison between measured and bootstrapped statistical quantities for the gross number of neutron counts in the 5×5-pixel ROI centered at (90°, 90°).

S	σ	μ	σ/μ
Measured	1.205×10^6	6.167×10^7	0.0195
Bootstrap	1.191×10^6	5.914×10^7	0.0201
Δ_S	-0.012	-0.041	0.031

Table 5.3. Comparison between measured and bootstrapped statistical quantities for the gross number of photon counts in the 5×5-pixel ROI centered at (90°, 90°).

S	σ	μ	σ/μ
Measured	4.754×10^6	3.391×10^8	0.0140
Bootstrap	5.425×10^6	3.327×10^8	0.0163
Δ_S	-0.14	-0.019	0.16

5.2.3. Uncertainty as a Function of Events Measured

Sections 5.2.2.1 and 5.2.2.2 both suggest that the relative uncertainty in the solution is expected to decrease as the number of measured events is increased. This conclusion is intuitive because the measured data should follow the laws associated with counting

statistics. However, it is important to verify that this logic is propagated through both the MLEM algorithm and the bootstrapping process. To do so, the bootstrap technique was used to estimate σ/μ for progressively increasing measurement times. Each data set was generated from a combination (or subset for the 2.5-minute case) of the repeated measurements used in Section 5.2.2. Figure 5.1 plots σ/μ curves for a selection of these combined data sets. These curves clearly show that the relative uncertainty in the solution decreases as the number of measured events increases. The curves are plotted on a log scale to emphasize the continued decrease in relative uncertainty at higher measurement times. The 5-minute curves are identical to those shown on a linear scale in Figure 5.1 (for neutrons) and Figure 5.2 (for photons); these curves are plotted as black squares for easy reference.

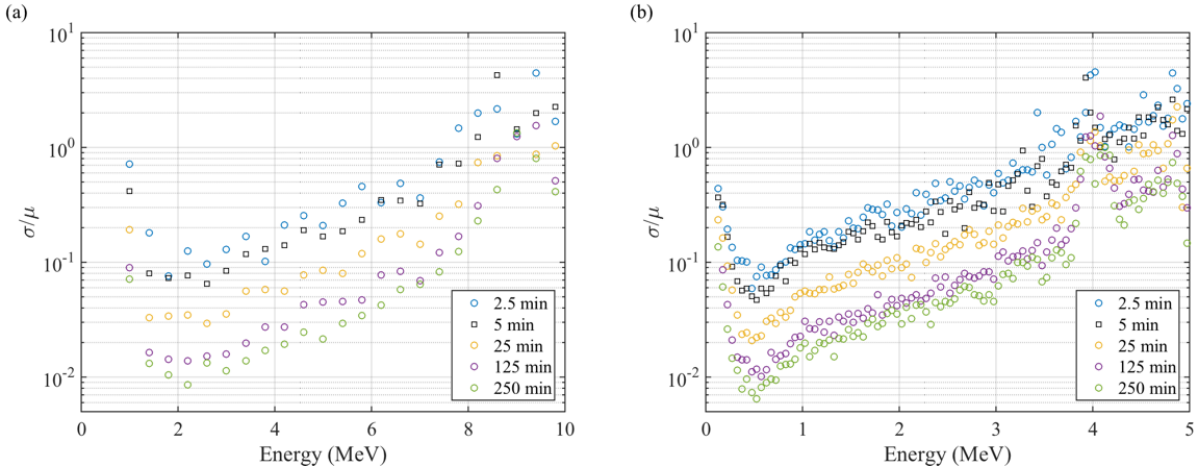

Figure 5.9. Relative uncertainty in the isolated spectra for neutrons (a) and photons (b) as a function of measurement time. Curves are shown for 2.5, 5, 25, 125, and 250-minute measurements.

It is not straightforward to determine a generalized functional dependence between the relative uncertainty and the number of measured events. However, an analysis of the trend in several neutron and photon energy bins suggests that the relative uncertainty decreases proportionally to approximately $1/\sqrt{N}$, where N is the total number of measured events. A

more accurate statement would be that N represents the number of measured events that unfold to that particular energy bin rather than the total number of measured events. While this value is not directly measureable, it will scale with the total number of measured events (assuming the experimental environment remains the same).

The spike in the photon σ/μ curve at approximately 4 MeV corresponds to a dip in the unfolded spectrum, which is a result of disagreement between the simulated dynamic range of the detectors and the true dynamic range. If the maximum allowable energy deposition used in the system matrix is greater than that used in measurement, then there will be a range of energies that will be detected with lower efficiency than predicted by simulation. This loss of efficiency produces a dip in the energy spectrum because the unfolding process cannot accurately correct the efficiency. It is difficult to precisely match the dynamic range between measurement and system matrix because small fluctuations in calibration (which may vary between detectors) could result in slightly different upper energy "thresholds". Typically, this disagreement will only affect one or two energy bins. However, this particular measurement was found to have a lower than typical upper energy threshold, which is why this artifact is so obvious.

5.2.4. Remarks

The resampling implementation utilized in this work yields a reasonably accurate estimate of the measurement variance (as shown in Section 5.2.2). It may be possible to further improve on this estimation by extending the resampling to the individually measured parameters. For example, in addition to resampling individual events, one could sample the energy depositions, TOF (for neutrons), and interaction location within a detector from the appropriate distributions. The reconstructed energy and angle would then need to be

recalculated, resulting in higher computation cost. This methodology was not explored in this work, but has shown promise for estimating backprojection cone uncertainty in the stochastic origin ensembles reconstruction technique and is encouraged as future work [105].

While the bootstrapping technique estimates the uncertainty in the solution due to statistical uncertainty in the measured data, there is also some statistical uncertainty present in the system matrix that has not been considered in this work. It may be possible to further extend the utility of the bootstrapping technique by using it to estimate the statistical uncertainty associated with the system matrix itself. The bootstrap system matrices could be generated in a similar fashion to the bootstrap data by resampling the individual seeds used to populate the system matrices. However, the use of bootstrap system matrices would further inflate the computation time required for each individual solution. For example, using K_{SM} system matrix realizations and K_D data realizations would increase the computation time by a factor of $K_{SM} K_D$ (relative to the standard non-bootstrap approach) assuming all possible combinations of system matrix and data realizations were combined. Similar to the data-only bootstrap approach, it would also be possible to reduce the required computation time through parallelization. However, the memory requirements would be increased by a factor of K_{SM}. Despite the additional challenges, the bootstrap system matrix approach could provide better understanding of the statistical validity of a simulated system matrix and is encouraged as future work.

In a related sense, previous work related to tomographic imaging has been performed to develop analytic models of how errors in the system matrix (and sensitivity map) propagate through to the final solution [106], [107]. These models can be used to determine the

necessary level of accuracy in the system matrix required to achieve a certain level of uncertainty in the solution. Previous work has also been performed to develop analytic models for the general noise properties associated with the MLEM algorithm [94], [104]. Further work is warranted to determine the suitability of such models for application to the spectrum-isolation technique. However, if these models can be sufficiently validated, then it may be possible to compute a comprehensive estimate of the uncertainty in a spectrum-isolation solution without using the computationally expensive bootstrapping approach.

5.3. Systematic Uncertainties

The bootstrapping technique provides a reasonable method for estimating the statistical uncertainty in a spectrum-isolation solution. However, it is also important to understand how systematic uncertainties within the system matrix impact the shape of the isolated spectra. Chapter 4 demonstrated that it is possible to obtain reasonably accurate energy spectra from the region around a detected source, even when the source was not located at the 2-m standoff used in the system matrix. Ideally, measurements of the same source will yield the same results, regardless of the location or standoff distance of the source. However, as the position of the source changes, the measured distribution recorded in the data vector, $\boldsymbol{b}$, will also change. These distributions are propagated through the system matrix during reconstruction and therefore any spatially dependent bias within the system matrix could cause the final solutions to be different. It is possible to estimate the extent of these systematic uncertainties by measuring the same source at different locations and evaluating any changes in the solution. The methodology used for this evaluation is further explained in Section 5.3.1.

This study was focused on how systematic uncertainties impact the shape of the isolated energy spectra, which are of particular importance because they are used to characterize the nature of the detected radioactive material. If the shape of the energy spectra varies greatly with source location, characterization becomes much more difficult. However, if the shapes are similar then it is possible to reliably analyze isolated spectra through techniques such as template matching (i.e. comparing a measured spectrum to a known reference spectrum).

While the magnitude of the spectrum is also important, Chapter 4 demonstrated that further work is required to reliably estimate the true emission rate of the source. As such, the quantitative analysis will be focused on the shape of the isolated energy spectra; however, the variation between reconstructed images and gross counts within an ROI will be discussed qualitatively.

5.3.1. Testing for Systematic Uncertainty

To test how systematic uncertainties within the system matrix vary, a series of N measurements were performed, each with the source at a different location (or standoff). The spectrum-isolation solution was then computed for each measurement and the isolated spectrum is generated from the 5×5-pixel region centered at the source location. The bootstrap technique was used to estimate the mean, μ_n, and standard deviation, σ_n, for each measured spectrum. As shown above, these estimates are made for each energy bin; the following analysis was performed on a bin-by-bin basis.

The observed mean, μ_T, and variance, σ_T^2, across the N measurements are computed using Equation (5.4) and Equation (5.5),

$$\mu_T = \frac{1}{N}\sum_{n=1}^{N} \mu_n \tag{5.4}$$

$$\sigma_T^2 = \frac{1}{N-1}\sum_{n=1}^{N} (\mu_n - \mu_T)^2 \tag{5.5}$$

where the total observed uncertainty, σ_T, will be equal to the quadrature sum of the statistical uncertainty, σ_S, and the systematic uncertainty, σ_Q:

$$\sigma_T^2 = \sigma_S^2 + \sigma_Q^2 \tag{5.6}$$

If, σ_S^2 is known, then a chi-squared test can be used to check if σ_T^2 is larger than what is expected due to statistical fluctuations alone by testing the null hypothesis $\sigma_T^2 \leq \sigma_S^2$ [8], [108]:

$$\chi^2 = \frac{(N-1)\sigma_T^2}{\sigma_S^2} \tag{5.7}$$

If the null hypothesis is rejected, then a systematic uncertainty has been observed. However, if the null hypothesis is accepted, then no systematic uncertainty has been observed. Accepting the null hypothesis does not necessarily imply that there is no systematic uncertainty present, only that it is not large enough (relative to the statistical uncertainty) to be observed.

While an exact model for σ_S^2 is not known, it can be approximated by propagating each of the bootstrapped statistical uncertainties, σ_n, through the calculation of μ_T such that

$$\sigma_S^2 \cong \frac{1}{N}\sum_{n=1}^{N} \sigma_n^2 \tag{5.8}$$

This test may be limited by the accuracy of the bootstrap estimate of the statistical uncertainty and also by the number of measurements available for computing μ_T and σ_T. However, it should provide a reasonable estimate as to whether any significant systematic deviations are present.

5.3.2. Impact of Location within Field of View

To test how systematic uncertainties within the system matrix vary as a function of source location, a 4.4 mCi ^{252}Cf was measured at nine different locations, each with a 2-m standoff. The locations were chosen to span a reasonable portion the upper-left quadrant of the FOV (as shown in Figure 5.10 and Figure 5.11). Each measurement lasted 15 minutes, which provided enough measured events to generate well converged isolated spectra with a level of statistical uncertainty that would be reasonably achievable in realistic measurement scenarios. A ^{252}Cf source was chosen so that a large energy range for both photons and neutrons could be probed simultaneously. While this strategy introduces energy dependent correlations that are not accounted for in this analysis, it provides a good approximation of the location dependent variance for a photon and neutron energy spectra produced through fission.

Table 5.4. Total number of measured neutron and photon events at each location and unfolded counts in the corresponding 5×5-pixel ROI. All measurements were performed at a 2-m standoff.

#	Location	Neutrons		Photons	
		Measured Events	ROI Counts	Measured Events	ROI Counts
1	(90°, 90°)	6.35×10^{4}	1.78×10^{8}	5.84×10^{5}	9.86×10^{8}
2	(110°, 90°)	6.98×10^{4}	1.93×10^{8}	6.55×10^{5}	1.04×10^{9}
3	(135°, 90°)	5.81×10^{4}	1.97×10^{8}	6.26×10^{5}	1.08×10^{9}
4	(90°, 65°)	6.91×10^{4}	1.89×10^{8}	6.42×10^{5}	9.53×10^{8}
5	(110°,65°)	7.04×10^{4}	1.90×10^{8}	6.97×10^{5}	1.03×10^{9}
6	(135°, 65°)	6.46×10^{4}	1.97×10^{8}	7.19×10^{5}	1.06×10^{9}
7	(90°, 45°)	5.70×10^{4}	1.89×10^{8}	5.69×10^{5}	8.53×10^{8}
8	(110°, 45°)	6.04×10^{4}	1.93×10^{8}	6.22×10^{5}	8.37×10^{8}
9	(135°, 45°)	5.98×10^{4}	2.00×10^{8}	6.47×10^{5}	9.03×10^{8}

Table 5.4 summarizes the source locations and number of neutron and photon events measured at each location. Also included in Table 5.4 are the number of unfolded counts in the 5×5 pixel ROIs centered at each location. These values are equivalent to the integral of the isolated spectra and are the factors used to normalize each spectrum, which allows for a comparison to be made between shapes. Ideally, the ROI counts for each particle would be identical (within the limits of statistical uncertainty) at all locations. However, it is especially clear that the unfolded photon counts for locations 7-9 fall significantly below the unfolded photon counts for locations 1-6. The drop in unfolded photon counts in locations 7-9 is a result of the broadened point-spread function, which is apparent in Figure 5.11.

Figure 5.10 and Figure 5.11 show the neutron and photon images, respectively, as a function of measurement location. The color scale, which represents the number of unfolded counts in a pixel, is fixed (for each particle type) to facilitate comparison between locations. In general, a similar trend can be seen for both photons and neutrons. In all cases, the hot-spot correctly locates the source. However, as the inclination angle is increased, the hot-spots suffer from increased blur. The broadened point-spread function is likely caused by two

related factors discussed in Chapter 3: the decrease in pixel area as a function of inclination and the associated increase in statistical uncertainty of the associated source-space bins of the system matrix. The photon images show significantly more noise than the neutron images, which is due to the amount of room return and secondary gammas not produced directly by the ^{252}Cf source, as discussed in Chapter 4.

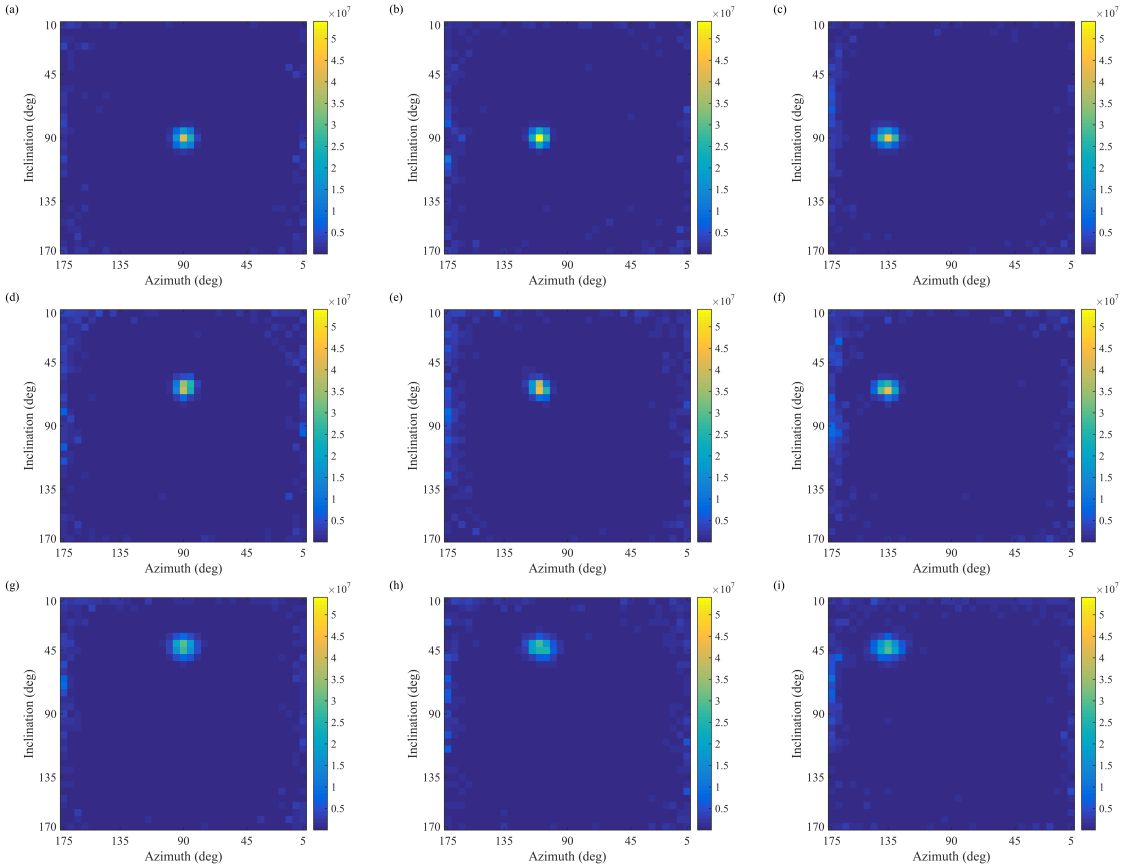

Figure 5.10. Neutron image for a ^{252}Cf source measured each of the nine source locations summarized in Table 5.4. The color scale is fixed across all images.

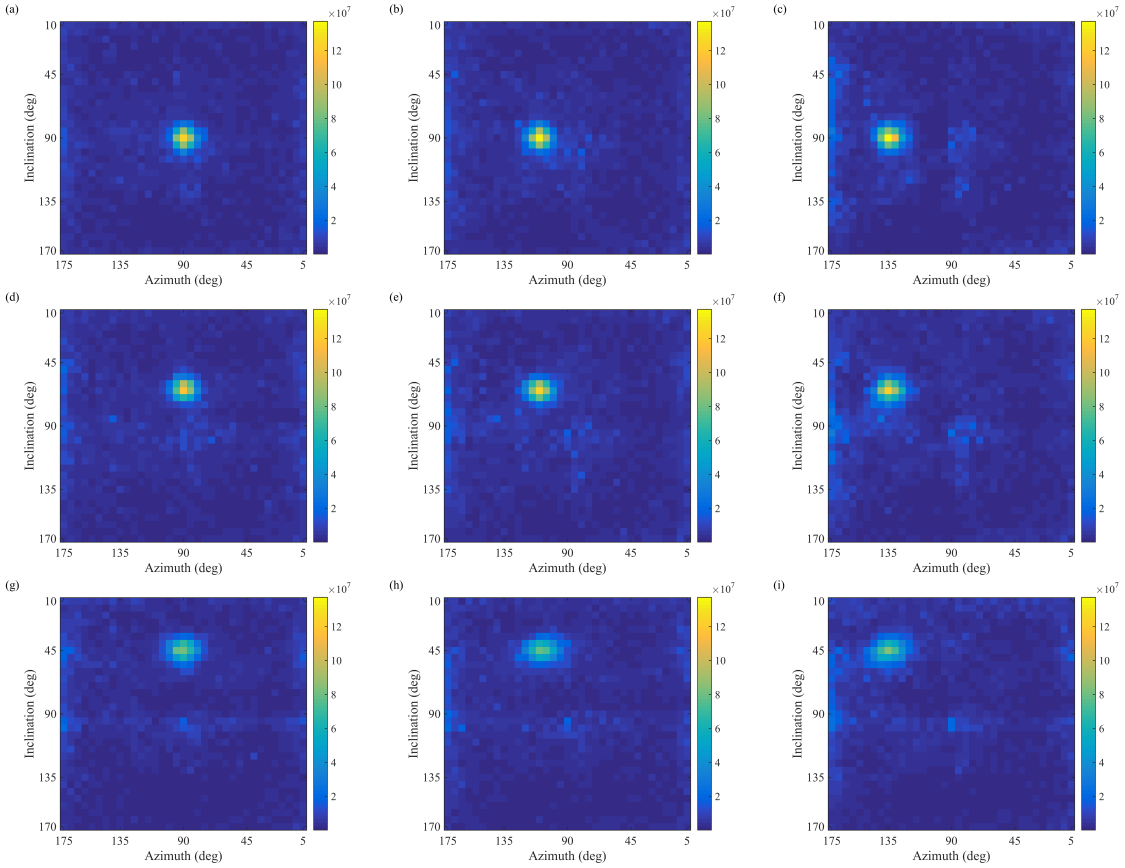

Figure 5.11. Photon image for a ^{252}Cf source measured at each of the nine source locations summarized in Table 5.4. The color scale is fixed across all images.

Figure 5.12 plots the mean neutron (a) and photon (b) spectra across each all 9 measurements. The black circles denote μ_T and the black error bars represent the expected statistical standard deviation, σ_S, for each energy bin. The colored error bars show the observed standard deviation, σ_T. The observed standard deviation is displayed as red when the null hypothesis is rejected and displayed as green when the null hypothesis is accepted (using a false alarm probability of α=0.05). Figure 5.13 presents the same information in terms of relative uncertainty, where the black circles represent σ_S/μ_T and the colored circles show σ_T/μ_T.

For both particle types, the observed variance in most energy bins was found to be dominated by the expected statistical variance. However, there are a few energy bins in

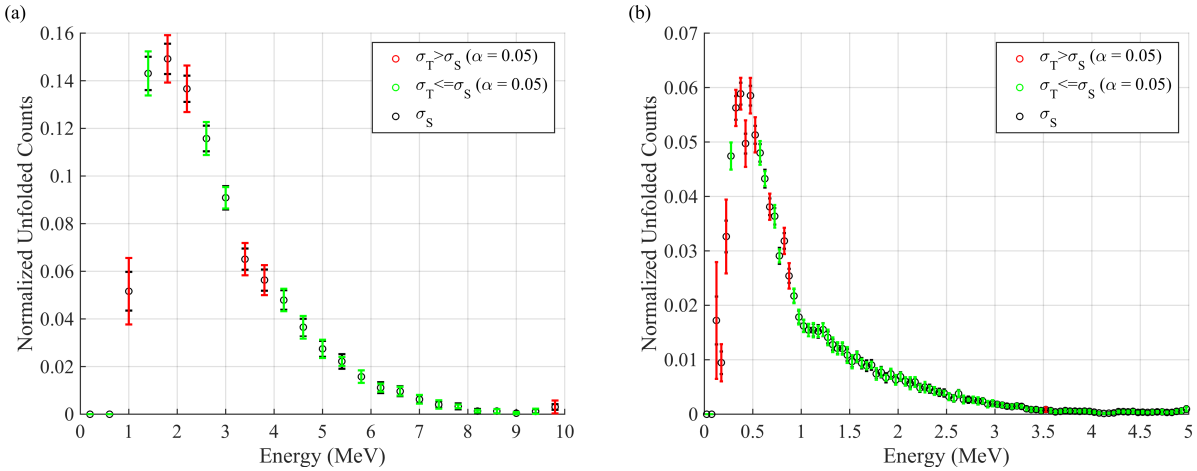

Figure 5.12. Observed uncertainty, σ_T, (shown as black bars) and expected statistical uncertainty, σ_S, (shown as red or green bars) for each energy bin in the mean neutron (a) and photon (b) spectra. Red bars denote energies in which a systematic uncertainty may have been observed.

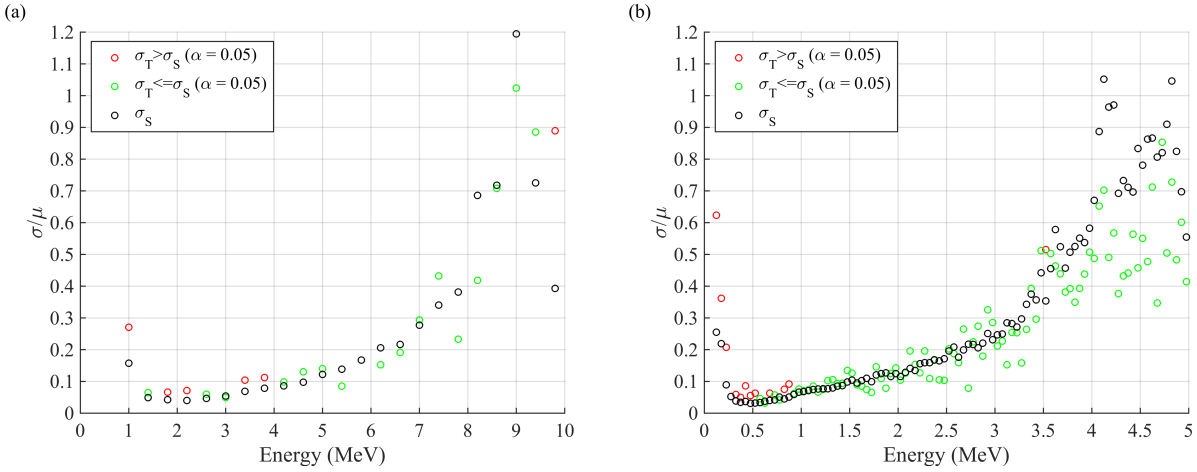

Figure 5.13. Observed relative uncertainty, σ_T/μ_T, (shown as red or green circles) and expected statistical uncertainty, σ_S/μ_T, (shown as black circles) for each energy bin in the neutron (a) and photon (b) spectra. Red circles denote energies in which a systematic uncertainty may have been observed.

which an additional source of uncertainty was detected. With both particles, a large systematic deviation was found in the first bin above threshold, which is not surprising because the first bins suffer from reconstruction noise and are especially subject to room return (as discussed in Chapter 4). Similarly, the highest energy neutron bin also shows a large systematic deviation. However, this bin also suffers from reconstruction noise resulting from neutrons higher than 10 MeV and misclassified particles, as discussed in Chapter 4.

In addition to the edge bins, a systematic deviation was observed at four neutron energy bins. However, both Figure 5.12 and Figure 5.13 suggest that the additional variation is relatively small. Recalling that the systematic and statistical components will add in quadrature, it is possible to estimate σ_Q/μ_T to fall between ~5%-8%, which is on the same order as the statistical uncertainty component. This estimate should be taken at face value, because a reliable quantification of the systematic uncertainty would require many more measurements with much lower statistical uncertainty. Nonetheless, it is important to see that systematic uncertainties in the system matrix do not dominate the variation in isolated neutron spectra from one location to another (at least at this level of statistical uncertainty).

For photons, a larger number of bins show an observed systematic deviation. However, with the exception of four bins (.65-.70, 0.80-0.85, 0.85-0.90, and 3.5-3.55 MeV), systematic deviations were only observed in the regions of the spectrum known to be impacted by room return and non-source photons (such as the ^{10}B(n,α) peak in the 0.45-0.50 MeV bin). The contribution of these effects is expected to change with the source location because different locations will place the source at different distances from different scattering surfaces. Considering the number of non-source photons detected, it is not surprising that systematic deviations are observed in these energy ranges. While the presence of these "non-source effects" does not mean that there are no other systematic uncertainties present, it is not possible to distinguish between reconstruction-related and source-related contributions. Nonetheless, the magnitude of these additional deviations is still encouraging. In most cases where a systematic deviation was observed, the total relative uncertainty still remains below 10% including a statistical contribution of ~3-5%. There is a single spurious point of observed systematic deviation that occurs in the 3.5-3.55 MeV bin, however, this is likely a

result of a large fluctuations seen in the estimated statistical uncertainty component in this region.

The results of this study show that the shape of the isolated photon and neutron spectra compare reasonably well across different locations in the FOV. Some systematic uncertainties were observed, but their impact was small and would not be expected to significantly impact the ability to characterize a detected source based on the shape of the isolated spectra. This study probed a large portion of the system matrix, and the lack of gross systematic variations speaks to the robustness of the simulation technique used to compute the system matrix.

While a much deeper analysis is required to determine the exact source of the observed systematic uncertainties, it is easy to speculate as to what the largest contributing factors might be. As the location of the source changes the scattering angle between a specific detector pair also changes. As a result, different reconstructed energy ranges will be impacted by uncertainties associated with the modeled resolution and light-output functions (for neutrons), especially at low energy depositions. Additionally, as the source is moved away from (90°, 90°), incident particles will be less likely to interact in the front plane PMTs, which reduces the impact of any model mismatch present in the PMT model.

5.3.3. Impact of Increased Standoff Distance

The variation of systematic uncertainties within the system matrix were also tested for by measuring at different standoff distances. In this test, the location was held constant at (90°, 90°) and the ^{252}Cf source was measured at three standoff distances: 2 m, 3 m, and 4 m. As with the previous test, ^{252}Cf was chosen to probe a range of the photon and neutron fission spectrum simultaneously. Table 5.5 summarizes the standoff distances, measurement times,

and number of neutron and photon events measured at each location. The number of unfolded counts in the 5×5 ROI, which are used to normalize each of the isolated spectra, are also shown.

The measurement time for the 2-m case remained at 15 minutes. The larger standoffs used longer measurement times to account for the decreased count rate, which is expected to fall off as $1/r^2$, where r is the source-to-detector distance. The correction in measurement times was based off the distances measured from the center of the system (as displayed in Table 5.5). However, it would have been more appropriate to scale the measurement times based off the distance from the front plane because that gives a better representation of the solid angle subtended by the DPI. As a result, a slightly lower than expected neutron count rate was achieved at the larger standoffs. However, because the isolated spectra are normalized for the chi-squared analysis, the decreased count rate should not impact the results. Interestingly, the number of measured photon events actually increases as a function of distance. This speaks to the magnitude of non-source photons being detected by the DPI.

Table 5.5. Total number of measured neutron and photon events at each location and unfolded counts in the corresponding 5×5-pixel ROI. All measurements were performed at (90°, 90°).

#	Distance	Time (min)	Neutrons		Photons	
			Measured Events	ROI Counts	Measured Events	ROI Counts
1	2m	15	6.35×10^4	1.78×10^8	5.84×10^5	9.86×10^8
2	3m	34	5.81×10^4	1.66×10^8	6.23×10^5	8.52×10^8
3	4m	60	5.65×10^4	1.70×10^8	7.01×10^5	8.69×10^8

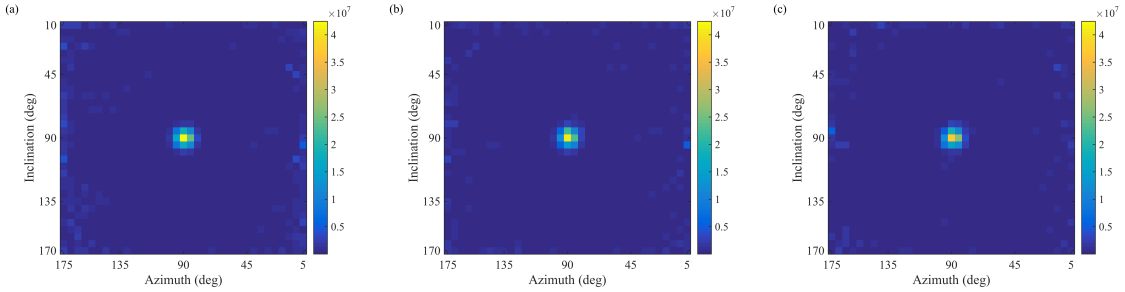

Figure 5.14. Neutron image for a ^{252}Cf located at (90°, 90°) with a 2-m (a), 3-m (b), and 4-m (c) standoff. The color scale is fixed across all images.

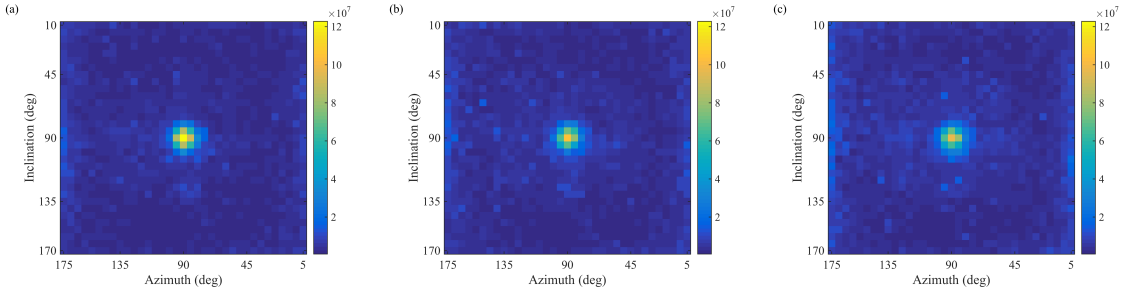

Figure 5.15. Photon image for a ^{252}Cf located at (90°, 90°) with a 2-m (a), 3-m (b), and 4-m (c) standoff. The color scale is fixed across all images.

Figure 5.14 and Figure 5.15 show the reconstructed neutron and photon images, respectively. The color scale, which represents the number of unfolded counts in a pixel, is fixed (for each particle type) to facilitate comparison between standoff distances. For both particles, the hot-spots remain well converged as the distance is increased. However, a decrease in the maximum intensity is seen, which corresponds with improper scaling of measurement time. The amount of photon signal outside the hot-spot region increases with distance as the ratio between source-photons and non-source-photons also increases.

Figure 5.16 and Figure 5.17 show the locations of observed systematic uncertainty, similar to Figure 5.12 and Figure 5.13. The σ_T/μ_T curves have significantly more scatter than those shown in Figure 5.13, which is a result of worse convergence in σ_T due to the lower number of measurements used in this study. As in Section 5.3.2, very few energy bins were found to have observable systematic deviations and those found are either in regions of high

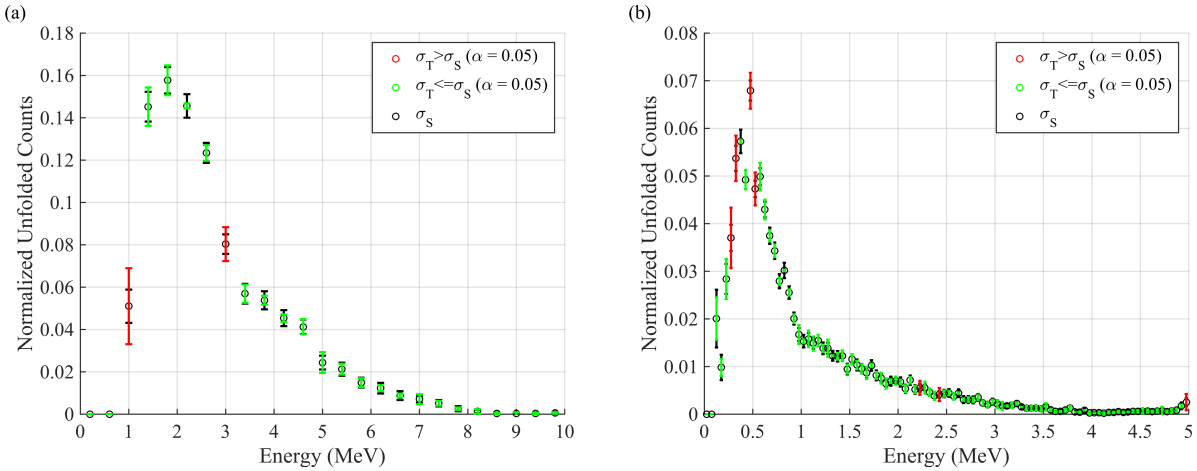

Figure 5.16. Observed uncertainty, σ_T, (shown as red or green bars) and expected statistical uncertainty, σ_S, (shown as black bars) for each energy bin in the mean neutron (a) and photon (b) spectra. Red bars denote energies in which a systematic uncertainty may have been observed .

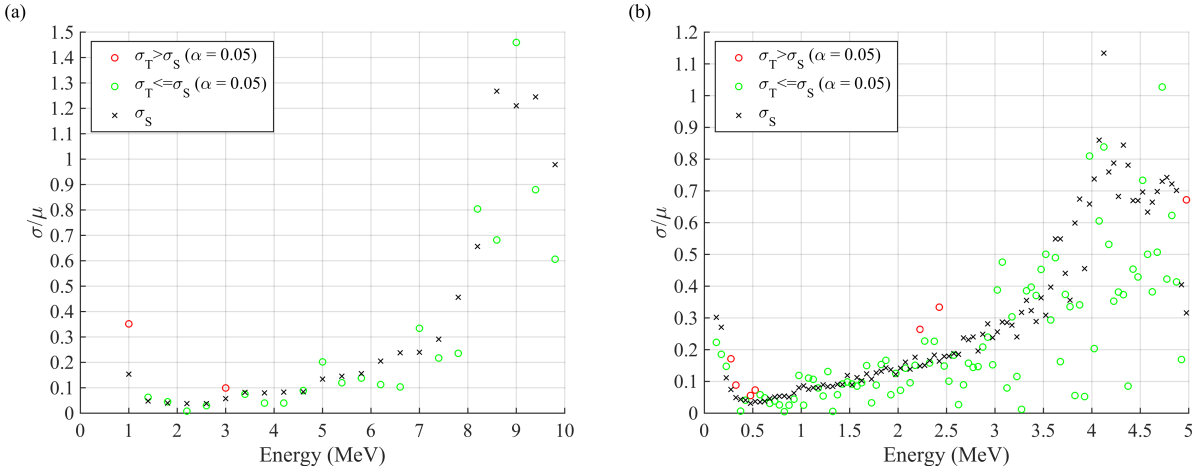

Figure 5.17. Observed relative uncertainty, σ_T/μ_T, (shown as red or green circles) and expected statistical uncertainty, σ_S/μ_T, (shown as black circles) for each energy bin in the neutron (a) and photon (b) spectra. Red circles denote energies in which a systematic uncertainty may have been observed.

statistical variation or have a relatively small contribution to the total observed relative uncertainty. One noticeable difference between the mean photon spectra shown in Figure 5.16(b) and Figure 5.12(b) is the magnitude of the 0.45-0.50 MeV bin. As previously mentioned, this peak does not come directly from the ^{252}Cf and therefore grows relative to the fission continuum as the source is moved further away and the ratio between detected source photons and total detected photons decreases.

It is expected that changing the standoff distance would have a lower impact on the shape of the isolated spectrum than changing location within the FOV. While the scattering angles between detector pairs will also vary as a function of distance, the variation will not be as dramatic as the variation resulting from a change in source location.

5.3.4. Remarks

The reliability of the bootstrap made it possible to estimate the extent of systematic uncertainties in the system matrix without having to perform numerous measurements at the same location to determine the contribution of statistical uncertainty. The impact of systematic uncertainties on the shape of the isolated spectra was tested for by measuring the same source at different locations and standoff distances. The results suggest that any systematic uncertainties within the system matrix will not significantly impact the ability to compare isolated spectra generated from different location within the FOV. However, this assessment could only be made at certain energy ranges which achieved a low enough statistical uncertainty. Fortunately, the usable energy ranges correspond well to the energies associated with SNM. A larger portion of the unfolded energy range could be inspected with longer measurement times, and with a great enough reduction in statistical uncertainty the level of systematic uncertainty could be quantified. Such a quantification may become especially desirable if the magnitude of the spectra is assessed in addition to the shape. If such a study is performed, precautions should be taken to reduce the impact of particles that do not come directly from the source.

Chapter 6. Localization and Characterization of Radioactive Material in Complex Environments

6.1. Motivation

The previous four chapters have described a measurement system and data processing methodology that is capable of locating and characterizing photon and neutron sources using a combination of imaging and localized spectroscopy. Chapter 4 demonstrated the utility of the spectrum-isolation method for analyzing both source and non-source locations to obtain the most information available about the environment being investigated. Chapter 5 demonstrated that the shapes of isolated spectra can be reliably compared across different source locations and standoff distances. These results suggest that the combination of the DPI and the spectrum-isolation technique form a powerful tool for detecting, localizing, and characterizing radioactive materials and is particularly well suited for identifying SNM.

These claims will be tested in this chapter, which will present two complex measurement scenarios involving SNM, multiple sources, and shielding. The results presented will show that the DPI is capable of localizing and characterizing all radioactive sources in these experiments. An in-depth analysis of the isolated photon and neutron spectra will show that not only can the radioactive material be identified using their characteristic signatures, but also that some determinations can be made regarding the presence and nature of shielding material.

6.2. The Energy Spectra of ^{9}Be(α, n) Neutron Sources

Up to this point, neutron results have only been shown for a single type of neutron source: ^{252}Cf. This source is an excellent choice for testing the ability of the DPI to detect SNM because the neutron energy spectrum emitted by ^{252}Cf is representative of the fission spectra emitted by SNM [3]. However, other neutron sources, such as those based on the (α, n) reaction in ^{9}Be, exist for a variety of non-weapons related research and industrial applications [109]. Due to the potential presence of (α, n) sources in non-proliferation and safeguards scenarios, it is important to be able to discriminate between (α, n) and fission sources [14]. Both of the experiments presented in this chapter include ^{9}Be(α, n) sources, and therefore discussion of the results will be facilitated by a better understanding of their characteristic energy spectra.

In ^{9}Be(α, n) sources, neutrons are produced through two main pathways: the ^{9}Be(α, n)^{12}C reaction and the ^{9}Be(α, α') ^{9}Be*→^{8}Be+n reaction [110]. Above ~2 MeV (neutron energy), the spectral features are dominated by the ^{9}Be(α, n)^{12}C reaction. This reaction produces neutrons with energies related to the incident energy of the α particle and the energy level populated by the residual ^{12}C nucleus [110], [111]. The result is several neutron groups with local maxima at approximately 3.2, 4.8, 6.8, 7.8, and 9.8 MeV [110]–[112]. As such, ^{9}Be(α, n) will have a higher average energy than fission neutrons, which are governed by the Watt distribution. Figure 6.1 compares the neutron spectra used by the built-in ^{252}Cf and ^{241}AmBe source models of MCNPX-PoliMi [58].

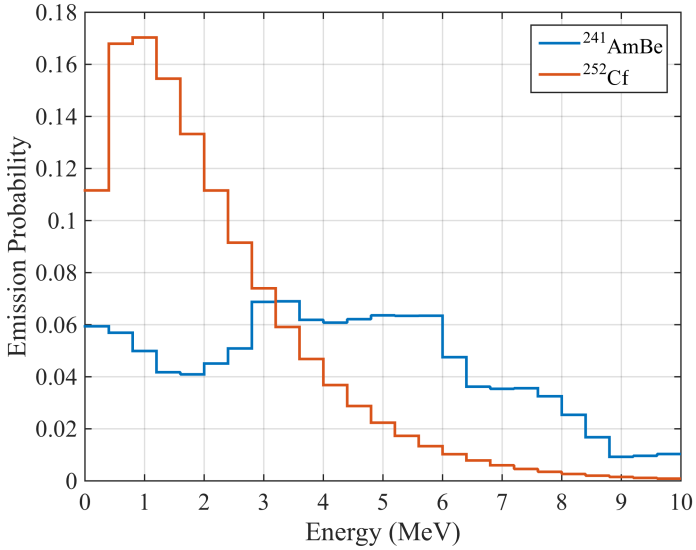

Figure 6.1. Neutron emission probabilities of ^{241}AmBe and ^{252}Cf computed using the MCNPX-PoliMi source models.

The α particles in ^{9}Be(α, n) reactions can be provided by a variety of long-lived α-emitters, including ^{238}Pu, ^{239}Pu, and ^{241}Am. It is worth noting that depending on the amount of plutonium contained, a PuBe source may be classified as SNM. The neutron energy spectra will show slight differences, depending on the α-emitting isotope used. These deviations are due to small differences in the energies of the α particles emitted by these isotopes. Additional differences can also be expected as a result of the exact composition of source compound, even between sources using the same α-emitting isotope [112]. However, because the expected deviations are limited to small differences in the intensities and width of the neutron groups, the general features of the neutron energy spectra will be similar regardless of the α-emitter or exact source composition [110], [112]. As such, it is possible to compare measured ^{9}Be(α, n) spectra to reference spectra even if the exact emitted neutron energy spectrum for the measured source is unknown. Such comparisons make it possible to determine the nature of a detected neutron source and will be used to discriminate ^{239}PuBe and ^{241}AmBe sources from fission sources in Section 6.3 and 6.4, respectively.

The gamma spectrum of a ^{9}Be(α, n) is expected to display a peak at approximately 4.4 MeV [113]. This gamma is associated with the de-excitation of the residual ^{12}C nucleus from the first excited state and is estimated to accompany approximately 60% of neutrons emitted by ^{9}Be(α, n) sources [113], [114]. While an approximately 3.2 MeV gamma ray may also be expected from de-excitation from the second excited state of ^{12}C, this gamma is much less probable and is not frequently observed [113]–[115]. In addition to these de-excitation gammas, the photon spectrum will also display any decay gammas associated with the α-emitting isotope.

6.3. Simultaneous Identification of Shielded ^{252}Cf and ^{239}PuBe

6.3.1. Experiment

A 60-minute measurement was taken with two neutron-emitting sources present: a 1-Ci (~1.75×10^{6} neutrons-per-second) ^{239}PuBe source located at (1.52 m, 134°, 93°) and a 4.4-mCi (~1.9×10^{7} neutrons-per-second) ^{252}Cf source located at (5.17 m, 71°, 90°) shielded by 10-cm of polyethylene. Approximately 8.1×10^{4} neutron events and approximately 8.9×10^{5} photon events were measured. A photograph of the measurement setup is shown in Figure 6.2.

Figure 6.2. Photograph of the experimental setup. The 1-Ci ^{239}PuBe source is located at (1.52 m, 134°, 93°) and the ^{252}Cf source is located at (5.17 m, 71°, 90°) behind 10-cm of polyethylene.

The 4.4-mCi ^{252}Cf source is the same source that has been used through the majority of this work. However, the results presented in Section 6.3.2 will highlight some of the differences in the isolated photon and neutron spectra that appear due to the presence of the polyethylene shield.

The source used in this experiment is documented as containing 16 g of ^{239}Pu, which puts it under the classification of category-III SNM. The ^{239}Pu is mixed with 8.2 g of Be and encapsulated in a vessel made of tantalum and stainless steel [116]. As mentioned in Section 6.2, the photon spectrum is expected to contain a 4.4-MeV gamma-ray signature as well as any decay gammas associated with ^{239}Pu. Table 6.1 lists several prominent ^{239}Pu gamma rays between 0.10 and 0.8 MeV [3]. While the DPI, in its current form, does not have the requisite energy resolution to fully resolve these peaks individually, it is possible to detect their combined signals.

Table 6.1. Prominent decay gamma rays of ^{239}Pu [3].

Energy (MeV)	γ/s-g
0.129	1.44×10^{5}
0.204	1.28×10^{4}
0.345	1.28×10^{4}
0.375	3.60×10^{4}
0.413	3.42×10^{4}
0.645	3.42×10^{2}
0.717	6.29×10^{1}

6.3.2. Results

Figure 6.3 shows the reconstructed neutron and photon images. For both particles, a hot-spot is seen at the correct location. Despite the much higher neutron output of the ^{252}Cf source, the ^{239}PuBe neutron hot-spot shows significantly more intensity than the ^{252}Cf hot-spot, which is a due to the larger standoff of the ^{252}Cf source as well as the presence of polyethylene shielding.

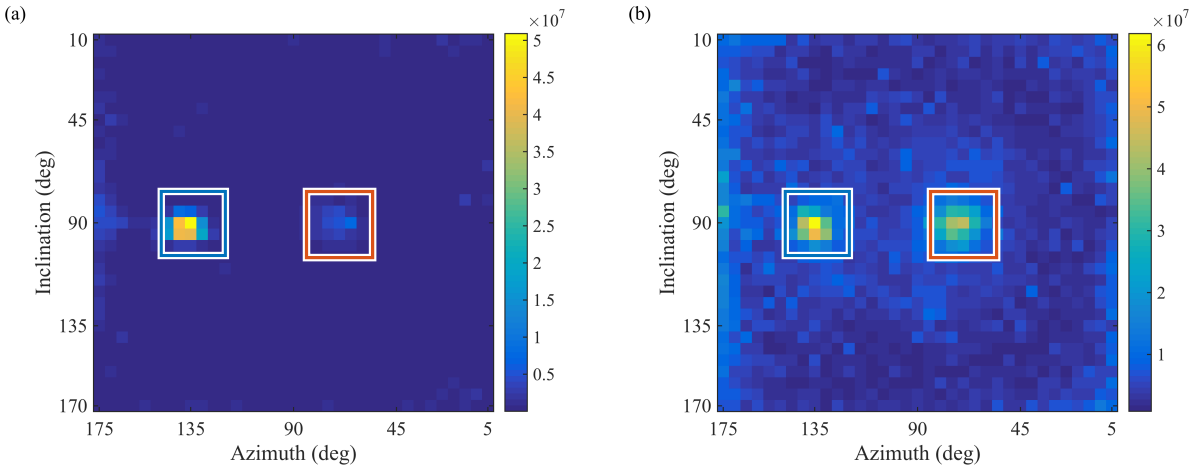

Figure 6.3. Reconstructed neutron (a) and photon (b) images. Both sources are correctly located at their respective positions. Colored boxes denote the 5×5-pixel ROIs used to generate the isolated spectra (blue for ^{239}PuBe and red for ^{252}Cf).

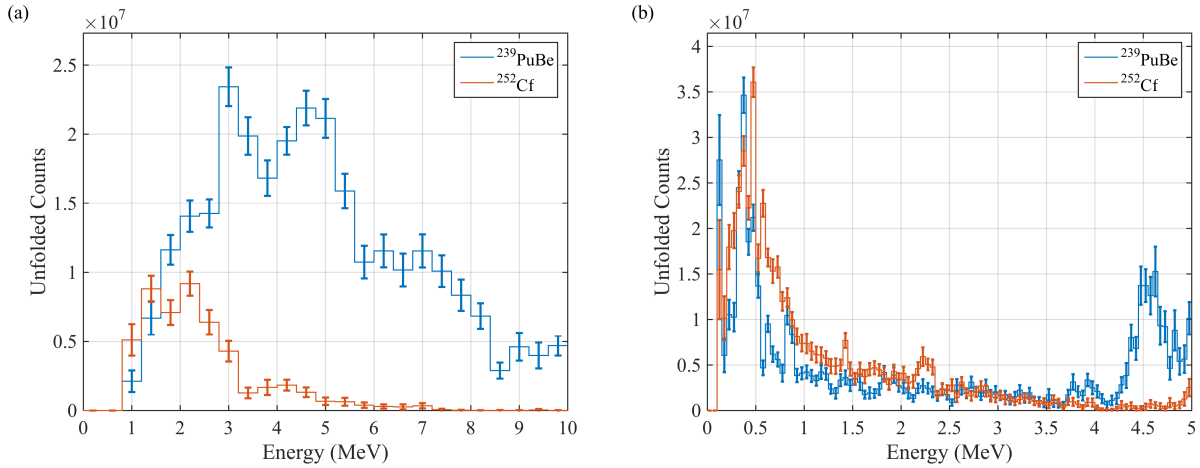

Figure 6.4. Isolated neutron (a) and photon (b) spectra. Error bars represent ±1σ and were generated using the bootstrap technique.

Figure 6.4 shows the isolated neutron and photon spectra generated from the 5×5-pixel regions outlined in Figure 6.3. The error bars represent ±1σ and were estimated using the bootstrap technique described in Chapter 5. While not displayed here, the relative uncertainty plots for all spectra show the expected trends (i.e. higher relative uncertainty in regions of the isolated spectra that correspond to a low number of measured events). While both the photon and neutron spectra are more complex than those shown in previous chapters, it is clear that very different sources have been detected in the two separate ROIs.

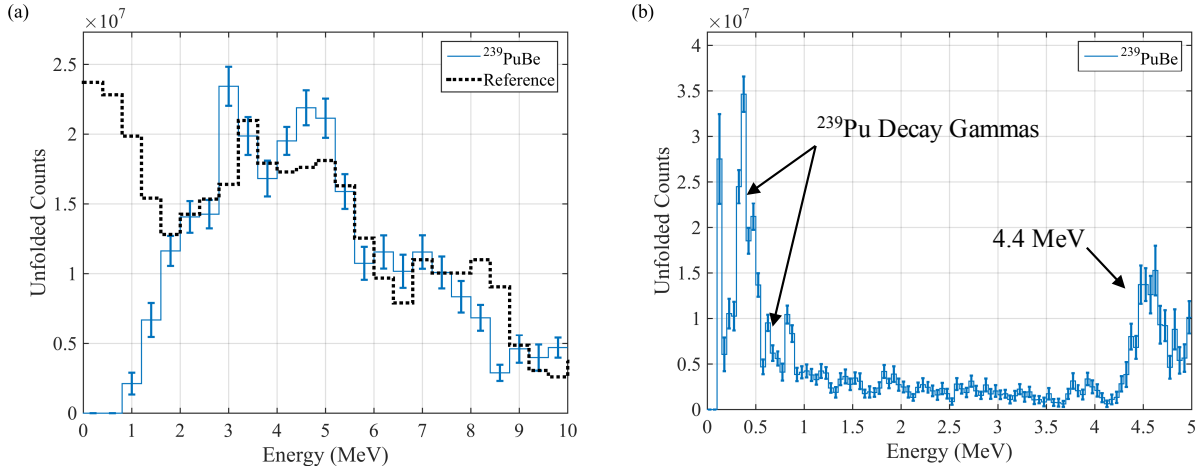

Figure 6.5. Isolated neutron (a) and photon (b) spectra from the 5×5-pixel ROI centered at (135°, 90°). Both neutron and photon signatures suggest the presence of a ^{9}Be(α, n) source. The neutron reference spectrum corresponds to a published PuBe spectrum for a source containing 80 g of plutonium [8], [112]. This reference spectrum has been scaled to match the intensity of the measured spectrum in the 2.0-2.4 MeV bin.

Figure 6.5 is used to present further analysis of the isolated spectra from the 5×5-pixel ROI centered at (135°, 90°). For reference, the isolated neutron spectrum is plotted against an unfolded spectrum for a PuBe source containing 80 g of plutonium. This spectrum was originally published in [112] and was reproduced in [8]. The reference spectrum is scaled to match the intensity of the measured spectrum in the 2.0-2.4 MeV bin. The measured spectrum compares well to the reference in most energies above 1.6 MeV, with many of the energy bins falling within or just outside the 1σ error bars. The disagreement below 1.6 MeV is due to threshold and low-energy model mismatch, as discussed in Chapter 4. The disagreements at higher energies are anticipated due to the expected fluctuations between ^{9}Be(α, n) sources of different sizes and compositions, as discussed in Section 6.2.

The isolated photon spectrum shows an obvious peak in the 4.4 MeV region. Several prominent features can also be identified below 1.0 MeV. Peaks are present in the 0.30-0.45 MeV bins and, to a lesser extent, the 0.60-0.75 MeV bins due to the ^{239}Pu decay gammas. A large spike in intensity is seen in the first bin (0.10-0.15 MeV), which could be due to the 0.129 MeV decay gamma. However, it is often difficult to distinguish the signal in this bin from reconstruction noise, as discussed in Chapter 4. A peak is present between 0.80 and 0.90 MeV, that is currently unidentified. In the absence of more detailed documentation regarding the source composition, it is difficult to speculate as to the origin of this peak. However, the presence of a small feature in this region can be confirmed in the coincidence spectrum as well as in an independently obtained CdZnTe spectrum[3]. The familiar peak in the 0.45-0.50 MeV bin is also present in the spectrum.

[3]CdZnTe spectrum was measured by Steven Brown using a Polaris II detector while the ^{239}PuBe source was shielded by approximately ~10 cm of paraffin. [21]. A special thanks is owed to Steven for providing the spectrum as well as his insight.

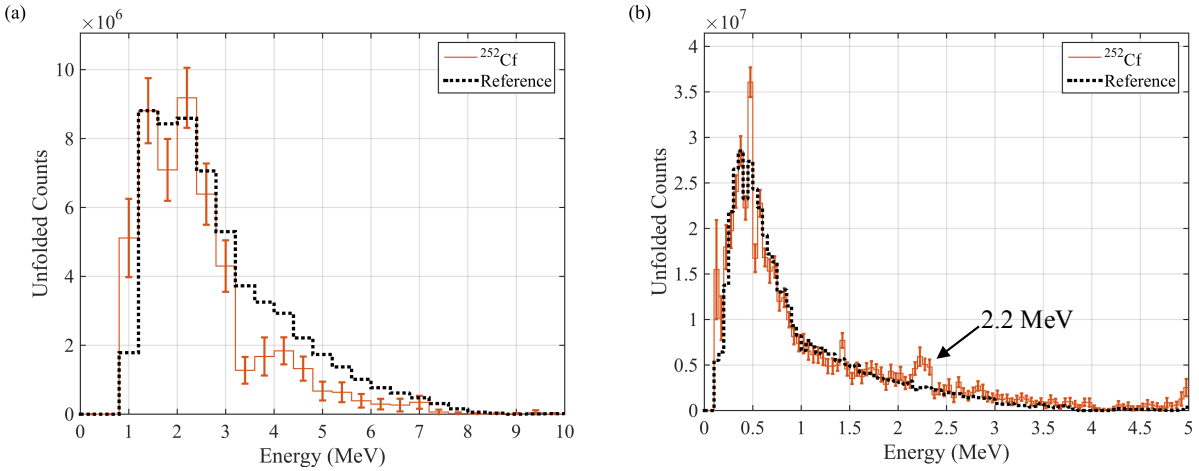

Figure 6.6. Isolated neutron (a) and photon (b) spectra from the 5×5-pixel ROI centered at (70°, 90°). Both spectra are generally representative of the reference spectra, and the photon spectrum suggests the presence of a hydrogenous material. The reference spectra correspond to a 250-minute measurement of the same source located at (2 m, 90°, 90°) and have been scaled to match the intensities of the 1.6-2.0 MeV bin and 0.35-0.40 MeV bin for neutrons and photons, respectively.

Figure 6.6 shows the isolated spectra for the 5×5-pixel ROI centered at (70°, 90°). In both cases, the reference spectra show the unfolded spectra from a 250-minute measurement of the same (unshielded) ^{252}Cf source located at (2 m, 90°, 90°). The reference spectra have been scaled to match the intensities of the 1.6-2.0 MeV bin and the 0.35-0.40 MeV bin for neutrons and photons, respectively. Due to the presence of the polyethylene shielding, the isolated spectra are not expected to match the reference spectra exactly. Rather, the reference spectra are shown specifically to highlight the deviations caused by the presence of a polyethylene shield.

While the neutron spectrum can still be considered representative of a Watt spectrum, there are energy bins where the deviation between the measured and reference spectra is larger than the associated uncertainty. There are several competing factors that make the expected shape of neutron spectrum difficult to assess. The general expectation is that the polyethylene shield will harden the spectrum (increase the average energy) by reducing the number of low-energy neutrons. However, this will be counteracted to some extent due to

the proximity of the source to the corner of the laboratory, which may increase the room-return signal that coincides with the direction of the source. It is worth pointing out that some of the structure in the spectrum may be explained by the neutron cross-section of ^{12}C, which is a major constituent of the polyethylene shield. The ^{12}C cross-section has several resonances between 1 and 10 MeV, including a notably broad resonance between ~3 and 4 MeV, which may explain the dip seen in the isolated neutron spectrum. Previous work by Lawrence et al. has shown that the features in the unfolded neutron response of a single EJ309 detector aligns well with the cross sections of various attenuating materials and that such features may be used to characterize intervening materials [117]. A more in depth analysis of the viability of using isolated spectra for similar characterization purposes is left as future work.

The photon spectrum matches the reference spectrum very well overall, with many of the energy bins agreeing within their associated uncertainty. The region around 2.2 MeV shows a statistically significant deviation from the reference spectrum, which is a result of the 2.2 MeV photon produced in the thermal neutron capture reaction: $^{1}H(n,\gamma)^{2}H$. The presence of a localized 2.2 MeV gamma signal signifies that there are thermal neutrons and a hydrogenous material present together. The detection of signals such as this allow for some determinations to be made on the detected object as a whole, rather than just the radioactive material.

Information on the material surrounding a radioactive source is important in certain applications, such as warhead verication. Additonally, the 2.2 MeV gamma signal is useful in non-proliferation applications where detecting shielded material is important, such as cargo screening. If the amount of polyethylene shielding were increased further, the neutron signal

from ^{252}Cf could be lost completely. However, the 2.2 MeV gamma signal could potentially still be used to determine the presence of a neutron-emitting material.

Aside from the 2.2 MeV signal, there is a deviation between the measured and reference spectra in the 0.45-0.50 MeV bin (associated with the ^{10}B(n, α) gamma-ray signal) that is much larger than the estimated uncertainty. This deviation is explained by the different standoff distances used in this experiment (5.17 m) and in the experiment from which the reference spectrum was obtained (2.0 m). As this signal does not come directly from the ^{252}Cf, it is expected to be larger (relative to the source signal) for larger standoff distances where the ratio between detected source photons and total detected photons is smaller. A small, unidentified feature is also noticeable in the 1.40-1.45 MeV bin.

6.3.3. Summary

The DPI has four major data pathways: imaging and localized spectroscopy for both photons and neutrons. Each of these pathways contributed, in-part, to the numerous conclusions drawn from this experiment. Table 6.2 briefly summarizes the conclusions drawn and the various data pathways used to obtain them.

Table 6.2. Summary of conclusions drawn and the data pathways used to facilitate them.

Conclusion	Neutron Image	Neutron Spectrum	Photon Image	Photon Spectrum	Details
2 neutron sources at (70°, 90°) and (135°, 90°)	X				Two hot-spots identified in neutron image.
1 fission source at (70°,90°)	X	X	X	X	Localized neutron spectrum compares well with Watt distribution. Localized photon spectrum consistent with fission.
1 non-fissile fission source at (70°,90°)	X	X	X	X	Above and absence of characteristic decay gammas expected from fissile sources.
1 non-fissile fission source shielded by hydrogenous material at (70°, 90°)	X	X	X	X	Above and localized 2.2 MeV signal in photon spectrum along with perturbed neutron spectrum
1 ^{9}Be(α, n) source at (135°, 90°). Potentially SNM.	X	X	X	X	Localized neutron and photon spectra show characteristics of a ^{9}Be(α, n) spectrum. Gamma decay lines consistent with ^{239}Pu.

6.4. Identifying Weapons-Grade Plutonium

In July 2015, the DPI was taken to the Device Assembly Facility at the Nevada National Security Site to measure various samples of category-I SNM. Three such samples were available for measurement:

1. BeRP Ball – a 4.5-kg sphere of weapons grade plutonium (WGPu)
2. Rocky Flats Shells – 13.1 kg of highly enriched uranium
3. Thor Core – a 4.1-kg disc of WGPu

Many measurements were performed with each of these samples in various shielded and unshielded configurations, and a brief discussion of a selection of the results can be found in [28] and [29]. The following section will be used to discuss one experiment involving the

Thor Core that is particularly applicable to several non-proliferation applications including treaty verification, emergency response, and active facilities monitoring.

6.4.1. The Thor Core

The Thor Core[4] is a 4.1-kg disc of weapons grade plutonium (WGPu), which qualifies it as category-I strategic SNM [5]. Figure 6.7 gives the dimensions of the sample as reported by [118]. Table 6.3 details the plutonium composition of the sample based off the values quoted in 1972 [118]. Due to the relatively short half-life of ^{241}Pu ($T_{1/2}$=14.29 years), these values should be adjusted for the buildup of ^{241}Am, which is produced through the β-decay of ^{241}Pu with a branching ratio of 99.99%, and will have discernable gamma-ray signatures. Table 6.4 makes this adjustment, while ignoring the negligible loss of ^{239}Pu ($T_{1/2}=2.41\times10^4$ years) and ^{240}Pu ($T_{1/2}=6.56\times10^3$ years). The balance of the ^{241}Pu branching ratio yields an α decay to ^{237}U. The very short half-life ($T_{1/2}$=6.75 days) of ^{237}U results secular equilibrium with ^{241}Pu, which allows for the strong gamma rays of ^{237}U to be associated with ^{241}Pu [3].

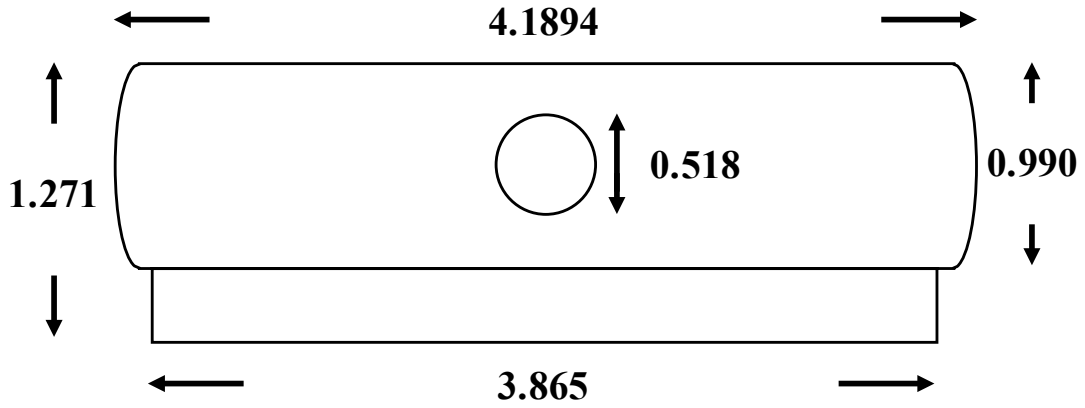

Figure 6.7. Diagram of the Thor Core with dimensions given in inches [118].

[4] The term "Thor Core" is used to reference the middle piece of the full Thor Core, which is the only piece that was made available for measurement. The full Thor Core is a three-piece subcritical plutonium assembly operated by Los Alamos National Laboratory[118], [120].

Table 6.3. Thor Core plutonium composition by isotope circa 1972 [118] .

Isotope	Atom %	Mass (g)
^{239}Pu	94.66	3867.69
^{240}Pu	5.02	205.11
^{241}Pu	0.32	13.07
Total:	100.00	4085.87

Table 6.4. Expected 2015 Thor Core composition by isotope.

Isotope	Mass (g)
^{239}Pu	3867.69
^{240}Pu	205.11
^{241}Pu	1.64
^{241}Am	11.43
Total:	4085.87

As a plutonium metal sample, the neutron energy spectrum will be well approximated by the Watt fission spectrum. Table 6.5 lists the prominent gammas signatures between 0.3 and 0.8 MeV expected from the Thor Core. While not listed in this Table 6.5, ^{241}Am has several strong decay gammas below 0.3 MeV, the most notable of which is the 0.059 MeV gamma ray emitted by ^{241}Am at a rate of 4.54×10^{10} γ/s-g. The intensity of these gammas necessitated the use of an increased threshold in the NaI(Tl) detectors (~0.25 MeV) to prevent saturation of the data-acquisition system. The increased threshold results in a minimum detectable photon energy of approximately 0.29 MeV.

Table 6.5. Prominent gamma signatures expected from the Thor Core.

^{239}Pu		^{240}Pu		^{241}Pu [α]		^{241}Am	
Energy (MeV)	**γ/s-g**	**Energy (MeV)**	**γ/s-g**	**Energy (MeV)**	**γ/s-g**	**Energy (MeV)**	**γ/s-g**
0.345	1.28×10^{4}	0.642	1.05×10^{3}	[α] 0.332	1.14×10^{6}	0.335	6.28×10^{5}
0.375	3.60×10^{4}			[α] 0.371	1.04×10^{5}	0.662	4.61×10^{5}
0.413	3.42×10^{4}					0.722	2.48×10^{5}
0.645	3.42×10^{2}						
0.717	6.29×10^{1}						

[α] The listed ^{241}Pu signatures come ^{237}U decay, which is in secular equilibrium with ^{241}Pu.

6.4.2. Experiment

An ~850-minute measurement was taken with three neutron-emitting sources present in the FOV: the Thor Core, ^{252}Cf and ^{241}AmBe. Each source was located at a standoff of approximately 2.0 m and lead shielding was used to reduce the ^{241}Am photon flux coming from the Thor Core and ^{241}AmBe source. The location, standoff, shielding, and approximate neutron emission rate for each of these three sources is summarized in Table 6.6.

Table 6.6. Source location, approximate neutron emission rate, and shielding for each of the three sources in the FOV.

Source	n/s	Location	Standoff (m)	Shielding
Thor Core	~7.9×10^5	(90°, 85°)	2.00	1.27-cm Lead
^{252}Cf	~3.0×10^5	(90°, 110°)	2.11	None
^{241}AmBe	~1.0×10^6	(141°, 85°)	2.07	10-cm Lead

Approximately 1.6×10^5 neutron events and 1.0×10^6 photon events were acquired. The high number of photon events acquired facilitated the use of a 0.025 MeV source-space energy bins in the photon system matrix, rather than the 0.050 MeV bins that have been used throughout this work. The expected energy signatures for the Thor Core and the ^{241}AmBe source are described in 6.4.1 and 6.2, respectively. The ^{252}Cf source is approximately 10 years old and displays photon spectrum characteristics similar to the ^{252}Cf source discussed in Section 4.4 of Chapter 4.

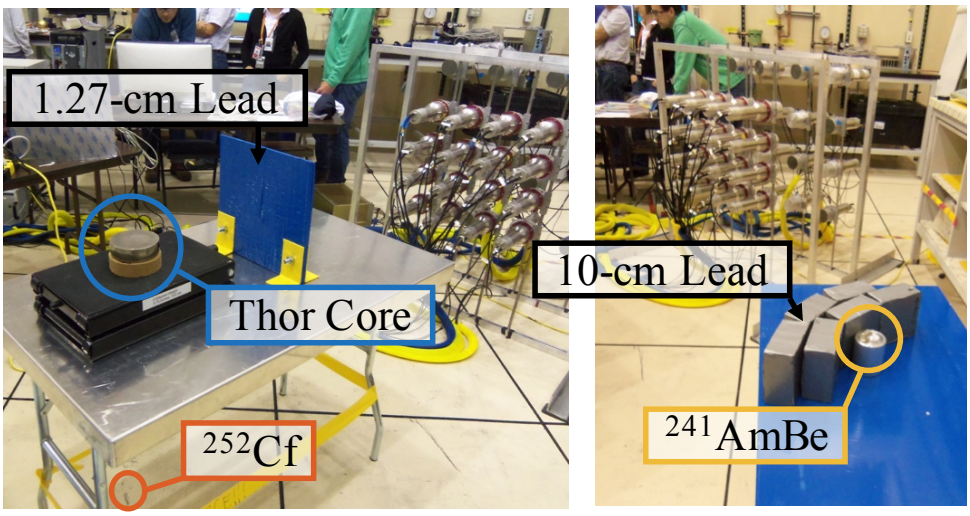

Figure 6.8. Photographs of the experimental setup. The Thor Core is located at (2.00 m, 90°, 85°) behind a 1.27-cm thick lead shadow-shield. The ^{252}Cf is located 4.5 cm above the floor directly below the Thor Core at (2.11 m, 90°, 110°). The ^{241}AmBe is located at (2.07 m, 141°, 85°) behind approximately 10 cm of lead shielding.

Figure 6.8 shows two photographs of the experimental setup. The Thor Core was oriented such that the flat sides of the disc were parallel to the floor, which was a safety precaution to prevent the source from tipping over during the unattended overnight measurement. The ^{252}Cf source was placed 4.5 cm above the floor, directly below the Thor Core. The ^{241}AmBe source was placed on a table to the left of the Thor Core (from the perspective of the DPI). The Thor Core was shielded by a 1.27-cm thick lead shadow-shield and the ^{241}AmBe source was shielded by 10 cm of lead bricks.

It is worth noting that while the expected gross neutron emission rate (reported in Table 6.6) for the Thor Core can be reasonably well estimated, the apparent emission rate observed by the DPI is affected by the orientation of the sample. Simulations have shown that the flat orientation used in this experiment results in a count rate that is ~63% lower than the neutron count rate detected using a face-on orientation. The reduction in measured count rate is a consequence of self-shielding caused by the size and mass of the sample.

Additionally, the observed emission rates of both the Thor Core and ^{241}AmBe source will be reduced by the lead shielding.

6.4.3. Results

Figure 6.9 shows the reconstructed neutron and photon images. While the neutron image shows three hot-spots all centered in the correct pixels, the photon image only locates two of the three sources (also at the correct location). The ^{241}AmBe hot-spot is absent, due to the significant amount of lead shielding present around the source. While the absence of the ^{241}AmBe photon hot-spot may be initially seen as a failure (and in some sense it is), there is an important piece of information to be learned from this. Neutron-emitting materials are expected to be accompanied by photons, and therefore, a corresponding photon hot-spot is expected for every neutron hot-spot. As such, the absence of a corresponding photon hot-spot is a signal that high-Z material may be present. While the presence of lead was known *a priori* in this measurement, the ability to obtain such information is important when investigating an unknown environment. It is worth pointing out that a photon-only detector of similar sensitivity would potentially be blind to the presence of the ^{241}AmBe source, which highlights a benefit of dual-particle sensitivity.

Figure 6.10 shows, for both photons and neutrons, a direct comparison between the isolated spectra from each of the three ROIs shown in Figure 6.9. There are obvious differences in both the photon and neutron spectra for all three sources, which are discussed in greater detail over the following pages.

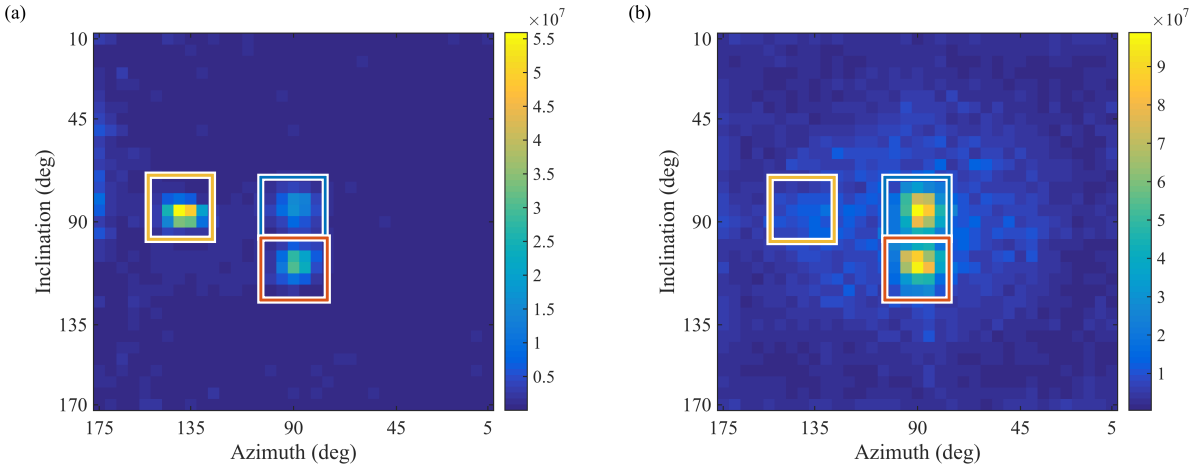

Figure 6.9. Reconstructed neutron (a) and photon (b) images. Neutron image correctly locates all three sources while photon image correctly locates the Thor Core and the ^{252}Cf. The ^{241}AmBe hot-spot is absent from the photon image due to heavy lead shielding. Colored boxes denote the 5×5-pixel ROIs used to generate the isolated spectra shown in Figure 6.10.

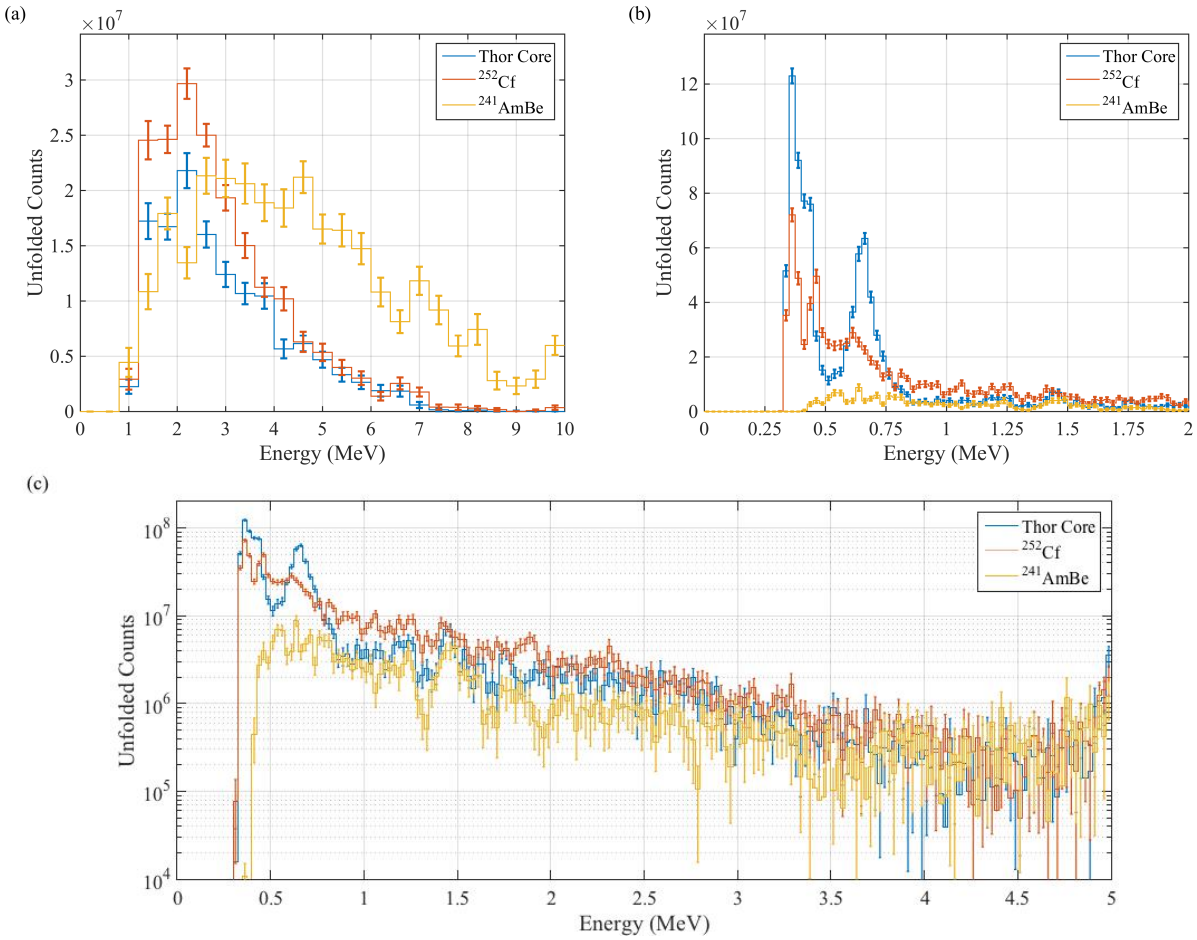

Figure 6.10. Isolated neutron (a) and photon (b), (c) corresponding to the 5×5-pixel ROIs shown in Figure 6.9. The photon spectra are shown on a linear scale over a reduced energy range in (b) and on a logarithmic scale over the full range in (c). Error bars represent ±1σ.

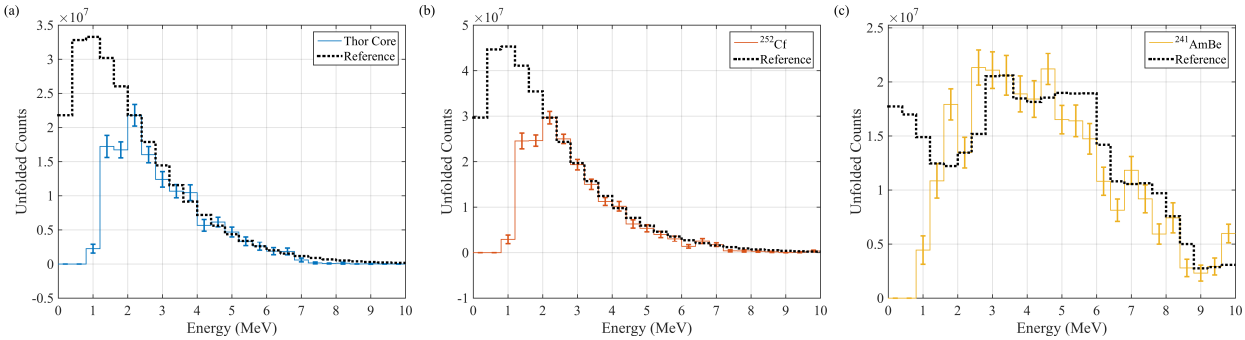

Figure 6.11. Isolated neutron spectra for the Thor Core (a), ^{252}Cf (b), and ^{241}AmBe (c) ROIs shown in Figure 6.9. The reference spectrum in (a) and (b) is the theoretical ^{252}Cf spectrum and the reference spectrum in (c) is the theoretical ^{241}AmBe spectrum. All reference spectra are scaled to match the intensity of the corresponding isolated spectrum in the 2.0-2.4 MeV energy bin. Error bars represent ±1σ.

Figure 6.11 shows how each of the isolated neutron spectra compare to corresponding reference spectra shown in Figure 6.1. Both fission sources are compared to the ^{52}Cf reference spectrum to emphasize the similarities in the neutron spectra between the two sources. In all cases the reference spectra are scaled to match the intensity of the measured spectrum in the 2.0-2.4 MeV energy bin. Acknowledging the expected variation in ^{9}Be(α, n) spectra, it is clear that all three spectra compare well to their references for energies above ~2 MeV. Both the Thor Core and the ^{252}Cf agree especially well, with the reference spectrum falling within the estimated uncertainty in almost all energy bins.

The neutron spectra alone facilitate discrimination between ^{9}Be(α, n) source and the fission sources. However, the neutron spectra do not allow for the Thor Core to be distinguished from the ^{252}Cf due to the similarities in the neutron energy distribution across fission sources. Fortunately, the availability of localized photon spectra makes this discrimination possible. It is apparent in Figure 6.10(b) and (c) that the isolated photon spectra for these two sources are very different and the forthcoming analysis will demonstrate that the spectral features are well aligned with the expected features of each source.

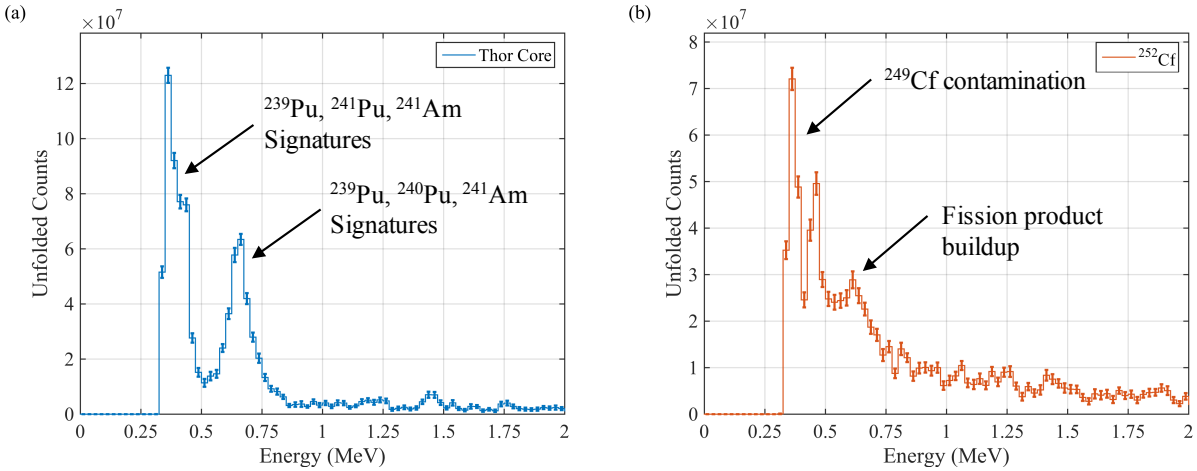

Figure 6.12. Isolated photon spectrum for the Thor Core (a) and the ^{252}Cf (b). Error bars represent ±1σ.

Figure 6.12 highlights the notable features of the isolated photon spectra for the Thor Core and the ^{252}Cf source. The Thor Core spectrum is dominated by two peaks located in the 0.300-0.475 MeV energy bins and the 0.550-0.750 MeV energy bins. While the DPI does not have the requisite resolution to individually resolve the individual emission lines of the Thor Core, it is clear that these peaks are well aligned with the energy ranges outlined in Table 6.5.

The ^{252}Cf spectrum appears to have more of a continuum than the Thor Core spectrum (which is seen more clearly in Figure 6.10 (b) and (c)). On top of this continuum are three prominent features. The peak between 0.350 and 0.400 MeV and the protrusion in the 0.650 MeV range are due to the age of the source, as discussed in Chapter 4 [93]. The third feature is the peak located in the 0.425-0.475 MeV energy bins, which is tentatively left as unidentified.

The age-related features in the ^{252}Cf spectrum appear at similar energies as the expected plutonium signatures, which makes it more difficult to discriminate between the two fission sources. However, the overall shape of the spectra makes discrimination between the two fission sources possible. It is worth noting that the difference in shape would be even more

apparent if ^{252}Cf source were newer, and displayed a more dominant fission gamma shape similar to that of the 4.4 mCi ^{252}Cf source shown in Figure 6.6 (b).

It is possible that the unidentified feature is related to the 0.478 MeV ^{10}B(n,α) feature seen in previously discussed experiments performed in the standard laboratory space. The DAF facility provided a much larger measurement space and the total neutron emission rate in this measurement (~2.1×10^{6} n/s) is an order of magnitude lower than the neutron emission rate of the previously measured 4.4 mCi ^{252}Cf source (~1.9×10^{7} n/s). These factors should both result in a lower rate of thermalized neutrons incident on the DPI, and therefore a lower ^{10}B(n,α) signal. However, in this particular experiment, the two fission sources were located directly between the DPI and the Fast-Neutron Coded-Aperture Imager [12], which was deployed with a large borated-polyethylene mask. As such, it is possible that the DPI is also detecting ^{10}B(n,α) gammas being emitted by the mask. If this theory is correct, a similar signal would also be expected in the Thor Core ROI. However, it is difficult to determine if such a signal is present because the relevant energy bins are contained within the low-energy peak of the isolated Thor Core spectrum.

Figure 6.13 shows a comparison between the isolated photon spectrum of the ^{241}AmBe ROI and a 5×5-pixel "background" ROI taken from a similar location, (40°, 85°), on the opposite side of the image. The ^{241}AmBe spectrum shows considerable overlap with the background spectrum. It is clear that there is no surplus signal in the 4.4 MeV region, which would have been the most likely gamma energy to pass through the 10 cm of lead shielding.

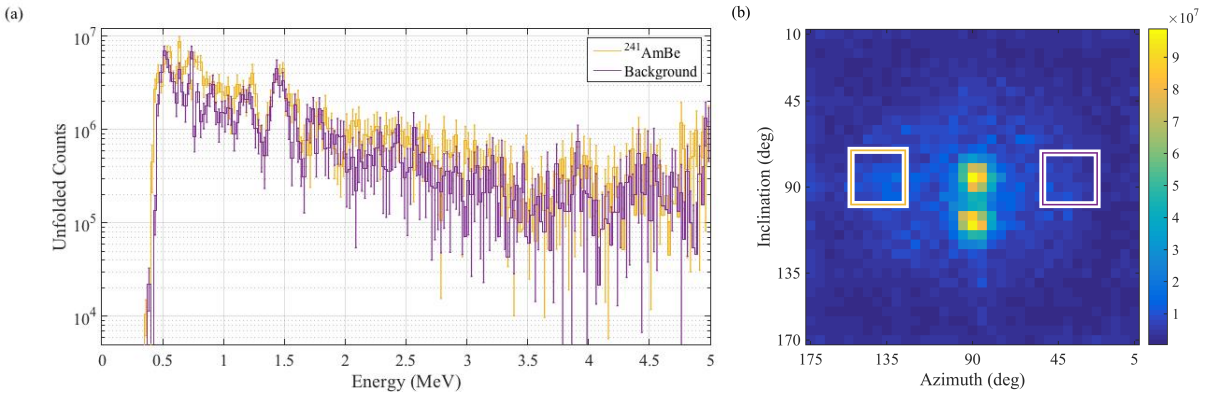

Figure 6.13. Comparison between the isolated spectrum (a) of the ^{241}AmBe ROI and the background ROI denoted by the purple box in (b). Error bars represent ±1σ.

6.4.4. Summary

The results presented in Section 6.4.3 demonstrate how the DPI was used to successfully locate a category-I SNM sample from a field of three neutron-emitting sources. The success of this experiment was highly dependent on the localized spectroscopy capabilities provided by the spectrum-isolation technique. In addition to locating the SNM sample, the four data-pathways of the DPI were used in various combinations to draw several other conclusions, which are summarized in Table 6.7. While no claims are made on the minimum time (or measured events) required to draw these conclusions, the small relative error associated with the isolated spectra suggests that the full 850-minute data set is not required.

Table 6.7. Summary of conclusions drawn and the data pathways used to facilitate them.

Conclusion	Neutron Image	Neutron Spectrum	Photon Image	Photon Spectrum	Details
3 neutron sources at (90°, 85°), (90°, 110°), and (140°, 85°)	X				Three hot-spots identified in neutron image.
2 fission sources at (90°, 85°) and (90°, 110°)	X	X			Localized neutron spectra compare well with Watt distribution.
1 non-fissile fission source located at (70°, 90°)	X	X	X	X	Localized neutron spectrum compares well with Watt distribution. Absence of characteristic decay gammas expected from fissile sources.
1 plutonium sample (SNM) located at (90°, 85°)	X	X	X	X	Localized neutron spectrum compares well with Watt distribution. Localized photon spectrum decay lines consistent with plutonium.
1 ^{9}Be(α, n) source at (140°, 85°)	X	X			Localized neutron spectrum compares well with ^{241}AmBe spectrum.
^{9}Be(α, n) shielded by high-Z material present at (140°, 85°)	X	X	X	X	3 neutron hot-spots but only 2 photon hot-spots. Localized photon spectrum compares well with background estimate.

6.5. Remarks

This chapter presented the results of two complex measurement scenarios that highlight the investigative capabilities of the DPI. In both cases, the DPI was able to successfully localize and characterize the SNM sample. This was possible through the use of the spectrum-isolation technique and the four data-pathways afforded by the versatility of the system. Section 6.3 demonstrated the capability of the DPI to discriminate between different types of neutron spectra and gave an example of how non-source signals, such as the 2.2 MeV ^{1}H capture gamma, can be used to draw conclusions on materials surrounding the source.

Section 6.4 proved that the DPI is capable of detecting, localizing, and characterizing a category-I SNM sample, which was one of the major goals of this work.

Many of the conclusions drawn from these experiments could also be drawn independently from the use of several, less versatile systems. However, one of the greatest advantages of the DPI is the ability to provide four synchronized data-pathways. These four pathways allow for the user to cross-reference localized photon and neutron data obtained concurrently from a single system, which is particularly advantageous in applications concerning the detection of SNM.

Chapter 7. Summary, Conclusions, and Future Work

7.1. Summary and Conclusions

At the outset of this work I established several non-proliferation and treaty verification scenarios as potential applications for robust radiation imaging techniques. These scenarios rely on the ability to accurately detect, localize, and characterize radioactive materials, specifically SNM. The goal of this work was to develop a versatile detection system and powerful data-processing algorithm that, when combined, are able to reliably meet these needs.

In Chapter 2 I introduced the DPI as a versatile detection system capable of providing data through four main pathways:

1. Neutron imaging
2. Photon imaging
3. Neutron spectroscopy
4. Photon spectroscopy

In Chapter 3 I introduced the spectrum-isolation technique, which is an image and spectrum reconstruction algorithm designed to extract information from these four pathways. In Chapter 2 and Chapter 3 I described the robust Monte Carlo simulation techniques used to compute the detailed system matrix that makes the spectrum-isolation technique successful. Chapter 4 demonstrates the capabilities of the spectrum-isolation technique by extracting a variety of useful information from the localized spectra of three increasingly complex measurements. These measurements also demonstrated the ability to obtain useful

information, such as estimated background and room-return contributions, from non-source locations in the image.

Having established the utility of the spectrum-isolation technique, I worked to determine the uncertainty associated with the reconstructed solutions and demonstrated that a bootstrapping technique could be used to reliably estimate statistical uncertainties using only a single measurement. Knowing the expected statistical deviations allowed for quantitative assessment of the systematic uncertainties within the system matrix. These uncertainties were investigated through the comparison of isolated spectra generated from the same source measured at a variety of locations and standoff distances. This comparison showed that while the magnitudes of the isolated spectra displayed some variations over the cases investigated, the normalized shapes of the isolated spectra were well aligned across all measurements. This conclusion is an important one because it implies that template matching can be used to compare measured spectra to expected distributions and draw concrete conclusions on any observed deviations – beyond those predicted by statistical uncertainty.

As a final proof of concept, I analyzed two complex environments, relevant to non-proliferation, using the methods outlined in this work. In both cases, the DPI was able to successfully locate and identify the SNM sample in a cluttered environment. In the first experiment, a ^{239}PuBe source (classified as category-III SNM) was distinguished from a polyethylene-shielded ^{252}Cf source. Additionally, the polyethylene shielding was identified by comparing the isolated ^{252}Cf spectra to measured reference spectra. In the second experiment, a 4.1 kg WGPu sample (classified as category-I SNM) was identified in a FOV that also contained a ^{252}Cf source and a lead-shielded ^{241}AmBe source. The non-SNM sources

were also correctly located and identified and the presence of lead shielding was determined by the absence of a photon signal from the known ^{241}AmBe location. The depth of the conclusions drawn from these final experiments truly demonstrate the contributions of this work towards the established need of reliably detecting, localizing, and characterizing special nuclear materials.

7.2. Suggestions for Future Work

At many points throughout this work attention was drawn to open challenges and avenues for future improvement. Admittedly, much of the analysis presented in this work was performed from a qualitative standpoint. However, the groundwork has been laid to move in the direction of more quantitative analysis. The viability of bootstrapping allows for detailed statistical analysis to automate detection and characterization. The implementation of such algorithms may improve the sensitivity of the system by removing the need to obtain "well-converged" spectra.

Additionally, with further work, accurate and reliable estimates of ROI intensity could enable the determination of characteristics such as the absolute activity and fissile mass. Chapter 3 demonstrated that the 5×5-pixel ROIs under-predicted the expected source strength. Furthermore, the under-prediction was not found to be consistent between different sources or different energies. With a better understanding of the influential factors, it may be possible to correct the under-prediction. This approach would open up the possibility of estimating the source strength of detected materials at a known distance. Furthermore, these corrections are likely to be of different strength for gammas and neutrons. If corrected, the absolute neutron to gamma ratio could be used to make further inferences on the size and shape of the detected objects.

In Chapter 6, some allusions were made to the possibility of characterizing intervening materials by comparing the attenuated spectra to suspected material cross sections. Such an analysis could yield information on both the properties and thicknesses of the intervening material, which could be used to estimate source strength of shielded nuclear material. The ability to accurately estimate uncertainty in the isolated spectra, such as through the use of the bootstrapping technique described in Chapter 5, is a necessary first step towards this goal. Knowing the uncertainty in the isolated spectra makes it possible to determine if deviations from an expected reference spectrum are within the statistical limitations of the measurement or if they are the result of attenuation by an intervening material. If an intervening material is detected, then the estimated uncertainties in the spectrum could be used to estimate the uncertainty on the calculated thickness of the intervening material. It is worth noting that this effort would benefit greatly from improvements to the energy resolution of the DPI.

Each of the above endeavors would benefit from further understanding of the statistical and systematic uncertainties associated with the system matrix. Several potential sources of model mismatch were alluded to and many warrant a more in-depth analysis than was afforded in this work. Features such as the flat top on the Watt distribution seemed to be fairly consistent and could likely be corrected for by including some estimate of PSD misclassification in the system matrix. The effect of statistical uncertainties within the system matrix itself were not considered in this work and should be studied further. The use of bootstrapping to estimate the statistical uncertainties of the system matrix may help provide a more comprehensive estimate of the statistical contributions to uncertainty in spectrum-isolation solutions. Additionally, the analytic noise-propagation models that have

been developed for tomographic image reconstruction may be useful for further characterizing uncertainty in the spectrum-isolation solutions [94], [104], [106], [107]. Models related to system matrix error would be especially useful because they can provide insight into the level of accuracy needed in the system matrix computation to achieve a desired level of uncertainty in the solutions [106], [107].

The system matrix itself also offers several avenues for improvement. Implementing a more optimal binning structure might include a strategic change of basis or even a full re-parameterization of the problem. Improvements could also be made to the accuracy of the overall model. Such work might include further improvement of the light-to-energy conversion and resolution functions, as well as the addition of new capabilities, such as the simulation of full light propagation and simulated pulse-shape discrimination. Efforts could be made to reduce the computation time required to simulate the system matrix. In addition to leveraging the previously mentioned analytic noise-propagation models, computation time could be reduced by strategically finding and removing less relevant regions of the model. Additionally, it may be possible to simulate fewer source space bins and simply interpolate to finer resolutions.

Although well developed, the DPI certainly has room for improvement. Chapter 2 showed that the spatial resolution of individual interactions limited the achievable angular resolution for both photons and neutrons the energy resolution of neutrons. Spatial resolution could be improved by using smaller detector cells, using pixelated read-outs (such as SiPMs), or simply moving the detectors further apart. The SiPM route is the most interesting because it would also result in a more compact form-factor and would not inherently reduce the efficiency. It would also be possible to improve photon energy

resolution by using higher resolution materials including, but not limited to, CsI, $LaBr_3$, or CdZnTe. However, due to the summation of front and back plane energy depositions, these improvements would be tempered by the lower resolution of the EJ-309 detectors. Additionally, improvements could be made in the pulse-shape discrimination capabilities of the scattering detectors by moving to a material such as stilbene.

With all of this interesting work available, maybe I should consider a second Ph.D.

.

Appendix A. Spectrum-Isolation Toolbox

A.1. Overview

A custom MATLAB toolbox was developed to handle the data analysis and visualization for the spectrum-isolation technique. This toolbox consists of three MATLAB classes and a graphical user interface, which facilitates in-depth investigation of the spectrum-isolation solutions. The following sections will briefly describe the purpose and functionality of each of these components. Due to its length, the full code will not be published in this thesis. However, the code is hosted on BitBucket and is available, in its entirety, upon request.

A.2. corr_events Class

The corr_events class handles the "Correlated_events" file that is created by the imaging subroutine of MPPost. This file contains the requisite information for determining the appropriate observation bin for each event including reconstructed energy, reconstructed angle, time-of-flight between interactions, and detectors in which the particle interacted. The Correlated_events files also include information related to the interaction type (including interactions ignored in this thesis). For simulated data, the file contains a flag denoting "ideal" events, which are events whose backprojection cone is expected to pass through the correct source location (e.g. events that undergo a single scatter in the first detector of interaction and do not interact in material outside the active detector volumes). The Correlated_events files for system-matrix simulations contain additional information describing the initial energy and origin of the simulated particle. This information is used by

the system_matrix class (described in Section A.3) to determine the appropriate source space bin for each detected event and is provided by the output of the MCNPX-PoliMi patch described in Appendix C.

A corr_events object is used to hold the measured data vector, $\boldsymbol{b}$, and is initialized with the desired energy thresholds, reconstructed-energy binning, and reconstructed-angle binning. Once initialized, functions are available to load and sort data from a Correlated_events file into the appropriate observation bins. Events falling outside the binning structure, or with interactions that occur below the desired threshold are ignored. Bootstrapped data realizations can also be generated during the loading and binning procedure. Functions are also available for loading pre-binned data, which makes it possible to use the toolbox (in a limited fashion) with data originating from different simulation techniques or even different systems. The properties of a corr_events object contain information on detector thresholds and observation-space binning and a populated object will also include the binned data vector and any associated bootstrapping realizations.

A.3. system_matrix Class

The system_matrix class is used to create system matrices and can operate on corr_events objects with the same observation-space binning structure to produce im_spec_sol objects, which contain the spectrum-isolation solutions (and are discussed in Section A.4). The system_matrix class is a subclass of the corr_events class and therefore also has the capability to handle Correlated_events files. A system_matrix object can be initialized as either a point-source or a continuous-source (utilized in this work) system matrix with slightly different behavior for each. In addition to source type, the particle type (neutron or photon), detector thresholds, reconstructed-energy binning, reconstructed-angle binning,

and source-space energy binning are required to initialize a system_matrix object. The source-space angular binning (pixel size and location) are determined when the system_matrix object is populated with data.

The system_matrix class contains several properties and functions related to populating the system matrix data. The system_matrix class uses the functionality inherited from the corr_events class to load and sort data in observation space, and also has separate functionality for sorting data in source-space. Data can be populated on either a bin-by-bin basis or on an event-by-event basis (which is considerably faster for expansive binning structures). In either case, the system_matrix class is able to leverage MATLAB's built in parallelization capabilities to process multiple Correlated_events files simultaneously. The system-matrix-population procedure is assisted by functions for properly normalizing the data according to the simulated emission probabilities. As with corr_events objects, system_matrix objects can be populated with a pre-binned data set, to facilitate the use of this toolbox with alternative systems.

After being populated, a system_matrix object can be used to compute the spectrum-isolation solution for a compatible corr_events object. There is functionality available to check if the observation-space binning of an existing corr_events object is equivalent to that of the system_matrix object. Additionally, a system_matrix object can be used to directly generate a compatible corr_events object from a Correlated_events file. The measured data (and any desired bootstrapped realizations) for a compatible corr_events object can be passed into the MLEM algorithm of the system_matrix object. The MLEM function will automatically determine the below-threshold energy bins to hold at 0 during reconstruction. Functionality is also available to allow for additional source-space bins (energy and/or pixel)

to be held at 0, which allows for reconstruction over a constrained FOV as determined by the user.

After the MLEM algorithm has completed the requested number of iterations for all provided realizations, the system_matrix object initializes an im_spec_sol object and populates it with the computed solution at each iteration. Information related to the development of the solution (e.g. log-likelihood, forward-projection, and data-residual) are also provided for each iteration. It should be noted that when bootstrapped solutions are requested, the per-iteration information is only provided for the measured data-set to constrain the im_spec_sol objects to a manageable size (typically less than 1 GB). Only the solution for the final iteration (as determined by the termination criterion discussed in Chapter 4) is stored for each bootstrapped realization.

The system_matrix class has utility functions available to determine the index of a particular source-space bin for a given angular location and energy. Plotting functions are available to visualize source space and observation space and also to display sensitivity maps over a specified energy range. The system_matrix class also holds several under-development functions related to ongoing work in areas such as bootstrapped system matrices, and re-binning procedures based on the singular-value decomposition of the system matrix.

A.4. im_spec_sol Class

The im_spec_sol class handles the spectrum-isolation solutions and provides functionality for analyzing various aspects of these solutions. An im_spec_sol object will hold the solution data for each iteration, as well as the final iteration of any bootstrapped solutions. An object will also contain information on source-space binning structure of the

solution as well as the observation-space binning structure of the corr_events and system_matrix objects used to compute the solution.

An im_spec_sol object will collapse the solution into images and spectra, as desired. The image can be displayed over the full energy range or over a subset of energies. Functionality is available to add regions-of-interest over a given pixel and energy range. The isolated spectra and total number of unfolded counts can then be computed and displayed for each ROI. If bootstrapped solutions are available, then the standard deviation and relative error can also be computed and displayed for the image and isolated spectra. Plotting functions are also available for the likelihood and log-likelihood functions as well as for the variance, mean, 1-, 2-, and infinity-norms of the data residual. Each of these parameters were investigated for use in determining a termination criterion.

A.5. Solution Interface

A graphical user interface, shown in Figure A.1, was developed to streamline the analysis of the information contained in im_spec_sol objects. The interface displays three figures, one for the image, one for the isolated spectra, and one for the stopping criterion. Any of these figures can be exported to .fig and .png files as necessary. The text below the file-loading interface (in the upper-right corner) displays the number of measured events used to compute the solution as well as the total number of unfolded events in the full solution.

The upper right figure displays the reconstructed image. Inputs are available to change the energy range of the image. Although not used in this work, it is also possible to apply Gaussian and median filters to the image.

The isolated-spectra figure, located in the upper left of the interface, will display all saved ROI upon loading. Additional ROI can also be added (and removed) through the ROI interface

located below this axis. The table located below this figure displays the properties of each ROI, including their centroid, size, and energy range. The table also displays the total number of unfolded counts contained within the ROI.

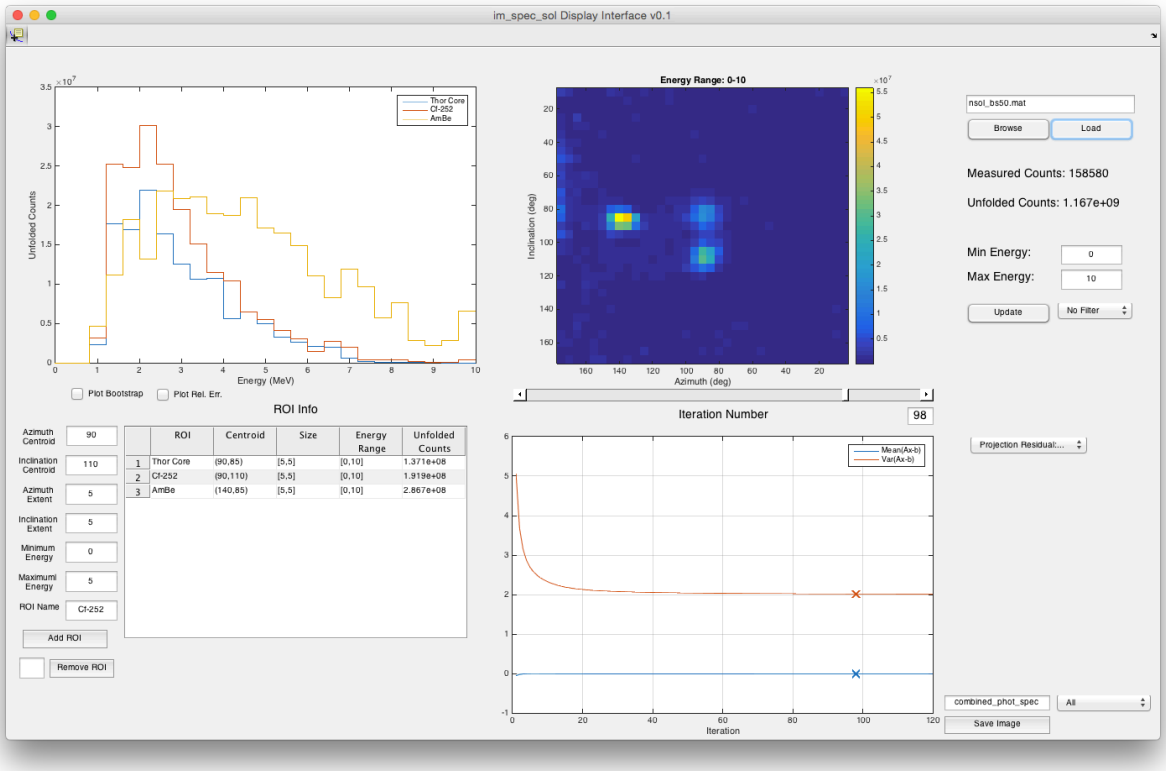

Figure A.1. Screenshot of the solution display interface. The interface displays the image over a specified energy range, a plot of the termination criterion as a function of iteration, and the isolated spectra for any defined ROIs. The iteration number can be varied to see how the image and isolated spectra develop.

The lower right figure of the interface is used to display information related to potential stopping criteria. In Figure A.1, the stopping criterion figure displays the variance (and mean) of the data residual, as a function of iteration. It is also possible to display the likelihood function, log-likelihood function, and 1- 2- and infinity-norms of the data residual using the drop-down menu located next to the upper right corner of the figure. The ‘x’ on

stopping criterion curves corresponds to the iteration being currently displayed in the reconstructed-image and isolated-spectra figures.

The slider located below the image can be used to change the iteration number being displayed, which allows the user to see how the solution develops as a function of iteration. Upon loading, the iteration number will default to the final iteration number as determined by the stopping criterion.

Bootstrapped error-bars and relative-error spectra can also be plotted for each ROI on the isolated spectrum figure. However, these plots will not change with the iteration slider as the bootstrapped solutions are only saved for their final iteration.

Appendix B. Auto-Slice Pulse-Shape Discrimination Algorithm

B.1. Overview

Chapter 2 discussed an algorithm for automatically determining discrimination curves for use with the charge-integration pulse-shape discrimination method. The methodology used in this algorithm is described in greater detail in this appendix, and a full assessment of the algorithms performance can be found in [36]. Note that the following description was taken from [36], and therefore the notation used may not be consistent with the notation used throughout the balance of this thesis.

B.2. Auto Slice PSD Algorithm

Auto Slice PSD determines a discrimination curve by using a multi-step process that includes slicing the data into smaller subsets, fitting the distribution of tail-to-total-integral ratios in each slice, and using the fits to find the optimal discrimination points that minimize misclassification in each slice. Once identified, these points can be used to fit a discrimination curve through the data set. Additionally, by analyzing the slice-by-slice fits it is possible to estimate the fraction of neutrons and photons misclassified by the discrimination curve.

B.3. Slicing the Data

The first step in determining a discrimination curve is to divide the full data set into smaller subsets by using linear slices. By slicing the data, it is possible for the discrimination points to be chosen such that they optimally separate a local region; this optimization process will be discussed in Section B.5. A histogram of the ratio of tail-to-total integrals for

the pulses contained in a slice can be accurately fit as a sum of two Gaussians, where one Gaussian models the neutron cluster and another models the photon cluster. The peaks are Gaussian in nature as a result of the stochastic processes inherent to converting an energy deposition to an output signal in a detector and photomultiplier tube. It should be noted that although a similar histogram can be computed for the full data set, it generally cannot be modeled as a sum of two Gaussians due to the shift in the means of the clusters as a function of total integral.

The slices used by this algorithm are linear and are defined by a slope and width, which are selected by the user and provided as inputs. Auto Slice PSD numbers slices in ascending order beginning with the slice that contains the pulses with the lowest total-integral. When comparing two or more slices in terms of location, slices with a larger slice number will be considered “to the right of” or “above” slices of a lower slice number.

The slope should be chosen such that the slices are as perpendicular to the data clusters as possible, which will help to preserve the Gaussian nature of each cluster when the slice is projected onto the ratio-histogram axes. As the photon and neutron clusters are neither parallel nor perfectly linear, it is not possible to be fully perpendicular to all regions of both clusters simultaneously. However, if the slice angle is reasonably close to the true perpendicular angle and the slice is sufficiently narrow, the Gaussian nature of the clusters will be maintained.

The width of the slices is defined as the distance between where the slice edges intercept the total-integral axis. Ideally, the width of the slices should be as narrow as possible to allow for a large number of points through which to fit the discrimination curve. However, in practice the width of the slices should be balanced such that the slices are wide enough to

contain enough pulses for the ratio histogram to be accurately fit, while still being narrow enough to avoid a significant shift in cluster mean. Although the slope and width of the slices are currently provided as user inputs, there is a plan for future software versions to automatically compute the optimal slice parameters.

Figure B.1 (a) shows the same data set seen in Chapter 2, Figure 2.5 overlaid with slices having a width of 0.1 V·ns and a slope of -6. The slope is approximately perpendicular to the clusters and was calculated by taking the value half way between the mean slopes for the aggregate neutron and photon clusters. Figure B.1 (b) shows the tail-to-total integral ratio histogram for the fifth slice in Figure B.1 (a), which has been highlighted. Tail-to-total integral ratios can fall between 0 and 1 in theory; however, the pulses evaluated in this study do not typically fall within the upper third of this range. As such the ratio histograms presented in this paper will be displayed over a constrained range for clarity.

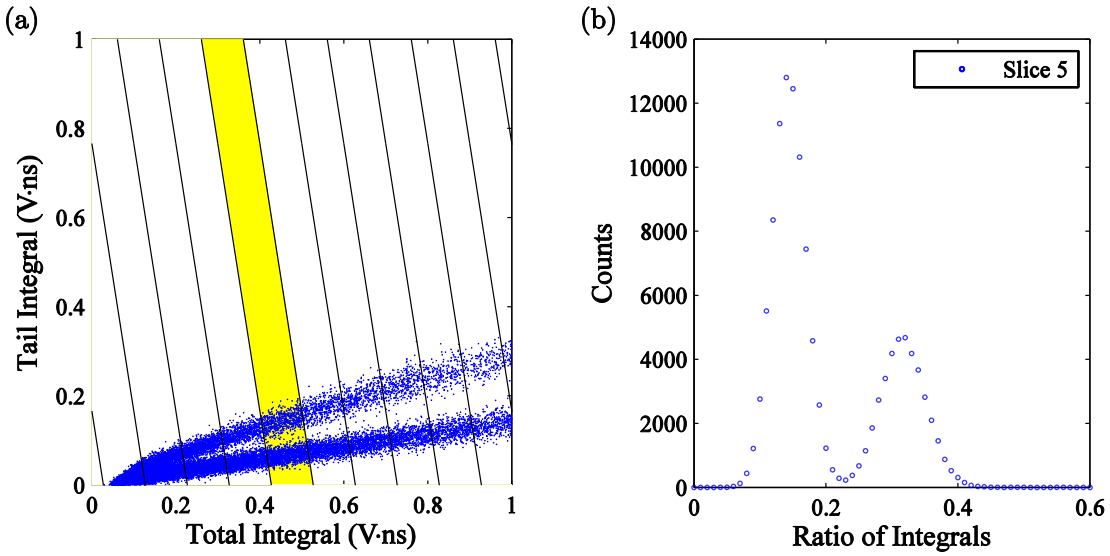

Figure B.1. Tail-integral-vs.-total-integral scatter plot overlaid with slices having a width of 0.1 V·ns and a slope of -6 (a). Tail-to-total integral ratio histogram for the fifth (highlighted) slice in of the tail-integral-vs.-total-integral scatter plot (b). Error bars are excluded from the ratio histogram because they would be smaller than the data point.

B.4. Fitting the Slices

Once the data have been subdivided into slices, an integral ratio histogram is computed for each slice, as shown in Figure B.1 (b). In general, these histograms will appear as two peaks, with the lower ratio peak representing the photon data and the higher ratio peak representing the neutron data. As such, the full histogram can be well modeled as a sum of two Gaussians, which is accomplished using a built-in curve-fitting routine in MATLAB. This routine utilizes a nonlinear optimization method to find the six parameters required to define two Gaussian curves: the amplitudes (a_1 and a_2), the means (b_1 and b_2), and c_1 and c_2, which are related to the widths. To assist with finding the most accurate solution, the routine can be supplied upper and/or lower bounds as well as initial guesses for each of the six parameters. For clarity, the parameters associated with the fit of the photon cluster will be denoted as a_γ, b_γ, and c_γ while the parameters associated with the fit of the neutron cluster will be denoted as a_n, b_n, and c_n. If it is important to specify the slice number, s, of a parameter, the slice number will be denoted as a parenthetical superscript (e.g. $a_n^{(s)}$).

This fitting routine works very well for slice histograms with two easily distinguishable peaks even when no information is provided about the expected parameter values (although the fit is found more quickly if some initial information is provided). However, when using sufficiently low energy thresholds the photon and neutron clusters begin to overlap in the low-energy-deposition region. Predictably, as this overlap occurs, the two peaks in the ratio histograms begin to move closer together (through descending slices) and eventually appear as a single peak. If it is assumed that the slices with overlapping data clusters do in fact contain pulses from both neutron and photon interactions, then it is still reasonable to fit the ratio histogram as a sum of two Gaussians. However, it is difficult for the MATLAB fitting

routine to fit histograms of this nature unless it is provided with estimates of the expected amplitudes, means, and widths of the two Gaussians. It is possible to estimate this required information reasonably well by using parameters from the previously fit slice as well as information gained from analyzing the data set as a whole.

Although there is only a small fraction of slices contained in the overlapping region, it is important to accurately fit the histograms for these slices because a small shift in the discrimination point can result in a significant change in particle misclassification. The same is not true for slices in regions of high cluster separation where a small shift in the discrimination point may not change the number of misclassified particles at all. Additionally, because the slices in the overlapping region contain a comparatively large number of pulses, proper fitting is required to get an accurate estimate of misclassification for the full data set. Due to the importance of fitting the slices in the overlapping region, several steps are taken within the processing algorithm to provide the MATLAB fitting routine with as much information as possible on the expected parameter values. The requisite information is provided by executing a pre-fitting algorithm on the full data set that results in an estimate of the mean value for both clusters in each slice. The slice-fitting algorithm is then executed beginning with a slice that shows reasonable separation and moving down through the overlapping region before fitting the remainder of the well-separated slices. By starting with a slice that can be reliably fit with minimal input (and using the resulting fit information to work backwards) it is possible to provide enough information to the MATLAB fitting routine to accurately fit slices with strongly overlapping peaks.

B.4.1 Pre-fitting Algorithm

Prior to fitting the individual slices, a pre-fitting algorithm is used to estimate the mean values of the photon and neutron clusters as a function of total integral. The estimation is performed by choosing a linear discriminator based on the ratio histogram for the full data set and temporarily classifying pulses above the curve as neutrons and pulses below the curve as photons. The temporary neutron and photon clusters can then be fit with separate second order polynomials that reasonably estimate where the Gaussian means will be located in a slice's ratio histogram. An example of these fits can be seen in Figure B.2. It is important to note that the estimates of the Gaussian means derived from the quadratic fits will only be used as input parameters to bound the search region and accelerate the fitting routine. These estimated means are not the same as means used for defining the Gaussians, b_γ and b_n, which are determined by the fitting routine.

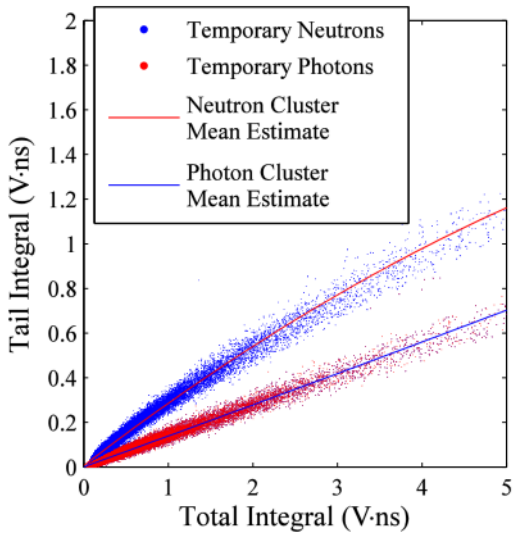

Figure B.2. Temporary classification of particles into neutrons and photons based on the linear discriminator chosen by the pre-fitting algorithm. The curves show the second-order polynomials that have been fit to each cluster in an attempt to estimate the means of the Gaussian fits during the slice-fitting algorithm.

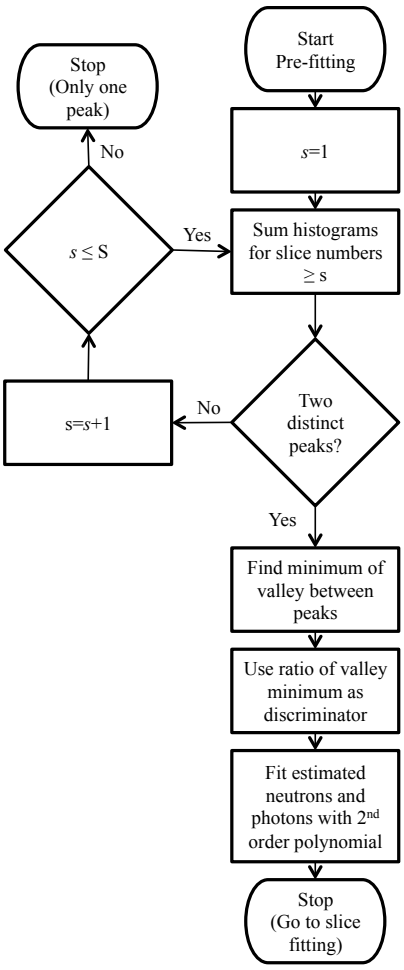

Figure B.3. Flowchart describing the pre-fitting algorithm, which is used to find reasonable estimates for the means of the Gaussian fits that will be computed during the slice-fitting algorithm.

The linear discriminator is found by computing an integral-ratio histogram for the full data set and using a peak finding routine to find the valley minimum located between the neutron and photon peaks. If the peak finding routine does not identify two well-defined peaks, the pulses from lowest slice number are removed and the ratio histogram is recomputed. This process is repeated until either two peaks are identified or all slices have been removed. In the latter case, the fitting process ends and an error is generated stating that two data clusters could not be found. A flowchart detailing the operation of the pre-fitting algorithm is shown in Figure B.3. In this flowchart, *s* represents the current slice number and *S* represents the total number of slices.

B.4.2 Slice-fitting Algorithm

The slice-fitting algorithm functions very similarly on each slice. The first step is to compute the estimated Gaussian means for the slice by finding where the previously computed photon and neutron cluster fits intercept the centerline of the slice and calculating the corresponding ratios. These values will be referred to as $\tilde{b}_\gamma$ and $\tilde{b}_n$, respectively. The MATLAB fitting routine is then invoked using upper bounds, lower bounds, and start points for the Gaussian means based on the expected means. The quality of the fit is assessed using the coefficient of determination, R^2, which is defined as the ratio of the sum of squares of the fit about the mean and the sum of squares of the data about the mean. The R^2 of the fit is checked against a threshold value of 0.95, below which the fit is not reliable for use in determining the optimal discrimination point. If the fit is deemed to be inaccurate, the slice histogram is refit using parameter constraints and start points based on the parameters of the nearest slice that has been previously fit. If the quality of the fit is still poor, the slice histogram is fit a third time using only a non-negativity constraint on the six parameters. If the starting slice must be refit, only the second refitting step is used because no other slice information is available. If either refitting step is utilized, the fit with the highest R^2 value is kept, regardless of whether it falls above or below the threshold.[5]

The parameters being fed to the fitting routine for the initial fit in each slice vary slightly depending on where along the clusters the slice is located. The four location categories that

[5] Fits with an R^2 value below the threshold typically occur at relatively high total-integral values where the low number of counts makes it difficult to achieve a statistically sound fit. The fits for these slices are kept because the separation of the clusters allows for fits that provide acceptable representations of both the neutron and photon peaks in spite of the associated R^2 values. While any slice's contribution to the discrimination curve can be removed by the user, the fits of every slice will be used when computing misclassification.

a slice can fall into are the starting slice, the slice immediately above the starting slice, slices where the clusters have completely overlapped and could be misconstrued as a single peak, and all other slices. The third region will be referred to as the "single-mean region" and may or may not exist, depending on the data set.

The starting slice is chosen to be the slice closest to 10% of the total number of slices. This percentage value was selected because it is typically high enough to be in the range of reasonably well-separated clusters while still being low enough to contain enough counts for reliable fitting. While this value is currently hard coded at 10%, it is worth noting that future revisions of the code could automatically find a suitable starting slice.

Existence of a single-mean region is triggered if a slice is found in which the falling edge of the photon fit crosses the half maximum of the neutron fit at a ratio larger than mean of the neutron fit. All slices below an existing trigger slice will be considered to be in the single-mean region. An example of a slice that would trigger the single-mean region can be seen in Figure B.4. In this slice, the photon fit evaluates to 283, which is the half-maximum of the neutron fit, at a ratio of approximately 0.287. This ratio is greater than the ratio of the neutron mean, which occurs at 0.169.

All slices bound the fit amplitudes, a_γ and a_n, by 0 and the total number of pulses in the slice. Additionally, all slices bound the widths, c_γ and c_n, by 0 and 0.5, which prevents unrealistically wide fits. For slices outside of the single-mean region, the fit means, b_γ and b_n, are restricted to fall between ±25% of $\tilde{b}_\gamma$ and $\tilde{b}_n$, respectively. If the slice is within the single-mean region, b_γ is allowed to range between 0 and 125% of $\tilde{b}_\gamma$, which allows for the photon

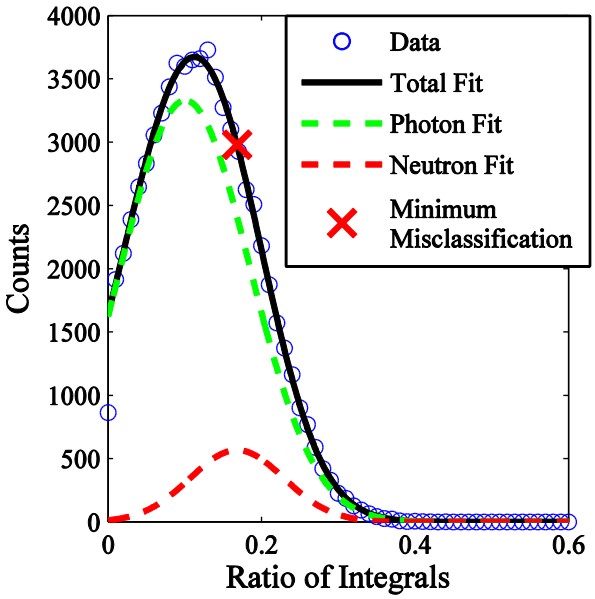

Figure B.4. Example of a slice in the single-mean region. In this slice, it is clear that the photon fit does not fall below the half-maximum of the neutron fit until well after the mean of the neutron fit. Error bars on the individual data points are not shown because they would be smaller than the data points themselves

fit to capture the low ratio pulses found in the early slices. Alternatively, b_n in the single-mean region must fall between 50% and 110% of b_n from the above slice. The estimated mean, $\tilde{b}_n$ is not used in the single-mean region because the quadratic fit used is not able to capture the rapid decrease in ratio of the neutron cluster. The asymmetric window around b_n is used to encourage the mean to move towards lower ratio values. Neither of the aforementioned refitting steps is used in the single-mean region due to the unique fitting parameters required for these slices.

The fit routine is generally provided an initial guess for each of the six parameters to encourage accurate and efficient fitting. The initial guesses for the peak amplitudes are equal to the amplitudes of the previously fit slice scaled by the ratio of the number of pulses contained in each slice. The initial guesses for the means are $\tilde{b}_\gamma$ and $\tilde{b}_n$ unless the slice is in the single-mean region where the initial guess for both means is $\tilde{b}_\gamma$. The initial guesses for

the width parameters are the widths from the previously fit slice. The slice immediately above the starting slice differs from most slices in that it uses information from the starting slice rather than the most recently fit slice (which would be slice 1). Initial guesses are not fed to the starting slice or to any slice that follows a slice with an $R^2 < 0.95$.

Figure B.5 shows the flowchart for the fitting algorithm. In this flowchart, s is a vector containing the slice processing order, S is the total number of slices, and i is a counter that can hold integer values between 1 and S. This notation varies slightly from the rest of this appendix in that $s[i]$ (rather than s) denotes the number of the slice currently being processed. Additionally, s_0 is the starting slice, $N^{(s[i])}$ is the number of pulses in slice $s[i]$, and $w^{(s[i])}$ and $d^{(s[i])}$ are related to the weighting of the slice and are defined in Section B.6.

The fitting algorithm described leads to reliable fits throughout all regions of the data, even in the presence of overlap. Figure B.6 shows a progression of slice fits through the overlapping region of the sample data set shown in Figure B.2. The histograms being fit come from slices that have a slope of -6 and a width of 0.025 V·ns, which is narrower than the width of the slices shown in Figure B.1 (a). The 'X' shown in each histogram marks the optimal discrimination point, which will be described further in Section B.5. Each of the six fits shown have an $R^2>0.999$ for the full histogram. It is important to note that while all of the slices shown have between approximately 75,000 and 150,000 counts, fits with an $R^2>0.990$ can be consistently obtained for slices with more than approximately 500 counts, and usable fits can be obtained for slices with approximately 100 counts. The ability to accurately fit slices

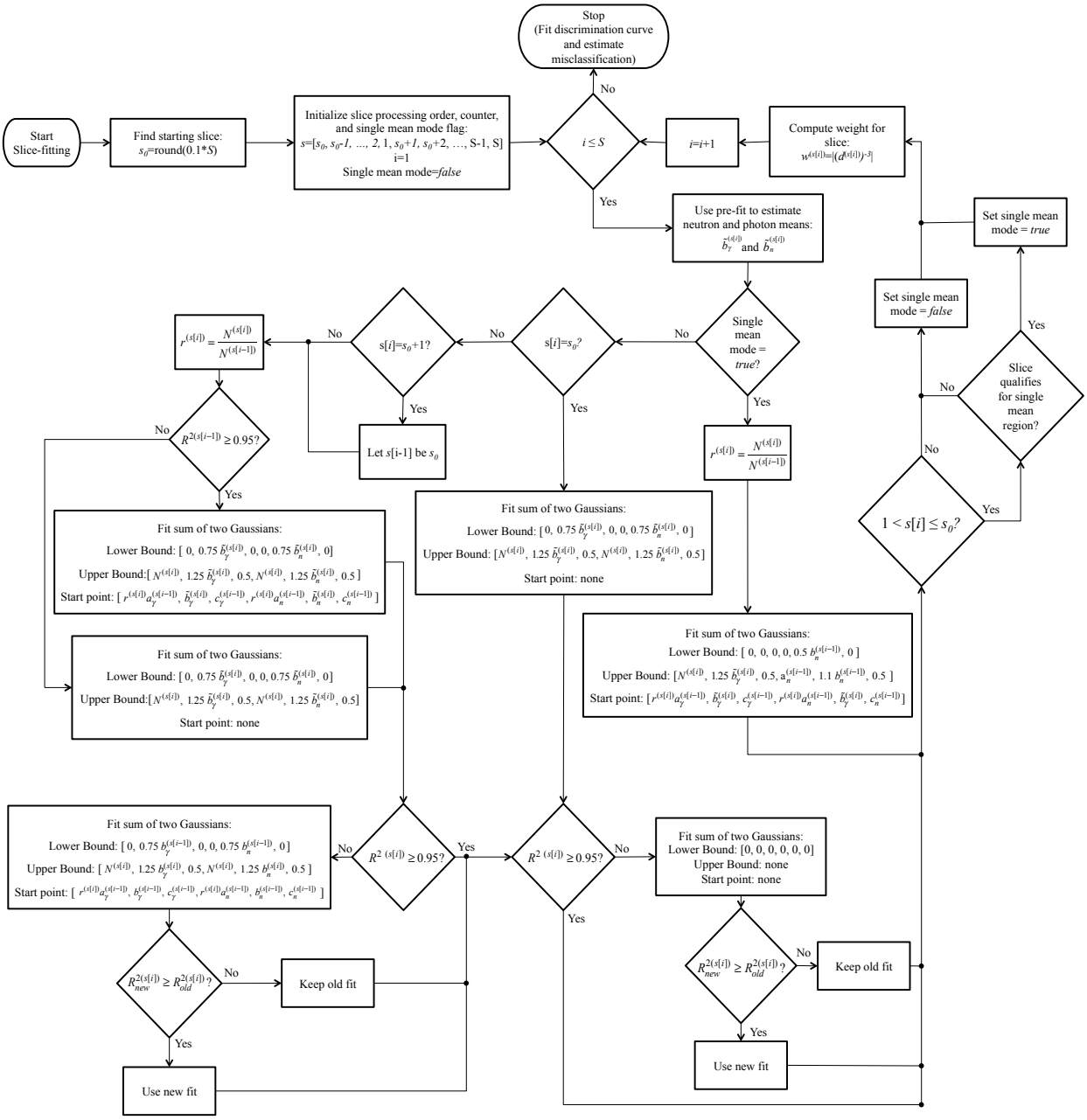

Figure B.5. Flowchart describing the operation of the slice-fitting algorithm.

with a low number of counts is a result of the previously known fit data being passed forward to each new slice. Therefore, the slice widths should be adjusted such that the starting slice contains on the order of one thousand counts, which will allow the fitting algorithm to begin with a reliably fit slice.

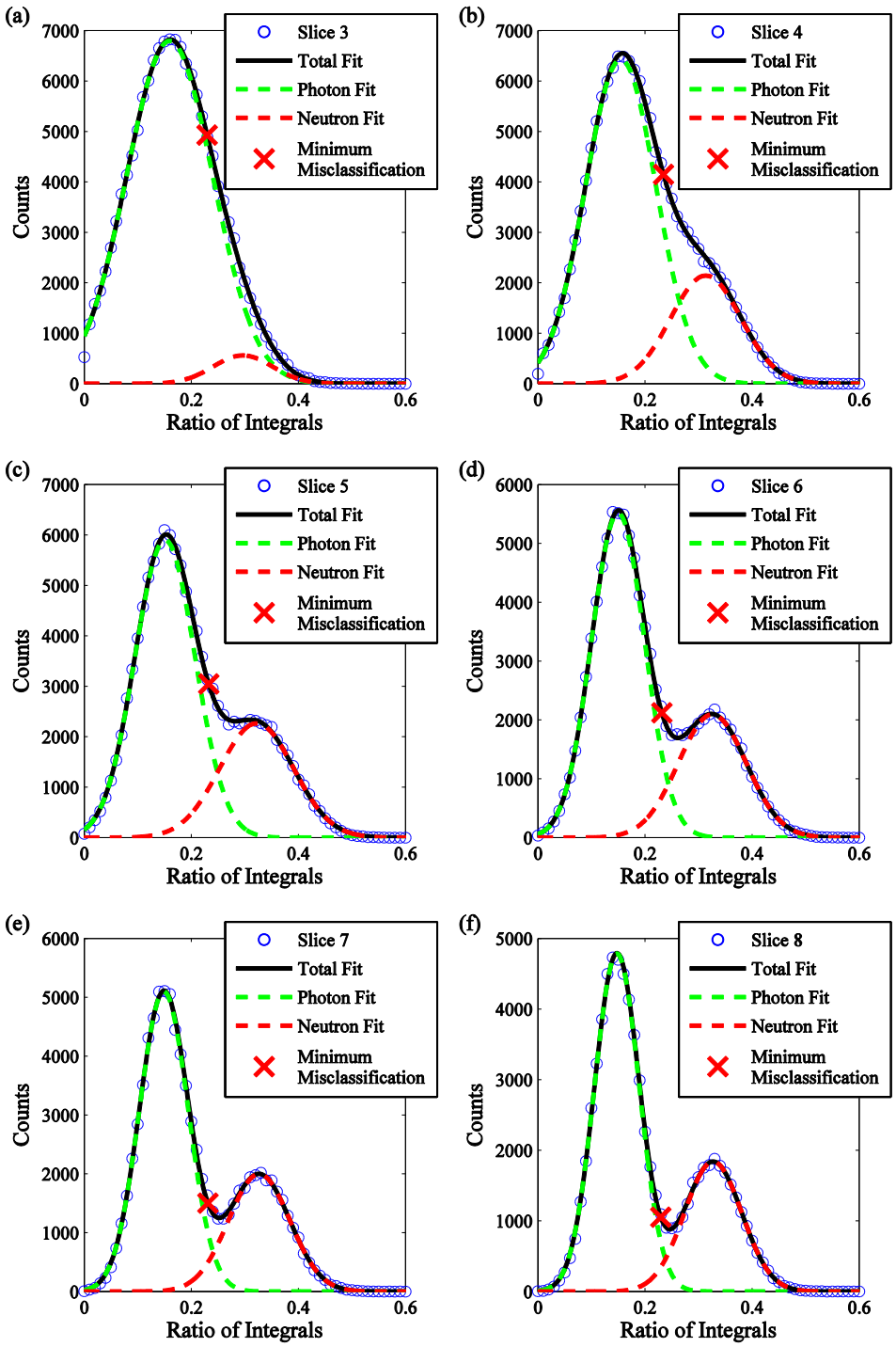

Figure B.6. Six slice histograms from the low-energy-deposition region of a tail-integral-vs.-total-integral scatter plot. Fits are shown for the full histogram (sum of two Gaussians) as well as for individual photon and neutron clusters (individual Gaussians). The 'X' marks the optimal discrimination point derived from analyzing the fits. All six full-histogram fits have an R^2>0.999. Error bars on the individual data points are not shown because they would be smaller than the data points themselves.

B.5. Choosing the Discrimination Points

The Auto Slice PSD algorithm uses the fit data to determine the optimal discrimination point within each slice, which is defined as the ratio that minimizes particle misclassification while accounting for any bias or normalization desired by the user. This ratio, $x_{opt,}$ is found by solving

$$x_{opt} = \underset{x\in[0,1]}{\arg\min} \left(\frac{k_\gamma}{M_\gamma} \int_x^1 a_\gamma e^{-\left(\frac{x'-b_\gamma}{c_\gamma}\right)^2} dx' + \frac{k_n}{M_n} \int_0^x a_n e^{-\left(\frac{x'-b_n}{c_n}\right)^2} dx' \right) \quad \text{(B.1)},$$

where M_γ and M_n are normalization factors, k_γ and k_n are bias parameters, and the remaining parameters are given by the fitting routine. The normalization factors and bias parameters will be described in the following paragraphs. The first integral in Equation (B.1) computes the portion of the photon fit that will be misclassified when setting x as the discrimination point and the second integral computes the portion of the neutron fit that will be misclassified.

The normalization factors can be set either to unity (for the unnormalized case) or to

$$M_j = \int_0^1 a_j e^{-\left(\frac{x-b_j}{c_j}\right)^2} dx, \; j = \gamma, n \quad \text{(B.2)}.$$

The unnormalized case will compute the optimal discrimination point by finding the ratio that misclassifies the smallest number of particles in the slice. However, if the data set contains an overwhelming number of pulses from one type of particle, the unnormalized minimization could result in a discrimination point that misclassifies a large percentage of the less prevalent particle. In the extreme case, where the fit of the less prevalent particle is strictly less than the fit of the more prevalent particle for all ratios, the discrimination point would misclassify all of the less prevalent particles. In some scenarios it may be desirable to

account for the imbalance in particle types, which is accomplished by utilizing the normalization factors from Equation (B.2). These normalization factors are the integral of each fit over the total range of possible tail-to-total-integral ratios, [0,1]. Using these factors allows for the minimization step in Equation (B.1) to equally penalize the misclassification of each particle type.

In some applications, it may also be advantageous to tune the weighting of each particle type to accomplish a specific goal. Particle weighting can be accomplished by using the bias parameters, k_γ and k_n, to adjust the penalization ratio during the minimization step. For example, if it is important to accurately detect neutrons, k_n could be increased such that it is more penalizing to misclassify neutrons than photons. Of course, increasing k_n would result in an increase of misclassified photons because optimal discrimination point would be pushed towards 0. The bias parameters can be used to find the appropriate balance between neutron and photon misclassification for a given application.

B.6. Fitting a Discrimination Curve and Estimating Particle Misclassification

Once a discrimination point has been chosen for each slice, the corresponding tail and total integral values are found by mapping the ratios to the midlines of the slice. A discrimination curve can be fit through the points on the tail-integral-vs.-total-integral scatter plot. This discriminator can take on a variety of forms including linear, quadratic, and two-function; a two-function discriminator is a combination of a quadratic curve in the low-energy-deposition region and a linear discriminator in the high-energy deposition region. During the fitting of the discrimination curve, each slice is assigned a weighting parameter,

$$w^{(s)} = \left|\left(d^{(s)}\right)^{-3}\right| \quad \text{(B.3)},$$

where $d^{(s)}$ is the Euclidean distance between the cluster means on the tail-integral-vs.-total-integral scatter plot. The exponent in Equation (B.3) was chosen to be negative to give higher importance to slices in which the data clusters are relatively close or overlapping. The magnitude of the exponent was chosen heuristically by assessing the tightness of the fit in the low-energy-deposition region over several data sets. This weighting parameter encourages a tighter fit in the overlapping region at the expense of allowing more freedom in regions of good separation. This tradeoff is acceptable because an inaccurate fit in the overlapping region can significantly impact misclassification, while an inaccurate fit in regions of good separation will have a negligible impact.

After the discrimination curve has been determined, it is possible to estimate the aggregate detection and misclassification ratios. Because the discrimination curve has been fit through the discrimination points, the true discrimination ratio may not be equivalent to the optimal discrimination ratio found during the minimization procedure. The true discrimination ratios can be determined by finding where the fit crosses the midline of each slice. The integral ratio associated with each of these intersection points will be denoted as $x^{\dagger(s)}$. Then, for a particular slice s, the following values can be computed:

$$\hat{p}_t^{(s)} = \int_0^1 a_\gamma^{(s)} e^{-\left(\frac{x-b_\gamma^{(s)}}{c_\gamma^{(s)}}\right)^2} dx \quad \text{(B.4)},$$

$$\hat{p}_d^{(s)} = \int_0^{x^{\dagger(s)}} a_\gamma^{(s)} e^{-\left(\frac{x-b_\gamma^{(s)}}{c_\gamma^{(s)}}\right)^2} dx \quad \text{(B.5)},$$

$$\hat{p}_m^{(s)} = \int_{x^{\dagger(s)}}^1 a_\gamma^{(s)} e^{-\left(\frac{x-b_\gamma^{(s)}}{c_\gamma^{(s)}}\right)^2} dx = \hat{p}_t^{(s)} - \hat{p}_d^{(s)} \quad \text{(B.6)},$$

$$\hat{n}_t^{(s)} = \int_0^1 a_n^{(s)} e^{-\left(\frac{x-b_n^{(s)}}{c_n^{(s)}}\right)^2} dx \quad \text{(B.7)},$$

$$\hat{n}_d^{(s)} = \int_{x^{\dagger(s)}}^{1} a_n^{(s)} e^{-\left(\frac{x-b_n^{(s)}}{c_n^{(s)}}\right)^2} dx \quad \text{(B.8)},$$

$$\hat{n}_m^{(s)} = \int_{0}^{x^{\dagger(s)}} a_n^{(s)} e^{-\left(\frac{x-b_n^{(s)}}{c_n^{(s)}}\right)^2} dx = \hat{n}_t^{(s)} - \hat{n}_d^{(s)} \quad \text{(B.9)},$$

where Equation (B.4) estimates the total number of photons in slice *s*, Equation (B.5) estimates the number of detected photons in slice *s*, Equation (B.6) estimates the number of misclassified photons in slice *s*, and Equation (B.7) through Equation (B.9) compute the same values for neutrons. Using these values, the aggregate software-estimated detection and misclassification ratios are defined as:

$$\hat{p}_d = \frac{\sum_s \hat{p}_d^{(s)}}{\sum_s \hat{p}_t^{(s)}} \quad \text{(B.10)},$$

$$\hat{p}_m = \frac{\sum_s \hat{p}_m^{(s)}}{\sum_s \hat{p}_t^{(s)}} \quad \text{(B.11)},$$

$$\hat{n}_d = \frac{\sum_s \hat{n}_d^{(s)}}{\sum_s \hat{n}_t^{(s)}} \quad \text{(B.12)},$$

$$\hat{n}_m = \frac{\sum_s \hat{n}_m^{(s)}}{\sum_s \hat{n}_t^{(s)}} \quad \text{(B.13)}.$$

Appendix C. System Matrix Simulation

C.1. MCNPX-PoliMi Input Deck

The following pages contain the MCNPX-PoliMi input deck used to simulate the system matrix used in this work. Both neutron and photon energy distributions are shown; however, the neutron energy distribution has been commented out. The file will run, as is, for photons and can be altered to simulate neutrons by changing the particle type to `par=1` and changing which energy distribution (`SI4`) is in use. The input deck must be run using a modified version of MCNPX-PoliMi, which can be found in Section C.3

```
twoPlane_0_15_25_30 photon hemi system matrix
c Cell Card
c
995 3 -0.001225 -95 10 11 12 13 14
     #111 #112 #113 #114 #121 #122 #123 #124
     #131 #132 #133 #134 #141 #142 #143 #144
     #411 #412 #413 #414 #421 #422 #423 #424
     #431 #432 #433 #434 #441 #442 #443 #444
     imp:n,p=1 $Air and source veto cell
996 3 -0.001225 -96 95 20 21 22 30 31 32
     #211 #212 #213 #214 #221 #222 #223 #224
     #511 #512 #513 #514 #521 #522 #523 #524
     #311 #312 #313 #314 #321 #322 #323 #324
     #611 #612 #613 #614 #621 #622 #623 #624
     #711 #712 #713 #714 #721 #722 #723 #724
     #731 #732 #733 #734 #741 #742 #743 #744
     #811 #812 #813 #814 #821 #822 #823 #824
     imp:n,p=1 $Air
999 0 96 imp:n,p=0
c
c Front plane liquid
111 1 -0.964 -10 13 14 imp:n,p=1
112 like 111 but trcl=112
113 like 111 but trcl=113
114 like 111 but trcl=114
121 like 111 but trcl=121
122 like 111 but trcl=122
123 like 111 but trcl=123
124 like 111 but trcl=124
131 like 111 but trcl=131
132 like 111 but trcl=132
133 like 111 but trcl=133
134 like 111 but trcl=134
141 like 111 but trcl=141
142 like 111 but trcl=142
143 like 111 but trcl=143
144 like 111 but trcl=144
c
c Front plane PMT
411 4 -0.51498 -12:-11 imp:n,p=1
412 like 411 but trcl=112
413 like 411 but trcl=113
414 like 411 but trcl=114
421 like 411 but trcl=121
422 like 411 but trcl=122
423 like 411 but trcl=123
424 like 411 but trcl=124
431 like 411 but trcl=131
432 like 411 but trcl=132
433 like 411 but trcl=133
434 like 411 but trcl=134
441 like 411 but trcl=141
442 like 411 but trcl=142
443 like 411 but trcl=143
444 like 411 but trcl=144
c
c Back plane liquid
211 1 -0.964 -20 23 24 imp:n,p=1
212 like 211 but trcl=213
213 like 211 but trcl=222
214 like 211 but trcl=224
221 like 211 but trcl=231
222 like 211 but trcl=233
223 like 211 but trcl=242
224 like 211 but trcl=244
c
```

```
c Back plane Liquid PMT
511 4 -0.51498 -22:-21 imp:n,p=1
512 like 511 but trcl=213
513 like 511 but trcl=222
514 like 511 but trcl=224
521 like 511 but trcl=231
522 like 511 but trcl=233
523 like 511 but trcl=242
524 like 511 but trcl=244
c
c Back plane NaI
311 2 -3.67 -30 imp:n,p=1
312 like 311 but trcl=314
313 like 311 but trcl=321
314 like 311 but trcl=323
321 like 311 but trcl=332
322 like 311 but trcl=334
323 like 311 but trcl=341
324 like 311 but trcl=343
c
c Back plane Liquid PMT
611 4 -0.51498 -32:-31 imp:n,p=1
612 like 611 but trcl=314
613 like 611 but trcl=321
614 like 611 but trcl=323
621 like 611 but trcl=332
622 like 611 but trcl=334
623 like 611 but trcl=341
624 like 611 but trcl=343
c
c Front plane Liquid Window
711 8 -2.51 -13:-14 imp:n,p=1
712 like 711 but trcl=112
713 like 711 but trcl=113
714 like 711 but trcl=114
721 like 711 but trcl=121
722 like 711 but trcl=122
723 like 711 but trcl=123
724 like 711 but trcl=124
731 like 711 but trcl=131
732 like 711 but trcl=132
733 like 711 but trcl=133
734 like 711 but trcl=134
741 like 711 but trcl=141
742 like 711 but trcl=142
743 like 711 but trcl=143
744 like 711 but trcl=144
c
c Back Plane Liquid Window
811 8 -2.51 -23:-24 imp:n,p=1
812 like 811 but trcl=213
813 like 811 but trcl=222
814 like 811 but trcl=224
821 like 811 but trcl=231
822 like 811 but trcl=233
823 like 811 but trcl=242
824 like 811 but trcl=244
c Blank line follows

c Surface Card
c Front plane Liquid
10  RCC -22.5 0.0 22.5    0.0 -6.3 0.0   3.81
c Front plane PMT Thick
11  RCC -22.5 0.635 22.5  0.0  6.5 0.0   3.81
c Front plane PMT skinny
12  RCC -22.5 7.135 22.5  0.0 17.2 0.0   2.94
c Front plane window thick
13  RCC -22.5 0.0 22.5   0.0 -1.2 0.0   3.25
c Front plane window skinny
14  RCC -22.5 0.0 22.5   0.0 0.635 0.0  3.9075
c
c Back Liquid scintillator
20  RCC -37.5 -36.3 37.5   0.0 -9.2 0.0    3.81
c Back PMT thick
21  RCC -37.5 -46.135 37.5  0.0 -6.5 0.0   3.81
c Back PMT skinny
22  RCC -37.5 -52.635 37.5  0.0 -17.2 0.0  2.94
c Back plane window thick
23  RCC -37.5 -45.5   37.5  0.0  1.6  0.0  3.25
c Back plane window skinny
24  RCC -37.5 -46.135 37.5 0.0 0.635 0.0 3.9075
c
c NaI scintillator
30  RCC -12.5 -38.2  37.5  0.0 -7.62 0.0   3.81
c Front part of NaI PMT
31  RCC -12.5 -45.82 37.5  0.0  4    0.0   3.81
c Back part of NaI PMT
32  RCC -12.5 -49.82 37.5  0.0 -14   0.0   2.94
c
c Source cell rejection to create hemisphere
95  RCC 0 -21.3 0 0 501 0 501
c
c Bounding sphere
96  SO 10000
c
c Blank Line Follows

c Data Card
mode n p
dbcn 12j 25000 $Stride shortened
PRDMP 2j 1
nps 300000000   $ Flat source for ~even stats
print    10 40 50 100 110 126 140
c
c ======Source========
c
sdef par=2            $Photons only
     pos= 0 -21.3 0   $System center
     RAD=200          $200 cm radius
     CEL=995          $only half of sphere
     ERG=D4           $use weighted erg dist
     vec= 0 0 1       $dummy sampling vector
     tme=d5 dir=d6
c
c Arbitrarily large time to reduce accidentals
SI5 0 9431195908872
SP5 0 1
c
SI6 0.923955 1
SP6 0 1
c
c Photon energies weighted in 50 keV bins
SI4  H 0.0 0.05  0.10  0.15  0.20  0.25
           0.30  0.35  0.40  0.45  0.50
           0.55  0.60  0.65  0.70  0.75
           0.80  0.85  0.90  0.95  1.00
           1.05  1.10  1.15  1.20  1.25
           1.30  1.35  1.40  1.45  1.50
           1.55  1.60  1.65  1.70  1.75
           1.80  1.85  1.90  1.95  2.00
           2.05  2.10  2.15  2.20  2.25
           2.30  2.35  2.40  2.45  2.50
           2.55  2.60  2.65  2.70  2.75
           2.80  2.85  2.90  2.95  3.00
           3.05  3.10  3.15  3.20  3.25
           3.30  3.35  3.40  3.45  3.50
           3.55  3.60  3.65  3.70  3.75
           3.80  3.85  3.90  3.95  4.00
```

```
           4.05  4.10  4.15  4.20  4.25
           4.30  4.35  4.40  4.45  4.50
           4.55  4.60  4.65  4.70  4.75
           4.80  4.85  4.90  4.95  5.00
SP4 D 0.0  0.0000 0.0133 0.0073 0.0057 0.0051
           0.0050 0.0048 0.0049 0.0046 0.0048
           0.0049 0.0048 0.0051 0.0050 0.0051
           0.0051 0.0053 0.0054 0.0057 0.0054
           0.0056 0.0058 0.0059 0.0061 0.0063
           0.0062 0.0062 0.0061 0.0063 0.0065
           0.0061 0.0067 0.0065 0.0067 0.0069
           0.0066 0.0071 0.0068 0.0073 0.0070
           0.0074 0.0070 0.0074 0.0071 0.0071
           0.0072 0.0073 0.0072 0.0077 0.0075
           0.0077 0.0076 0.0075 0.0072 0.0073
           0.0077 0.0074 0.0074 0.0075 0.0074
           0.0076 0.0073 0.0075 0.0077 0.0078
           0.0078 0.0077 0.0078 0.0084 0.0084
           0.0086 0.0091 0.0090 0.0092 0.0103
           0.0107 0.0107 0.0116 0.0116 0.0131
           0.0140 0.0149 0.0141 0.0147 0.0190
           0.0187 0.0195 0.0197 0.0181 0.0228
           0.0246 0.0228 0.0274 0.0242 0.0253
           0.0245 0.0258 0.0289 0.0287 0.0265
c
c Neutron energies weighted in 250 keV bins
c SI4  H 0.0 0.25  0.5   0.75  1
c          1.25  1.5   1.75  2
c          2.25  2.5   2.75  3
c          3.25  3.5   3.75  4
c          4.25  4.5   4.75  5
c          5.25  5.5   5.75  6
c          6.25  6.5   6.75  7
c          7.25  7.5   7.75  8
c          8.25  8.5   8.75  9
c          9.25  9.5   9.75  10
c SP4 D 0.0 0.0000  0.0725    0.0329    0.0233
c          0.0184  0.0170    0.0164    0.0155
c          0.0161  0.0157    0.0153    0.0162
c          0.0167  0.0176    0.0167    0.0169
c          0.0179  0.0182    0.0196    0.0207
c          0.0208  0.0208    0.0215    0.0210
c          0.0226  0.0242    0.0240    0.0247
c          0.0246  0.0257    0.0266    0.0262
c          0.0306  0.0317    0.0347    0.0377
c          0.0401  0.0442    0.0458    0.0489
c
c ======Materials=======
c
c Liquid Scintillator
m1   NLIB=70c PLIB=04p
      1001   0.555443       $H
      6012.50c   0.444557   $C
c
c NaI Scintillator
m2   NLIB=70c PLIB=04p
     11023  -0.153373       $Na
     53127  -0.846627       $I
c
c Air
m3    NLIB=70c PLIB=04p
      7014  -0.755636       $N
      8016  -0.231475       $O
     18040 -0.012838        $Ar-40 at 99.6035%
     18036 -0.000043        $Ar-36 at 0.3336%
     18038 -0.000008        $Ar-38 at 0.00629%
c
c Homogenized PMT
m4   NLIB=70c PLIB=04p
     14000.60c  -0.0933168  $Si
      8016  -0.1312437      $O
      5010  -0.006402       $B at 19.9% B-10
      5011  -0.001590       $B at 81.1% B-11
     11023  -0.0096386      $Na
     13027  -0.0040993      $Al
     26000.50c  -0.2481451  $Fe
     28000.50c  -0.5049603  $Ni
      7014  -0.0005934      $N
     18040 -1.008186e-5     $Ar-40 at 99.6035%
     18036 -3.376699e-8     $Ar-36 at 0.3336%
     18038 -6.366738e-9     $AR-38 at 0.00629%
c
c Polyethylene
m5   NLIB=70c PLIB=04p
      1001   -0.14371       $H
      6012.50c   -0.856284  $C
c
c Lead
m6 NLIB=70c PLIB=04p
     82000.50c -1.0         $Pb
c
c Polystyrene
m7 NLIB=70c PLIB=04p
      1001      0.499994    $H
      6012.50c  0.500006    $C
c
c BK7
m8    NLIB=70c PLIB=04p
     14028 -0.323138999     $Si
      8016  -0.483882614    $O
      5010 -0.00664357  $B at 19.9% B-10
      5011 -0.02674123  $B at 81.1% B-11
     56138 -0.027496631     $Ba
     11023 -0.077153875     $Na
     19039 -0.052216449     $K
     33075 -0.002726626     $As
c
c ========Translations========
c
c Front Plane Translations
tr112 15   0.0  0.0
tr113 30   0.0  0.0
tr114 45   0.0  0.0
tr121 0.0   0.0 -15
tr122 15   0.0 -15
tr123 30   0.0 -15
tr124 45   0.0 -15
tr131 0.0   0.0 -30
tr132 15   0.0 -30
tr133 30   0.0 -30
tr134 45   0.0 -30
tr141 0.0   0.0 -45
tr142 15   0.0 -45
tr143 30   0.0 -45
tr144 45   0.0 -45
c
c Back Plane Liquid Translations
tr213  50   0.0   0.0
tr222  25   0.0  -25
tr224  75   0.0  -25
tr231  0.0   0.0  -50
tr233  50   0.0  -50
tr242  25   0.0  -75
tr244  75   0.0  -75
c
c Back Plane NaI Translations
tr314  50   0.0    0.0
tr321 -25   0.0   -25
```

```
tr323  25   0.0   -25
tr332  0.0   0.0   -50
tr334  50   0.0   -50
tr341 -25   0.0   -75
tr343  25   0.0   -75
c
c =======Tallies============
c
c ======Advanced Options=========
c
c PHYS:P 10 0 0 0 1
c EMCPF: Upper Energy Limit for Detailed Phys
c IDES:  Electron Production by Photons 0/1:
c     will produce e- in MODE E or Brem photons
c     in the case of a thick target brem
c     model/will not as per
c NOCOH: Coherent Scattering 0/1:will/will not
c ISPN:  Photonuclear Reactions 1/0/-1
c     biased/none/analog
c NODOP: Doppler Broadening 0/1:will/will not
c
PHYS:N J 20
c
CUT:P 2J 0
c Time - Lower Energy Cutoff - Weight
c
Cut:N 2J 0
c
c =========PoliMi Options==========
c
IPOL 0 1 1 1 J 2 88
               111 112 113 114 121 122 123 124
               131 132 133 134 141 142 143 144
               411 412 413 414 421 422 423 424
               431 432 433 434 441 442 443 444
               211 212 213 214 221 222 223 224
               511 512 513 514 521 522 523 524
               311 312 313 314 321 322 323 324
               611 612 613 614 621 622 623 624
               711 712 713 714 721 722 723 724
               731 732 733 734 741 742 743 744
               811 812 813 814 821 822 823 824
c
c (1) Neutron-photon source type, with correct
c     multiplicity
c (2) Neutrons from induced fission
c (3) Photon correlation
c (4) Time delay in photon emission following a
c     fission event
c (5) Not used
c (6) Collisions print out only for histories
c     with events giving energy
c     released in at least N det cells
c (7) Number of cells for which collision data
c     printout is required
c (8) Cell numbers for collision data printout
c
RPOL J 2e-3
c (1) neutron rxn energy cutoff
c (2) photon Rxn energy cutoff
c print data. print birth info to extra files
FILES 21 DUMN1 13j 1 neutrons.erg
```

C.2. MPPost Input Deck

The following pages contain the MPPost input deck used to process each seed in the system matrix simulation. It should be noted that many of the options included in this input do not apply to the system matrix simulation. Unused options include the MLEM related options listed in the “Imaging System” block, which apply to outdated system-matrix computation methods.

```
# ~~~
```

```
# ~~~~~~~~~~~~~~~~~~~~~~~~~~~~~~~~~~~~~~~~~~~~~~~~~~~~~~~~~~~~~~~~~~~~~~~~~~~~~~~~
# I/O FILE INFORMATION
# ~~~~~~~~~~~~~~~~~~~~~~~~~~~~~~~~~~~~~~~~~~~~~~~~~~~~~~~~~~~~~~~~~~~~~~~~~~~~~~~~
polimi_det_in           648_flat_scaled_neutron_500cm0.d     # MCNP-PoliMi detector filename
import_pulses            no          # If processing pulse list (from measurements or simulation)
turn to yes
output_file             test         # Desired output name
label_output            yes          # Place labels at the top of the output files
separate_det_response   yes          # Print individual distributions for each detector
list_of_pulses          no          # Print a list mode file of all collected pulses
incident_light          no          # Data written to list of pulses no = incident energy (MeV)
                                    #    yes = write the max potential LIGHT (MeVee)
event_inventory_on      no          # Print out a table summarizing all events in the file
collision_history       no          # Print summary of how collisions make pulses in the detector
time_file_on            no          # Use TIME file to obtain start times for each history
time_file_name                      # Name of the TIME file
overwrite_files         yes         # Allow the code to overwrite old files
comma_delimited         yes         # Output files delimited by a comma

# ~~~~~~~~~~~~~~~~~~~~~~~~~~~~~~~~~~~~~~~~~~~~~~~~~~~~~~~~~~~~~~~~~~~~~~~~~~~~~~~~
# MEMORY
# ~~~~~~~~~~~~~~~~~~~~~~~~~~~~~~~~~~~~~~~~~~~~~~~~~~~~~~~~~~~~~~~~~~~~~~~~~~~~~~~~
division_size   16000   # MB, size of segments to divide the file
cushion         200     # number of lines added to the arrays to prevent overstepping arrays

# ~~~~~~~~~~~~~~~~~~~~~~~~~~~~~~~~~~~~~~~~~~~~~~~~~~~~~~~~~~~~~~~~~~~~~~~~~~~~~~~~
# DETECTOR INFORMATION
# ~~~~~~~~~~~~~~~~~~~~~~~~~~~~~~~~~~~~~~~~~~~~~~~~~~~~~~~~~~~~~~~~~~~~~~~~~~~~~~~~
time_dependent          yes              # Perform analysis by time instead of by history
NPS                     1               # NPS used in the MCNP run
detector_type           1 1 4 0 0 0 0 0 0   # Type of Detector - list for each cell number
                                        #   0 = Non Active Volume (i.e. PMT)
                                        #   1 = Liquid Organic Scintillator
                                        #   2 = He3 (Cannot be run with other types)
                                        #   3 = Plastic Organic Scintillator
                                        #   4 = NaI
                                        #   5 = CaF2
                                        #   6 = LaBr3
threshold           0.02 0.02 0.02
# MeVee, Threshold for event detection - list for each cell number
upper_threshold     3.18 3.18 3.18
# MeVee, the max acceptable light for event detection - list for each cell number
detector_cell_numbers ( 111 112 113 114 121 122 123 124 131 132 133 134 141 142 143 144 ) &
                      ( 211 212 213 214 221 222 223 224 ) &
                      ( 311 312 313 314 321 322 323 324 ) &
                      ( 411 412 413 414 421 422 423 424 431 432 433 434 441 442 443 444 ) &
                      ( 511 512 513 514 521 522 523 524 ) &
                      ( 611 612 613 614 621 622 623 624 ) &
                      ( 711 712 713 714 721 722 723 724 731 732 733 734 741 742 743 744 ) &
                      ( 811 812 813 814 821 822 823 824 )
# Above are cell numbers of the detectors
#NOTE: To group cells add ( ) around the group. There must be a space before and after each (

# ~~~~~~~~~~~~~~~~~~~~~~~~~~~~~~~~~~~~~~~~~~~
# Capture Neutron Profile ( Works in CLYC cells)
# ~~~~~~~~~~~~~~~~~~~~~~~~~~~~~~~~~~~~~~~~~~~
ncp_on                          no
# yes/no, option to produce a phd based on the energy released in each capture
# (on automatically for clyc)
ncp_low                         0               # MeV, lower recorded neutron energy value
ncp_high                        5               # MeV, upper recorded neutron energy value
ncp_incr                        0.1             # MeV, bin width for recorded neutron energy values
capture_material        3007,5010
# List zaid for materials relevent caputre events can occur in, up to 10

# ~~~~~~~~~~~~~~~~~~~~~~~~~~~~~~~~~~~~~~~~~~~~~~~~~~~~~~~~~~~~~~~~~~~~~~~~~~~~~~~~
# DETECTOR INFORMATION - Pulse Height
# ~~~~~~~~~~~~~~~~~~~~~~~~~~~~~~~~~~~~~~~~~~~~~~~~~~~~~~~~~~~~~~~~~~~~~~~~~~~~~~~~
pulse_height_on     no                  # Print pulse height distributions
```

```
sum_then_light      no                  # Convert the sum of all contributing particles energy to
light
cross_talk_on       no                  # Eliminate histories with cross talk

# Pulse Generation Time - ns, Light collection time for a pulse
organic_liq_pgt     10
organic_pl_pgt      10
nai_pgt             10
caf2_pgt            10
labr3_pgt           10
clyc_pgt                      10

# Deadtime - ns, deadtime of the detector between pulses
organic_liq_dt       0
organic_pl_dt        0
nai_dt               0
caf2_dt              0
labr3_dt             0
clyc_dt                 0

histogram_start      0                  # MeVee, Min value for the pulse height distribution
histogram_stop      10                  # MeVee, Max value for the pulse height distribution
bin_step            0.01                # MeVee, Bin step - top side of the bin

# ~~~~~~~~~~~~~~~~~~~~~~~~~~~~~~~~~~~~
# ORGANIC SCINTILLATOR
# ~~~~~~~~~~~~~~~~~~~~~~~~~~~~~~~~~~~~
calibration_regions  1                                  # Number of independently fit neutron light
regions
region_type          3
# Specify which form for the coefficients, if multiple regions list selections
# Type    Form       How to enter values on the neutron_calibration line
                                                #   1 = Ax^2+Bx+C  -> E1 E2 A B C
                                                #   2 = Ax^2/(x+B) -> E1 E2 A B
                                                #   3 = A(Bx-C(1-exp(Dx^E)))  -> E1 E2 A B C D E
                                                   #  Where E1 and E2 are the lower and upper
energy bounds respectivly in MeVee
neutron_calibration  0 50 1  0.6682 1.625 -0.3866 1.05
#Neutron Calibration - see above for entry instructions
#For multiple regions add an '&' to the end of the line and continue next region on the next line
photon_calibration      1.000  0.000         # A,B: Parameters for photon light conversion - Ax+B
carbon_light_constant   0.02                # Constant value for carbon light conversion
deuterium_fit_type      2
# Specify which form for the coefficients for deuterium light conversion: 1 or 2
deuterium_calibration   1 0.74692 3.5522 -0.1977 1
                                              # Enter coefficients for chosen deuterium fit type
                                                #   1 = Ax^4+Bx^3+Cx^2+Dx+E  -> A B C D E
                                                #   2 = A(Bx-C(1-exp(Dx^E))) -> A B C D E
clyc_n_calib           .6465      # Constant value for light conversion for capture events in CLYC

# ~~~~~~~~~~~~~~~~~~~~~~~~~~~~~~~~~~~~
# Energy Resolution
# ~~~~~~~~~~~~~~~~~~~~~~~~~~~~~~~~~~~~
light_resolution_on       yes             # Turns on/off the a Gaussian Energy Broadening
organic_liq_p_lgt     9.8532 0 4738.66
# Coefficients A,B,C for Gaussian Broadening: A*LO+B*Sqrt(LO)+C
organic_liq_n_lgt     9.8532 0 4738.66
organic_pl_p_lgt      10.083 311.77 431.58
organic_pl_n_lgt      10.083 311.77 431.58
nai_lgt                                     # For Inorganics leave blank to use defaults
caf2_lgt                                    # or specify Coefficients as
labr3_low_lgt                      # Coefficients A,B,C for Gaussian Broadening: A*LO+B*Sqrt(LO)+C
labr3_high_lgt
clyc_lgt              3.6218  -79.1285  3092.1

# ~~~~~~~~~~~~~~~~~~~~~~~~~~~~~~~~~~~~
# Time Resolution
# ~~~~~~~~~~~~~~~~~~~~~~~~~~~~~~~~~~~~
tme_resolution_on   yes                  # Turns on time broadening
```

```
organic_liq_tme     1
organic_pl_tme      1
nai_tme             10
caf2_tme            24
labr3_tme           1
clyc_tme

# ~~~~~~~~~~~~~~~~~~~~~~~~~~~~~~~~~~~~~
# Voxels
# ~~~~~~~~~~~~~~~~~~~~~~~~~~~~~~~~~~~~~
cell_voxels_on  yes
cells_to_voxel          111        211     311              # Cell numbers that are to be voxeled
xVox           -30 15 30   -50 25 50   -50 25 50
yVox           -6.3 6.3 0.0   -45.5 9.2 -36.3   -45.82 7.62 -38.2
zVox           -30 15 30   -50 25 50   -50 25 50
# Start, step, max for voxelation
#for multiple cells repeat start,step,stop
#start1,step1,stop1,start2,step2,stop2

# ~~~~~~~~~~~~~~~~~~~~~~~~~~~~~~~~~~~~~~~~~~~~~~~~~~~~~~~~~~~~~~~~~~~~~~~~~~~~~~~~~~~~~~~~~~~~
# TIME-OF-FLIGHT, CORRELATION, and AUTOCORRELATION INFORMATION
# ~~~~~~~~~~~~~~~~~~~~~~~~~~~~~~~~~~~~~~~~~~~~~~~~~~~~~~~~~~~~~~~~~~~~~~~~~~~~~~~~~~~~~~~~~~~~
tof_on                  no      # yes/no, Turn on TOF distributions (cannot have a start detector)
cross_correlation_on    no      # yes/no, Turn on cross correlation function
auto_correlation_on     no      # yes/no, Turn on auto correlation function
start_detector          100     # Cell number of the start detector
time_start              -100.5
# ns, time for the correlation plot to start (NOTE: there has to be a decimal point, even if it is
#just 100.0)
time_stop               100.5
# ns, time for the correlation plot to stop (NOTE: there has to be a decimal point, even if it is
#just 100.0)
time_increment          1       # ns, time increment between the bins - top side of the bin
cc_window_incr         1000    # ns, time window for correlation events for time dependent analysis
# ~~~~~~~~~~~~~~~~~~~~~~~~~~~~~~~~~~~~~
# Pulse Height Correlation
# ~~~~~~~~~~~~~~~~~~~~~~~~~~~~~~~~~~~~~
pulse_correlation_on   no       # yes/no, turn on pulse height correlation analysis
pc_min                 0        # MeVee, Minimum value for pulse height binning
pc_max                 5        # MeVee, Maximum value for pulse height binning
pc_incr                0.05     # MeVee, increment for pulse height binning
stop_pulse_only        yes      # Ignore start detector pulse height
# ~~~~~~~~~~~~~~~~~~~~~~~~~~~~~~~~~~~~~
# CAPTURE GATED DETECTORS
# ~~~~~~~~~~~~~~~~~~~~~~~~~~~~~~~~~~~~~
capture_gate_on     no          # Run the capture gated detector response
cap_low             0           # ns, start time for binning the time to capture histogram
cap_high            2000        # ns, stop time for binning the time to capture histogram
cap_incr            10          # ns, bin size the time to capture histogram

# ~~~~~~~~~~~~~~~~~~~~~~~~~~~~~~~~~~~~~~~~~~~~~~~~~~~~~~~~~~~~~~~~~~~~~~~~~~~~~~~~~~~~~~~~~~~~
# IMAGING SYSTEM
# ~~~~~~~~~~~~~~~~~~~~~~~~~~~~~~~~~~~~~~~~~~~~~~~~~~~~~~~~~~~~~~~~~~~~~~~~~~~~~~~~~~~~~~~~~~~~
imaging_system_on  yes       # yes/no, turn on the imaging system
longdistance       yes       # yes/no, turn on long distance
window_front      5     # Time window used to discriminate double scatters in plane 1 for neutrons
                         # (implemented before and after the trigger)
window_start       5        # Start of time window used to correlate neutrons
window_end         100      # Time window used to correlate neutrons
window_gamma       25       # Time window used to correlate gammas
                            # (implemented before and after the trigger)
backprojection     no       # yes/no, run back projection algorithm
sphere_center      0 0 0    # X, Y, and Z coordinates of the center of the back projection sphere
sphere_radius      500      # Radius of the back projection sphere
sphere_mesh        2        # Degrees per mesh point
cone_thickness     2       # Thickness of the back projection cones
mlem_input_data    no      # yes/no, outputs data to use with MLEM algorithm
mlem_angle_bin     10      # Angle binning used for MLEM
p_emin            0       # Min cutoff energy in MeVee for back projection imaging photons & MLEM
```

```
p_ebin           0.05     # Energy Binning in MeVee for back projection imaging photons & MLEM
p_emax           6        # Max cutoff energy in MeVee for back projection imaging photons & MLEM
n_emin           0        # Min cutoff energy in MeVee for back projection imaging neutrons & MLEM
n_ebin             0.25  # Energy Binning in MeVee for back projection imaging neutrons & MLEM
n_emax            15     # Max cutoff energy in MeVee for back projection imaging neutrons & MLEM
uncertaintythickness no    # yes/no
distancecheck        no    # yes/no

# ~~~~~~~~~~~~~~~~~~~~~~~~~~~~~~~~~~~~~~~~~~~~~~~~~~~~~~~~~~~~~~~~~~~~~~~~~~~~~~~~~~~~~~~~~~~~
# He3 MODULE
# ~~~~~~~~~~~~~~~~~~~~~~~~~~~~~~~~~~~~~~~~~~~~~~~~~~~~~~~~~~~~~~~~~~~~~~~~~~~~~~~~~~~~~~~~~~~~
he3_multiplicity     no     # yes/no: Turn on the He3 module
number_of_windows    256    # Number of windows to evaluate
window_increment     16     # Window increment in microseconds
deadtime_type        1      # Control which model is applied for dead time
                            #   1 = Type I, applied to each tube only
                            #   2 = Type II, applied to each tube then fed into an amplifier
                            #   3 = Type III, AWCC style, detector, into amp, into OP amp
detector_deadtime    4      # Detector dead time in microseconds
amplifier_deadtime   0.5    # Level I amplifier dead time in microseconds
amp_2_deadtime       0.03   # Level II amplifier dead time in microseconds
max_multiplicity     500    # Maximum multiplicity expected (for array size handling)
trigger_type         1      # Control how the multiplicity windows are triggered
                            #   1 = Constant window
                            #   2 = Open on trigger (Reverse)
                            #   3 = Open on trigger (Forward)
pre_delay            4.5    # Predelay after event trigger in microseconds
long_delay           1024   # Delay between R+A window and A window in microseconds
run_time             105.33 # Time the source is distributed over in seconds
output_style         3      # Controls what data is printed to a file
                            #   1 = All multiplicity distributions + Feynman-Y + S,D,T
                            #   2 = Last multiplicity distribution + S,D,T rates
                            #   3 = Last multiplicity distribution + Mean, Variance, Feynman-Y
generation_analysis_on yes  # yes/no, analysis of the neutron generations captured
paralyzable         no      # yes/no, yes treats He-3 detectors as paralyzable, no treated as non-
paralyzable
# ~~~~~~~~~~~~~~~~~~~~~~~~~~~~~~~~~~~~~~
# Select Capture Event Type
# ~~~~~~~~~~~~~~~~~~~~~~~~~~~~~~~~~~~~~~
output_sort_file    no      # Print out a file with all sorted events
sort_ipt            1       # Particle type to sort by, set -1 to ignore
sort_nxs            2003    # Material of interaction to sort by, set to -1 to ignore
sort_ntyn           0       # Interaction type to sort by, set to -1 to ignore

# ~~~~~~~~~~~~~~~~~~~~~~~~~~~~~~~~~~~~~~~~~~~~~~~~~~~~~~~~~~~~~~~~~~~~~~~~~~~~~~~~~~~~~~~~~~~~
# Scintillator Multiplicity MODULE
# ~~~~~~~~~~~~~~~~~~~~~~~~~~~~~~~~~~~~~~~~~~~~~~~~~~~~~~~~~~~~~~~~~~~~~~~~~~~~~~~~~~~~~~~~~~~~
scint_mult          no      # Turn on Scintillator Multiplicity
neutrons_only       no      # Only process neutron multiplicities (i.e. np -> n and nnppp -> nn)
digitizer_window    480     # ns, Length of the digitizer window
digitizer_gap       16      # ns, Delay between successive digitizer windows
digitizer_end       220     # ns, Time at end of digitizer window where pulses are not seen
digitizer_lag       80      # ns, Time at the beginning of digitizer window before a pulse can be
seen
sm_dist_on          yes     # yes/no, Pulse height distributions for each multiplicity combination

# ~~~~~~~~~~~~~~~~~~~~~~~~~~~~~~~~~~~~~~~~~~~~~~~~~~~~~~~~~~~~~~~~~~~~~~~~~~~~~~~~~~~~~~~~~~~~
# Variance Reduction
# ~~~~~~~~~~~~~~~~~~~~~~~~~~~~~~~~~~~~~~~~~~~~~~~~~~~~~~~~~~~~~~~~~~~~~~~~~~~~~~~~~~~~~~~~~~~~
apply_weight        no     # yes/no, use the non-unity weights of particles
```

C.3. MCNPX-PoliMi Patch

The following pages contain the patch applied to MCNPX-PoliMi to create simulated system matrices. This patch allows for the initial direction of the source particle to be determined as a function of a randomly sampled position. The patch will sample the direction from a cone aligned with the positive the *z*-axis. The patch computes the rotation matrix required to rotate between the positive *z*-axis and the desired cone axis, which points between the initial position of the particle and center of the DPI. This matrix rotates the original sampled direction such that the particle is emitted towards the DPI. To use this patch, the `vec` flag in the MCNPX-PoliMi input deck must be set to `vec=0 0 1.` The opening angle of the cone is defined using the `dir` flag in the MCNPX-PoliMi input. The patch is included as a standalone file named "patch_startp.txt" and is applied during compilation of MCNPX-PoliMi.

```
*loc
/*sp6e        1*
*ins
cPoliMi
!!!!!!!!!!!!! same data in subroutines Startp, Collpn and Sournew !!!!!!!!!!!!!!
      parameter (nymax=50)                                                      !
      dimension int1sec(nymax), rea7sec(7,nymax)  !save data to print           !
      common /PNcommon/iter56,lwsav,eisav,e0sav,int1sec,rea7sec,y1,y2,ny        !
!!!!!!!!!!!!!!!!!!!!!!!!!!!!!!!!!!!!!!!!!!!!!!!!!!!!!!!!!!!!!!!!!!!!!!!!!!!!!!
      if(nps.eq.1) then
        iter56=0
        if(ipol(1).eq.-56 .and. ipol(5).gt.1) then
         print *,'startp ERROR: it is not allowed to perform a weighted'
     +          ,' phnuclear run with multiple loading ipol(5)=',ipol(5)
         stop
        endif
        if(rpol(6).ne.0 .and. ipol(1).lt.0) then
         print *,'startp ERROR: it is not allowed to perform a weighted'
     +          ,' phnuclear run with Delayed Neutrons ipol(1)=',ipol(1)
         stop
        endif
      endif
cPoliMi-END
*loc
/*sp         94*
*ins
cPoliMi
!   skip the energy check for PoliMi mixed source option ±99
      if(abs(ipol(1)).eq.99) goto 220
cPoliMi-END
!
```

```
    *loc
    /*sp        112*
    *ins
    cPoliMi
    *com
    *ins
      220 continue
          if(ipol(1).eq.0 .or. abs(ipol(1)).eq.54 .or.
         +   abs(ipol(1)).eq.56 .and. iter56.eq.0) then
          call gain_pax (igain_all_pls_source, ipt, 1, wgt, wgt*erg)
    cPoliMi-END
    *loc
    /*sp4b       19*
    *ins
    cPoliMi
          endif
    cPoliMi-END
    *loc
    /*sp4a       55*
    *ins
    cPoliMi
    *com
    *com
    *com
    *ins
      300 continue
          if(abs(ipol(1)).eq.99) goto 310 !skip check for PoliMi mixed source ±99
          if((mcal.lt.2.eqv.erg.le.elc(ipt)).and.nter.eq.0)                                  !/*sp6f
22*/
         & call errprn(1,nwse,4,erg,zero,'erg',' ',                                          !/*sp6f
23*/
         & 'source energy less than energy cutoff.')                                        !/*sp6f
24*/
      310 continue
    cPoliMi-END
    *loc
    /*sp6d        7*
    *ins
    cPoliMi
          starttme=tme
          if(ipol(1).eq.0 .or. abs(ipol(1)).eq.54 .or.
         +   abs(ipol(1)).eq.56 .and. iter56.eq.0) then

              y = yyy+21.3
              vhold = -xxx/sqrt(xxx*xxx+y*y+zzz*zzz)
              z = zzz/sqrt(xxx*xxx+y*y+zzz*zzz)
              y = y/sqrt(xxx*xxx+y*y+zzz*zzz)
              c = -z
              d = 1-c
              s = sqrt(vhold*vhold+y*y)

              uhold = y
    c          vhold = -x

              if(uhold.ne.0.0 .or. vhold.ne.0.0) then
                  whold = uhold
                  uhold = uhold/sqrt(whold*whold+vhold*vhold)
                  vhold = vhold/sqrt(whold*whold+vhold*vhold)
              endif

              uold(1) = uuu
              uold(2) = vvv
              uold(3) = www

              uuu = uold(1)*(c+uhold*uhold*d) + uold(2)*(uhold*vhold*d)
         +     + uold(3)*(vhold*s)
              vvv = uold(1)*(vhold*uhold*d) + uold(2)*(c+vhold*vhold*d)
         +     + uold(3)*(-uhold*s)
              www = uold(1)*(-vhold*s) + uold(2)*(uhold*s) + uold(3)*c
```

```
           uold(1) = uuu
           uold(2) = vvv
           uold(3) = www

           uuu = uuu/sqrt(uold(1)*uold(1)+uold(2)*uold(2)
     +     +uold(3)*uold(3))
           vvv = vvv/sqrt(uold(1)*uold(1)+uold(2)*uold(2)
     +     +uold(3)*uold(3))
           www = www/sqrt(uold(1)*uold(1)+uold(2)*uold(2)
     +     +uold(3)*uold(3))

          call upspare(i00,i00)
!         increments #nparticle also in standard run
!*******************        Patch for Kyle       **********************
! Print photon energy to file when ngen option called
           if(ipol(1).eq.0) then
              if(kufil(1,4).gt.0) then     !check of sampled multiplicities
                 write(kufil(1,4),'(I10,f9.4,3F10.4)') nps, erg,
     +             xxx, yyy, zzz
              endif
           endif
       else
c          print *,'Startp> nps,iter56',nps,iter56
          call sournew
!         upspare is called in sournew
       endif
cPoliMi-END
```

Appendix D. Relevant Cross Sections

D.1. Overview

Throughout this thesis several nuclear reaction mechanisms have been discussed. This appendix will be used to display the reaction cross sections for these interactions. Cross sections will be displayed for specific elements or isotopes. In each case, the total cross section will be displayed as a dashed, black line and any additional cross sections relevant to this work will be displayed as solid, colored lines.

D.2. Incident Neutron Cross Sections

Figure D.1-D.4 display the relevant neutron cross sections for ^{1}H, natural C, and ^{10}B. All cross sections come from the ENDF/B-VII.1 database [92]. The detected neutron interactions in this work come from elastic scatter of neutron energies between ~0.35 and 10 MeV. However, the interaction cross sections are shown for energies down to 1×10^{-8} MeV to accommodate the capture and (n, α) reactions, which become more prominent for slower neutrons. The following symbols will be used in the legends as necessary:

1. σ_T: Neuron total cross section
2. σ_{ES}: Neutron elastic-scatter cross section
3. σ_γ: Neutron capture cross section
4. σ_α: (n, α) reaction cross section

Figure D.1 shows the elastic scattering and neutron capture cross sections for ^{1}H. Neutron elastic scattering on ^{1}H is the necessary for neutron detection in EJ-309 scintillators. Elastic scattering and neutron capture are also important when neutron-emitting sources

are in the presence of hydrogenous materials, such as the polyethylene-shielded ^{252}Cf source discussed in Chapter 6. Neutron capture on hydrogen is the mechanism that produces the 2.2 MeV gamma ray that was used to verify the presence of a hydrogenous material.

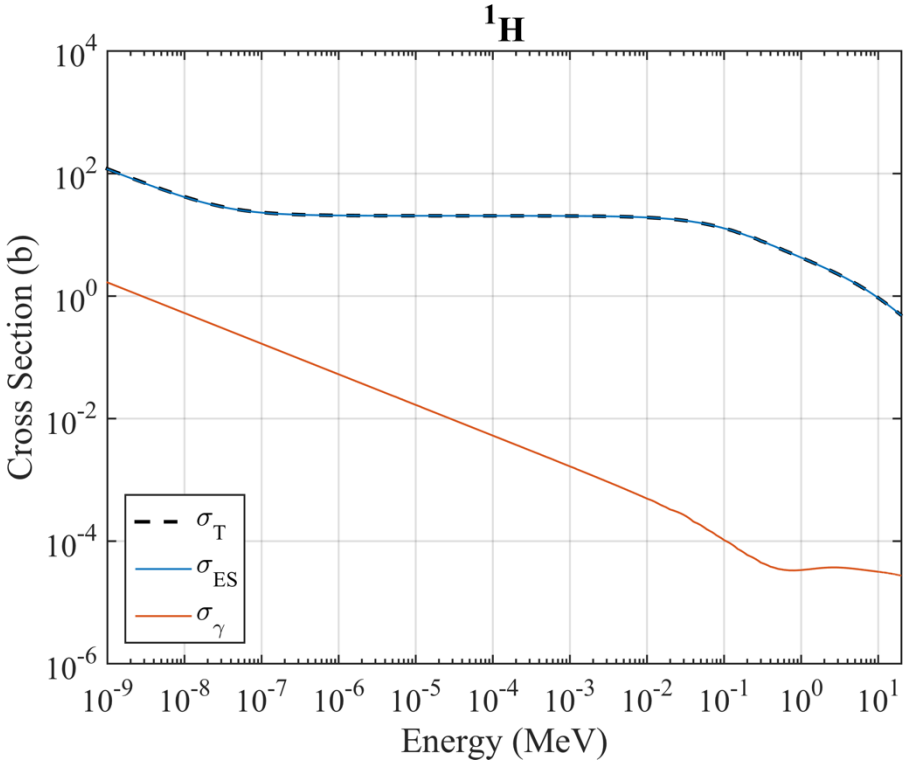

Figure D.1. Total, elastic scatter, and neutron capture cross sections for ^{1}H.

Figure D.2 shows the elastic scattering cross section for natural carbon. Neutron elastic scattering on carbon occurs in EJ-309 scintillators and also in materials such as polyethylene. The carbon cross sections are also shown in Figure D.3 for the energies between 0.1 and 20 MeV to emphasize the elastic scatter resonances in this region.

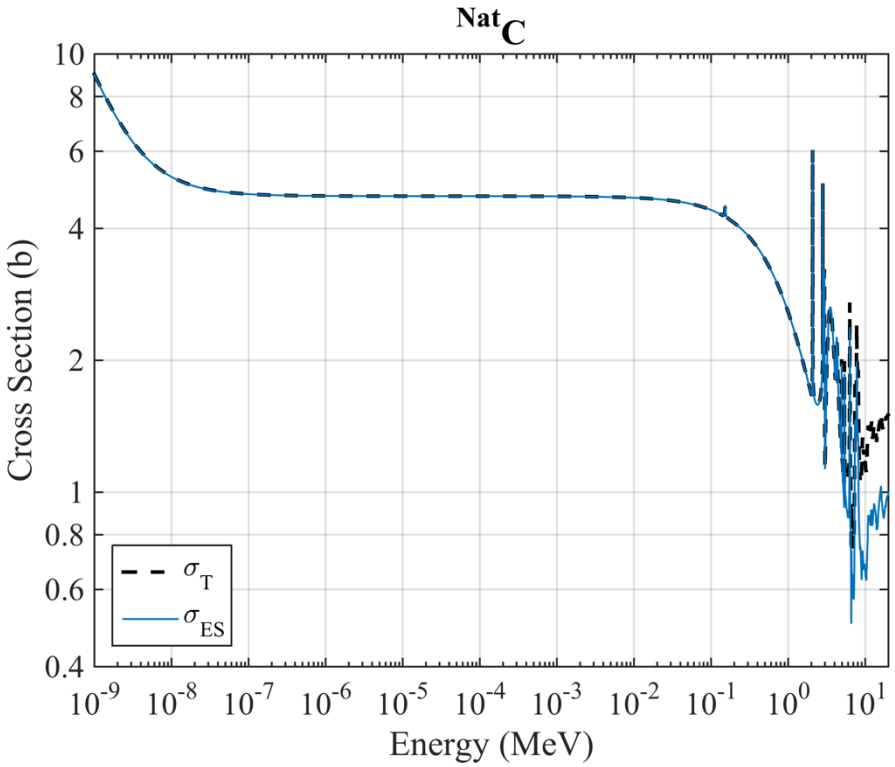

Figure D.2. Total and elastic scatter cross sections for natural carbon.

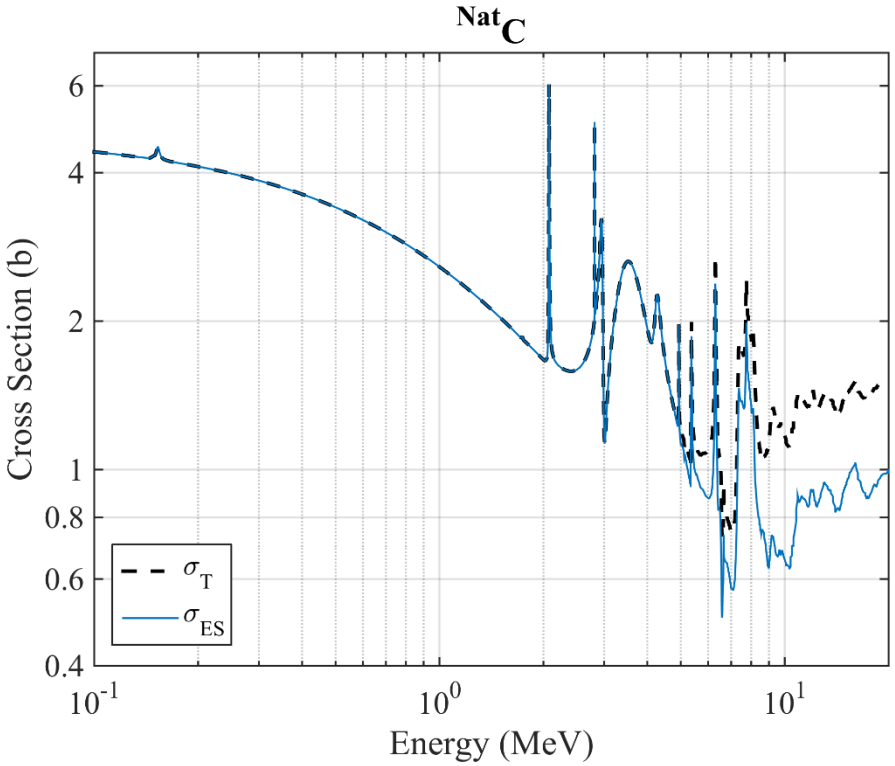

Figure D.3. Fast-neutron resonant structure of natural carbon.

Figure D.4 shows the cross section for the $^{10}B(n, \alpha)^{7}Li$ reaction. This reaction occurs in the PMTs and the BK7 optical window of the EJ-309 detectors is the source of the 0.478 MeV gamma ray that was detected in measurements with a high thermal-neutron flux. ^{10}B is ~20% abundant in natural B (with the rest being ^{11}B), and although B is present only in small quantities, the (n, α) cross section is large relative to the hydrogen and carbon cross sections shown above.

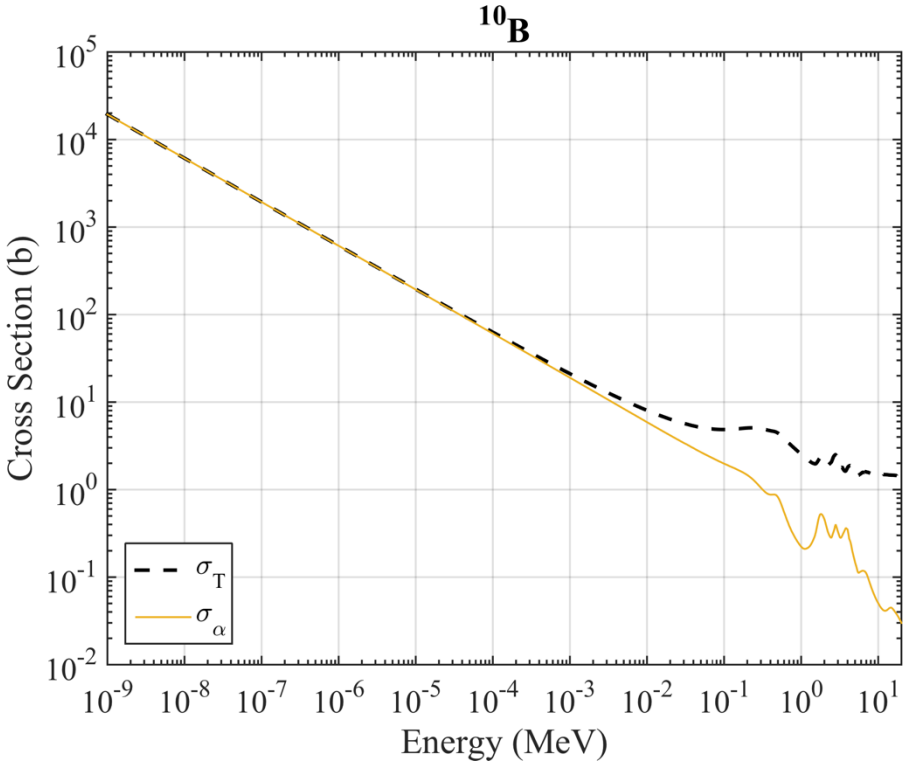

Figure D.4. Total and (n, α) interaction cross sections for ^{10}B.

D.3. Incident Photon Cross Sections

Figure D.5-Figure D.9 display the photon-total (σ_T), Compton scatter (σ_C), and photoelectric absorption (σ_P) cross sections for H, C, Na, I, and Pb. The cross sections for pair production are not shown because pair production did not have a noticeable impact on this work. The cross sections are displayed between 0.01 and 10 MeV. All cross sections come from the NIST XCOM database [119].

In this work, the hydrogen and carbon cross sections are relevant to Compton scattering in the EJ-309 detectors. Figure D.5 and Figure D.6 show that Compton scattering is the dominant interaction for both of the EJ-309 constituents, especially above the ~80 keV minimum energy required for an incident photon to interact above a 40 keV threshold in both planes.

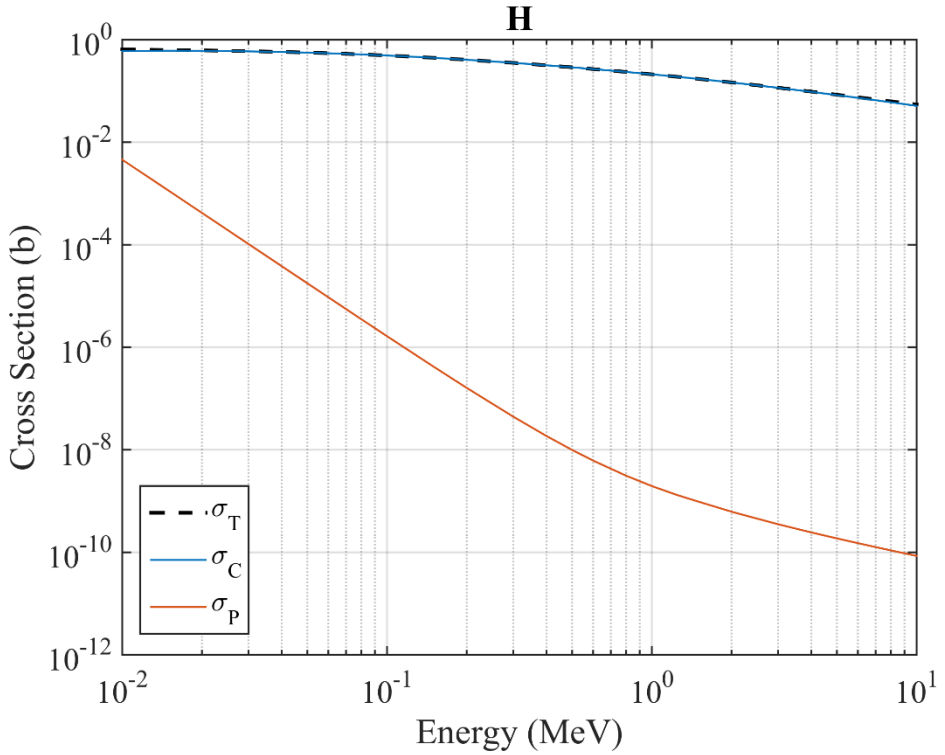

Figure D.5. Photon cross sections for hydrogen.

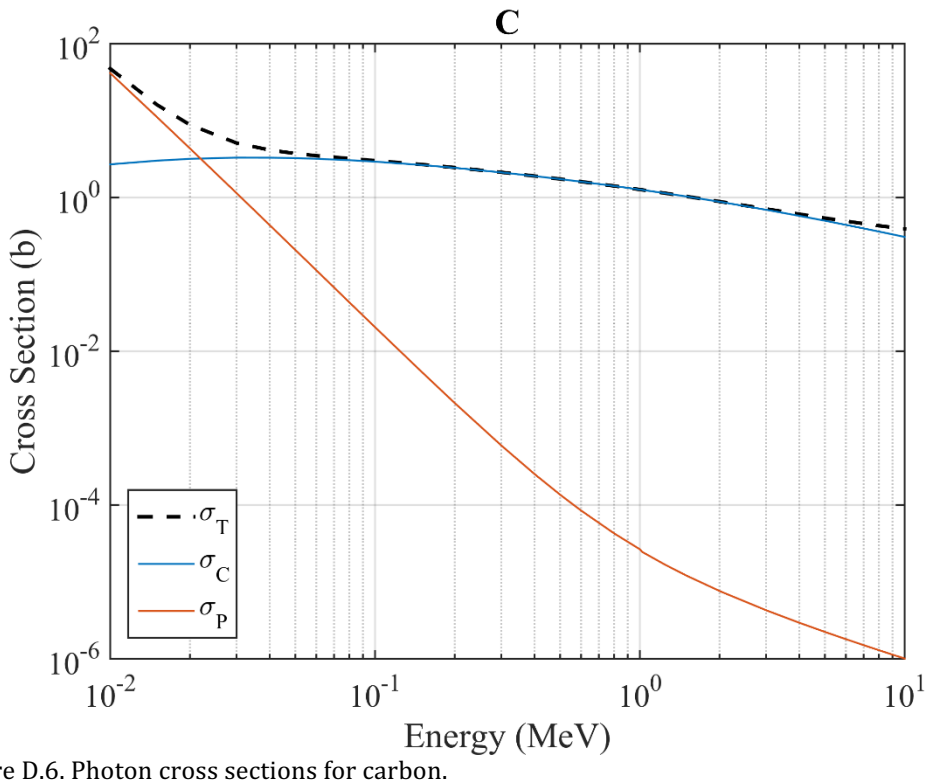

Figure D.6. Photon cross sections for carbon.

The sodium and iodine cross sections are relevant to the NaI(Tl) detectors in the back plane of the DPI. Figure D.8 shows that iodine has a dominant photoelectric absorption cross section for energies below ~0.3 MeV. At higher energies, and in sodium for energies above ~0.04 MeV, Compton scattering is the dominant interaction. While some photons will undergo photoelectric absorption after Compton scattering, others will escape without depositing their full energy in the NaI(Tl) detector. The system matrix models these effects, which helps the spectrum-isolation technique to reconstruct incomplete energy depositions at their full incident energy.

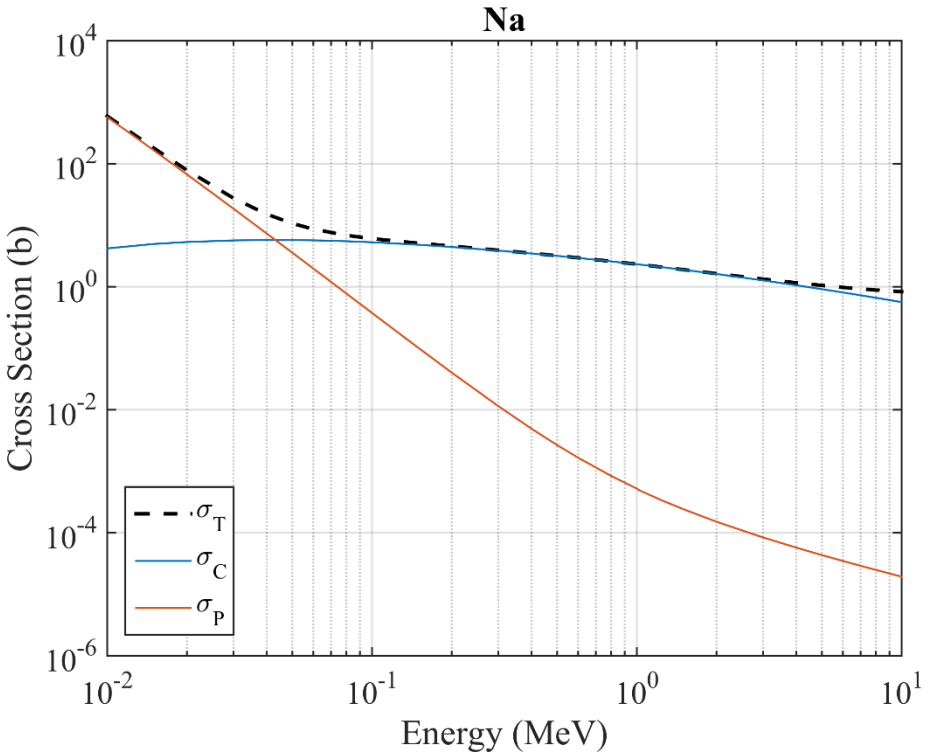

Figure D.7. Photon cross sections for sodium.

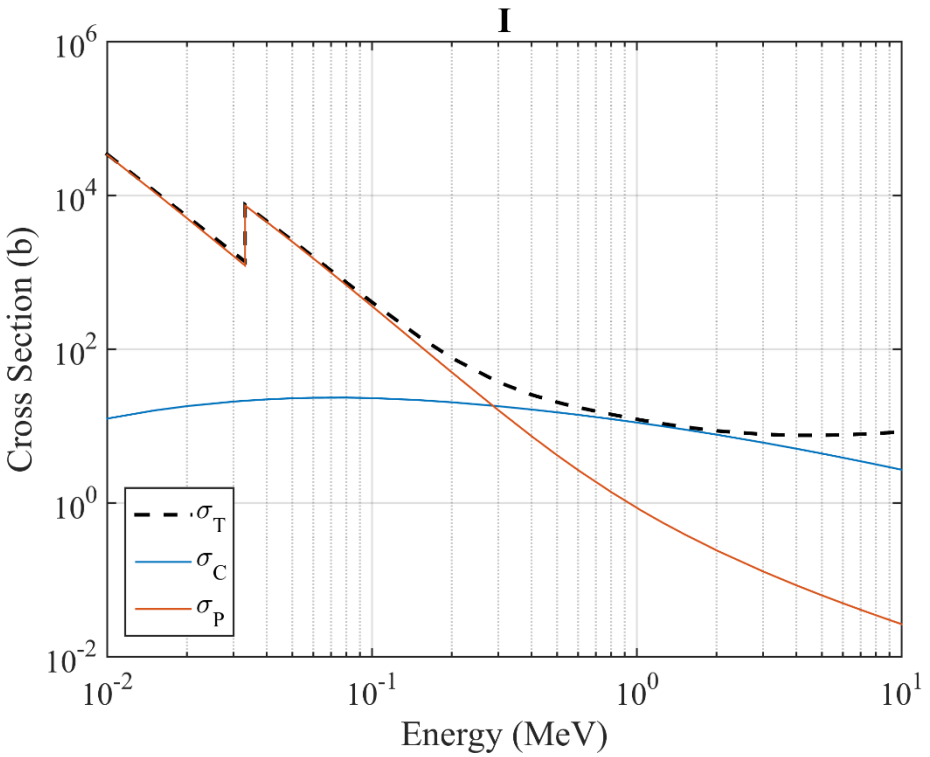

Figure D.8. Photon cross sections for iodine.

Figure D.9 shows the photon cross sections for lead, which are relevant to the lead shielding used to shield the ^{241}AmBe source in the weapons-grade plutonium measurement discussed in Chapter 6. Photoelectric absorption is the dominant interaction above ~0.5 MeV.

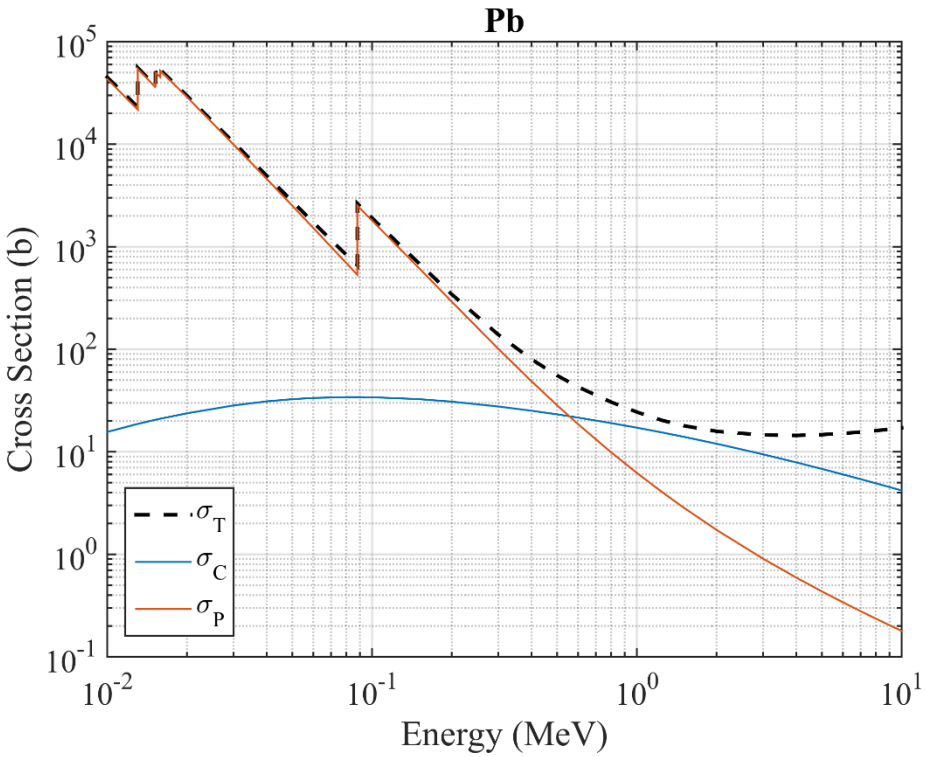

Figure D.9. Photon cross sections for lead.

References

[1] International Atomic Energy Agency, "Treaty on the Non-Proliferation of Nuclear Weapons," 1968.

[2] United States of America and Russian Federation, "Treaty Between the United States of America and the Russian Federation on Measured for the Further Reduction and Limitation of Strategic Offensive Arms," 2010.

[3] Los Alamos National Laboratory, *Passive Nondestructive Assay of Nuclear Materials*. 1991.

[4] D. Henzlova, R. Kouzes, R. McElroy, P. Peerani, M. Aspinall, K. Baird, A. Bakel, M. Borella, M. Bourne, L. Bourva, F. Cave, R. Chandra, D. Chernikova, S. Croft, G. Dermody, A. Dougan, J. Ely, E. Fanchini, P. Finocchiaro, V. Gavron, M. Kureta, K. D. Ianakiev, K. Ishiyama, T. Lee, C. Martin, K. McKinny, H. O. Menlove, C. Orton, A. Pappalardo, B. Pedersen, D. Peranteau, R. Plenteda, S. Pozzi, M. Schear, M. Seya, E. Siciliano, S. Stave, L. Sun, M. T. Swinhoe, H. Tagziria, S. Vaccaro, J. Takamine, A.-L. Weber, T. Yamaguchi, and H. Zhu, "Current Status of Helium-3 Alternative Technologies for Nuclear Safeguards," Los Alamos, NM (United States), Dec. 2015.

[5] "10 CFR 74 - Material Control and Accounting of Special Nuclear Material," 2016.

[6] International Atomic Energy Agency, "RFP 26070-EO Specifications for Gamma Imaging System," 2015.

[7] National Nuclear Security Administration Office of Nonproliferation and Arms Control and Misistry of Defence Atomic Weapons Establishment, "Joint U.S.-U.K. Report on Technical Cooperation for Arms Control," 2015.

[8] G. F. Knoll, *Radiation Detection and Measurement*, 4th ed. John Wiley & Sons, 2010.

[9] K. P. Ziock, C. J. Hailey, T. B. Gosnell, J. H. Lupton, and F. A. Harrison, "A gamma-ray imager for arms control," *IEEE Trans. Nucl. Sci.*, vol. 39, no. 4, pp. 1046–1050, 1992.

[10] S. Zelakiewicz, R. Hoctor, A. Ivan, W. Ross, E. Nieters, W. Smith, D. McDevitt, M. Wittbrodt, and B. Milbrath, "SORIS—A standoff radiation imaging system," *Nucl. Instruments Methods Phys. Res. Sect. A Accel. Spectrometers, Detect. Assoc. Equip.*, vol. 652, no. 1, pp. 5–9, Oct. 2011.

[11] P. Marleau, J. Brennan, E. Brubaker, and J. Steele, "Results from the coded aperture neutron imaging system," in *IEEE Nuclear Science Symposuim & Medical Imaging Conference*, 2010, pp. 1640–1646.

[12] P. Hausladen, J. Newby, F. Liang, and M. Blackston, "The Deployable Fast-Neutron Coded- Aperture Imager : Demonstration of Locating One or More Sources in Three Dimensions Prepared by," 2013.

[13] N. Mascarenhas, J. Brennan, K. Krenz, P. Marleau, and S. Mrowka, "Results with the neutron scatter camera," in *2008 IEEE Nuclear Science Symposium Conference Record*, 2008, vol. 56, no. 3, pp. 3368–3371.

[14] J. Brennan, E. Brubaker, R. Cooper, M. Gerling, C. Greenberg, P. Marleau, N.

Mascarenhas, and S. Mrowka, "Measurement of the Fast Neutron Energy Spectrum of an (241)Am-Be Source Using a Neutron Scatter Camera," *IEEE Trans. Nucl. Sci.*, vol. 58, no. 5, pp. 2426–2430, Oct. 2011.

[15] A. Poitrasson-Rivière, M. C. Hamel, J. K. Polack, K. L. Mcmillan, K. Ide, S. D. Clarke, M. Flaska, and S. A. Pozzi, "Design Considerations of a Dual-Particle Imager for Non-Proliferation Applications," in *Proceedings of INMM 52nd Annual Meeting*, 2011.

[16] J. Brennan, E. Brubaker, A. Nowack, J. Steele, M. Sweany, and D. Throckmorton, "Bubble masks for time-encoded imaging of fast neutrons," in *2013 IEEE Nuclear Science Symposium and Medical Imaging Conference (2013 NSS/MIC)*, 2013, pp. 1–7.

[17] J. Brennan, E. Brubaker, M. Gerling, N. Le Galloudec, P. Marleau, K. McMillan, and A. Nowack, "Results from field tests of the two-dimensional Time-Encoded Imaging System," 2014.

[18] J. Goldsmith, J. Brennan, M. Gerling, S. Kiff, N. Mascarenhas, and J. Van de Vreugde, "MINER - A Mobile Imager of Neutrons for Emergency Responders," in *Sandia National Laboratories Internal Report*, 2014.

[19] A. C. Madden, P. F. Bloser, D. Fourguette, L. Larocque, J. S. Legere, M. Lewis, M. L. McConnell, M. Rousseau, and J. M. Ryan, "An imaging neutron/gamma-ray spectrometer," in *Proceedings of SPIE 8710, Chemical, Biological, Radiological, Nuclear, and Explosives (CBRNE) Sensing*, 2013, vol. 8710, p. 87101L.

[20] A. Poitrasson-Rivière, M. C. Hamel, J. K. Polack, M. Flaska, S. D. Clarke, and S. A. Pozzi, "Dual-particle imaging system based on simultaneous detection of photon and neutron collision events," *Nucl. Instruments Methods Phys. Res. Sect. A Accel. Spectrometers, Detect. Assoc. Equip.*, vol. 760, pp. 40–45, Oct. 2014.

[21] S. T. Brown, Y. A. Boucher, J. Mann, Y. Zhu, and Z. He, "Thermal neutron source location using a 3-D position-sensitive CdZnTe detector array," in *2013 IEEE Nuclear Science Symposium and Medical Imaging Conference (2013 NSS/MIC)*, 2013, pp. 1–5.

[22] J. K. Polack, A. Poitrasson-Riviere, M. C. Hamel, K. Ide, K. L. McMillan, S. D. Clarke, M. Flaska, and S. A. Pozzi, "Dual-particle imager for standoff detection of special nuclear material," in *2011 IEEE Nuclear Science Symposium Conference Record*, 2011, no. 1, pp. 1494–1500.

[23] S. A. Pozzi, S. Clarke, M. Flaska, A. Poitrasson-Rivière, J. K. Polack, and K. Ide, "Dual-Particle Imaging System for Standoff SNM Detection in High-Background-Radiation Environments," US 2012/0256094 (not granted), 2012.

[24] M. C. Hamel, A. Poitrasson-Rivière, J. K. Polack, S. D. Clarke, M. Flaska, and S. A. Pozzi, "Design and Analysis of a Two-Plane Dual-Particle Imaging System," in *Proceedings of the INMM 54th Annual Meeting*, 2013.

[25] A. Poitrasson-Rivière, J. K. Polack, M. C. Hamel, D. D. Klemm, K. Ito, A. T. McSpaden, M. Flaska, S. D. Clarke, S. A. Pozzi, A. Tomanin, and P. Peerani, "Angular-resolution and material-characterization measurements for a dual-particle imaging system with mixed-oxide fuel," *Nucl. Instruments Methods Phys. Res. Sect. A Accel. Spectrometers, Detect. Assoc. Equip.*, vol. 797, pp. 278–284, Oct. 2015.

[26] M. C. Hamel, J. K. Polack, A. Poitrasson-Riviere, D. D. Klemm, M. Flaska, S. D. Clarke, S. A. Pozzi, A. Tomanin, and P. Peerani, "Time-of-flight neutron spectrum unfolding for mixed-oxide nuclear fuel and plutonium metal using a dual-particle imager," in *2014 IEEE Nuclear Science Symposium and Medical Imaging Conference (NSS/MIC)*, 2014, pp. 1–5.

[27] J. K. Polack, A. Poitrasson-Riviere, M. C. Hamel, K. Ito, S. D. Clarke, M. Flaska, S. A. Pozzi, A. Tomanin, and P. Peerani, "Image reconstruction of shielded mixed-oxide fuel using a dual-particle imaging system," in *2014 IEEE Nuclear Science Symposium and Medical Imaging Conference (NSS/MIC)*, 2014, no. 3, pp. 1–4.

[28] S. A. Pozzi, M. C. Hamel, J. K. Polack, M. L. Ruch, T. L. Beames-Canivet, and S. D. Clarke, "Dual-Particle Imaging for Treaty Verification," in *Proceedings of INMM 57th Annual Meeting*, 2016.

[29] J. Mattingly, J. Hutchinson, C. Sullivan, J. Stinnett, M. Kamuda, and M. Alamaniotis, "CNEC and CVT Subcritical Experiments with Category I Special Nuclear Material at the Nevada National Security Site Device Assembly Facility Gamma Spectroscopic Identification of SNM Isotopic Composition," in *Proceedings of INMM 57th Annual Meeting*, 2016.

[30] J. K. Polack, A. Poitrasson-Riviere, M. C. Hamel, M. F. Becchetti, K. Ide, S. D. Clarke, M. Flaska, and S. A. Pozzi, "Image reconstruction using a three-plane, dual-particle imager for standoff detection of special nuclear material," in *2012 IEEE Nuclear Science Symposium and Medical Imaging Conference Record (NSS/MIC)*, 2012, pp. 118–121.

[31] M. C. Hamel, J. K. Polack, A. Poitrasson-Rivière, M. Flaska, S. D. Clarke, S. A. Pozzi, A. Tomanin, and P. Peerani, "Stochastic image reconstruction for a dual-particle imaging system," *Nucl. Instruments Methods Phys. Res. Sect. A Accel. Spectrometers, Detect. Assoc. Equip.*, vol. 810, pp. 120–131, Feb. 2016.

[32] J. K. Polack, M. C. Hamel, A. Poitrasson-Riviere, P. Marleau, M. Flaska, and S. A. Pozzi, "Spectrum Isolation in Multi-Source Image Reconstruction Using a Dual-Particle Imager," in *Proceedings of INMM 56th Annual Meeting*, 2015.

[33] L. A. Shepp and Y. Vardi, "Maximum Likelihood Reconstruction for Emission Tomography," *IEEE Trans. Med. Imaging*, vol. 1, no. 2, pp. 113–122, Oct. 1982.

[34] S. A. Pozzi, S. D. Clarke, W. J. Walsh, E. C. Miller, J. L. Dolan, M. Flaska, B. M. Wieger, A. Enqvist, E. Padovani, J. K. Mattingly, D. L. Chichester, and P. Peerani, "MCNPX-PoliMi for nuclear nonproliferation applications," *Nucl. Instruments Methods Phys. Res. Sect. A Accel. Spectrometers, Detect. Assoc. Equip.*, vol. 694, pp. 119–125, Dec. 2012.

[35] S. A. Pozzi, E. Padovani, and M. Marseguerra, "MCNP-PoliMi: a Monte-Carlo code for correlation measurements," *Nucl. Instruments Methods Phys. Res. Sect. A Accel. Spectrometers, Detect. Assoc. Equip.*, vol. 513, no. 3, pp. 550–558, Nov. 2003.

[36] J. K. Polack, M. Flaska, A. Enqvist, C. S. Sosa, C. C. Lawrence, and S. A. Pozzi, "An algorithm for charge-integration, pulse-shape discrimination and estimation of neutron/photon misclassification in organic scintillators," *Nucl. Instruments Methods Phys. Res. Sect. A Accel. Spectrometers, Detect. Assoc. Equip.*, vol. 795, pp. 253–267, Sep. 2015.

[37] R. W. Todd, J. M. Nightingale, and D. B. Everett, "A proposed γ camera," *Nature*, vol. 251, no. 5471, pp. 132–134, Sep. 1974.

[38] D. B. Everett, J. S. Fleming, R. W. Todd, and J. M. Nightingale, "Gamma-radiation imaging system based on the Compton effect," *Proc. Inst. Electr. Eng.*, vol. 124, no. 11, p. 995, 1977.

[39] M. Singh, "An electronically collimated gamma camera for single photon emission computed tomography. Part I: Theoretical considerations and design criteria," *Med. Phys.*, vol. 10, no. 4, p. 421, 1983.

[40] D. Herzo, R. Koga, W. A. Millard, S. Moon, J. Ryan, R. Wilson, A. D. Zych, and R. S. White,

"A large double scatter telescope for gamma rays and neutrons," *Nucl. Instruments Methods*, vol. 123, no. 3, pp. 583–597, Feb. 1975.

[41] V. Schonfelder, R. Diehl, G. G. Lichti, H. Steinle, B. N. Swanenburg, A. J. M. Deerenberg, H. Aarts, J. Lockwood, W. Webber, J. Macri, J. Ryan, G. Simpson, B. G. Taylor, K. Bennett, and M. Snelling, "The Imaging Compton Telescope Comptel on the Gamma Ray Observatory," *IEEE Trans. Nucl. Sci.*, vol. 31, no. 1, pp. 766–770, 1984.

[42] G. W. Phillips, "Gamma-ray imaging with Compton cameras," *Nucl. Instruments Methods Phys. Res. Sect. B Beam Interact. with Mater. Atoms*, vol. 99, no. 1–4, pp. 674–677, May 1995.

[43] Y. F. Du, Z. He, G. F. Knoll, D. K. Wehe, and W. Li, "Evaluation of a Compton scattering camera using 3-D position sensitive CdZnTe detectors," *Nucl. Instruments Methods Phys. Res. Sect. A Accel. Spectrometers, Detect. Assoc. Equip.*, vol. 457, no. 1–2, pp. 203–211, Jan. 2001.

[44] A. Poitrasson-Rivière, "Development of a Dual-Particle Imaging System for Nonproliferation Applications," 2016.

[45] S. A. Pozzi, M. Flaska, A. Enqvist, and I. Pázsit, "Monte Carlo and analytical models of neutron detection with organic scintillation detectors," *Nucl. Instruments Methods Phys. Res. Sect. A Accel. Spectrometers, Detect. Assoc. Equip.*, vol. 582, no. 2, pp. 629–637, Nov. 2007.

[46] ELJEN Technolgies, "Ej-309 Liquid Scintillator Pulse-Shape Discrimination Properties," 2010.

[47] S. Marrone, D. Cano-Ott, N. Colonna, C. Domingo, F. Gramegna, E. . Gonzalez, F. Gunsing, M. Heil, F. Käppeler, P. . Mastinu, P. . Milazzo, T. Papaevangelou, P. Pavlopoulos, R. Plag, R. Reifarth, G. Tagliente, J. . Tain, and K. Wisshak, "Pulse shape analysis of liquid scintillators for neutron studies," *Nucl. Instruments Methods Phys. Res. Sect. A Accel. Spectrometers, Detect. Assoc. Equip.*, vol. 490, no. 1–2, pp. 299–307, Sep. 2002.

[48] I. A. Pawełczak, S. A. Ouedraogo, A. M. Glenn, R. E. Wurtz, and L. F. Nakae, "Studies of neutron–gamma pulse shape discrimination in EJ-309 liquid scintillator using charge integration method," *Nucl. Instruments Methods Phys. Res. Sect. A Accel. Spectrometers, Detect. Assoc. Equip.*, vol. 711, pp. 21–26, May 2013.

[49] A. Enqvist, C. C. Lawrence, B. M. Wieger, S. a. Pozzi, and T. N. Massey, "Neutron light output response and resolution functions in EJ-309 liquid scintillation detectors," *Nucl. Instruments Methods Phys. Res. Sect. A Accel. Spectrometers, Detect. Assoc. Equip.*, vol. 715, no. January 2016, pp. 79–86, Jul. 2013.

[50] ET Enterprises, "9821B Series Data Sheet," 2012.

[51] M. Flaska and S. A. Pozzi, "Identification of shielded neutron sources with the liquid scintillator BC-501A using a digital pulse shape discrimination method," *Nucl. Instruments Methods Phys. Res. Sect. A Accel. Spectrometers, Detect. Assoc. Equip.*, vol. 577, no. 3, pp. 654–663, Jul. 2007.

[52] A. Poitrasson-Rivière, B. A. Maestas, M. C. Hamel, S. D. Clarke, M. Flaska, S. A. Pozzi, G. Pausch, C.-M. Herbach, A. Gueorguiev, M. F. Ohmes, and J. Stein, "Monte Carlo investigation of a high-efficiency, two-plane Compton camera for long-range localization of radioactive materials," *Prog. Nucl. Energy*, vol. 81, pp. 127–133, May 2015.

[53] A. Di Fulvio, T. H. Shin, M. C. Hamel, and S. A. Pozzi, "Digital pulse processing for NaI(Tl) detectors," *Nucl. Instruments Methods Phys. Res. Sect. A Accel. Spectrometers, Detect.*

Assoc. Equip., vol. 806, pp. 169–174, Jan. 2016.
[54] CAEN, "720 Digitizer Family Data Sheet," 2013.
[55] CAEN, "730 Digitizer Family Data Sheet," 2015.
[56] K. Ide, M. F. Becchetti, M. Flaska, A. Poitrasson-Riviere, M. C. Hamel, J. K. Polack, C. C. Lawrence, S. D. Clarke, and S. A. Pozzi, "Analysis of a measured neutron background below 6MeV for fast-neutron imaging systems," *Nucl. Instruments Methods Phys. Res. Sect. A Accel. Spectrometers, Detect. Assoc. Equip.*, vol. 694, pp. 24–31, Dec. 2012.
[57] L. S. Waters, "MCNPX User's manual version 2.3.0," 2002.
[58] E. Padovani, S. A. Pozzi, S. D. Clarke, and E. C. Miller, "MCNPX-PoliMi V2.0 Users Manual," 2012.
[59] E. C. Miller, S. D. Clarke, M. Flaska, S. Prasad, S. A. Pozzi, and E. Padovani, "MCNPX-PoliMi Post-processing Algorithm for Detector Response Simulations," *J. Nucl. Mater. Manag.*, vol. XL, no. 2, pp. 34–41, 2012.
[60] E. C. Miller, A. Poitrasson-Rivière, A. Enqvist, J. L. Dolan, S. Prasad, M. M. Bourne, K. Weinfurther, and S. D. Clarke, "MCNPX-PoliMi Post-Processor (MPPost) Manual," 2012.
[61] M. A. Norsworthy, A. Poitrasson-Rivière, M. L. Ruch, S. D. Clarke, and S. A. Pozzi, "Evaluation of Neutron Light Output Response Functions in Organic Scintillators," submitted to *Nucl. Instruments Methods Phys. Res. A*.
[62] J. B. Birks, "Organic Liquid Scintillators," in *The Theory and Practice of Scintillation Counting*, London: Elsevier, 1964, pp. 269–320.
[63] S. P. Ahlen, B. G. Cartwright, and G. Tarlé, "Return to unsaturated response of polymeric scintillators excited by relativistic heavy ions," *Nucl. Instruments Methods*, vol. 147, no. 2, pp. 321–328, Dec. 1977.
[64] K. Roemer, G. Pausch, C.-M. Herbach, Y. Kong, R. Lentering, C. Plettner, J. Stein, M. Moszynski, . Swiderski, and T. Szczesniak, "A technique for measuring the energy resolution of low-Z scintillators," in *2009 IEEE Nuclear Science Symposium Conference Record (NSS/MIC)*, 2009, pp. 6–11.
[65] M. L. Ruch, M. Flaska, and S. A. Pozzi, "Pulse shape discrimination performance of stilbene coupled to low-noise silicon photomultipliers," *Nucl. Instruments Methods Phys. Res. Sect. A Accel. Spectrometers, Detect. Assoc. Equip.*, vol. 793, no. March 2016, pp. 1–5, Sep. 2015.
[66] R. M. Preston, J. E. Eberhardt, and J. R. Tickner, "Neutron-Gamma Pulse Shape Discrimination Using Organic Scintillators With Silicon Photomultiplier Readout," *IEEE Trans. Nucl. Sci.*, vol. 61, no. 4, pp. 2410–2418, Aug. 2014.
[67] M. Grodzicka, T. Szczesniak, M. Moszynski, D. Wolski, L. Swiderski, K. Grodzicki, S. Korolczuk, J. Baszak, and P. Schotanus, "Study of n-γ discrimination by zero-crossing method with SiPM based scintillation detectors," in *2014 IEEE Nuclear Science Symposium and Medical Imaging Conference (NSS/MIC)*, 2014, pp. 1–3.
[68] M. L. Ruch, P. Marleau, and S. A. Pozzi, "Proof of Principle Simulation of a Handheld Neutron Scatter Camera," submitted to *Advances in Nuclear Nonproliferation Technology and Policy Conference*, 2016.
[69] J. A. Fessler, "Statistical Methods for Image Reconstruction Image Reconstruction Methods," 2004.
[70] J. A. Fessler, *Image reconstruction: Algorithms and analysis*. 2008.
[71] G. Fehrenbacher, R. Meckbach, and P. Jacob, "Unfolding the response of a Ge detector

used for in-situ gamma-ray spectrometry," *Nucl. Instruments Methods Phys. Res. Sect. A Accel. Spectrometers, Detect. Assoc. Equip.*, vol. 383, no. 2–3, pp. 454–462, 1996.
[72] M. Matzke, "<title>Unfolding of particle spectra</title>," in *International Conference Neutrons in Research and Industry*, 1997, vol. 2867, pp. 598–607.
[73] L. J. Meng and D. Ramsden, "An inter-comparison of three spectral-deconvolution algorithms for gamma-ray spectroscopy," *IEEE Trans. Nucl. Sci.*, vol. 47, no. 4, pp. 1329–1336, 2000.
[74] L. Cartegni and S. A. Pozzi, "Simulation of the neutron response matrix for a liquid scintillator and spectrum unfolding," in *Oak Ridge National Laboratory Internal Report*, 2005, no. ORNL/TM-2004/315.
[75] S. P. Tripathy, A. K. Bakshi, V. Sathian, S. M. Tripathi, H. R. Vega-carrillo, M. Nandy, P. K. Sarkar, and D. N. Sharma, "Measurement of 241Am-Be spectra (bare and Pb-covered) using TLD pairs in multi-spheres: Spectrum unfolding by different methods," *Nucl. Instruments Methods Phys. Res. Sect. A Accel. Spectrometers, Detect. Assoc. Equip.*, vol. 598, no. 2, pp. 556–560, 2009.
[76] C. Mertens, C. De Lellis, and F. Tondeur, "Neutron-photon discrimination and spectrum unfolding with a stilbene detector," *Appl. Radiat. Isot.*, vol. 68, no. 4–5, pp. 957–960, 2010.
[77] D. Xu and Z. He, "Gamma-ray Energy-imaging Integrated Deconvolution," in *IEEE Nuclear Science Symposium Conference Record, 2005*, 2005, vol. 2, pp. 882–886.
[78] D. Xu and Z. He, "Gamma-ray energy-imaging integrated spectral deconvolution," *Nucl. Instruments Methods Phys. Res. Sect. A Accel. Spectrometers, Detect. Assoc. Equip.*, vol. 574, no. 1, pp. 98–109, Apr. 2007.
[79] H. H. Barrett, T. White, and L. C. Parra, "List-mode likelihood," *J. Opt. Soc. Am. A*, vol. 14, no. 11, p. 2914, Nov. 1997.
[80] W. Wang, C. G. Wahl, J. M. Jaworski, and Z. He, "Maximum-Likelihood Deconvolution in the Spatial and Spatial-Energy Domain for Events With Any Number of Interactions," *IEEE Trans. Nucl. Sci.*, vol. 59, no. 2, pp. 469–478, Apr. 2012.
[81] A. R. De Pierro, "A modified expectation maximization algorithm for penalized likelihood estimation in emission tomography," *IEEE Trans. Med. Imaging*, vol. 14, no. 1, pp. 132–137, Mar. 1995.
[82] L. Parra and H. H. Barrett, "List-mode likelihood: EM algorithm and image quality estimation demonstrated on 2-D PET," *IEEE Trans. Med. Imaging*, vol. 17, no. 2, pp. 228–235, Apr. 1998.
[83] R. H. Huesman, G. J. Klein, W. W. Moses, Jinyi Qi, B. W. Reutter, and P. R. G. Virador, "List-mode maximum-likelihood reconstruction applied to positron emission mammography (PEM) with irregular sampling," *IEEE Trans. Med. Imaging*, vol. 19, no. 5, pp. 532–537, May 2000.
[84] A. P. Dempster, N. M. Laird, and D. B. Rubin, "Maximum Likelhood from Incomplete Data via the EM Algorithm," *J. R. Stat. Soc. Ser. B*, vol. 39, no. 1, pp. 1–38, 1977.
[85] E. Veklerov, J. Llacer, and E. J. Hoffman, "MLE reconstruction of a brain phantom using a Monte Carlo transition matrix and a statistical stopping rule," *IEEE Trans. Nucl. Sci.*, vol. 35, no. 1, pp. 603–607, Feb. 1988.
[86] J. Llacer and E. Veklerov, "Feasible images and practical stopping rules for iterative algorithms in emission tomography," *IEEE Trans. Med. Imaging*, vol. 8, no. 2, pp. 186–193, Jun. 1989.

[87] N. Bissantz, B. A. Mair, and A. Munk, "A multi-scale stopping criterion for MLEM reconstructions in PET," in *2006 IEEE Nuclear Science Symposium Conference Record*, 2006, vol. 6, pp. 3376–3379.
[88] N. Bissantz, B. A. Mair, and A. Munk, "A statistical stopping rule for MLEM reconstructions in PET," in *2008 IEEE Nuclear Science Symposium Conference Record*, 2008, no. m, pp. 4198–4200.
[89] A. Gaitanis, G. Kontaxakis, G. Spyrou, G. Panayiotakis, and G. Tzanakos, "PET image reconstruction: A stopping rule for the MLEM algorithm based on properties of the updating coefficients," *Comput. Med. Imaging Graph.*, vol. 34, no. 2, pp. 131–141, Mar. 2010.
[90] University of Michigan ARC-TS, "Flux." [Online]. Available: http://arc-ts.umich.edu/systems-and-services/flux/.
[91] MathWorks, "Copmutational Advantages of Sparse Matrices." [Online]. Available: http://www.mathworks.com/help/matlab/math/computational-advantages-of-sparse-matrices.html.
[92] M. B. Chadwick, M. Herman, P. Obložinský, M. E. Dunn, Y. Danon, A. C. Kahler, D. L. Smith, B. Pritychenko, G. Arbanas, R. Arcilla, R. Brewer, D. A. Brown, R. Capote, A. D. Carlson, Y. S. Cho, H. Derrien, K. Guber, G. M. Hale, S. Hoblit, S. Holloway, T. D. Johnson, T. Kawano, B. C. Kiedrowski, H. Kim, S. Kunieda, N. M. Larson, L. Leal, J. P. Lestone, R. C. Little, E. A. McCutchan, R. E. MacFarlane, M. MacInnes, C. M. Mattoon, R. D. McKnight, S. F. Mughabghab, G. P. A. Nobre, G. Palmiotti, A. Palumbo, M. T. Pigni, V. G. Pronyaev, R. O. Sayer, A. A. Sonzogni, N. C. Summers, P. Talou, I. J. Thompson, A. Trkov, R. L. Vogt, S. C. van der Marck, A. Wallner, M. C. White, D. Wiarda, and P. G. Young, "ENDF/B-VII.1 Nuclear Data for Science and Technology: Cross Sections, Covariances, Fission Product Yields and Decay Data," *Nucl. Data Sheets*, vol. 112, no. 12, pp. 2887–2996, Dec. 2011.
[93] R. . Gehrke, R. Aryaeinejad, J. . Hartwell, W. . Yoon, E. Reber, and J. . Davidson, "The γ-ray spectrum of 252Cf and the information contained within it," *Nucl. Instruments Methods Phys. Res. Sect. B Beam Interact. with Mater. Atoms*, vol. 213, pp. 10–21, Jan. 2004.
[94] H. H. Barrett, D. W. Wilson, and B. M. W. Tsui, "Noise properties of the EM algorithm. I. Theory," *Phys. Med. Biol.*, vol. 39, no. 5, pp. 833–846, May 1994.
[95] B. Efron and R. J. Tibshirani, "An Introduction to the Bootstrap," *SIAM Rev.*, vol. 36, no. 4, pp. 677–678, Dec. 1994.
[96] D. R. Haynor and S. D. Woods, "Resampling estimates of precision in emission tomography," *IEEE Trans. Med. Imaging*, vol. 8, no. 4, pp. 337–343, 1989.
[97] I. Ruczinski, C. Kooperberg, and M. LeBlanc, "Logic Regression," *J. Comput. Graph. Stat.*, vol. 12, no. 3, pp. 475–511, Sep. 2003.
[98] M. Ibaraki, K. Matsubara, K. Nakamura, H. Yamaguchi, and T. Kinoshita, "Bootstrap methods for estimating PET image noise: experimental validation and an application to evaluation of image reconstruction algorithms," *Ann. Nucl. Med.*, vol. 28, no. 2, pp. 172–182, Feb. 2014.
[99] I. Buvat, "A non-parametric bootstrap approach for analysing the statistical properties of SPECT and PET images.," *Phys. Med. Biol.*, vol. 47, no. 10, pp. 1761–1775, 2002.
[100] C. Lartizien, J.-B. Aubin, and I. Buvat, "Comparison of Bootstrap Resampling Methods for 3-D PET Imaging," *IEEE Trans. Med. Imaging*, vol. 29, no. 7, pp. 1442–1454, Jul. 2010.

[101] M. Ibaraki, K. Matsubara, K. Nakamura, H. Yamaguchi, and T. Kinoshita, "Bootstrap methods for estimating PET image noise: experimental validation and an application to evaluation of image reconstruction algorithms," *Ann. Nucl. Med.*, vol. 28, no. 2, pp. 172–182, Feb. 2014.
[102] I. Buvat, "A non-parametric bootstrap approach for analysing the statistical properties of SPECT and PET images," *Phys. Med. Biol.*, vol. 47, no. 10, p. 311, May 2002.
[103] D. W. Wilson and B. M. W. Tsui, "Noise properties of filtered-backprojection and ML-EM reconstructed emission tomographic images," *IEEE Trans. Nucl. Sci.*, vol. 40, no. 4, pp. 1198–1203, 1993.
[104] D. W. Wilson, B. M. W. Tsui, and H. H. Barrett, "Noise properties of the EM algorithm. II. Monte Carlo simulations," *Phys. Med. Biol.*, vol. 39, no. 5, pp. 847–871, May 1994.
[105] M. C. Hamel, "Private Communication," 2016.
[106] J. Qi and R. H. Huesman, "Propagation of Errors From the Sensitivity Image in List Mode Reconstruction," *IEEE Trans. Med. Imaging*, vol. 23, no. 9, pp. 1094–1099, Sep. 2004.
[107] J. Qi and R. H. Huesman, "Effect of errors in the system matrix on maximum a posteriori image reconstruction," *Phys. Med. Biol.*, vol. 50, no. 14, pp. 3297–3312, Jul. 2005.
[108] A. O. Hero, *Statistical Methods for Signal Processing*. XanEdu, 2013.
[109] H. R. Vega-Carrillo, V. M. Hernández-Dávila, T. Rivera-Montalvo, and A. Sánchez, "Characterization of a 239-PuBe Isotopic Neutron Source," *Proc. ISSSD 2012*, no. 1, pp. 64–69, 2012.
[110] K. W. Geiger and L. Van Der Zwan, "Radioactive neutron source spectra from 9Be(α, n) cross section data," *Nucl. Instruments Methods*, vol. 131, no. 2, pp. 315–321, Dec. 1975.
[111] R. L. Lehman, "The origin of neutron groups in Be(α,n) sources," *Nucl. Instruments Methods*, vol. 60, no. 3, pp. 253–260, Apr. 1968.
[112] M. E. Anderson and R. A. Neff, "Neutron energy spectra of different size 239Pu Be(α,n) sources," *Nucl. Instruments Methods*, vol. 99, no. 2, pp. 231–235, Mar. 1972.
[113] H. R. Vega-Carrillo, E. Manzanares-Acuña, A. M. Becerra-Ferreiro, and A. Carrillo-Nuñez, "Neutron and gamma-ray spectra of 239PuBe and 241AmBe," *Appl. Radiat. Isot.*, vol. 57, no. 2, pp. 167–170, Aug. 2002.
[114] J. Scherzinger, J. R. M. Annand, G. Davatz, K. G. Fissum, U. Gendotti, R. Hall-Wilton, E. Håkansson, R. Jebali, K. Kanaki, M. Lundin, B. Nilsson, A. Rosborge, and H. Svensson, "Tagging fast neutrons from an 241Am/9Be source," *Appl. Radiat. Isot.*, vol. 98, pp. 74–79, Apr. 2015.
[115] C. M. Cialella and J. A. Devanney, "A combination neutron and gamma ray spectrometer," *Nucl. Instruments Methods*, vol. 60, no. 3, pp. 269–277, Apr. 1968.
[116] D. B. Barber, "PuBe MRC-270 Documentation." 1964.
[117] C. C. Lawrence, "Neutron Spectrum Unfolding with Organic Scintillators for Arms-control Verification," 2014.
[118] R. B. Kidman, "Reckoning THOR," 1972.
[119] M. J. Berger, J. H. Hubbell, S. M. Seltzer, J. Chang, J. S. Coursey, R. Sukumar, and D. S. Zucker, "XCOM: photon cross sections database," *NIST Stand. Ref. Database*, vol. 8, pp. 87–3597, 1998.
[120] G. E. Hansen and H. C. Paxton, "Thor, A Thorium-Reflected Plutonium-Metal Critical Assembly," *Nucl. Sci. Eng.*, vol. 71, no. 3, pp. 287–293, 1979.